UNIVERSITY OF OKLAHOMA

GRADUATE COLLEGE

THREE-DIMENSIONAL FULLY COUPLED GEOMECHANICAL MODELING OF THE RESPONSE OF OKLAHOMA FAULTS TO SALTWATER DISPOSAL

A DISSERTATION

SUBMITTED TO THE GRADUATE FACULTY

in partial fulfillment of the requirements for the

Degree of

DOCTOR OF PHILOSOPHY

By

BEHZAD HEMAMI
Norman, Oklahoma
2021

Downloaded from SHAREOK. Persistent Handle URL: https://hdl.handle.net/11244/330231

THREE-DIMENSIONAL FULLY COUPLED GEOMECHANICAL MODELING OF THE RESPONSE OF OKLAHOMA FAULTS TO SALTWATER DISPOSAL

A DISSERTATION APPROVED FOR THE
MEWBOURNE SCHOOL OF PETROLEUM AND GEOLOGICAL ENGINEERING

BY THE COMMITTEE CONSISTING OF

Dr. Ahmad Ghassemi, Chair

Dr. Brett M. Carpenter

Dr. Jean-Claude Roegiers

Dr. Xingru Wu

Dr. Mashhad Fahes

© Copyright by BEHZAD HEMAMI 2021
All Rights Reserved.

To my beloved mother **Monireh P. Hemami**

who loves unconditionally,

and to my wife, love of my life, **Parastoo Imantalab**

who sacrificed herself to fulfill my dream.

Acknowledgements

It is a pleasure to express my deep sense of thanks and gratitude to my advisor and guide, Prof. Ahmad Ghassemi, for his support, and helpful advice throughout my research. He is not only my advisor, but my mentor from whom I learn how a person can be ethical, successful, powerful, humble, and considerate at the same time. Without his support and supervising, the completion of this dissertation would not be possible.

I would like to thank the rest of my Ph.D. committee: Prof. Roegiers, Dr.Wu, Dr.Fahes, and Dr. Carpenter for their helpful guidance and encouragement. I benefited a lot from their pertinent comments and suggestions.

I greatly appreciate the Mewbourne School of Petroleum and Geological Engineering staff, especially Katie Shapiro for their help and encouragement. I would also want to thank Itasca Consulting Group for providing me the software for my research.

My particular gratitude goes to my dear family, especially my parents-in-law, Mohammadreza Imantalab and Nahid Yadegarian for their continued encouragement and support over the past years.

Last but not the least, I like to appreciate my colleagues and friends for their contribution to my Ph.D. program. I would also like to thank my deepest gratitude to Dr. Maysam Pournik for all he has done for me.

Table of Contents

Acknowledgements v

Table of Contents vi

List of Tables ix

List of Figures x

Abstract xxix

Introduction 1

1.1 Background on Induced Seismicity 1

1.1.1 Geothermal Reservoirs 3

1.1.2 Hydraulic Fracturing 4

1.2 Induced Seismicity Mechanism 4

1.3 Wastewater Disposal and Seismicity in Oklahoma, US 10

1.4 Research Objectives 14

1.5 Dissertation Outline 14

Model Development 17

2.1 Formulation 17

2.1.1 Fluid Mass Balance 17

2.1.2 Fluid Transport (Darcy's Law) 17

2.2 Explicit Finite Difference 18

2.3 Distinct Element Method 18

2.4 Hydraulic Modelling in 3DEC 21

Basement Fault Reactivation in Response to Injection into Overlying Sedimentary Reservoir 24

3.1 Introduction 24
3.2 Poroelastic Response of Target Layers and Adjacent Layers to the Fluid Injection 27
3.3 Effect of $S_{H,max}$ Azimuth and Fault Strike Direction 32
3.4 Effect of Hydromechanical Properties of the Reservoir, the Basement, and the Fault Zone on Fault Reactivation 40
3.4.1 Fault Damage Zone 40
3.4.2 Sedimentary-Crystalline Rock Nonconformity 44
3.4.3 Scenario 3 45
3.4.4 Scenario 4 62
3D Geomechanical Modeling of the Response of the Wilzetta Fault to Saltwater Disposal 70
4.1 Introduction 70
4.2 The Wilzetta Fault Zone 71
4.3 Numerical Model 78
4.4 Simulation Setup 78
4.5 Simulation Results 85
4.5.1 Scenario 1- Cases 1 and 2: Impermeable and Permeable Faults with Low Arbuckle Permeability 85
4.5.2 Scenario 1- Cases 3 and 4: Impermeable and Permeable Faults with High Arbuckle Permeability 96
4.5.3 Scenario 2: Hydraulic Communication Between Geological Layers via Fault Damage Zones, Low and High Arbuckle Permeability 97

4.5.4 Scenario 3: Injection from Mazkoori and Wilzetta flows into an isolated compartment.....105
4.6 Discussion.....111
4.7 Conclusion.....113
Application of Coupled Discrete Element Model.....116
5.1 Numerical Analysis of Shear Stimulation and Permeability Enhancement in Granite.....116
5.1.1 Introduction.....116
5.1.2 Motivation and Objectives.....117
5.1.3 Literature Review.....118
5.1.4 Problem Setup.....122
5.1.5 Calculation of Hydraulic Aperture from the 3-D Scanning Contours of the Two Surfaces of Fractures.....125
5.1.6 Sierra White Granite Using the Surface Topography.....137
5.2 Numerical Investigation of the Slippage of a Natural Fracture Resulting from an Approaching Hydraulic Fracture.....144
5.2.1 Introduction.....144
5.2.2 Simulation Results.....145
5.2.3 Summary and Conclusions.....153
Conclusions and Future Work.....154
References.....157

List of Tables

Table 1: Rock mechanical and hydraulic properties used in the simulations (Hemami et al, 2021). 27

Table 2: Two scenarios with different cases are defined based on the possible relative angle of $S_{H,max}$ azimuth and fault strike orientations (β-ϕ, Figure 12).....33

Table 3: Different scenarios for the study of the effect of hydromechanical properties of the basement, the reservoir, and the fault zone on fault reactivation. 41

Table 4: Properties of the reservoir (sandstone) in scenario 3, case 2 (Jagear et al. 2009) .50

Table 5: Years of operation (until Nov 2011), the total injected volume of fluid ($\times 10^6$ m^3), and subsurface target formation for high-volume injection wells and Stasta 1 and 2 wells (OCC, http://www.occeweb.com/og/ogdatafiles2.htm). 74

Table 6: Rock mechanical and hydraulic properties used in the simulations. ((1) Yu 2017; (2) Carell 2014; (3) Cappa 2009; (4) Chester 1993); (5) Kolawole et al. 2019).....75

Table 7: Different scenarios and cases in the model.....84

Table 8: Fracture mechanical and hydraulic properties (after calibration) of Sierra White granite.....124

Table 9: Mechanical and hydraulic properties of Sierra White granite (all values were measured at The Halliburton Rock Mechanics Laboratory at The University of Oklahoma) 125

List of Figures

Figure 1: (a) An injected finite fluid into a poroelastic sphere causes an increase in pore pressure (ΔPp) which results in expansion of the sphere by the value of $\Delta V_{unconstrained}$. To force the sphere back to its initial volume, external confining stress of $\Delta\sigma_{unconstrained}$ should be applied on its outer boundary. (b) If the sphere is enclosed by an infinite impermeable elastic body, there is a constrained volume change ($\Delta V_{constrained}$) which is less than $\Delta V_{unconstrained}$. Very soft and very stiff elastic medium result in $\Delta\sigma_{constrained} \simeq 0$ and $\Delta\sigma_{constrained} \simeq \Delta\sigma_{unconstrained}$, respectively.....7

Figure 2: (a) Normal stress (σ_n), shear stress (τ_s,), and pore pressure (Pp) must meet the Coulomb criteria, $|\tau_s| = c + \mu(\sigma_n - Pp)$ for fault failure (c is cohesion, and in frictional faults is zero). (b) Coulomb criteria in terms of half-sum ($\boldsymbol{\sigma m = \sigma 1 + \sigma 3 - 2Pp2}$) and half-difference ($\boldsymbol{\sigma s = \sigma 1 + \sigma 32}$) of $\boldsymbol{\sigma 1'}$and $\boldsymbol{\sigma 3'}$. Any change in the state of stress caused by fluid injection or withdrawal that moves the initial point (σ_{im} , σ_{is}) to ($\sigma_{im}+\Delta\sigma_m$, $\sigma_{is}+\Delta\sigma_s$) on the Coulomb line results in fault reactivation and a seismic event. $\Delta\sigma_s$ is poroelastic effect and implying that fluid injection or withdrawal causes total stress alteration. (c) Two mechanisms of injection change Mohr circle representation of stress state before (black solid circle) and after perturbation. Dashed blue and red circles are Mohr circle representations due to pore pressure buildup (decrease of effective normal stress) and poroelastic effect, respectively. 9

Figure 3: Cumulative number of events ($M_w \geq 2.7$) and cumulative moment in Oklahoma since 2007 (Petersen, 2017). 10

Figure 4: The number of M_w >3 earthquakes in Oklahoma vs California from 1990 to 2019. California earthquake counts are shown as a blue bar and Oklahoma earthquake counts are

shown as a red bar (from: https://www.usgs.gov/media/images/number-m3-earthquakes-oklahoma-vs-california-1990-2019). 11
Figure 5: Three end-member reservoir types within the Arbuckle: (A) fracture dominated, (B) paleokarst dominated, and (C) facies-controlled porosity and permeability (Franseen et al. (2004)). 13
Figure 6: Comparison of the structure and main entities in a continuum (left) and a discrete (right) model (https://www.itascacg.com/software/distinct-element-method) 19
Figure 7: Idealized relation between hydraulic aperture and effective normal stress for a rock joint (effective stress is positive in compression). u_{h0} and u_{res} are the joint apertures at zero normal stress and the minimum (residual) value for the aperture respectively. For efficiency in the explicit calculation, a maximum value of hydraulic aperture (u_{max}) which is the maximum value used in flow rate calculation is assumed. 23
Figure 8: The model dimension, fault geometry, and boundary condition (not drawn to scale). The values of fault strike orientation (ϕ) and the azimuth of $S_{H,max}$ (β) are 60° and 85°, respectively. Boundary conditions account for vertical stress on the top, roller boundaries on the sides, and fixed displacement on the bottom of the model. The yellow dot on the fault shows the shortest point on the fault from the injection well. 26
Figure 9: A schematic illustration shows how stress arching due to depletion forms in the overburden as the reservoir pulls away from the surface (Toomey et al., 2017). 29
Figure 10: The contours of (a) ΔPp, (b) $\Delta\tau_{xy}$, (c) $\Delta\ \sigma_{xx}$, and (d) $\Delta\ \sigma_{yy}$ on a horizontal cross-section of the model at the middle depth of the sandstone induced by the injection of water with a constant rate of 0.05 m^3/s (27000 bbl/day) after six months at the center of the domain and in the middle depth of the sandstone layer (Figure 8). 30

Figure 11: The contours of (a) ε_{xx}, (b) ε_{yy}, and (c) ε_{zz} on a horizontal cross-section of the model at the middle depth of the sandstone induced by the injection of water with a constant rate of 0.05 m^3/s (27000 bbl/day) after six months at the center of the domain and in the middle depths of the sandstone layer. In x and y-directions, within and beyond a certain distance from the well, the injection induces extension and contraction, respectively. In the z-direction (vertical direction), injection causes the expansion of the reservoir.....31

Figure 12: Different scenarios based on different values of fault strike orientation (ϕ) and the azimuth of $S_{H,max}$ (β). In this study, three values of ϕ = 40°, 50°, and 60° and two values of β = 80° and 85°are studied (Table 2). This is in agreement with Mohr-Coulomb theory in which fracture takes place in planes that pass through the direction of the intermediate principal stress and are equally inclined at an angle less than 45◦ from the direction of the maximum principal stress. 33

Figure 13: Sneario2, case 3-β = N85°E and ϕ = 60° (β- ϕ = 25°): (a) ΔPp and (b) ΔCFS on the fault plane induced after 4 years of injection with a rate of 0.03 m^3/s (16300 bbl/day). Red solid and dashed lines show the reservoir upper and lower boundaries, respectively. The white dashed line is the vertical line on the fault plane that has the shortest distance from the injection well. (Figure 8).....35

Figure 14: Sneario2, case 3-β = N85°E and ϕ = 60° (β- ϕ = 25°): a) $\Delta\sigma_n$ and b) $\Delta\tau_s$ on the fault plane induced after 4 years of injection with a rate of 0.03 m^3/s (16300 bbl/day). Red solid and dashed lines show the reservoir upper and lower boundaries, respectively. 36

Figure 15: Sneario2, case 3-β = N85°E and ϕ = 60° (β- ϕ = 25°): Depth profiles of change of CFS (MPa), pore pressure (MPa), total normal stress (MPa), and shear stress (MPa) (Upper figure), and profile of change of poroelastic stress (MPa) and pore pressure (MPa)

components of ΔCFS (Lower Figure) along the white dashed line on the fault plane along the cross-section W-w (Figure 13) after 4 years of injection. Solid red lines indicate the fault boundaries and the red dashed lines the lower boundary of the reservoir. 37

Figure 16: Scenario 1, (β = N80°E): Depth profiles of a) CFS and b) ΔCFS (MPa) along the dashed line on the fault plane along the cross-section W-w (Figure 13) after 4 years of injection. Solid red lines indicate the fault boundaries and the red dashed lines the lower boundary of the reservoir. 38

Figure 17: Scenario 2 (β = N85°E): Depth profiles of a) CFS and b) ΔCFS (MPa) along the dashed line on the fault plane along the cross-section W-w (Figure 13) after 4 years of injection. Solid red lines indicate the fault boundaries and the red dashed lines the lower boundary of the reservoir. 39

Figure 18: (a) Fault zone structure (b) permeability and (c) Young's modulus 42

Figure 19: Schematics of the nonconformity contact region. (a) Type 0 – sharp contact expected to prevent fluid pressure front penetrates across the contact and while causes fluid flow parallel to the interface in the target layer (b) Type I – phyllosilicate-dominated zone above the crystalline basement prevents fracture propagation across the nonconformity and downward fluid migration (except in the fault zones) (c) Type II – secondary-mineralization-dominated zone. All nonconformity types may be cut by structural discontinuities. Blue arrows show the possible injected fluid flow paths (Petrie et al 2020). 45

Figure 20: Scenario 3, Case 1 (η_{res} = 0.25): Induced (a) pore pressure ((ΔPp, MPa) and b) CFS (ΔCFS, MPa) on the fault plane after 4 years of injection with a constant rate of 0.03 m^3/s (16300 bbl/day). The red solid and dashed lines show the upper and lower reservoir boundaries, respectively. Impermeable Type I nonconformity contact prevents fluid flow to

the basement. CFS increases on the whole fault plane by two mechanisms. At reservoir and shallow basement depths, direct pore pressure (destabilizing) dominates the poroelastic effect which is stabilizing. At greater depths, the reduction in normal stress causes increase of CFS. 47

Figure 21: Scenario 3, Case 1 (η_{res} = 0.25): Induced (a) normal stress ($\Delta\sigma_n$, MPa) and (b) shear stress ($\Delta\tau_s$, MPa) on the fault plane after 4 years of injection with a constant rate of 0.03 m^3/s (16300 bbl/day). The red solid and dashed lines show the upper and lower reservoir boundaries, respectively. At greater depths where the pressure front does not propagate, due to the poroelastic effect, normal stress decreases and increases CFS. Shear stress change values are less than normal stress change by an order of magnitude.....48

Figure 22: Scenario 3, Case 1 (η_{res} = 0.25): Depth profiles of change of CFS (MPa), pore pressure (MPa), total normal stress (MPa), and shear stress (MPa) (Upper figure), and profiles of change of poroelastic stress (MPa) and pore pressure (MPa) components of ΔCFS (Lower Figure) along the white dashed line on the fault plane along the cross-section W-w (Figure 19b) after 4 years of injection. Solid red lines indicate the fault boundaries and the red dashed lines the lower boundary of the reservoir. At greater depths, the only process responsible for the ΔCFS increase is poroelastic effect, and direct pore pressure does not have any contribution.....49

Figure 23: Scenario 3, Case 2 (η_{res} = 0.3): Induced (a) pore pressure ((ΔPp, MPa) and b) CFS (ΔCFS, MPa) on the fault plane after 4 years of injection with a constant rate of 0.03 m^3/s (16300 bbl/day). The red solid and dashed lines show the upper and lower reservoir boundaries, respectively. Impermeable Type I nonconformity contact prevents fluid flow to the basement. CFS increases on the whole fault plane by two mechanisms. At reservoir and

shallow basement depths, direct pore pressure (destabilizing) dominates the poroelastic effect which is stabilizing. At greater depths, the reduction in normal stress causes an increase in CFS. The maximum ΔCFS (the tendency for failure) occurs at the basement and the reservoir interface.....51

Figure 24: Scenario 3, Case 2 (η_{res} = 0.3): Induced (a) normal stress ($\Delta\sigma_n$, MPa) and (b) shear stress ($\Delta\tau_s$, MPa) on the fault plane after 4 years of injection with a constant rate of 0.03 m^3/s (16300 bbl/day). The red solid and dashed lines show the upper and lower reservoir boundaries, respectively. At greater depths, the pressure front does not propagate, and poroelastic effect is the only process in increasing CFS. Shear stress change values are less than normal stress change by an order of magnitude.....52

Figure 25: Scenario 3, Case 2 (η_{res} = 0.3): Depth profiles of change of CFS (MPa), pore pressure (MPa), total normal stress (MPa), and shear stress (MPa) (Upper figure), and profiles of change of poroelastic stress (MPa) and pore pressure (MPa) components of ΔCFS (Lower Figure) along the white dashed line on the fault plane along the cross-section W-w (Figure 23b) after 4 years of injection. Solid red lines indicate the fault boundaries and the red dashed line shows the lower boundary of the reservoir. At greater depths, the only process responsible for the ΔCFS increase is poroelastic effect, and direct pore pressure does not have any contribution.....53

Figure 26: The pore pressure change (ΔPp, MPa) (upper figures), normal stress change ($\Delta\sigma_n$, MPa) (middle figures), and shear stress change ($\Delta\tau_s$, lower figures) in sandstone group at depth of 1600 m after 4 years of injection for (a) case 1 (left column) and (b) case 2 (right column). In case 2 (η_{res} = 0.3), the induced pore pressure and normal stress are less and more

than in case 1 (η_{res} = 0.25), respectively. The shear stress changes are similar in both cases. 55

Figure 27: Scenario 3: Comparison of depth profiles of (a) ΔPp, (b) $\Delta\sigma_n$, and (c) $\Delta\tau_s$ of case 1 (η_{res} = 0.25) and case 2 (η_{res} = 0.3) along the white dashed lines (Figure 20b and Figure 23b). It can be seen that less induced ΔPp and $\Delta\sigma_n$ are generated in the reservoir with higher η_{res}. At the greater depths where there is no pore pressure elevation, more reduction in normal stress is induced in case 1. Shear stresses in both cases are almost similar. Solid red lines are the fault boundaries. The red dashed line shows the lower boundary of the reservoir. 56

Figure 28: Scenario 3: Comparison of depth profiles (a) ΔCFS (MPa), (b) $\Delta\tau_s$ -$\mu\Delta\sigma_n$ (MPa), and (c) μΔPp (MPa) of case 1 (η_{res} = 0.25) and case 2 (η_{res} = 0.3) along the white dashed line (Figure 20b and Figure 23b). In case 1, ΔCFS is greater than case 2 on the whole fault plane. Solid red lines are the fault boundaries. The red dashed line shows the lower boundary of the reservoir.....57

Figure 29: Scenario 3, Case 4: Depth profiles of change of CFS (MPa), pore pressure (MPa), total normal stress (MPa), and shear stress (MPa) (Upper figure), and profiles of change of poroelastic stress (MPa) and pore pressure (MPa) components of ΔCFS (Lower Figure) along the vertical line on the fault plane that has the shortest distance to the injection well. The red lines are the fault boundaries. Solid red lines are the fault boundaries. The red dashed line shows the lower boundary of the reservoir. 59

Figure 30: Scenario 3: Comparison of depth profiles of (a) ΔPp, (b) $\Delta\sigma_n$, and (c) $\Delta\tau_s$ of case 1 (α # 1) and case 4 (α = 1 for all layers) along the vertical line on the fault plane that has the shortest distance from the well. At the reservoir and shallow depths, both pore pressure elevation and induced increase of normal stress on the faults are higher in case 4 than in case

1. At greater depths, there is no excess pore pressure and induced normal stresses are similar in cases 1 and 4. Induced shear stresses are similar, and have insignificant values. Solid red lines are the fault boundaries. The red dashed line shows the lower boundary of the reservoir. 60

Figure 31: Scenario 3: Comparison of depth profiles of (a) ΔCFS, (b) $\Delta\tau_s$ -$\mu\Delta\sigma_n$, and (c) $\mu\Delta Pp$ of case 1 (α # 1) and case 4 (α = 1 for all layers) along the vertical line on the fault plane that has the shortest distance from the well. ΔCFS is almost similar in cases 1 and 4. At the shallow basement, the assumption of the incompressible rock grains causes an overestimation of the fault tendency for reactivation (higher ΔCFS). Solid red lines are the fault boundaries. The red dashed line shows the lower boundary of the reservoir. 61

Figure 32: Comparison of ΔPp, ΔCFS, $\Delta\sigma_n$, and $\Delta\tau_s$ on the fault plane in response to injection between case 1 (right column) and case 2 (left column) of scenario 4. Solid red lines are the fault boundaries. The red solid and dashed lines show the upper and lower boundaries of the reservoir.....63

Figure 33: Scenario 4, case 2: Depth profiles of change of CFS (MPa), pore pressure (MPa), total normal stress (MPa), and shear stress (MPa) (upper figure), and profile of change of poroelastic stress (MPa) and pore pressure (MPa) of components of CFS (lower figure) along the dashed line on the fault plane (Figure 32) after 4 years of injection. Solid red lines are the fault boundaries. The red dashed line shows the lower boundary of the reservoir. The maximum ΔCFS occurs in the shallow basement. 64

Figure 34: Comparison of a) ΔPp, b) $\Delta\sigma_n$, and c) $\Delta\tau_s$ of case 1 (η_{res} = 0.25) and case 2 (η_{res} = 0.3) of scenario 3 along the white dashed line (the closest point on the fault to the well, Figure 32). Less ΔPp is generated in case 2 with higher η_{res}. Induced shear stresses are almost

similar in both cases. Solid red lines are the fault boundaries. The red dashed line shows the lower boundary of the reservoir. 65

Figure 35: Comparison of a) ΔCFS, b) $\Delta\tau_s$ -$\mu\Delta\sigma_n$, and c) μΔPp of case 1 (η_{res} = 0.25) and case 2 (η_{res} = 0.3) of scenario 3 along the white dashed line (Figure 32). In both cases, the fault has the maximum ΔCFS in the shallow basement. Solid red lines are the fault boundaries. The red dashed line shows the lower boundary of the reservoir. 66

Figure 36: Scenario 4, Case 3: Depth profiles of change of CFS (MPa), pore pressure (MPa), total normal stress (MPa), and shear stress (MPa) (Upper figure), and profiles of change of poroelastic stress (MPa) and pore pressure (MPa) components of ΔCFS (Lower Figure) along the vertical line on the fault plane that has the shortest distance to the injection well. The red lines are the fault boundaries. Solid red lines are the fault boundaries. The red dashed line shows the lower boundary of the reservoir. 67

Figure 37: Scenario 4: Comparison of depth profiles of (a) ΔPp, (b) $\Delta\sigma_n$, and (c) $\Delta\tau_s$ of case 1 (α # 1) and case 4 (α = 1 for all layers) along the vertical line on the fault plane that has the shortest distance from the well. At the reservoir and shallow depths, both pore pressure elevation and induced increase of normal stress on the faults are higher in case 4 than in case 1. At greater depths, there is no excess pore pressure and induced normal stresses are similar in cases 1 and 4. Induced shear stresses are similar, and have insignificant values. Solid red lines are the fault boundaries. The red dashed line shows the lower boundary of the reservoir. 68

Figure 38: Scenario 3: Comparison of depth profiles of (a) ΔCFS, (b) $\Delta\tau_s$ -$\mu\Delta\sigma_n$, and (c) μΔPp of case 1 (α # 1) and case 4 (α = 1 for all layers) along the vertical line on the fault plane that has the shortest distance from the well. ΔCFS is almost similar in cases 1 and 4.

At the shallow basement, the assumption of the incompressible rock grains causes an overestimation of the fault tendency for reactivation (higher ΔCFS). Solid red lines are the fault boundaries. The red dashed line shows the lower boundary of the reservoir.....69
Figure 39: (a) Oklahoma fault map (Oklahoma Geological Survey (OGS), http://www.ou.edu/ogs/data/fault). The fault traces and the area of interest are shown by red lines and the blue box, respectively. (b) Location of injection wells in the area of interest (Oklahoma Corporation Commission (OCC), http://www.occeweb.com/og/ogdatafiles2.htm) (c) Earthquakes between 2009 and 2011 in the area of interest (OGS, http://www.ou.edu/ogs/research/earthquakes/catalogs).....72
Figure 40: Stratigraphic section of the study area above the Precambrian basement (Dycus, 2013) 73
Figure 41: (a) The 3D view of the model and the location of the faults b) the sketch of interface elements representative of faults c) the plan of the domain and location of the faults and injection wells. Since most events (especially ~M_w = 5 events, Figure 39) were located on the splay branch of the Wilzetta fault (shown by the dashed white line) and the Meeker Prague fault, we pay special attention to this splay of Wilzetta fault in this study.....80
Figure 42: Schematic for (a) scenario 1: there is no communication between Arbuckle group and the basement, and fluid diffuses into Arbuckle in semi-restricted and infinitely open volume in cases with impermeable and permeable, respectively; (b) scenario 2: fluid penetrates the deeper depths through the damage zone; (c) scenario 3: there is only a damage zone around a part of the Wilzetta fault, and there is a bounded volume in Arbuckle group in which wastewater accumulated resulting in pore pressure elevation. 83

Figure 43: Scenario 1: The change of pore pressure (MPa) in Arbuckle group at a depth of 1.6 km in Nov 2011 (after 12 years and 10 months of injection) for (a) case 1, and (b) case 2. The change of pore pressure on the splay branch of Wilzetta fault plane along the W-w for (c) case 1 and (d) case 2. The top and the lower boundaries of Arbuckle group are shown by the red solid and dashed lines, respectively. The white dashed line is the vertical line on the fault plane that has the shortest distance to the Mazkoori well.....87

Figure 44: Scenario 1: The pore pressure change (MPa) in Arbuckle group at depth of 1.6 km at the end of 2001 (left), 2005 (middle), and 2010 (right) for (a) case 1 and (b) case 2. 88

Figure 45: Scenario 1: The pore pressure change (MPa) on the splay branch of Wilzetta fault plane along the cross-section W-w at the end of 2001 (left), 2005 (middle), and 2010 (right) for (a) case 1 and (b) case 2. The top and the lower boundaries of Arbuckle group are shown by the red solid and dashed lines, respectively. The white dashed line is the vertical line on the fault plane that has the shortest distance to the Mazkoori well.....89

Figure 46: Scenario 1: Change in the horizontal total stresses ($\Delta\sigma_{xx}$ and $\Delta\sigma_{yy}$) (MPa) of Arbuckle group at depth of 1600 m in Nov 2011 (after 12 months and 10 months of injection) for (a) case 1 and (b) case 2 induced by injection. $\Delta\sigma_{xx}$ (east-west) and $\Delta\sigma_{yy}$ (north-south) are shown in the left and right figures, respectively. 90

Figure 47: Scenario 1, case 1: Variation of CFS (MPa) at three points located on the fault plane along the dashed line on the splay branch of Wilzetta fault plane along the cross-section W-w (Figure 45) during simulation for (a) $\mu = 0.63$ and (b) $\mu = 0.75$. For the value of $\mu = 0.63$, CFS becomes positive (fault failure) at depth of 1600m. The fault remains stable during injection for $\mu = 0.75$. Due to permeable faults, there is less pressure buildup in this

case than in case 1, and therefore the fault fails at the lower coefficient of friction of 0.63. 91

Figure 48: Scenario 1, case 1: Depth profiles of change of CFS (MPa), pore pressure (MPa), total normal stress (MPa), and shear stress (MPa) (Upper figure), and profile of change of poroelastic stress (MPa) and pore pressure (MPa) components of CFS (Lower Figure) along the dashed line on the splay branch of Wilzetta fault plane along the cross-section W-w (Figure 43) in a) Dec 2001 and b) Nov 2011. Solid red lines are the fault boundaries. The red dashed line shows the lower boundary of the reservoir. (μ = 0.75).....92

Figure 49: Scenario 1, case 2: Variation of CFS (MPa) at three points located on the fault plane along the dashed line on the splay branch of Wilzetta fault plane along the cross-section W-w (Figure 45) during simulation for (a) μ = 0.66 and (b) μ = 0.75. For the value of μ = 0.66, CFS becomes positive (fault failure) at depth of 1600m. The fault remains stable during injection for μ = 0.75. 94

Figure 50: Scenario 1, case 2: Depth profiles of change of CFS (MPa), pore pressure (MPa), total normal stress (MPa), and shear stress (MPa) (Upper figure), and profile of change of poroelastic stress (MPa) and pore pressure (MPa) components of ΔCFS (Lower Figure) along the dashed line on the splay branch of Wilzetta fault plane along the cross-section W-w (Figure 45) in (a) Dec 2001 and (b) Nov 2011. Solid red lines are the fault boundaries. The red dashed line shows the lower boundary of the reservoir. (μ = 0.75).....95

Figure 51: Scenario 1: The change of pore pressure (MPa) in Arbuckle group at depth of 1600 m in Nov 2011(after 12 years and 10 months of injection) for (a) case 3, and (b) case 4.....96

Figure 52: Earthquakes (a) between 2000 and 2010, (b) in 2011before the main shock (M_w 5.7), and (c) in 2011 after the main shock (M_w 5.7) (OGS, http://www.ou.edu/ogs/research/earthquakes/catalogs). 97

Figure 53: The damage zone exists only in a portion and some splay branches of the Wilzetta Fault in (a) case 6 and (b) case 7 of scenario 2. The white dashed line shows the portion and splay branches of the Wilzetta faults for which the damage zone is defined in the model. The locations of high-volume injection wells are shown by green dots. 98

Figure 54: Scenario 2, Case 7: The pore pressure change (MPa) in Arbuckle group at depth of 1600 m at the end of 2001, 2005, 2010, and Nov 2011. 100

Figure 55: Scenario 2, case 7: The pore pressure change (MPa) on the splay branch of Wilzetta fault plane along the cross-section W-w in Dec 2001, 2005, 2010, and Nov 2011. The top and the lower boundaries of Arbuckle group are shown by the red solid and dashed lines, respectively. The white dashed line is the vertical line on the fault plane that has the shortest distance to the Mazkoori well. 101

Figure 56: Scenario 2, case 7: Variation of CFS (MPa) at three points located on the fault plane along the dashed line on the splay branch of Wilzetta fault plane along the cross-section W-w (Figure 55) during simulation for (a) $\mu = 0.65$ and (b) $\mu = 0.75$. For the value of $\mu = 0.65$, CFS becomes positive (fault failure) at depth of 1600m. The fault remains stable during injection for $\mu = 0.75$. At all depths, the CFS has the maximum value due to Mazkoori well operation, and after 2005 remains almost constant. 103

Figure 57: Scenario 2, case 7: Depth profiles of change of CFS (MPa), pore pressure (MPa), total normal stress (MPa), and shear stress (MPa) (Upper figure), and profile of change of poroelastic stress (MPa) and pore pressure (MPa) components of ΔCFS (Lower Figure)

along the dashed line on the splay branch of Wilzetta fault plane along the cross-section W-w (Figure 55) in (a) Dec 2001 and (b) Nov 2011. Solid red lines are the fault boundaries. The red dashed line shows the lower boundary of the reservoir. (μ = 0.75).....104
Figure 58: Scenario 3: The pore pressure change (MPa) in Arbuckle group at depth of 1600 m in Dec 2001, 2005, 2010, and Nov 2011. Since injection is performed in a bounded area, in contrast to previous scenarios, the pore pressure increases continuously.....106
Figure 59: Scenario 3: The pore pressure change (MPa) on the splay branch of Wilzetta fault plane along the cross-section W-w in Dec 2001, 2005, 2010, and Nov 2011. The top and the lower boundaries of Arbuckle group are shown by the red solid and dashed lines, respectively. The white dashed line is a vertical line on the fault plane that has the shortest distance to the Mazkoori well. 107
Figure 60: Scenario 3: Variation of CFS (MPa) during simulation for (a) μ = 0.72 and (b) μ = 0.75. The CFS becomes zero in 2011 at depth of 1600 m for μ = 0.72. In contrast to scenarios 1 and 2, CFS continues to increase at all depths. Due to the poroelastic effect at greater depths, the rate of CFS increase is higher than shallower depths. 109
Figure 61: Scenario 3: Depth profiles of change of CFS (MPa), pore pressure (MPa), total normal stress (MPa), and shear stress (MPa) (Upper figure), and profile of change of poroelastic stress (MPa) and pore pressure (MPa) components of ΔCFS (Lower Figure) along the dashed line on the splay branch of Wilzetta fault plane along the cross-section W-w (Figure 59) in (a) Dec 2001 and (b) Nov 2011. Solid red lines are the fault boundaries. The red dashed line shows the lower boundary of the reservoir. (μ = 0.75).....110
Figure 62: The setup of numerical simulation. The BC is applied in three stages. First, a constant confining pressure is applied on the external surface of the sample by normal

traction on each gridpoint. Second, by applying initial pressure on both wells, the fracture pressure is uniform and constant. Then, by fixing the upper platen and moving the lower platen, the desired axial stress is generated in the sample. Finally, in the last stage, the upper platen is fixed. 123
Figure 63: Determination of the aperture from the real fracture surface. 126
Figure 64: The discretized rectangle on the fracture. An increasing number of discretization (finer mesh) leads to a more precise estimation of the hydraulic aperture calculation. 127
Figure 65: Sierra White granite, SW-S3 sample (Yu and Ghassemi 2018): Top: the topography of the fracture surfaces (the output of the scanning machine). Bottom: Exported data into 3DEC and regeneration of the topography fracture surfaces. The dark blue in the 3DEC surfaces indicates the cropped area. The color indicates the distance (mm) between the high point and the lowest point. 128
Figure 66: Sierra White granite SW-T1 (Yu and Ghassemi, 2018): Top: the topography of the fracture surfaces (the output of the scanning machine). Bottom: Exported data into 3DEC and regeneration of the topography fracture surfaces. The dark blue in the 3DEC surfaces indicates the cropped area. The color indicates the distance (mm) between the high point and the lowest point. 129
Figure 67: SW-S3 sample of Sierra White granite: Flow rate (ml/min) (a) with similar normal stiffness value during loading stage and (b) with a decreased value of normal stiffness to 5×10^{12} Pa/m. This decrease enables the numerical model to simulate the reduction in permeability due to degradation and gauge production during the unloading stage.....131
Figure 68: SW-S3 sample of Sierra White granite: (a) normal stress and (b) shear stress of the fracture during the test. The boundary condition (no displacement for rigid platens)

causes the stress relaxation after slippage at which the normal stress decreases by ~8 MPa. 132
Figure 69: : SW-S3 sample of Sierra White granite: Pore pressure (MPa) of the fracture during loading episode for injection pressure (P_{inj}) (a) 8MPa, (b) 12 MPa, (c) 16 MPa, (d) 20 MPa, (e) 24 MPa, and (f) 28 MPa 132
Figure 70: SW-S3 sample of Sierra White granite: Normal stress (MPa) of the fracture during loading episode for injection pressure (P_{inj}) (a) 8MPa, (b) 12 MPa, (c) 16 MPa, (d)20 MPa, (e)24 MPa, and (f) 28 MPa 134
Figure 71: SW-S3 sample of Sierra White granite: Normal displacement (μm) of the fracture during loading stages for injection pressure (P_{inj}) (a) 8MPa, (b) 12 MPa, (c) 16 MPa, (d) 20 MPa, and (e) 24 MPa. Closure is negative.....135
Figure 72: SW-S3 sample of Sierra White granite: failure on the fracture surface at the injection pressure of (a) 20 MPa, (b) 24 MPa, and (c) 28 MPa. Shear displacement (μm) of the fracture during loading stages for injection pressure (P_{inj}) (a) 20 MPa, (b) 24 MPa, and (c) 28 MPa.....136
Figure 73: Shear displacement contour (μm) and vectors of the fracture after slippage at the injection pressure of 28 MPa. For a better view, the vectors around the injection and production wells are shown separately. 137
Figure 74: The aperture of the fracture surface in the simulation (calculated from the real topography reported by Ye and Ghassemi (2019)) at zero stress (left) and after applying boundary conditions (right).....138
Figure 75: SW-S3 sample of Sierra White granite: Flow rate (ml/min) a) with constant normal stiffness value during loading stage and b) with the decreased value of normal

stiffness to 5×10^{12} Pa/m. This decrease enables the numerical model to simulate the reduction in permeability due to degradation and gauge production during the unloading stage.....138
Figure 76: Pore pressure (MPa) of the fracture that has real topography during loading stages when injection pressure is (a) 8 MPa, (b) 12 MPa, (c)16 MPa, (d)20 MPa, and (d)24 MPa. 139
Figure 77: Comparison of the pore pressure (MPa) distribution and discharge vector on the fracture surface for SW-S3 sample for Sierra White granite when aperture is uniform (right) and nonuniform (calculated by the real topography of the fracture surfaces) at an injection pressure of 24 MPa.....140
Figure 78: SW-S3 sample of Sierra White granite: Normal stress (MPa) of the fracture during loading episode for injection pressure (P_{inj}) (a) 8MPa, (b) 12 MPa, (c) 16 MPa, (d)20 MPa, and (e) 24 MPa when the fracture does not have a uniform aperture. 141
Figure 79: SW-S3 sample of Sierra White granite: Normal displacement (μm) of the fracture during loading episode for injection pressure (P_{inj}) (a) 8MPa, (b) 12 MPa, (c) 16 MPa, (d) 20 MPa, and (e) 24 MPa when the fracture does not have a uniform aperture.....142
Figure 80: Shear displacement (μm) after slippage at the injection pressure of 28 MPa. .143
Figure 81: Shear displacement contour (μm) and vectors of the fracture after slippage at the injection pressure of 28 MPa. Enlarged views of displacement vectors around the injection and production wells are shown in the boxes.....143
Figure 82: Test setup for (a) Case I and (b) Case II. The pre-defined hydraulic fracture does not touch the natural fracture in Case II, and reaches the natural fracture in Case I. The boundary and loading condition includes applying the confining pressure, and moving down

the upper platen while the lower one is fixed. After the axial stress reaches the desired value (~5.5 MPa and 30 MPa in Case I and II, respectively) the upper platen is fixed. (c) Dimension and geometry of the pre-defined hydraulic fracture in Case I (left) and Case II (right).....146

Figure 83: Aperture of the propagating hydraulic fracture after 0.3, 2, and 4 ms of propagation (left, middle, and right respectively. Both the aperture at zero normal stress and residual aperture (minimum hydraulic aperture) are 0.1 mm. 146

Figure 84: Case I: Induced normal (up) and shear (down) displacements (μm) of natural fracture when pressure of the notch is 5, 15, 22 MPa (left, middle, and right respectively). (Closure is negative) 148

Figure 85: Case I: Induced normal (up) and shear (down) displacements (μm) of natural fracture after 0.3, 2, and 4 ms of propagation (left, middle, and right respectively). (Closure is negative) 148

Figure 86: The comparison of the experimental (dashed line) and the numerical simulation (solid line) results of Case I. Sections I and II corresponds to the notch pressurization and hydraulic fracture propagation, while section III is due to slippage of the natural fracture after fluid flows into the natural fracture and pressurizes it.....150

Figure 87: Case I: Normal (up) and shear (down) stress (MPa) of natural fracture when the pressure of the notch is 0 (equilibrium condition), 5, 15, 22 MPa (from left to right respectively). (Compression is positive).....151

Figure 88: Case II: Induced normal (up) and shear (down) displacements (μm) of natural fracture when the pressure of the notch is 5, 15, 23 MPa (left, middle, and right, respectively). (Closure is negative).....152

Figure 89: Case II: Induced normal (up) and shear (down) displacements (μm) of natural fracture by propagating hydraulic fracture after 0.13, 1.8, 3 ms of propagation. (left, middle, and right respectively). (Closure is negative). 153

Abstract

In the last decade, parts of the Central United States experienced marked increase in the number of small to moderate-sized earthquakes. Among all states, Oklahoma has experienced the most increase in the number of earthquakes. The seismic activity has been attributed to injection of wastewater produced from oil/gas activities. Induced seismicity is associated with injection (or production) operation in the subsurface which perturbs the in-situ pore pressure and total stresses. It is expected that injection causes nearby faults reactivation at reservoir depths by reducing normal effective stress acting on the fault plane. But, the majority of notable induced earthquakes happen on faults within the basement kilometers away from injection wells. In some cases (e.g. Prague 2011 sequence), there are many years delay between the start of injection operation and induced earthquakes. Many studied have been performed to explain the discrepancy between the observation and what happened in the reality. Many of them neglected the poroelastic effect, and only focused on the direct pore pressure. Many others, did not consider other determining factors such as hydromechanical properties of the reservoir and the basement, fault architecture, etc.

In the absence of a comprehensive geomechanical study of induced seismicity and the fact that Oklahoma was the host of the most induced seismicity events in the last decade, we evaluated the different possible scenarios of injection-induced seismicity by the construction of a conceptual geomechanical model. We studied the direct role of pore pressure diffusion and the indirect poroelastic stress transfer effect on the failure of a favorably oriented strike-slip fault with an initial condition similar to Oklahoma. By using a three-dimensional coupled numerical model, we study the effect of different factors such as mechanical properties

of the reservoir and the fault zone, the relative direction of in-situ stress and fault strike, etc. on the response of the fault to the injection.

We show that when the relative angle of horizontal maximum stress azimuth and fault strike orientations is 27° to 28°, faults are in the most critical condition. Our results show how solely poroelastic effect can cause fault reactivation in the deep basement faults when fluid is injected into a sealed reservoir. Also, the results indicate that presence of damage zone causes penetration of the injected fluid to the deep depth which has two different effects on the fault stability. The dominant effect is the direct pore pressure effect (destabilizing) which competes with poroelastic effect (stabilizing). The magnitude of poroelastic effect in some cases causes more tendency of fault reactivation at greater depths. We also show that injection in compliant reservoirs, either with or without fault damage zone, lessens the tendency of fault for failure.

As a practical study, using a three-dimensional fully coupled poroelastic model, we study the 2011 Prague, Oklahoma sequence. We utilized the 3D model to analyze the Wilzetta fault system response to saltwater injection in the underpressured subsurface layers, especially Arbuckle group and the basement, to evaluate the conditions that might have led to the increased seismicity. In view of the data-limited nature of the problem, we have considered multiple plausible scenarios, and use the available data to evaluate the hydromechanical response of the faults of interest in the study area. Numerical simulations show that the injection of large volumes of fluid into Arbuckle group tends to bring the part of the Wilzetta faults in Arbuckle group and basement into failure. Our model revealed that injection into an open or semi-restricted reservoir causes fault reactivation on epicenters of 2011 events

but in 2001 (10 years before the Prague 2011 sequence). We showed that injection of the reported volume into a bounded reservoir can explain the 2011 sequence spatiotemporally.

We also study the hydroshearin phenomenon. To reproduce shear stimulation process which results in improvement of fluid flow in tight reservoirs and EGS sites series of novel experiments were performed on granite and shale samples at RGSRG Lab at the University of Oklahoma. The results shed light on the shear processing for both before and after shear slip, and are useful to understand the relationship between different factors such as shear and normal effective stresses on the fracture, shear and normal displacements, dilation, and self-propping phenomenon, etc. Using a 3D coupled discrete element model, we study the physical processes of the experiment better. Utilizing a similar numerical method, we evaluated another experiment (performed at RGSRG Lab, the University of Oklahoma) that addressed interaction of a propagating hydraulic fracture and a natural fracture. There is an acceptable match between the lab results and the numerical model. We showed that there are two distinct types of induced shear stress on a natural fracture from an approaching hydraulic fracture. The first one is when the hydraulic fracture does not hit the natural fracture. After they hit, fluid flow in the natural fracture causes the second and more pronounced displacement on the fracture.

Introduction

1.1 Background on Induced Seismicity

Tectonic activities cause accumulation of elastic strain energy over geological timescale, and this energy can be released as a sudden eruption of seismic energy. These earthquakes have been considered natural events. However, there is plenty of evidence that confirms some seismic activities have man-made sources (Healy et al. 1968, Hsieh and Bredehoeft 1981, Keranen 2013). Many engineering projects such as civil engineering, mining engineering, and energy-related engineering have been reported responsible for induced seismicity. For example, construction of large dams (Simpson 1986, Simpson et al. 1988, Ge et al., 2009), mining operations (Hasegawa et al. 1988, Li et al. 2007), oil and gas depletion (Segal 1989, Elsworth et al. 2016), hydraulic operations (Tester et al. 1989, Majer et al. 2007, Häring et al. 2008, Holland 2013, Atkinson et al. 2016), CO2 storage and sequestration (Bachu 2008, Benson and Cole 2008, Bickle 2009, Kaven et al. 2015), and wastewater disposal by injection into deep subsurface aquifers (Healy et al. 1968, Kernane et al. 2013, Ellsworth 2013).

Evaluation of induced seismicity potential has become one of the principal concerns of subsurface-energy-related projects including fluid extraction or injection. The main objective of this study was to investigate the contribution of poromechinacal processes to fluid injection-induced earthquakes. This results in an improvement of our understanding of injection-induced seismicity leading to enhancement of fluid injection projects, and seismic hazard assessment.

Between 1962 and 1967, Colorado experienced increased seismicity near Denver. These events are among the first confirmed injection-induced seismicity (Healy et al. 1968, Hsieh

and Bredehoeft 1981, van Poollen and Hoover 1970). These seismic events occurred after the US army started injecting wastewater in 1962 in a disposal well at depth of 3.7 km in Colorado. The well was located in the Rocky Mountain Arsenal (RMA) through which wastewater was injected into the Precambrian fractured crystalline basement rocks. Lower-permeable boundaries reduced pressure dissipation, and caused delayed seismicity after the ending of injection (Hsieh and Bredehoeft 1981). From 1962 through 1966, almost 4 million barrels of chemical waste fluid were injected through the well. Overall, 100's of earthquakes with large enough magnitudes to be felt occurred starting 1962 through the years. The well was shut-in in 1966 after which the US Geological Survey reported many events with the largest magnitude of 4.5, 5.1, and 5.3 in 1967. The proposed mechanism was that pore pressure elevation which reduced the normal stress acting on the nearby fault resulted in decrease in the frictional strength. Also, it was suggested that the contraction of hot rocks due to the injection of relatively cold water causes a reduction of normal stress on the fault plane as well (van Poollen and Hoover 1970). Later, the US Geological Survey, the US Department of Defense, and Chevron oil company performed a test to examine the hypothesis of induced seismicity by fluid injection (Raleigh et al. 1976). They conducted an experiment at the Rangely Oil Field in Colorado, USA. A waterflood project was operated at this time. Hydro-mechanical properties and in-situ conditions of the reservoir were estimated by laboratory experiments and geomechanical models, respectively. Observation of seismic activities and focal plane solutions of earthquakes revealed there was a fault located in the injection zone. Utilizing the hydromechanical properties and in-situ state of stress, a pressure threshold was evaluated. Fluid injection and extraction alter-nation caused fluid pressure to fluctuate about the pressure threshold. Seismic events occurred when pore pressure was above the critical

value and no seismic activities were observed for values of pressure below the threshold confirmed the hypothesis that these earthquakes were induced by the fluid pressure. Later, the hypothesis was supported by similar experiments (e.g. Matsushiro, Japan, Ohtake, 1974). Oil and gas depletion can cause induced seismicity. In the 1920s, many seismic events occurred near the Goose Creek oil field in south Texas. Field subsidence of 1 m caused by oil production has been reported between 1917 and 1925 (Pratt and Johnson 1926). Earthquakes induced by oil production and field subsidence occurred in 1936 in the Wilmington field in California (Segal 1989). Many other seismic events have been considered to be induced. For example earthquakes in the Baldwin Hills, California (Hamilton and Meehan 1971); the Wilmington, California (Kovach 1974); Paradox Valley, western Colorado (Ake et al. 2005); Groningenfield in the Netherlands (van Thienen–Visser and Breunese 2015); near Ashtabula, Ohio (Seeber et al. 2004); and earthquakes near El Dorado, Arkansas, in the 1980s (Cox 1991), Oklahoma 2010s earthquakes (Keranen et al 2018).

As mentioned, many subsurface energy-related activities, such as geothermal energy extraction, hydraulic fracturing operation, and wastewater co-produced with oil/gas disposal, etc can cause induced seismicity. Some examples from mentioned activities are provided below.

1.1.1 Geothermal Reservoirs

Extraction of heat from geothermal reservoirs has been performed by circulating water through hot subsurface rocks and conducting it into the surface steam turbine or heat exchanger (Brown et al. 2012). Geothermal energy extraction has been performed from high permeable reservoirs or stimulated reservoirs (Enhanced Geothermal Systems, EGS). Induced seismicity has been reported from both types of reservoirs. Seismic activities at the Fenton Hill, New Mexico Enhanced Geothermal System (EGS) site (Brown et al. 2012) is

an example. After injection of 21000 m3 water in 2.5 days, many seismic events have been recorded most of which were too small (microseismic events). Another example of induced seismicity in association with the geothermal extraction project is the EGS project in Basel, Switzerland (Häring et al. 2008). During injection of almost 12000 m3 of water into the crystalline granite in six days, an increase of microseismic activity (with three events with Mw >3) was observed which resulted in termination of the scheduled stimulation plans. Geothermal extraction in Gallen, Switzerland was another project that eventually in 2013 was suspended due to the increase of seismic activities.

1.1.2 Hydraulic Fracturing

The unconventional reservoir is the one that cannot produce hydrocarbon at economic flow rates or volume without the assistance of stimulation treatments (e.g. hydraulic fracturing) or specific technologies (e.g. horizontal wells). Hydraulic fracturing includes pressurizing the rock to create fractures along lateral sections of horizontal wells. While hydraulic fracturing operation has been reported with the association of events with magnitude of $-3 < M_w < 0$, sometimes was accompanied by $M_w > 0$ (NRC 2013, Warpinksi et al 2009, 2012). The largest induced earthquakes that have been reported due to hydraulic fracturing operation are two M_w 4.4 events that occurred in 2014 in Alberta and British Columbia (Rubinstein and Mahani 2015), and two M_w 4.5 and 4.6 events that occurred in 2015 in British Columbia (Atkinson et al. 2016, Norbeck 2016).

1.2 Induced Seismicity Mechanism

The occurrence of a seismic event by activation of a pre-existing fault requires in-situ stress and pore pressure to reach a critical condition. This condition can be reached when the frictional resistance (the product of the friction coefficient times the normal effective stress on the fault) is overcome by the shear stress on the fault. This criterion of fault failure which is

referred to as Coulomb criteria is a limit for the in-situ stresses and pore pressure on the fault plane. Not all stress and pore pressure perturbations associated with fluid injection or extraction lead to a seismic event. The perturbation that increases the shear stress or de-creases the normal stress is destabilizing and causes the fault to become closer to critical conditions. On the other hand, some perturbations are stabilizing and move the fault farther away from critical conditions. The magnitude of perturbations also must be large enough to bring the fault to critical condition. It should be noted that not all slips are considered as seismic, for example sometimes they respond aseismically.

It should be mentioned that injection in a reservoir with permeable rocks (e.g. sandstone) and crystalline impermeable rocks tend to have different effects. Fluid flows and is stored in the pores and the fracture networks in permeable rocks and the crystalline impermeable rocks, respectively. In a reservoir with permeable rocks, the pore pressure elevation in the rock induces total stress change in the reservoir and the surrounding rock. In impermeable crystalline rocks, the matrix stress induced by injection is negligible (except the case with a very dense fracture network, NCR 2016) while pore pressure perturbation can be transmitted for several kilometers. The physical mechanism responsible for the induced stress perturbation caused by fluid injection or extraction is explained in the following.

Injection (or depletion) of fluid into (or from) a permeable rock causes change in both pore pressure and in the stress field. The latter can occur not only in the reservoir but also in the surrounding rock. The physical mechanism responsible for the induced stress perturbation caused by fluid injection or extraction is explained in the following.

A rise in pore pressure in an unstrained permeable rock causes an increase in volume (Figure 1a). This is similar to what is induced by an increase in temperature induces on a free-to-

deform rock. If a finite fluid volume is injected into a poroelastic sphere which is enclosed by an infinite impermeable elastic body, an increased pore pressure of ΔPp is generated which is proportional to the volume of injected fluid. Now, by removing the sphere from the surrounding body, the sphere expands freely by the value of $\Delta V_{unconstrained}$ (Figure 1a). To force the expanded sphere back to its initial volume, it is required to apply external confining stress of $\Delta\sigma_{unconstrained}$. We assume that this step is done under a drained condition so that the sphere pore pressure change remains ΔPp. The sphere is now restored to its initial shape, and fits exactly in its original position. We now 'glue' the sphere back into the elastic body and remove the applied external confining stress of $\Delta\sigma_{unconstrained}$ after which it is relaxed. When the system reaches equilibrium, the final state includes a constrained volume change ($\Delta V_{constrained}$) which is less than $\Delta V_{unconstrained}$ because the expansion of the sphere is resisted by the elastic body. This $\Delta V_{constrained}$ is associated with induced stress of $\Delta\sigma_{constrained}$. $\Delta\sigma_{constrained}$ is isotropic and uniform inside the porous sphere, and nonuniform in the surrounding body. The magnitude of the induced stress in the elastic body decays away from the sphere, becoming insignificant at a distance about twice the sphere radius. The induced volume change and stress vary based on the mechanical properties of the elastic body and porous medium. For example, very soft and very stiff elastic medium result in $\Delta\sigma_{constrained} \simeq 0$ and $\Delta\sigma_{constrained} \simeq \Delta\sigma_{unconstrained}$, respectively.

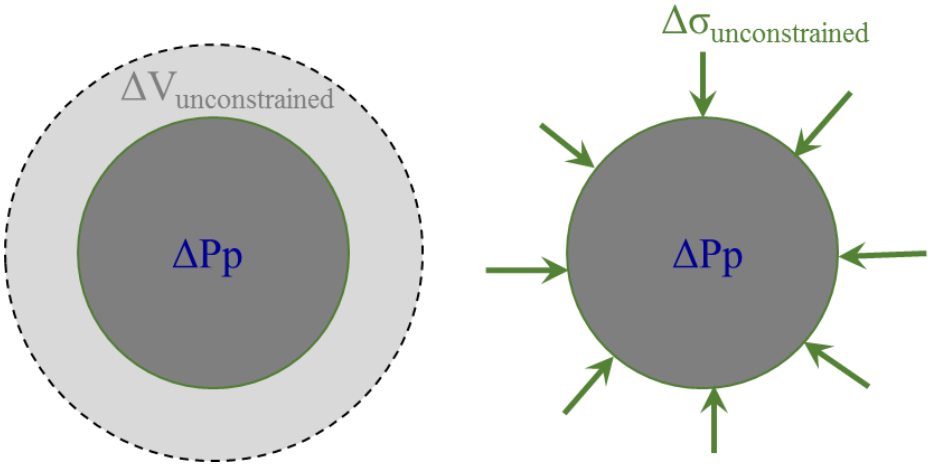
Cheng (1993, 2016) showed that when a bounded part of an unbounded domain, that is initially under a constant confining stress and pore pressure, is flooded by fluid injection resulting in a pressure buildup of Pp, the induced poroelastic confining stress (compression is positive) is given by

$$\frac{\sigma_{xx} + \sigma_{yy} + \sigma_{zz}}{3} = \frac{4\eta P_p}{3} \tag{1.1}$$

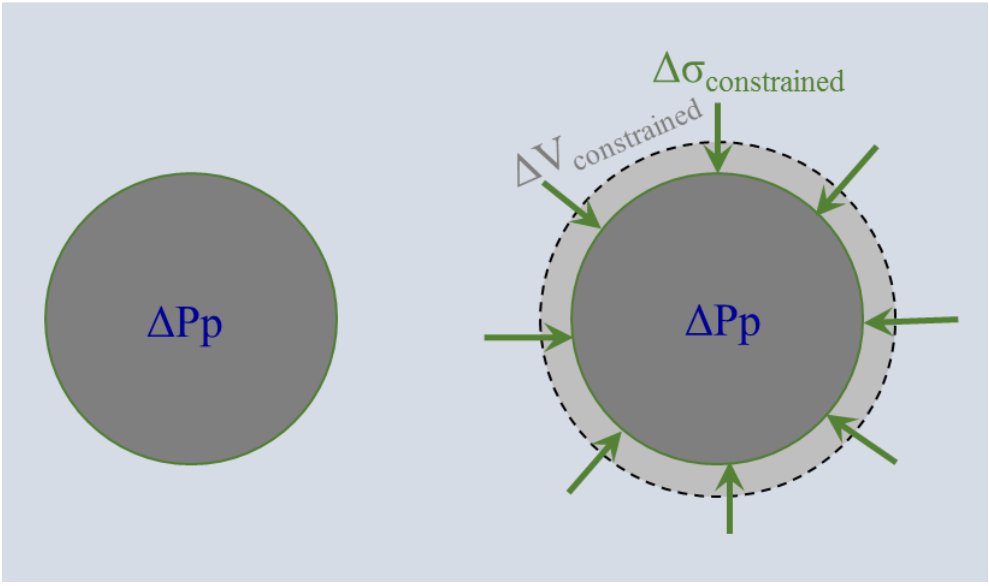
in which is η a poroelastic stress coefficient and given by

$$\eta = \frac{\alpha(1-2\nu)}{2(1-\nu)} \tag{1.2}$$

where ν and are α the Poisson ratio and Biot effective stress coefficient, respectively.



(a)



(b)

Figure 1: (a) An injected finite fluid into a poroelastic sphere causes an increase in pore pressure (ΔPp) which results in expansion of the sphere by the value of $\Delta V_{unconstrained}$. To force the sphere back to its initial volume, external confining stress of $\Delta\sigma_{unconstrained}$ should be applied on its outer boundary. (b) If the sphere is enclosed by an infinite impermeable elastic body, there is a constrained volume change ($\Delta V_{constrained}$) which is less than $\Delta V_{unconstrained}$. Very soft and very stiff elastic medium result in $\Delta\sigma_{constrained} \simeq 0$ and $\Delta\sigma_{constrained} \simeq \Delta\sigma_{unconstrained}$, respectively.

The complicated condition of the subsurface for instance the reservoir shape and size, heterogeneities in the hydromechanical properties of the layer, etc affect the induced stress perturbation. In fractured rock, more conductivity and less storage of fractures than permeable rocks cause the perturbation in pore pressure may transmit several kilometers.

As mentioned earlier in this section, normal stress (σ_n), shear stress (τ_s,), and pore pressure (P_p) must be in a critical condition for fault slip. This condition is expressed by a criterion referred to as the Coulomb criteria, $|\tau_s| = c + \mu (\sigma_n - P_p)$ (c is cohesion, and in frictional faults is zero). The Coulomb criterion states that fault slip initiates when driving shear stress on the fault is equal to the shear strength magnitude meaning that fault remains stable as long as shear strength is larger than shear magnitude. It is possible to express the Coulomb criteria in terms of half-sum ($\sigma_m = \frac{(\sigma_1+\sigma_3)-2P_p}{2}$) and half-difference ($\sigma_s = \frac{\sigma_1+\sigma_3}{2}$) of σ'_1 and σ'_3 (Figure 2b).

As long as the state of effective stress is under the slip criterion, the fault remains stable. Any change in the state of stress caused by fluid injection or withdrawal that moves the initial point (σ_{im} , σ_{is}) to ($\sigma_{im}+\Delta\sigma_m$, $\sigma_{is}+\Delta\sigma_s$) on the Coulomb line results in fault failure. It should be noted that $\Delta\sigma_s$ indicates the poroelastic effect meaning that fluid injection or withdrawal causes total stress alteration. It is noteworthy that not every perturbation is destabilizing. For example, a negative $\Delta\sigma_s$ is stabilizing while a negative $\Delta\sigma_m$ is destabilizing. Figure 2 shows that how fluid injection and withdrawal results in fault slip. Figure 2c illustrates how two possible mechanisms of injection change Mohr circle representation of stress state before and after perturbation. Dashed blue and red circles are Mohr circle representations due to pore pressure buildup (decrease of effective normal stress) and poroelastic effect, respectively.

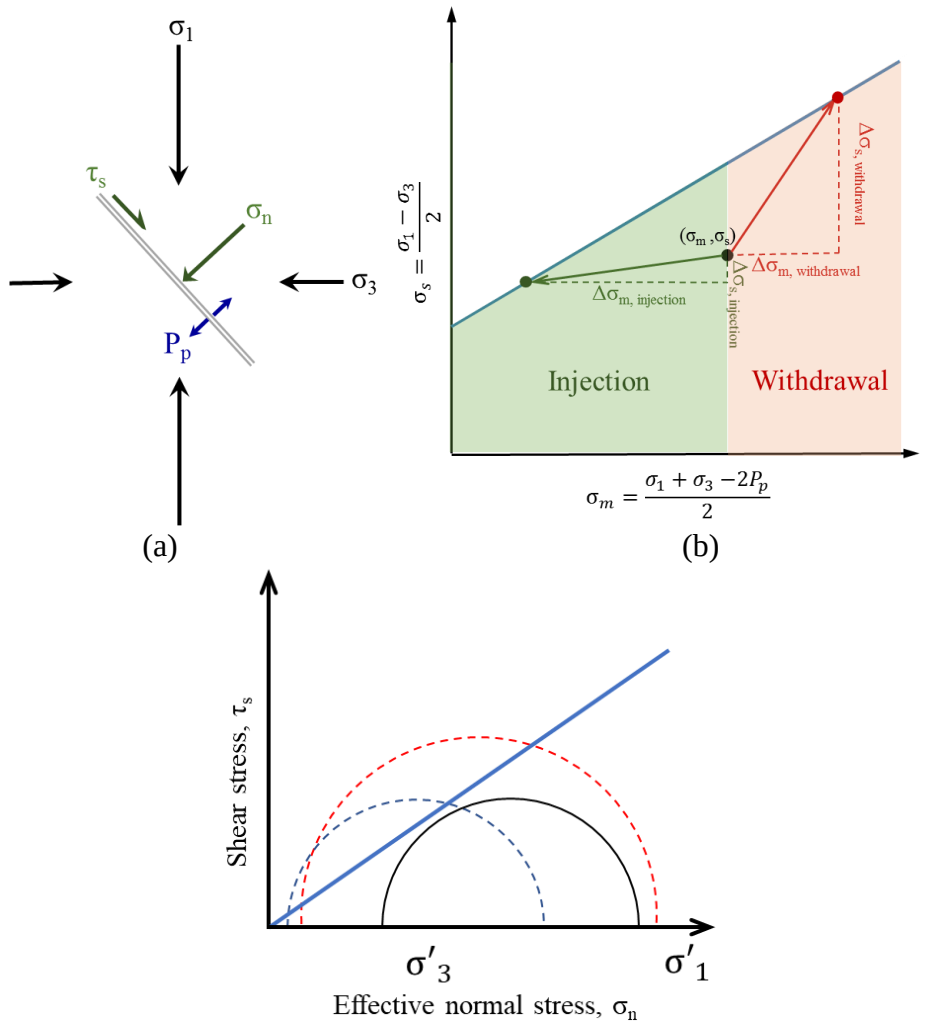


Figure 2: (a) Normal stress (σ_n), shear stress (τ_s,), and pore pressure (Pp) must meet the Coulomb criteria, $|\tau_s| = c + \mu (\sigma_n - Pp)$ for fault failure (c is cohesion, and in frictional faults is zero). (b) Coulomb criteria in terms of half-sum ($\sigma_m = \frac{(\sigma_1+\sigma_3)-2P_p}{2}$) and half-difference ($\sigma_s = \frac{\sigma_1+\sigma_3}{2}$) of σ'_1 and σ'_3. Any change in the state of stress caused by fluid injection or withdrawal that moves the initial point (σ_{im} , σ_{is}) to ($\sigma_{im}+\Delta\sigma_m$, $\sigma_{is}+\Delta\sigma_s$) on the Coulomb line results in fault reactivation and a seismic event. $\Delta\sigma_s$ is poroelastic effect and implying that fluid injection or withdrawal causes total stress alteration. (c) Two mechanisms of injection change Mohr circle representation of stress state before (black solid circle) and after perturbation. Dashed blue and red circles are Mohr circle representations due to pore pressure buildup (decrease of effective normal stress) and poroelastic effect, respectively.

1.3 Wastewater Disposal and Seismicity in Oklahoma, US

Earthquakes in the central and eastern United States (CEUS) has been historically rare. The average number of earthquakes with M_w >3 per year was 21 in the CEUS between 1967 and 2000 (Ellsworth 2013). Starting in 2001, there was a noteworthy surge in the number of felt events that accelerating in 2009 (Figure 3, Ellsworth 2013, Petersen 2017). In 2014, more earthquakes with M_w > 3 were recorded in Oklahoma than in California for the first time in recorded history (Figure 4, United States Geological Survey, USGS). These earthquakes occurred close to oil and gas activity and led to widespread concern about potential damage from induced seismicity. Many researchers suggested that these seismic activities are related to oil and gas operations, in particular, the disposal of saltwater co-produced with oil and gas into deep subsurface reservoirs (Frohlich et al. 2011, Horton 2012, Keranen et al. 2013, Kim 2013, Hornbach et al. 2015).

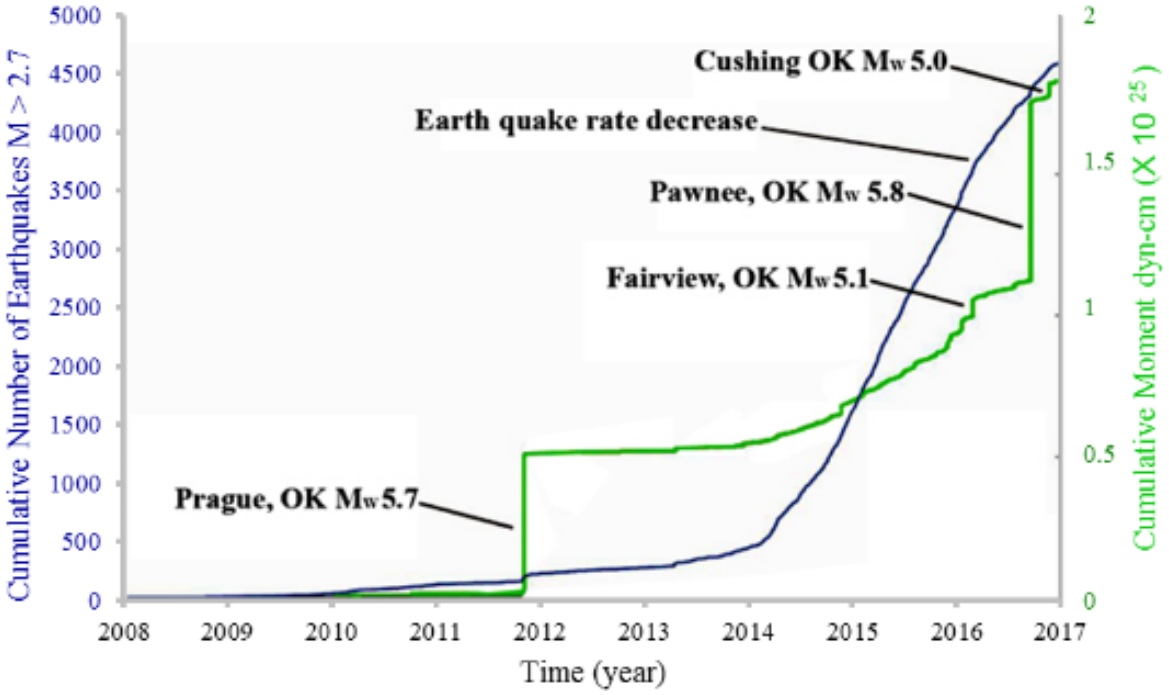


Figure 3: Cumulative number of events ($M_w \geqslant 2.7$) and cumulative moment in Oklahoma since 2007 (Petersen, 2017).

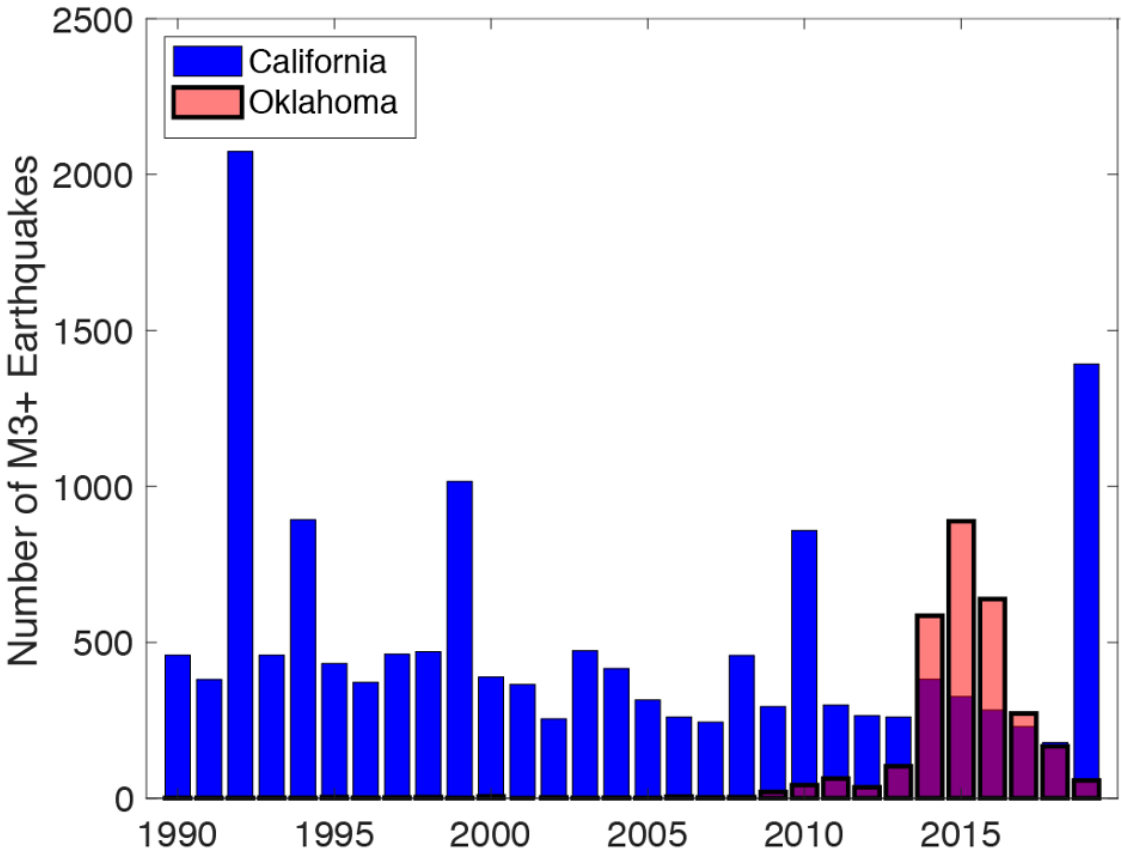


Figure 4: The number of M_w >3 earthquakes in Oklahoma vs California from 1990 to 2019. California earthquake counts are shown as a blue bar and Oklahoma earthquake counts are shown as a red bar (from: https://www.usgs.gov/media/images/number-m3-earthquakes-oklahoma-vs-california-1990-2019).

Oil and gas production started in Oklahoma in 1906. Oil and gas production in Oklahoma during 1906 was approximately 18.1 million barrels of oil (MMBO) and 0.62 MMBOE, and piked at ~278 MMBO in 1927 (Oklahoma Corporation Commission, OCC) and at ~399 MMBOE in 1990 (Holland and Murray 2014, Oklahoma Corporation Commission, OCC), respectively. Horizontal well technology and stimulation methods (e.g. hydraulic fracturing) have made Oklahoma one of the largest producers in the United States in the last two decades. On the other hand, produced oil and gas is usually accompanied by water production. Holland and Murray (2014) estimated the volume of oil and gas co-produced water ~800 to

~930 MMbbl between 2000 and 2011. In general, water that is produced from oil/gas extraction is injected through the oil/gas wells as a part of EOR operations (e.g. water-flooding), or it is disposed into the high permeable sedimentary formations.

In the United States, Class II UIC (underground injection control) wells are utilized to inject flow-back water after hydraulic fracturing operations and saline water co-produced with oil and gas. In the 1980s, the UIC program which was executed by the U.S. Environmental Protection Agency (EPA) defined six different types of wells (Class I to VI) to control and manage injections of fluid into the subsurface. Enhanced oil-recovery injection (EORI) and salt-water disposal (SWD) are the two main applications of Class II UIC wells. OCC (Oklahoma Corporation Commission) reported that in 2011 Oklahoma has 9630 class II UIC wells among which 5506 and 4124 are EORI and SWD wells, respectively. In 2011, 1093 MMbbl in Oklahoma were injected as EOR operations with the Desmoinesian and Atokan-Morrowan zones receiving the highest EOR injected fluid volumes (Holland and Murray 2014). This volume was 891.9 MMbbl in Oklahoma for SWD wells with the Arbuckle and Devonian to Middle Ordovician zones receiving the highest SWD volumes (Murray and Holland 2014). EOR injected volumes into Arbuckle and underlying basement was negligible which indicates that EORI had small on induced seismic events. On the other hand, volumes that mostly were injected through SWD wells into the Arbuckle (which overlies the crystalline basement) were responsible for the induced seismic activities in the last decade.

The Arbuckle is Cambrian and early Ordovician in age and was deposited in the midcontinent when the shallow epeiric Sauk Sea covered the present-day central and eastern United States (CEUS). The Arbuckle group is one of the units constructing the Great American

Carbonate Bank that was deposited onto the Precambrian craton by the Sauk Sea. Widespread weathering and karstification happened in the Arbuckle during the early Ordovician when it was exposed to the atmosphere and meteoric water (Loucks 2006, Murray 2014). The Arbuckle is mainly carbonate rock with intermittent sand and shale (Murray and Holland 2014). Extensive fracturing due to tectonic activities and several stages of diagenetic alterations such as dolomitization, dissolution, etc. have opposite effects on the porosity and permeability. Franseen et al. (2004) defined three end-member reservoir types within the Arbuckle: (A) fracture dominated, (B) paleokarst dominated, and (C) facies controlled porosity and permeability. Although there are zones of high porosity and permeability, there are also areas of dense and non-porous zones up to hundreds of feet thick (Carr et al. 1986).

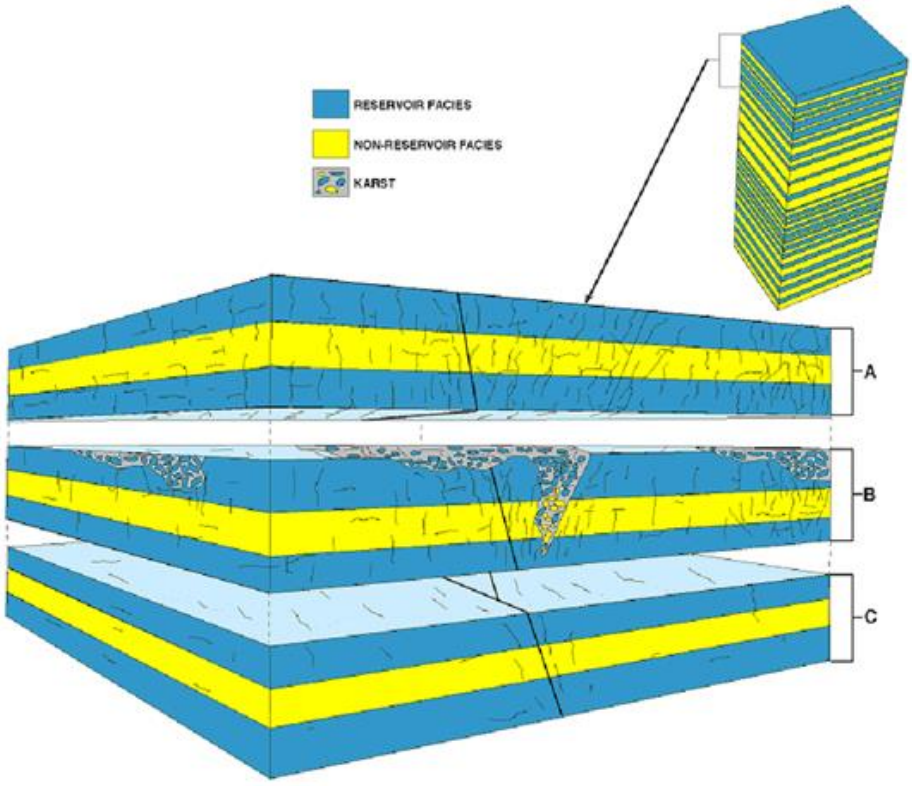


Figure 5: Three end-member reservoir types within the Arbuckle: (A) fracture dominated, (B) paleokarst dominated, and (C) facies-controlled porosity and permeability (Franseen et al. (2004)).

1.4 Research Objectives

The main objective of this work is to shed light on the injection mechanism and its potential for faults reactivation. For this purpose, a three-dimensional coupled fluid-mechanical model is constructed to study a detailed mechanism. In brief, the effect of the following factors on the fault response to saltwater injection are studied:

- Fault strike orientation and in-situ maximum horizontal stress azimuth
- Hydromechanical properties of reservoir and fault zone.
- Reservoir-basement interface and fault architecture

As an application of our model, the 2011 Prague, Oklahoma earthquake sequence has been studied. Using a 3D model, the potential effect of injection in Oklahoma on the Prague, 2011 earthquakes is studied. The last chapter includes the application of a 3D distinct element model to simulate two experimental works developed and performed at Reservoir Geomechanics and Seismicity Research Lab (RGSRG Lab) at the University of Oklahoma (Yu and Ghassemi 2017 and 2019, Hu and Ghassemi 2019). The first experiment includes the "hydroshearing" phenomenon in which the roughness of the sheared fractures causes the fracture network permeability enhancement. The second experiment studies interaction of a natural and an approaching hydraulic fracture.

1.5 Dissertation Outline

Similar to other geological engineering fields, induced seismicity studies must deal with the reality of uncertainty and incomplete comprehension of the physics and mechanisms of subsurface processes. Direct determination of hydro-mechanical properties and condition of subsurface is limited to the near well zones, and indirect measurements include many uncertainties and assumptions. Despite advances in earthquake experiments and simulations that

enhance our understanding of induced seismicity, there are a lot of uncertainties that make it difficult to quantify earthquakes.

The main objective of this work is to develop a fundamental understanding of induced seismicity using a coupled poromechanical model. In the following, the studies that are performed in this research are introduced.

In Chapter 1, the induced seismicity phenomenon and its mechanism are discussed. Also, the history of wastewater disposal in Oklahoma and its effect on increased seismic events are reviewed.

In Chapter 2, the coupled poromechanical numerical formulation used in this study is briefly described. Also, the methods (finite difference and discrete element methods) by which rock discontinuities including fractures and faults were modeled in this work ex-plained.

In Chapter 3, using a 3D fully coupled model, different factors such as hydromechanical effect, principal stresses orientation, etc on fault reactivation are studied. This includes a generic fault located in a zone with a geology setting similar to Oklahoma where hosted the most induced earthquakes in the last decade.

In Chapter 4, we present a study that focused on one of the largest earthquakes associated with wastewater disposal, the 2011 Mw 5.6 earthquake near Prague, Oklahoma, USA. In this study, mechanisms that could explain the almost 12 years delay between the start of injection operation and the Mw 4.8 foreshock shock were investigated.

In Chapter 5, 3D fully coupled discrete element models are used to simulate two experimental tests to improve our understanding of the complicated process in tests. The first part provides the results of the numerical hydro-mechanical coupled model of the shear stimulation tests based on the experimental results from Reservoir Geomechanics and Seismicity

Research Lab at the University of Oklahoma (Yu & Ghassemi 2017, 2019). The numerical model is carried out using 3DEC, a discrete element software (3DEC, Itasca, 2016), for Sierra White granite. In the second part, a 3D discrete element model is utilized to investigate the complex stress and pore pressure distributions in a test in which slippage of a natural fracture resulting from an approaching hydraulic fracture was studied.

In Chapter 6, the results of this study are discussed, and conclusions are made. Also, future work in this area is suggested.

Model Development

2.1 Formulation

The modeling work in this study was conducted with FLAC3D and 3DEC (Itasca, 2016 and 2018) in which explicit finite difference and distinct element programs are used, respectively. First, the basic hydro-mechanical equations are briefly explained, and in the next sections, the numerical methods are discussed. The following hydro-mechanical equations are as follows (Cheng 2016, Itasca 2018).

2.1.1 Fluid Mass Balance

$$\frac{\partial P_p}{\partial t} = -M\left[\boldsymbol{\nabla}.\boldsymbol{q}^F + \alpha\frac{\partial \varepsilon_v}{\partial t}\right] \tag{2.1}$$

where P_p is fluid pressure, M is the Biot modulus, ε_v is the volumetric strain.

2.1.2 Fluid Transport (Darcy's Law)

$$\boldsymbol{q}^F = -k^F\boldsymbol{\nabla}\left(P_p - \rho_f\,\boldsymbol{g}.\boldsymbol{x}\right) \tag{2.2}$$

where k^F, g, x are the fluid mobility coefficient ($k^F = \kappa/\mu_f$, where κ is the intrinsic permeability, and μ_f is the fluid dynamic viscosity, and ρ_f is fluid density), gravity vector, and displacement vector, respectively.

The mechanical constitutive relation for elastic material is

$$\frac{\partial \sigma_{ij}}{\partial t} + \alpha\frac{\partial P_f}{\partial t}\delta_{ij} = 2G\left(\frac{\partial \varepsilon_{ij}}{\partial t} - \alpha_s\frac{\partial T}{\partial t}\delta_{ij}\right) + \left(K - \frac{2G}{3}\right)\left(\frac{\partial \varepsilon_{kk}}{\partial t} - \beta_s\frac{\partial T}{\partial t}\right)\delta_{ij} \tag{2.3}$$

Where σ_{ij} and ε_{ij} are total stresses and strains, α is Biot's effective stress coefficient, K and G are bulk and shear modulus, and δ_{ij} is Kronecker delta.

2.2 Explicit Finite Difference

The numerical method used in FLAC3D (Itasca 2018) is an explicit finite difference method. To study the mechanical behavior of a continuous medium when it reaches equilibrium or steady plastic flow, the solution in FLAC3D is described by the following three approaches (Itasca 2018):

(1) finite difference approach (space and time derivatives of a variable are estimated by finite differences, assuming linear variations of the variable over finite space and time intervals, respectively);

(2) discrete-model approach (the continuous medium is replaced by a discrete equivalent one in which all forces involved (applied and interactive) are concentrated at the nodes of a three-dimensional mesh used in the medium representation.); and

(3) dynamic-solution approach (the inertial terms in the equations of motion are used as numerical means to reach the equilibrium state of the system under consideration.)

The laws of motion for the continuum are, using these approaches, transformed into discrete forms of Newton's law at the nodes. The resulting system of ordinary differential equations is then solved numerically using an explicit finite difference approach in time. For more detail, the reader is referred to Itasca (2018).

2.3 Distinct Element Method

The numerical method used in 3DEC is a distinct element method that is categorized as a discontinuum analysis technique. The distinct element method (DEM) is a numerical solution to study the mechanical behavior of discontinuous bodies. Using deformable polygonal-shaped blocks, Cundall (1971, 1979) developed the DEM to solve rock and soil mechanic problems. The main distinction between a discontinuous and a continuous body is the exist-

ence of interfaces or contacts between the discrete bodies of which the system consists. Figure 6 depicts schemes of a continuum and a discrete model, and their main entities. Discontinuum methods have different categories based on the way (1) contacts, and (2) the discrete bodies are represented in the numerical formulation. A numerical model should be capable of recognizing (1) behavior of the discontinuities, and (2) behavior of the solid material to be able to model a discontinuous system (e.g. rock mass problems).

In the first place, the model must recognize the existence of contacts or interfaces between the discrete bodies that make up the system. Numerical methods are divided into two groups by the way they treat behavior in the normal direction of motion at contacts. In the first group, using a soft-contact approach, a finite normal stiffness is considered to represent the determinable stiffness at contact or joint. In the second group, using a hard-contact approach, any interpenetration at contacts of the two bodies that form the contact is prevented. The type of contacts in a numerical model should be chosen based on the physics of the problem rather than numerical convenience. The location of the contact should be identified in a model. Mechanical behavior of the solid material of the discontinuous system is the second type of mechanical behavior.

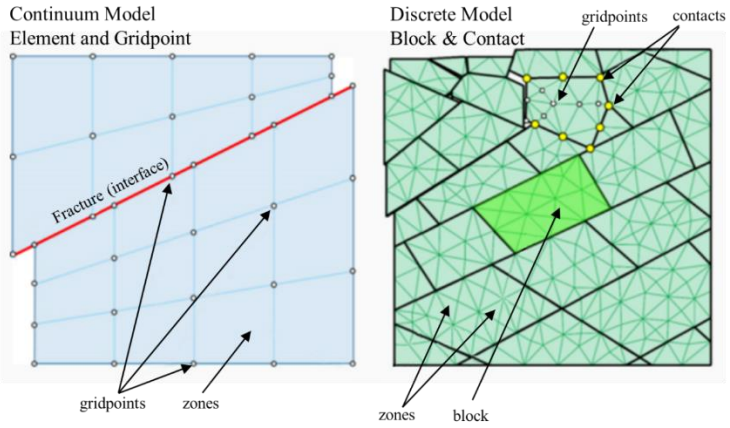


Figure 6: Comparison of the structure and main entities in a continuum (left) and a discrete (right) model (https://www.itascacg.com/software/distinct-element-method)

There are two types of behavioral representation: rigid or deformable materials. When most deformations on the system are due to displacements along discontinuities, the assumption of material rigidity can be useful. The deformation also can be taken into account by two methods: (1) the direct method of introducing deformability and (2) by the superposition of several mode shapes for the whole body. Although several programs based on continuum mechanics (e.g. finite element, finite-difference, boundary element) which use "interface" or "slide lines" have been applied to solve rock mass-related problems, there are restrictions to using these methods to solve a problem with discontinuities. First, for many intersecting interfaces, the logic may break down. Second, there is no automatic scheme for new contacts recognition.

The block is the fundamental geometric entity for the distinct element calculation. The 3DEC model is created by either "cutting" a single block into many smaller blocks, or creating separate blocks and joining them together. Each block is an independent entity that may be detached from other blocks, or may interact with other blocks via surface forces. Each block is connected to adjacent blocks via point contacts. Contact may be considered a boundary condition that applies external forces to each block. Each contact is divided into sub-contacts for both rigid and deformable blocks. Interaction forces between blocks are applied at sub-contacts. A discontinuity is a geologic feature that separates a physical mass into distinct parts. Discontinuities include joints, faults and fractures, and other discontinuous features in a rock mass. To be represented in 3DEC, a discontinuity must have a trace length scale that is approximate of the same order as the engineering structure being analyzed. A discontinuity in 3DEC is defined by at least one contact between blocks. Deformable blocks are composed of tetrahedral finite-difference zones. Mechanical changes (e.g., stress/strain) are calculated

within each zone. The block constitutive (or material) model represents the deformation and strength behavior prescribed to the zones of deformable blocks in a 3DEC model. Several constitutive models are available in 3DEC to simulate different types of behavior commonly associated with geologic materials. The joint constitutive model represents the normal and shear interaction between blocks at their contact (sub-contact) points. The joint model includes normal and shear elastic stiffness components, and limiting shear and tensile strength components. The basic joint model is the Coulomb-slip model. A certain number of steps is required to arrive at an equilibrium (or steady-flow) state for a static solution. In 3DEC, joint normal stiffness and shear stiffness are represented by linearly elastic springs. The shear resistance of the joint is usually characterized by the Coulomb slip law. Dilational response can be represented by prescribing a dilation angle.

2.4 Hydraulic Modelling in 3DEC

The governing equation for fluid flow in joints is based on a simplified form of the Navier-Stokes equation. For two parallel, impermeable boundaries, Navier-Stokes equation for an incompressible fluid simplifies to the Reynolds equation (Batchelor 1967):

$$(\frac{u^3}{12\mu}\phi_{,i})_{,i} = 0 \qquad (2.4)$$

where $u = u(x_i)$ is the distance between the impermeable boundaries at some point x_i ($i = 1, 2$) in the plane, ϕ is the fluid potential ($p + \rho gz$); g is the acceleration due to gravity; ρ is the fluid density; μ is the fluid viscosity; z is the elevation from the datum, and p is the pressure in the fluid.

From Eq. 2.1, the fluid flow rate per unit width of the plates is

$$q_i = \frac{-u^3}{12\mu}\phi_{,i} \qquad (2.5)$$

and the permeability of a fracture is $u^2/12$.

In Eq. 2.4, u = u (xi) is the actual distance between two rough surfaces of the joint at the point xi. Characteristically, variation of the joint aperture occurs on a much smaller scale than the characteristic length of the model (e.g., characteristic length of the problem), and it is helpful to find a relation between qi and ϕ,i that is valid on the macro scale of the joint, but which disregards the local variations of aperture. A relationship of the same form as that of Eq. 2.4 may be useful, except that uh is now a macro parameter related to "Representative Elementary Area" (REA). The joint macro properties are related to a "point" of a joint which represents an area of the joint, termed the "Representative Elementary Area" or REA, with a characteristic length that is much larger than the characteristic length of the joint surface roughness, and much smaller than the characteristic length of the model. The hydraulic aperture, uh, is a function of the mechanical aperture, um, which is defined as the average distance between the joint surfaces. It is difficult to measure the mechanical aperture directly. Most authors assume that uh = um. Detournay (1980) has proposed a relation between the hydraulic aperture, uh, and the joint deformation, Δum:For this model, the aperture at zero stress, u_{h0}, and the residual hydraulic aperture, u_{res}, must be defined. For efficiency in the explicit calculation, a maximum value of hydraulic aperture (u_{max}) which is the maximum value used in flow rate calculation is defined. It is also assumed that joints are be fully saturated and the degree of saturation is always one (1). Pore pressures can be positive or zero (0). No negative pore pressures are possible. For more detail, the reader is referred to Itasca (2016).

$$u_h = f u_m = u_{h0} + f \Delta u_m \tag{2.6}$$

Then the cubic law is as

$$q_i = \frac{-(u_{h0} + f \Delta u_m)^3}{12\mu} \phi_{,i} \tag{2.7}$$

Where u_{h0} is the joint aperture at zero normal stress; and Δu_n is the joint normal displacement (positive denoting opening). Joint aperture is also bound by a lower value, u_{res}, which is the minimum (residual) value for the aperture, below which mechanical closure does not affect the contact permeability. For this model, the aperture at zero stress, u_{h0}, and the residual hydraulic aperture, u_{res}, must be defined. For efficiency in the explicit calculation, a maximum value of hydraulic aperture (u_{max}) which is the maximum value used in flow rate calculation is defined. It is also assumed that joints are be fully saturated and the degree of saturation is always one (1). Pore pressures can be positive or zero (0). No negative pore pressures are possible. For more detail, the reader is referred to Itasca (2016).

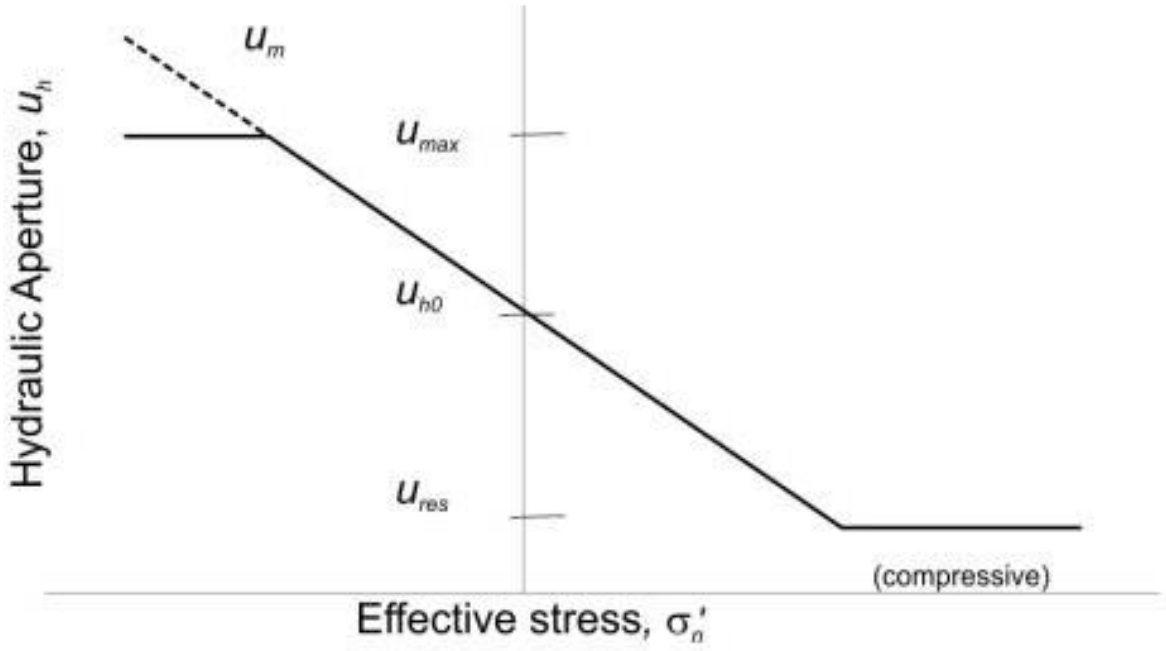


Figure 7: Idealized relation between hydraulic aperture and effective normal stress for a rock joint (effective stress is positive in compression). u_{h0} and u_{res} are the joint apertures at zero normal stress and the minimum (residual) value for the aperture respectively. For efficiency in the explicit calculation, a maximum value of hydraulic aperture (u_{max}) which is the maximum value used in flow rate calculation is assumed.

Basement Fault Reactivation in Response to Injection into Overlying Sedimentary Reservoir

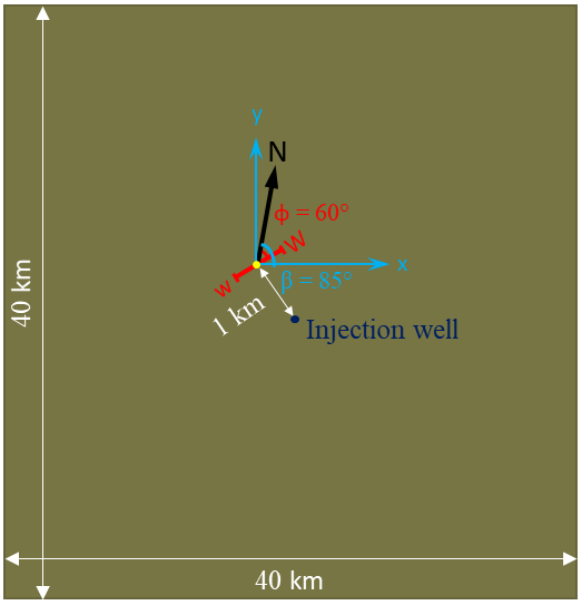
3.1 Introduction

As mentioned in chapter 1, there are two main processes in fluid-injection-induced fault reactivation. The first one is the direct effect of pore pressure diffusion resulting in decrease of normal effective stress on faults. The second process is poroelastic effect that can favor or hinder fault reactivation depending on the relative injector location and fault. In many previous studies on the effect of injection on fault reactivation, only the direct effect of pore pressure increase on the faults was evaluated (Keranen et al. 2014, Hornbach et al. 2016, Ortiz et al. 2019) while in others the indirect effect of change in stress on the fault also has been evaluated (Lee and Ghassemi 2011, Safari and Ghassemi 2016; Cheng and Ghassemi, 2019, Chang and Segal 2016, Fan et al. 2019, Haddad and Eichhubl, 2020, Hemami et al. 2020). In almost all of the previous studies, it is assumed that the faulting regime is normal or reverse regimes, while induced seismicity commonly occurred in strike-slip stress regimes. In this chapter, the effect of different factors on fault reactivation in a geological setting similar to Oklahoma (as mentioned in Chapter 1, the host of majority of induced seismic events in the 2010s) are studied. The results can be applied to areas underlain by a similar basement to Oklahoma in the Central United States and other parts of the world with fluid injection operations.

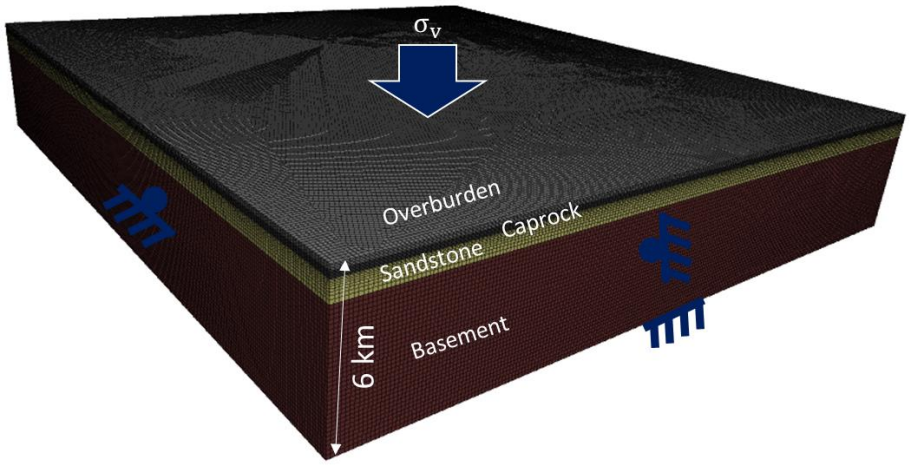
In this chapter, we study fault reactivation in association with fluid injection in subsurface with strike-slip stress regime and the effect of different factors such as principal horizontal stresses and faults orientation, hydromechanical properties of the fault zone and subsurface layers, etc. We constructed a 3D fully coupled four-layer geometry including a sandstone

reservoir overlain by a thick low-permeable caprock and a thick overburden layer, respectively. The sandstone layer is underlain by basement rocks. There is a high permeable damage zone around the fault that acts as a conduit for injected fluid. The model has dimensions of 40 × 40 × 5.5 km in the x-, y-, and z-directions, respectively (Figure 8). In our model x- and y-directions are corresponded to the maximum and minimum horizontal stresses, respectively. The fault extends up from the basement at depth of 5.5 km and cuts the overlaying sandstone layer (Keranen et al. 2013; Kolawole et al., 2019), and includes a 100 m damage zone. In all cases (unless mentioned otherwise), we assume the hydraulic and mechanical properties of subsurface layers are identical to Table 1. The stress regime is strike-slip, and the orientation of the maximum principal stress ($S_{H,max}$) is in N85°E. In section 3.3, it will be shown that $S_{H,max}$ azimuth of N85°E and fault strike orientation of 60° make the faults to be in the most critical condition. The gradients of the maximum and minimum horizontal stresses, and overburden gradient are $\frac{\partial S_{H,max}}{\partial z} = 30\ \frac{MPa}{km}$, $\frac{\partial S_{h,min}}{\partial z} = 15\ \frac{MPa}{km}$ $\frac{\partial S_{vertical}}{\partial z} = 25\ \frac{MPa}{km}$, respectively. These are similar to the condition in Oklahoma (Hair 2012, Alt and Zoback 2017). We assumed an underpressured system that has a fluid equivalent pore pressure gradient of ≈9 MPa/km (Carell 2014, Nelson et al. 2015). In all cases, a fluid with a rate of 0.03 m^3/s (16300 bbl/day) from the injection well located at the middle of the target reservoir is injected into the sandstone layer (Figure 8) for four years. The fluid has a viscosity and bulk modulus of 0.001 Pa s and 2 GPa, respectively (similar to what was injected in Wilzetta well in Oklahoma, Holland, personal correspondence). To evaluate fault reactivation potential, here we use the Mohr-Coulomb failure criterion and define a failure potential as $CFS=\tau_s-\mu(\sigma_n-Pp)$, where μ is the coefficient of friction, Pp is pore fluid pressure, and τ_s

and σ_n are shear and total normal tractions acting on the fault, respectively (the sign convention is compression positive). A positive CFS shows fault reactivation. The pore pressure and poroelastic effects are considered in this research by a fully coupled 3D model.



(a)



(b)

Figure 8: The model dimension, fault geometry, and boundary condition (not drawn to scale). The values of fault strike orientation (ϕ) and the azimuth of $S_{H,max}$ (β) are 60° and 85°, respectively. Boundary conditions account for vertical stress on the top, roller boundaries on the sides, and fixed displacement on the bottom of the model. The yellow dot on the fault shows the shortest point on the fault from the injection well.

As mentioned, the model includes four layers of overburden, caprock, sandstone, and the basement. The boundary condition consists of the roller, fixed, and applied traction on the sides, bottom, and top of the model, respectively. The top and the bottom of the model are located at depths of 0.8 km and 6 km, respectively.

Table 1: Rock mechanical and hydraulic properties used in the simulations (Hemami et al, 2021).

	Overburden	Caprock	Sandstone	Basement	Fault
Permeability (mD)	10 ($\approx 10^{-14}$ m^2)	0.01 ($\approx 10^{-17}$ m^2)	10 ($\approx 10^{-14}$ m^2)	0.01 ($\approx 10^{-17}$ m^2)	30 ($\approx 3\times 10^{-14}$ m^2)
Porosity, ϕ	0.1	0.13	0.1	0.01	0.1
Bulk Modulus, K (GPa)	22	21	54	67	8
Shear Modulus, G (GPa)	12	19	30	30	6
Friction angle, φ (°)	30	30	31.5	35	35
Biot's coefficient	0.8	0.7	0.8	0.4	0.9
Poroelastic stress coefficient, η	0.22	0.29	0.25	0.08	0.33
Thickness (km)	0.2	0.2	0.8	5	

3.2 Poroelastic Response of Target Layers and Adjacent Layers to the Fluid Injection

As mentioned, the main process for injection-induced earthquakes is pore pressure increase which results in reduction of effective normal stress on the fault, and may cause faults to slip under the ambient stress state. But this is not the only process that controls the subsurface fault reactivation. Pore pressure changes also lead to additional poroelastic stress which may contribute to fault slip. The theory of poroelasticity and observations at injection target (or

depleted hydrocarbon) reservoirs indicate that the in-situ stress field does not remain constant, and evolve during injection (or depletion) in time and space (Biot 1941, Cheng 2016, Rice and Cleary 1976, Segal 1987, Lorenz et al. 1991). The controlling parameters of the in-situ stress change are dependent on the site-specific hydromechanical properties and structural geometry.

Fluid injection tends to expand the reservoir rock. For a flat-lying, infinite reservoir, expansion in the vertical direction leads to the ground surface uplift, and in the horizontal direction is resisted by the surrounding rocks which are pushed outward from the center of the reservoir. Therefore, injection causes induced compressive stress in the injection site. This stress decays to zero and then becomes tensile due to strain compatibility requirements. That is the dilated zone, pulls on the surrounding rock leading to the zone of horizontal extension in the neighboring rocks above and below the reservoir. For real reservoirs which have a finite volume, injection (production) creates a stress arch in the overburden, and causes the total vertical stress acting on the reservoir changes during injection (production). In fact, in finite-volume reservoirs, the sideburden prevents the surface from following the reservoir. This arching effect (or shielding of stress by the overburden) causes the full weight of the overburden not to be sensed by the reservoir as the pore pressure changes. As a result, the uplift (subsidence) at the surface is less than that at the top of the reservoir (FJÆR 2008, Toomey, 2017). Figure 9 illustrates how depletion causes stress arching forms in the overburden due to stretching of the overburden as the reservoir pulls away from the surface (Toomey et al., 2017). Immediately above the reservoir, there is unloading in overburden, and the magnitude of the vertical stress decreases. Stress transfers to the loading zones (Figure 9) referred to as pillars of stress arch.

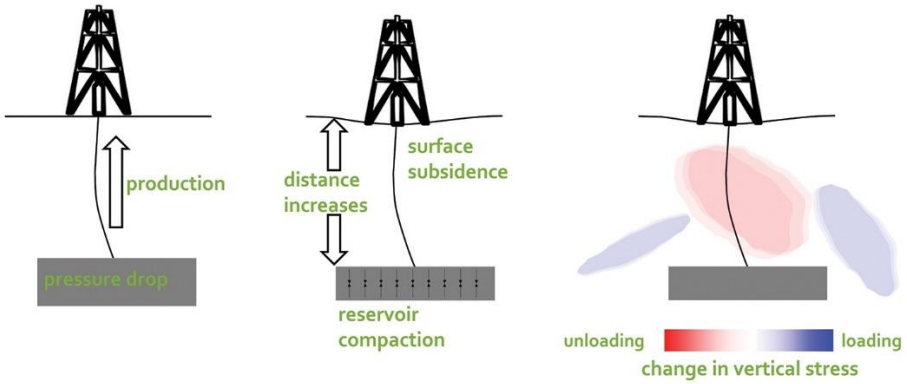


Figure 9: A schematic illustration shows how stress arching due to depletion forms in the overburden as the reservoir pulls away from the surface (Toomey et al., 2017).

In the injection target reservoir (and in general where the pore pressure is increased due to the injection), the induced normal traction on fault increases due to the poroelastic effect which results in increased stability if the fault is within the poroelastic compression. Tensile stresses develop ahead of the compressional domain which can be destabilizing. The magnitude of the poroelastic stress is a function of the rock poroelastic properties. The stress change is also transferred to the rocks above and below, affecting fault reactivation in those zones (Cheng and Segall, 2016 and 2017). Cooling and development of thermal stress may also cause fracture/fault instability (Ghassemi and Tao 2016) but its potential effect in Oklahoma seismicity has not been analyzed.

For a better understanding of the effect of injection on the reservoir, we conduct a simple simulation in our model in which saltwater (with properties as mentioned in 3.1) is injected at a constant rate of 0.05 m^3/s (27000 bbl/day) in the injection well (Figure 8) into the middle depth of sandstone layer for six months, and the induced deformation and stress are studied. Figure 10 depicts the induced pore pressure, σ_{xx}, σ_{yy}, σ_{xy} on a horizontal cross-section of the model at the middle depth of the sandstone. It is obvious that the injection causes an increase of total σ_{xx}, σ_{yy} and both decrease and increase of σ_{xy} around the injection well. It should be

noted that the value of shear stress change is much less than those of normal stresses. Figure 11 shows the normal strains in the x-, y-, and z-directions (ε_{xx}, ε_{yy}, ε_{zz}) on a horizontal cross-section of the model at the middle depth of the sandstone. Within a certain distance from the well, ε_{xx} and ε_{yy} are extensional, and beyond that the strain is contraction. ε_{zz} is negative indicating that the reservoir is expanding in the vertical direction.

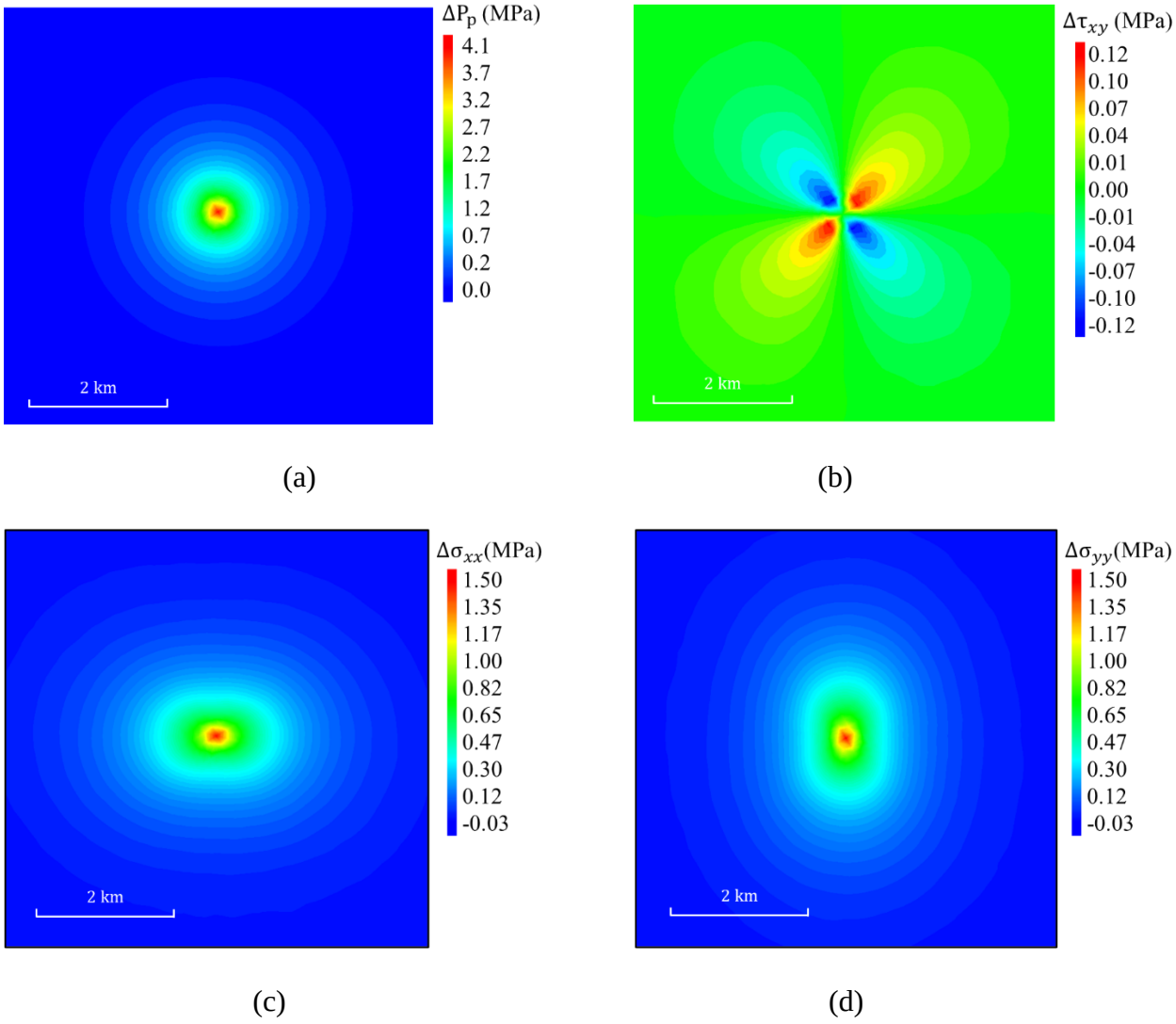


Figure 10: The contours of (a) ΔPp, (b) $\Delta\tau_{xy}$, (c) $\Delta\ \sigma_{xx}$, and (d) $\Delta\ \sigma_{yy}$ on a horizontal cross-section of the model at the middle depth of the sandstone induced by the injection of water with a constant rate of 0.05 m^3/s (27000 bbl/day) after six months at the center of the domain and in the middle depth of the sandstone layer (Figure 8).

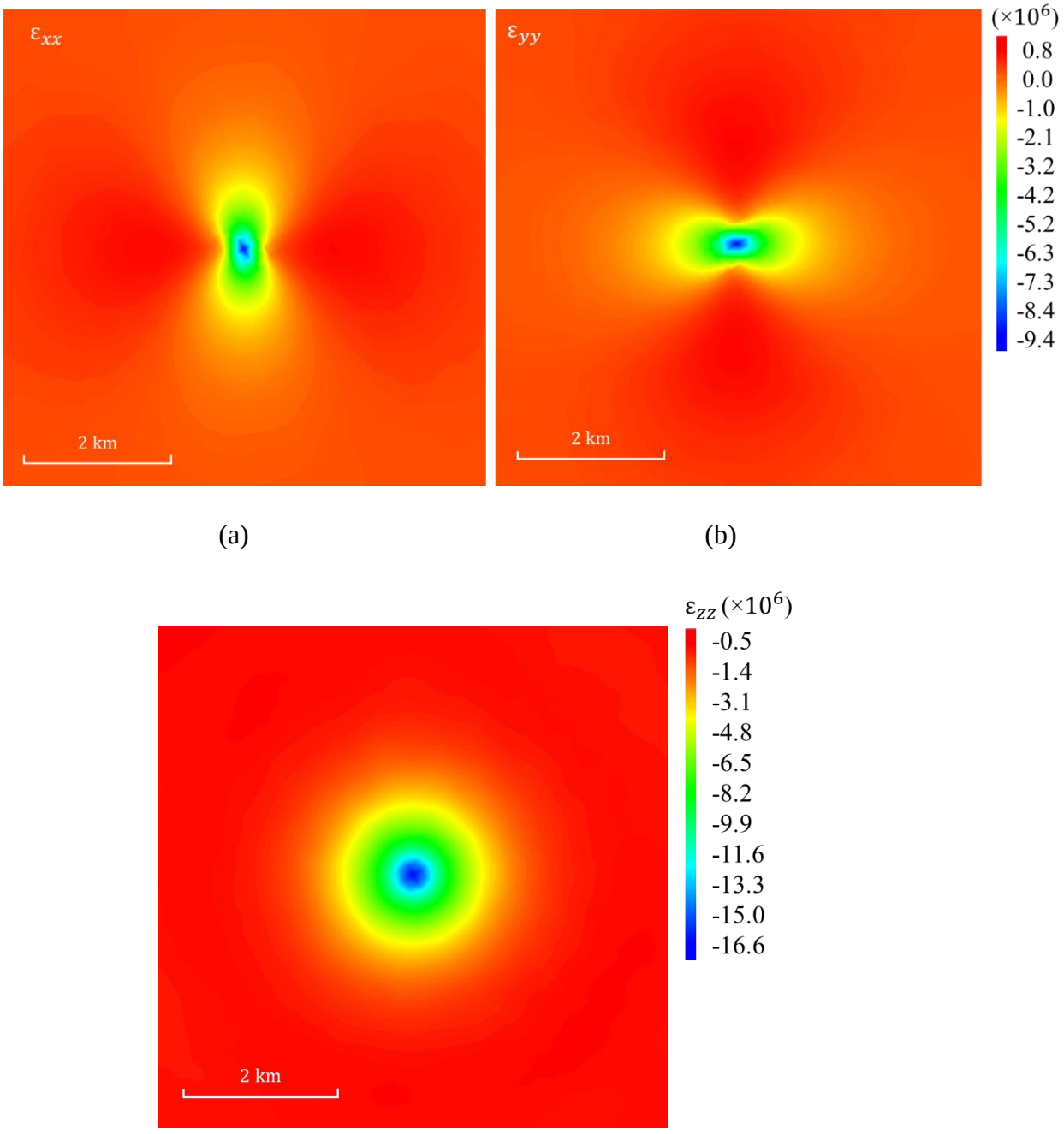


Figure 11: The contours of (a) ε_{xx}, (b) ε_{yy}, and (c) ε_{zz} on a horizontal cross-section of the model at the middle depth of the sandstone induced by the injection of water with a constant rate of 0.05 m^3/s (27000 bbl/day) after six months at the center of the domain and in the middle depths of the sandstone layer. In x and y-directions, within and beyond a certain distance from the well, the injection induces extension and contraction, respectively. In the z-direction (vertical direction), injection causes the expansion of the reservoir.

3.3 Effect of $S_{H,max}$ Azimuth and Fault Strike Direction

In this section, the effect of $S_{H,max}$ azimuth and fault strike orientation on the fault reactivation is discussed. Holland (2013) demonstrated that in Oklahoma strike-slip motion on steeply dipping faults dominates the focal mechanism distribution, and fault strikes were limited to the range of 0° to 180°. He mentioned, "In Oklahoma, the optimal fault strike orientation ranges between 40°– 60° and 130°– 150° and represent fault orientations most likely to have an earthquake". A wide range for the direction of the maximum principal stress ($S_{H,max}$) was proposed by the previous studies (Dart, 1990). For example, von Schonfeldt (1973) and Hooker and Johnosn (1969) reported N65°E and N94°E for $S_{H,max}$ azimuth using hydraulic fracturing and overcoring methods, respectively. Alt and Zoback (2017) compiled new information on the state of stress in Oklahoma to compare it with both mapped faults and faults inferred from earthquake epicenters and focal plane mechanisms. They demonstrated that all of the data show remarkably uniform stress directions, and reported that the orientation of the maximum horizontal stress in Oklahoma, is about N85°(±5°)E. Considering the gradient of principal horizontal stresses and pore pressure in 3.1, it can be shown that the relative angle of $S_{H,max}$ azimuth and fault strike orientations (β-ϕ, Figure 12) is 27° to 28° when the faults are in the most critical condition. Here, to ensure that different hydromechanical properties and possible local stress reorientation do not affect the fault, two scenarios are defined (Table 2). The azimuths of $S_{H,max}$ (β) are N80°E and N85°E in scenarios 1 and 2, respectively. Each scenario has three cases in which the fault strike orientation is 40°, 50°, 60° (Table 2). All scenarios are in agreement with Mohr-Coulomb theory in which fracture takes place in planes that pass through the direction of the intermediate principal stress

and are equally inclined at an angle less than 45° (β-ϕ < 45°) from the direction of the maximum principal stress (Jaeger et al. 2009). Again, in all scenarios a fluid with a rate of 0.03 m^3/s (16300 bbl/day) for four years from the injection well located at the middle of the target reservoir is injected into the sandstone layer (Figure 8).

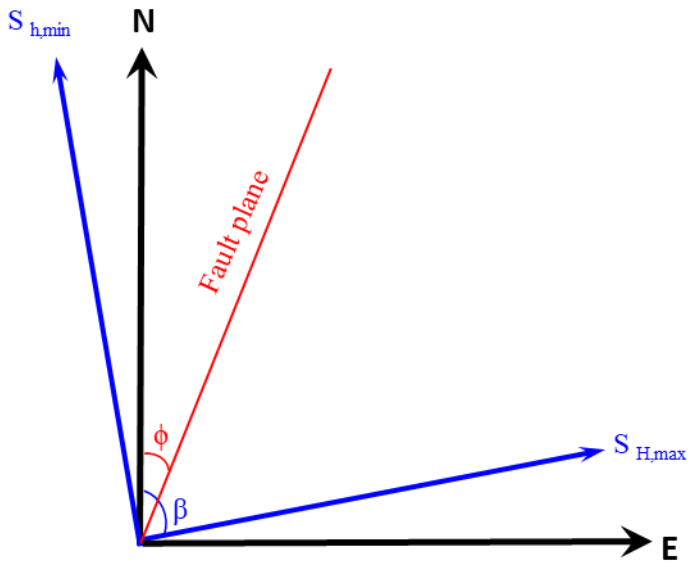


Figure 12: Different scenarios based on different values of fault strike orientation (ϕ) and the azimuth of $S_{H,max}$ (β). In this study, three values of ϕ = 40°, 50°, and 60° and two values of β = 80° and 85°are studied (Table 2). This is in agreement with Mohr-Coulomb theory in which fracture takes place in planes that pass through the direction of the intermediate principal stress and are equally inclined at an angle less than 45◦ from the direction of the maximum principal stress.

Table 2: Two scenarios with different cases are defined based on the possible relative angle of $S_{H,max}$ azimuth and fault strike orientations (β-ϕ, Figure 12).

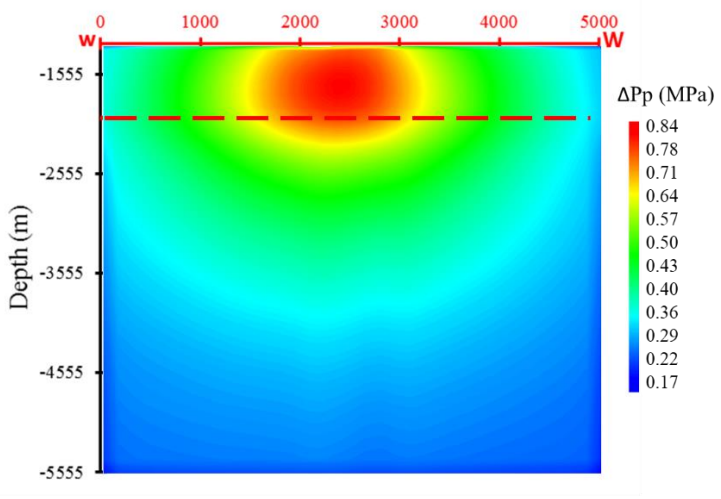
Scenario 1: β = N80°E	Case 1: ϕ = 40°	Case 2: ϕ = 50°	Case 3: ϕ = 60°
Scenario 2: β = N85°E	Case 1: ϕ = 40°	Case 2: ϕ = 50°	Case 3: ϕ = 60°
ϕ = Fault strike orientation, β = Azimuths of $S_{H,max}$			

The results show that the change of CFS (ΔCFS) and its components (ΔPp, $\Delta\sigma_n$, $\Delta\tau_s$) are similar in all scenarios. It can be explained by the theory of poroelasticity (Biot 1941, Jaeger 2009, Cheng 2015) that in a homogeneous isotropic material, the gradient of pore pressure (which only depends on the hydromechanical properties) acts as an additional body force. Here only the results of the case with β = N85°E and ϕ = 60° are shown. Figure 13 shows the ΔPp and ΔCFS are both positive on the fault plane in response to the injection. Due to the damage zone around the fault, pore pressure penetrates the greater depths that (5.5 km), and induces pore pressure of up to 0.84 MPa on the fault plane. Figure 14 depicts the $\Delta\sigma_n$ and $\Delta\tau_s$ (components of ΔCFS). It is obvious that due to the increased pore pressure, the $\Delta\sigma_n$ is positive all over the fault plane and is stabilizing. The shear stress both increases and decreases on the fault plane, and the values are less than the normal stress change ($\Delta\sigma_n$) (by an order of magnitude). The induced shear stress at reservoir depths is located on the whole fault plane while at the basement depths is on the edge of the fault. The magnitudes induced shear stress is more pronounced in the basement.

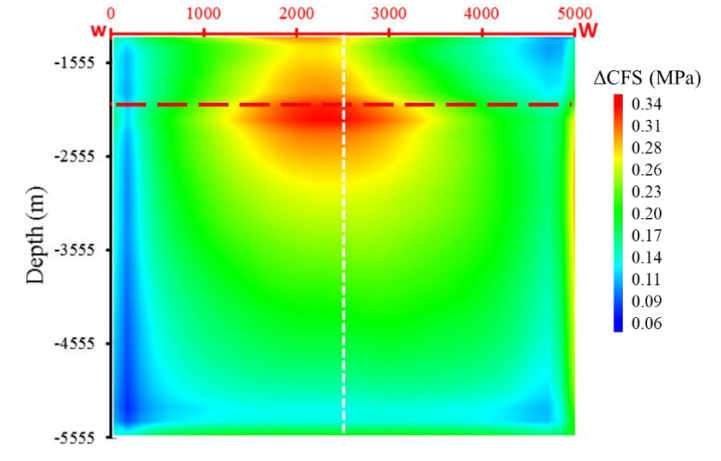
Figure 15 demonstrates the profiles of change of Coulomb failure stress (ΔCFS) and its components (ΔPp, $\Delta\sigma_n$, and $\Delta\tau_s$) along the white dashed line (the vertical line that has the shortest distance to the injection well) on the fault plane (Figure 13). It can be seen that CFS has the most increase in the shallow basement and therefore the fault has the most tendency for failure in the shallow basement. It should be noted that due to the shear stress change on the fault plane ($\Delta\tau_s$), the maximum of ΔCFS is not necessarily located on the zone that has the shortest distance to the well (Figure 13).

Since changes of CFS in all scenarios are identical, the initial state of stress of the fault zone determines which case becomes more critical after injection. Figure 16 and Figure 17 depict

the initial profiles of Coulomb failure stress (CFS) along the white dashed line on the fault plane (Figure 13) for both scenarios. As expected, cases 2 (β = N80°E and ϕ = 50°, β-ϕ = 30°) of scenario 1 and case 3 of scenario 2 (β = N85°E, ϕ = 60°, β-ϕ = 25°) have the most critical condition.

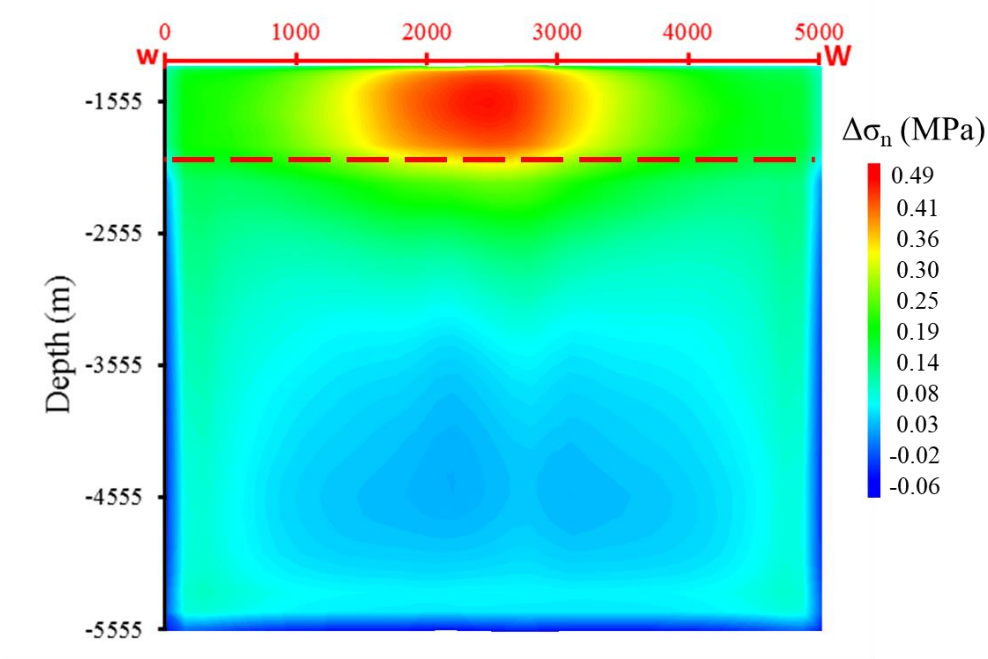


(a)

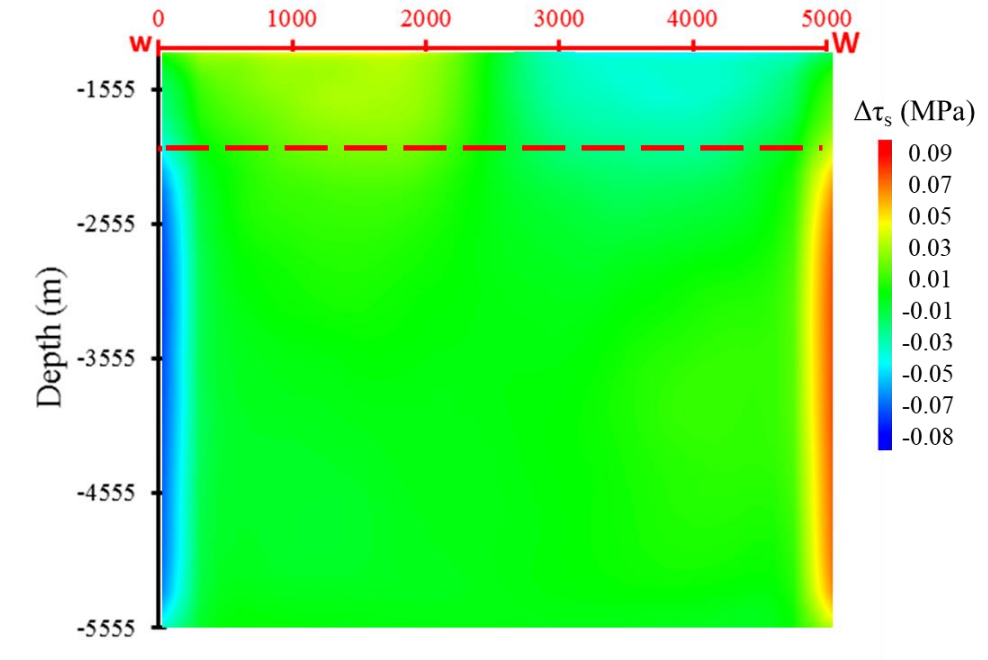


(b)

Figure 13: Sneario2, case 3-β = N85°E and ϕ = 60° (β- ϕ = 25°): (a) ΔPp and (b) ΔCFS on the fault plane induced after 4 years of injection with a rate of 0.03 m^3/s (16300 bbl/day). Red solid and dashed lines show the reservoir upper and lower boundaries, respectively. The white dashed line is the vertical line on the fault plane that has the shortest distance from the injection well. (Figure 8).



(a)



(b)

Figure 14: Sneario2, case 3-β = N85°E and ϕ = 60° (β- ϕ = 25°): a) $\Delta\sigma_n$ and b) $\Delta\tau_s$ on the fault plane induced after 4 years of injection with a rate of 0.03 m^3/s (16300 bbl/day). Red solid and dashed lines show the reservoir upper and lower boundaries, respectively.

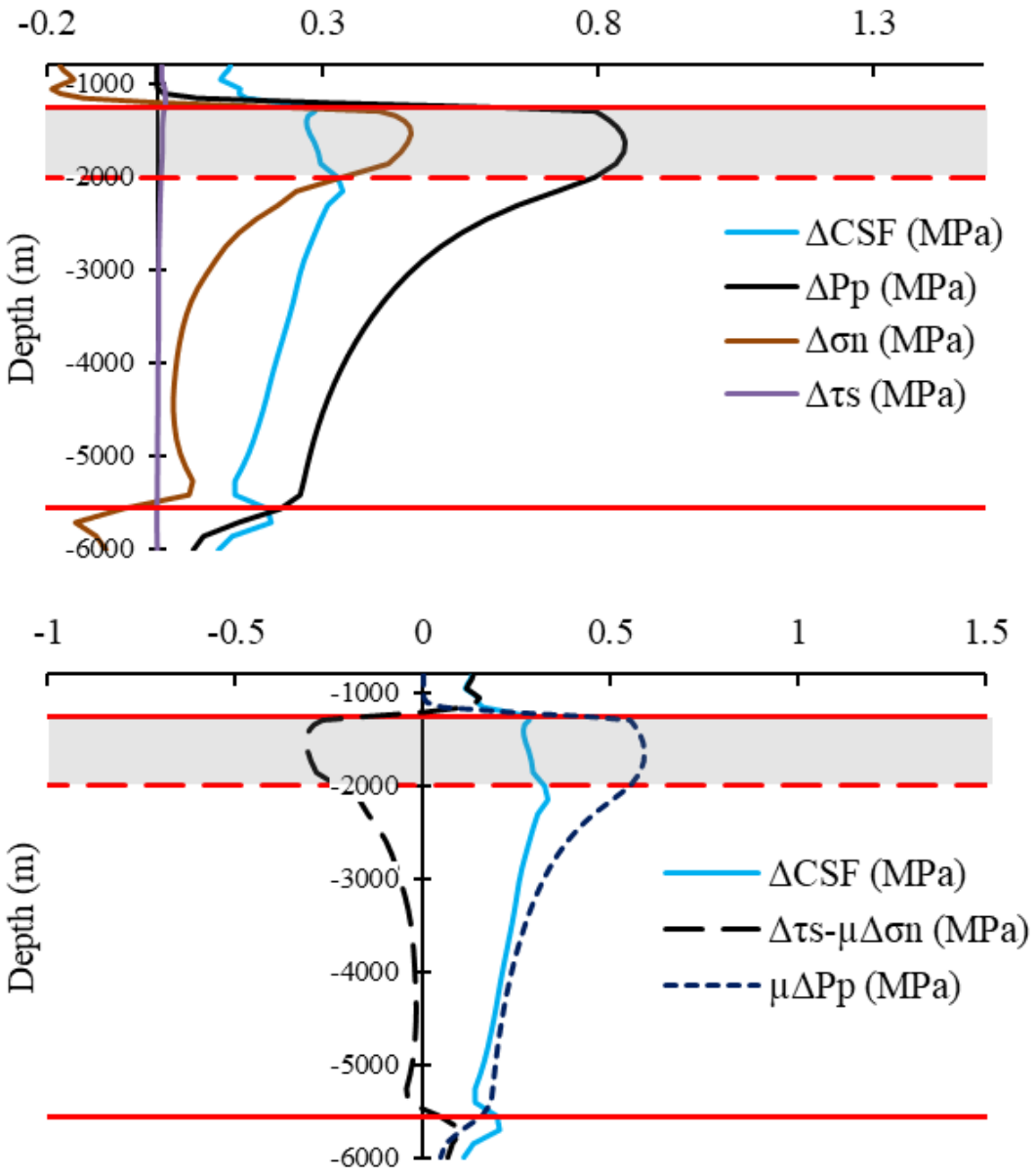


Figure 15: Sneario2, case 3-β = N85°E and ϕ = 60° (β- ϕ = 25°): Depth profiles of change of CFS (MPa), pore pressure (MPa), total normal stress (MPa), and shear stress (MPa) (Upper figure), and profile of change of poroelastic stress (MPa) and pore pressure (MPa) components of ΔCFS (Lower Figure) along the white dashed line on the fault plane along the cross-section W-w (Figure 13) after 4 years of injection. Solid red lines indicate the fault boundaries and the red dashed lines the lower boundary of the reservoir.

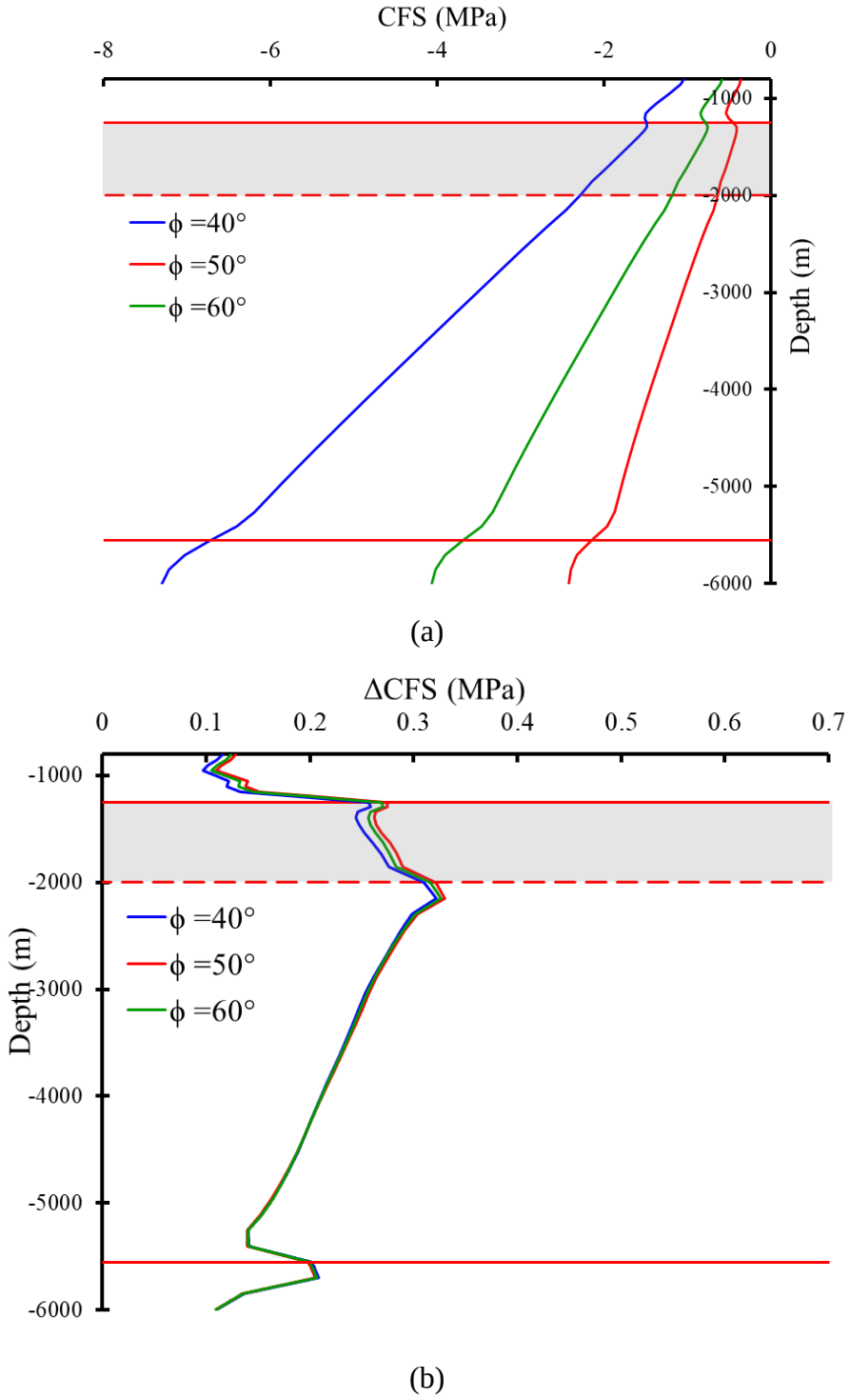
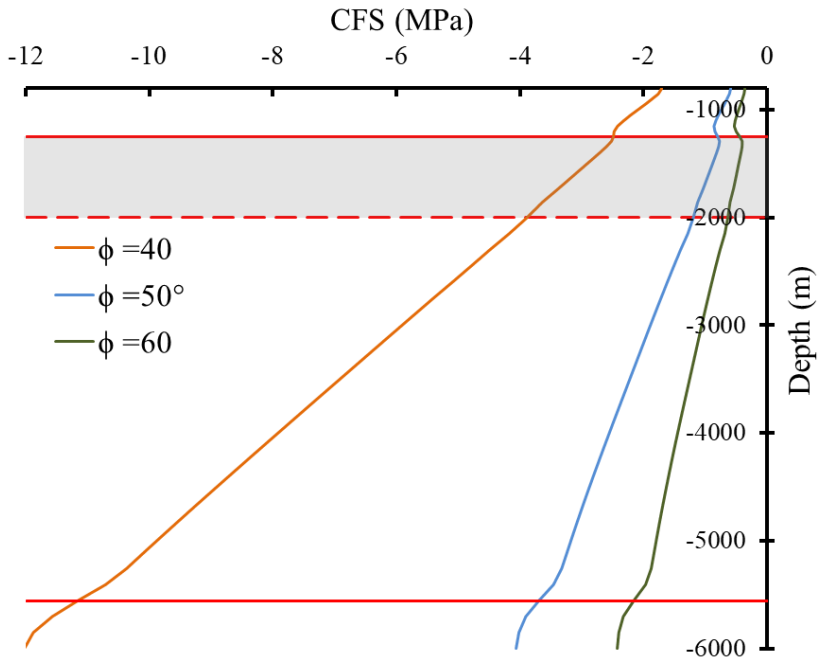
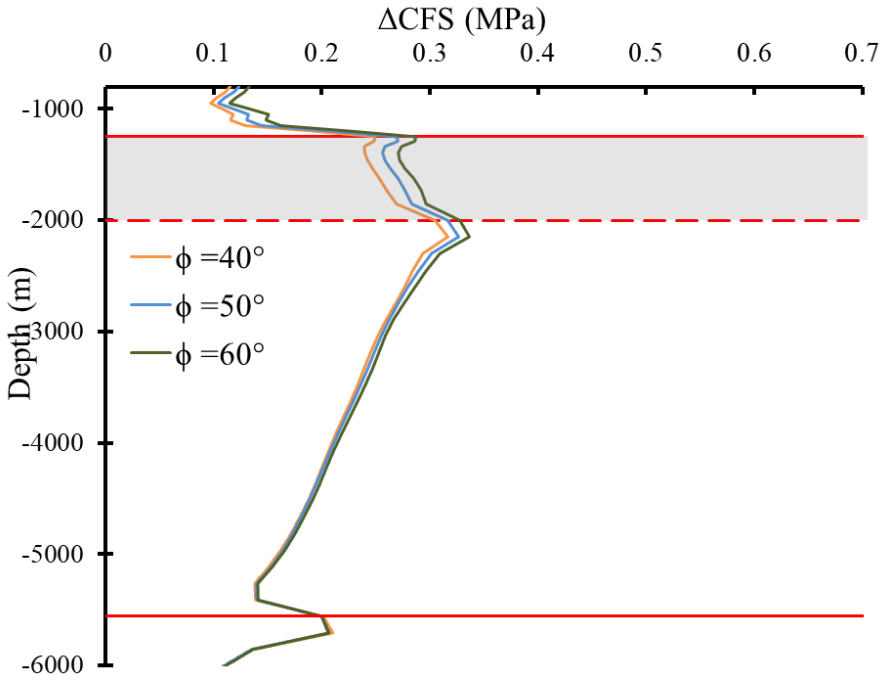


Figure 16: Scenario 1, (β = N80°E): Depth profiles of a) CFS and b) ΔCFS (MPa) along the dashed line on the fault plane along the cross-section W-w (Figure 13) after 4 years of injection. Solid red lines indicate the fault boundaries and the red dashed lines the lower boundary of the reservoir.



(a)



(b)

Figure 17: Scenario 2 (β = N85°E): Depth profiles of a) CFS and b) ΔCFS (MPa) along the dashed line on the fault plane along the cross-section W-w (Figure 13) after 4 years of injection. Solid red lines indicate the fault boundaries and the red dashed lines the lower boundary of the reservoir.

3.4 Effect of Hydromechanical Properties of the Reservoir, the Basement, and the Fault Zone on Fault Reactivation

In this section, we study the effect of hydraulic and mechanical properties of the reservoir, fault zone, and the basement on fault reactivation. We also consider the different types of sedimentary-basement interface nonconformity zone and their potential for controlling the fluid pressure and flow. To consider all possible cases, we define two scenarios with different cases (Table 3). Before we present the results, the potential effect of fault architects and different types of sedimentary-basement nonconformity on the injected fluid are briefly explained here.

In scenario 3, it is assumed there is no damage zone around the fault zone. Also, it is assumed that there is a continuous Type I reservoir-basement nonconformity with an altered zone (Petrie et al. 2020) which acts as a barrier to the downward migration of injected fluid. The altered zone includes a 50-m-thick altered zone that has lower permeability (an order of magnitude) than the basement rocks.

In scenario 4, it is assumed that there is a sharp interface (Type 0 will be explained in section 3.4.2, Petrie et al. 2020) between the reservoir and basement. In this scenario, the fault zone includes an impermeable fault core and a fault damage zone with higher permeability (30 mD) than the reservoir. Cases defined for this scenario can be found in Table 3.

3.4.1 Fault Damage Zone

Based on the field observations, usually fault zones include two distinguished structures (Caine et al. 1996, Chester et al. 1993, Mitchell and Faulkner 2009): (1) One or several highly granulated fault cores in the center (2) a damage zone located on the sides of the fault core and created by stressing and distributed cracking in earlier earthquakes (Figure 18a). The damage zone is the deformed volume adjacent to the fault core and includes fractures

over a wide range of length scales, subsidiary faults, veins, stylolites, cleavage, deformation bands, and folds (Faulkner et al. 2010, Rinaldi et al. 2014).

Table 3: Different scenarios for the study of the effect of hydromechanical properties of the basement, the reservoir, and the fault zone on fault reactivation.

<table>
<tr><td colspan="4">Scenario 3:
-The fault zone has an impermeable fault core
-No damage zone around the fault zone
-There is a continuous Type I[a] reservoir-basement nonconformity contact</td></tr>
<tr><td>Case 1:
η_{res}[b] = 0.25</td><td>Case 2:
η_{res}[b] = 0.3</td><td>Case 3:
The fault does not extend up from the basement into the reservoir.</td><td>Case 4:
$\alpha = 1$ for all layers</td></tr>
<tr><td colspan="4">Scenario 4:
-The fault zone includes an impermeable fault core and a high-permeable damage zone
-There is a Type 0[a] reservoir-basement nonconformity contact</td></tr>
<tr><td>Case 1:
η_{res}[b] = 0.25</td><td>Case 2:
η_{res}[b] = 0.3</td><td colspan="2">Case 3:
$\alpha = 1$ for all layers and fault zone</td></tr>
<tr><td colspan="4">[a] Petrie et al., 2020 [b] η = Poroelastic stress coefficient</td></tr>
</table>

High-permeability damage zones around previously active faults create a conduit-like system along the borders of faults, diffusing elevated fluid pressures from injection sites to

greater distances and deeper levels, that can reactivate long-dormant fault segments and trigger subsequent earthquakes.

Damage zones rocks are characterized by higher fracture density and lower Young's modulus than the host rock (Figure 18b and c). The width of damage zones varies from a few centimeters to hundreds of meters based on the maturity of a fault the accumulated displacements (Perrin et al. 2016, Savage and Brodsky 2011).

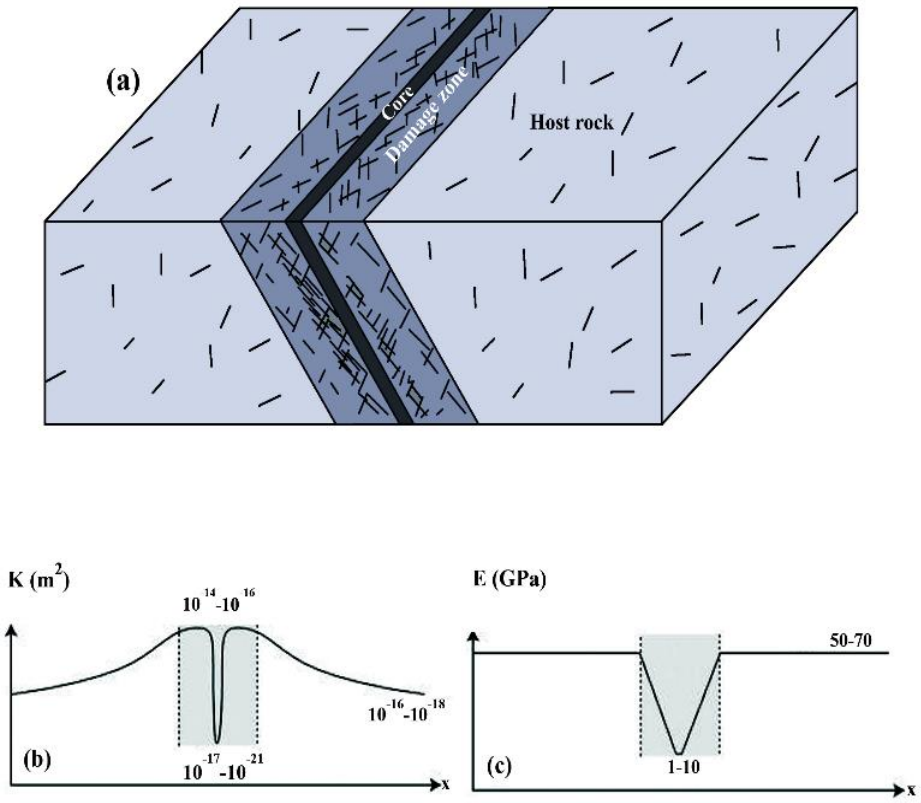


Figure 18: (a) Fault zone structure (b) permeability and (c) Young's modulus of fault zone (Chester, 1993; Cappa, 2009)

Many factors including mechanical damage, crack healing, chemical alteration, etc result in very complicated fault structures. The damage zone hydromechanical properties are affected by many factors such as lithology, the relative dip of bedding to the slip direction of the fault,

the slip mode, etc. Therefore, the fault zone properties (including damage core and damage zone) reflect the material properties and deformation history within a fault zone.

In respect of fluid flow, depending on the relative percentage of fault core and damage zone structures and the inherent variability in grain scale and fracture permeability, a fault zone can act as a conduit, barrier, or combined conduit-barrier (Caine et al. 1996). During an earthquake, a fault core can behave as a conduit and as a barrier when pores are filled by mineral precipitation following deformation (Chester and Logan 1986). Yeyha et al. (2018) mentioned some examples (Dixie Valley fault zone and Traill fault, East Greenland) in which the fault core acted as a short-lived fluid flow conduit that then rapidly sealed to form a barrier to flow. Therefore, it is necessary to identify the stage of fault evolution for the construction of a conceptual model for a special fault zone.

Pressure buildup and fluid flow in fault zones are affected by the permeability structure and permeability anisotropy which are highly dependent on the fault slip and the stressing (Yeyha et al. 2018, Caine and Forster 1999).

Chester et al. (1993), by observations of the internal structures of the San Andreas fault, realized that the fault core is bounded by a zone of the damaged host rock. This damage zone can create a permeability anisotropic along the fault. This permeability anisotropy affects notably the fluid flow and pattern of fluid pressure buildup within fault zones. Mandle et al. (1977) pointed out there is less storage capacity in the zone of deformation within a fault zone which resulting in lower fluid storage capacity, fluid discharge, and fluid pressure recovery during an earthquake. This may lead to heterogeneous fluid pressure buildup within the zone.

3.4.2 Sedimentary-Crystalline Rock Nonconformity

A low-permeable altered/weathered basement rocks along the sedimentary layer and basement nonconformity interface zone can control the cross-contact fluid flow and within the reservoir resulting to lessen seismic hazard (Kerner 2015, Oritz 2019, Petrie et al. 2020).

Petrie et al. (2020) summarized geologic observations obtained from the nonconformity zone, the altered rock volume surrounding the nonconformable contact (Figure 19). This zone has different thicknesses and is characterized by mineralogic and structural alteration of the protolith rocks adjacent to the nonconformity. Petrie et al. (2020) described nonconformity zones associated with Precambrian granite, gabbro, gneiss, and schists overlain by a porous sedimentary layer containing sandstone and mixed carbonate–clastic sequences. They defined three end-member types of nonconformity zones. Type 0 is a sharp contact between the sedimentary layer and the basement rocks. At a Type 0 nonconformity, due to the notable difference between the permeabilities of sedimentary and basement rocks, direct fluid pressure migration across the contact is prohibited and leading to flow parallel to the contact. Type I and II are phyllosilicate-rich and dominated by non-phyllosilicate secondary minerals, respectively. Petrie et al. (2020) reported that weathering, deformation, diagenesis, and fluid–rock interactions cause the nonconformity zone to be hydraulically heterogeneous at scales of millimeters to tens of meters. This causes the fluid flow and fluid pressures front propagation to move away from the injection well. Illustrating variations in rock properties at the nonconformity zone is necessary for subsurface fluid injection, as the hydromechanical properties of the rocks in the nonconformity zones affect the subsurface response.

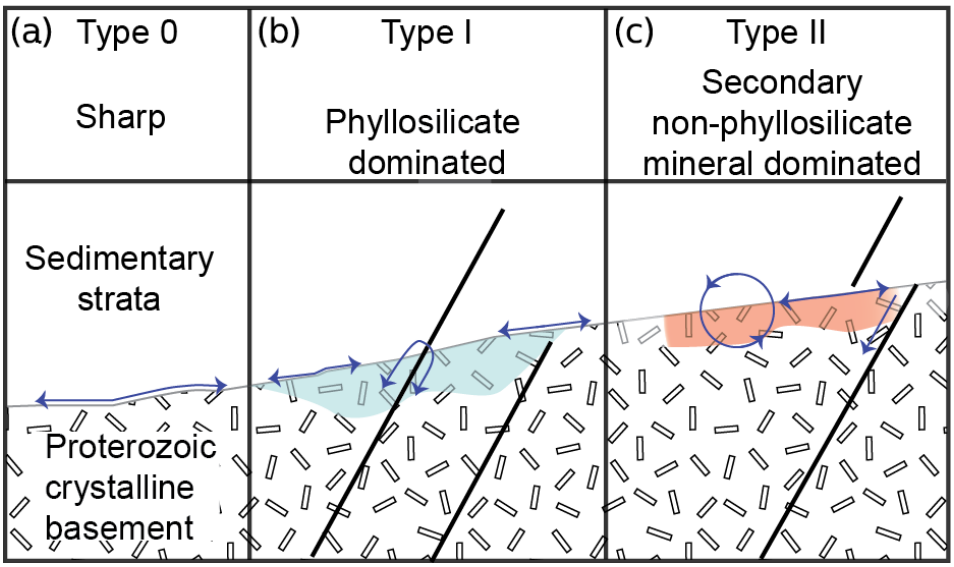


Figure 19: Schematics of the nonconformity contact region. (a) Type 0 – sharp contact expected to prevent fluid pressure front penetrates across the contact and while causes fluid flow parallel to the interface in the target layer (b) Type I – phyllosilicate-dominated zone above the crystalline basement prevents fracture propagation across the nonconformity and downward fluid migration (except in the fault zones) (c) Type II – secondary-mineralization-dominated zone. All nonconformity types may be cut by structural discontinuities. Blue arrows show the possible injected fluid flow paths (Petrie et al 2020).

3.4.3 Scenario 3

Case 1: The hydromechanical properties of the reservoir and the basement are identical are shown in Table 1. Figure 20 shows the induced pore pressure and CFS of the fault plane after four years of continuous injection with a constant rate of 0.03 m^3/s (16300 bbl/day). The maximum induced pore pressure is 1.48 MPa, and due to the low-permeable contact (Type I), the pressure front cannot propagate into the basement for more than only a few tens of meters. Figure 20b shows ΔCFS is positive on the whole fault plane meaning that injection causes the fault to become closer to the failure. Again, It should be noted that due to the poroelastic effect, the maximum of ΔCFS and ΔPp does not happen in the same location on the fault plane. Figure 21a shows the change of normal stress of the fault plane. It is obvious

that the injection causes increase of normal stress where there is pore pressure buildup (the target reservoir and few tens of meters of the basement). At the greater depths, poroelastic effect causes reduction of normal stress on the fault plane however the values are less than those at the reservoir depth. This reduction at greater depths causes the CFS to increase and illustrates how the tendency of fault reactivation increases where there is no direct fluid diffusion and pore pressure elevation. There are two zones of increased and decreased shear stress on the fault plane. The absolute values of shear stress change on the fault plane are less than the change of normal stress by an order of magnitude (Figure 21b), and therefore does not have a significant contribution to CFS change. Figure 22 shows the depth profiles of change of Coulomb failure stress (ΔCFS) and its components (ΔPp, $\Delta\sigma_n$, and $\Delta\tau_s$) along the white dashed line (the closest point on the fault to the well, Figure 20b) on the fault plane. As mentioned, the pore pressure elevation occurs only at reservoir depth and shallow basement. At these depths, as it can be seen in Figure 22, there is a competition between pore pressure increase (destabilizing) and poroelastic effect (stabilizing) to change CFS. At greater depth, where there is no fluid pore pressure due to diffusion, the normal stress reduction is the only process by which CFS decreases. This case shows that how poroelastic effect ($\Delta\tau_s$-$\mu\Delta\sigma_n$) can affect basement faults at greater depths where there is no direct fluid pressure buildup.

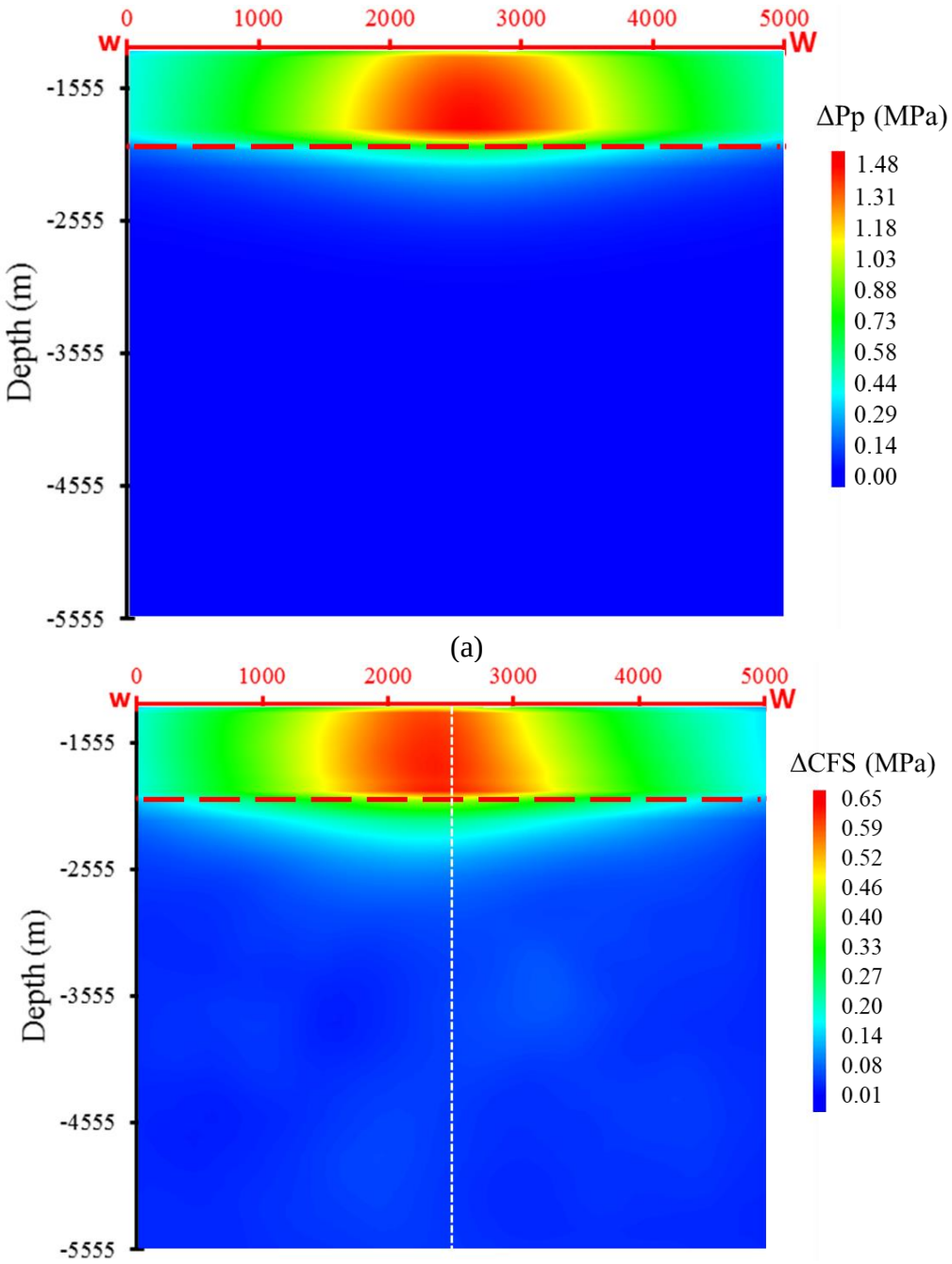
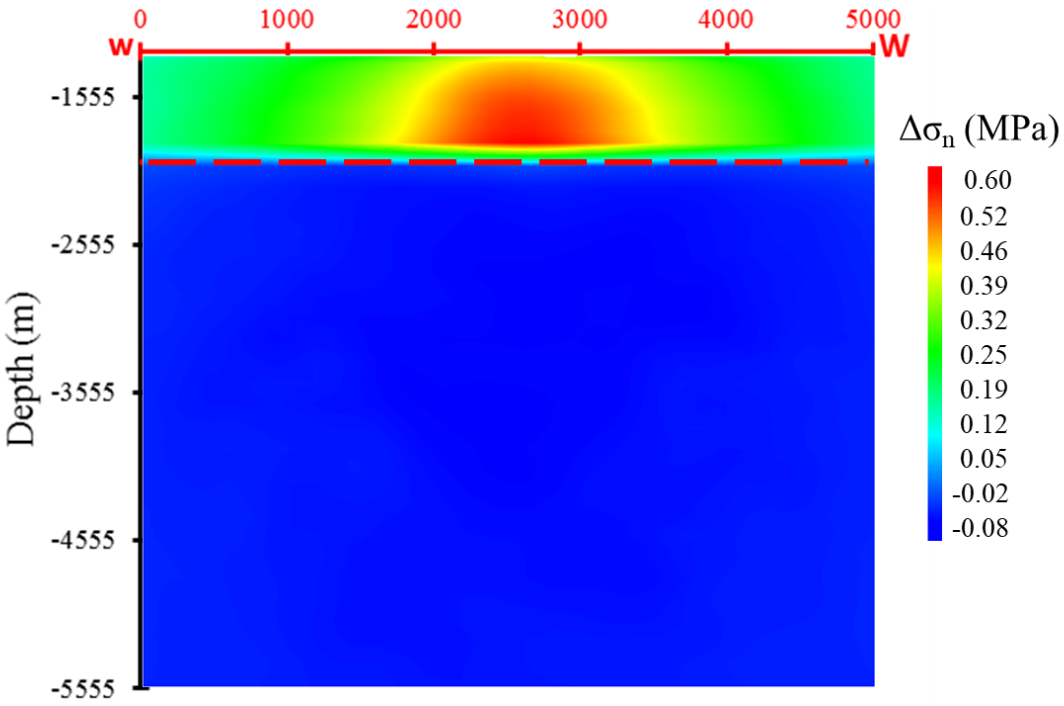
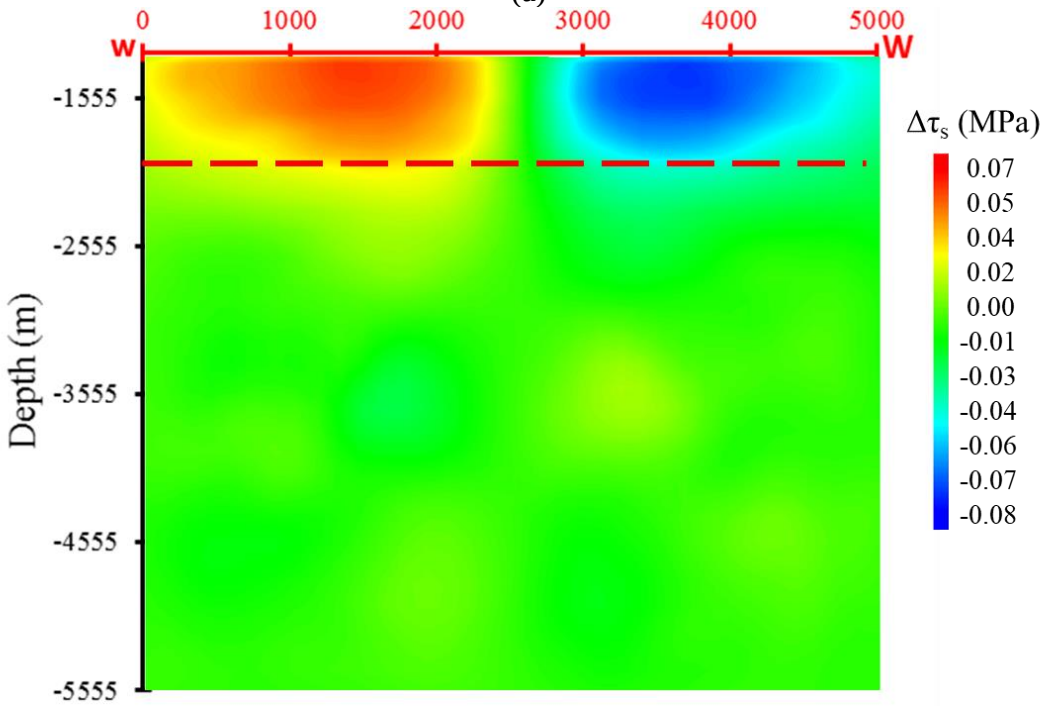


Figure 20: Scenario 3, Case 1 (η_{res} = 0.25): Induced (a) pore pressure ((ΔPp, MPa) and b) CFS (ΔCFS, MPa) on the fault plane after 4 years of injection with a constant rate of 0.03 m^3/s (16300 bbl/day). The red solid and dashed lines show the upper and lower reservoir boundaries, respectively. Impermeable Type I nonconformity contact prevents fluid flow to the basement. CFS increases on the whole fault plane by two mechanisms. At reservoir and shallow basement depths, direct pore pressure (destabilizing) dominates the poroelastic effect which is stabilizing. At greater depths, the reduction in normal stress causes increase of CFS.



(a)



(b)

Figure 21: Scenario 3, Case 1 (η_{res} = 0.25): Induced (a) normal stress ($\Delta\sigma_n$, MPa) and (b) shear stress ($\Delta\tau_s$, MPa) on the fault plane after 4 years of injection with a constant rate of 0.03 m^3/s (16300 bbl/day). The red solid and dashed lines show the upper and lower reservoir boundaries, respectively. At greater depths where the pressure front does not propagate, due to the poroelastic effect, normal stress decreases and increases CFS. Shear stress change values are less than normal stress change by an order of magnitude.

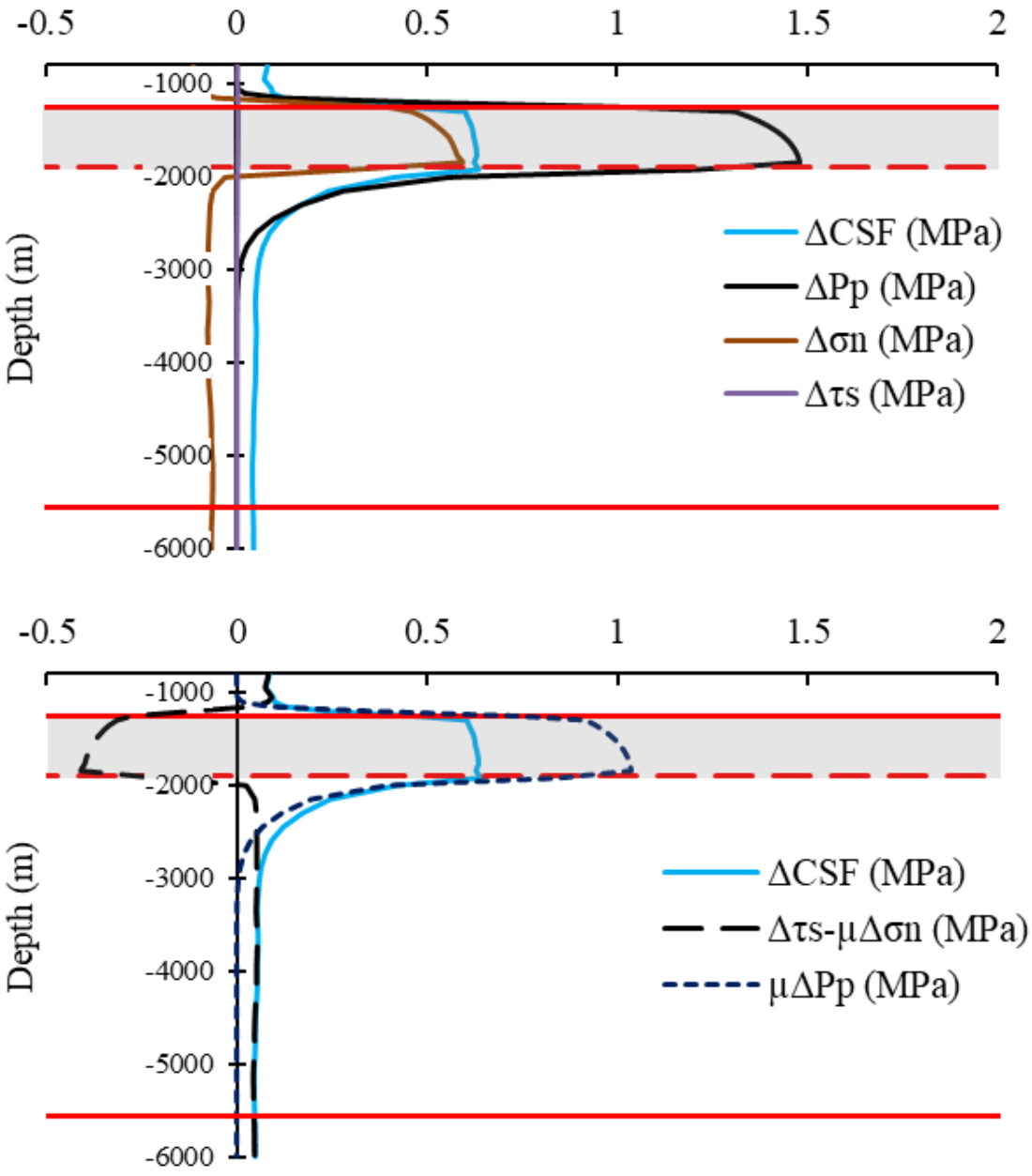


Figure 22: Scenario 3, Case 1 (η_{res} = 0.25): Depth profiles of change of CFS (MPa), pore pressure (MPa), total normal stress (MPa), and shear stress (MPa) (Upper figure), and profiles of change of poroelastic stress (MPa) and pore pressure (MPa) components of ΔCFS (Lower Figure) along the white dashed line on the fault plane along the cross-section W-w (Figure 19b) after 4 years of injection. Solid red lines indicate the fault boundaries and the red dashed lines the lower boundary of the reservoir. At greater depths, the only process responsible for the ΔCFS increase is poroelastic effect, and direct pore pressure does not have any contribution.

Case 2: In this case, every detail of the problem was kept identical to case 1 except the properties of the reservoir. Table 4 shows the hydromechanical properties of the reservoir (sandstone). It should be mentioned that the properties belong to Ohio sandstone (Jagear et al., 2009), and are assumed here only to study the response of compliant reservoirs to injection. In this scenario, the poroelastic stress coefficient (η_{res}) is 0.3 while in case 1, η_{res} = 0.25. Figure 23 shows the changes of pore pressure and CFS on the fault plane after four years of injection. The pore pressure increases up to 1.28 MPa (0.2 MPa less than case 1 with η_{res} = 0.25). CFS has the highest increase in the shallow basement. Figure 24 shows the normal stress ($\Delta\sigma_n$) and shear stress ($\Delta\tau_s$) on the fault plane. Similar to case 1, the normal stress increases where the pore pressure increases (reservoir depths) and decreases at the greater depths of the basement. The maximum shear stress change occurs at the shallow basement. Similar to other cases, values of the shear stress change are insignificant compared to other cases. Figure 25 shows the profiles of change of Coulomb failure stress (ΔCFS) and its components (ΔPp, $\Delta\sigma_n$, and $\Delta\tau_s$) along the white dashed line (vertical line on the fault plane that has the shortest distance from the injection well, Figure 23b) on the fault plane.

Table 4: Properties of the reservoir (sandstone) in scenario 3, case 2 (Jagear et al. 2009)

Permeability (mD)	10
Porosity, ϕ	0.19
Bulk Modulus, K (GPa)	8.4
Shear Modulus, G (GPa)	6.8
Friction angle, φ (°)	30
Biot's coefficient	0.74
Poroelastic stress coefficient, η	0.3

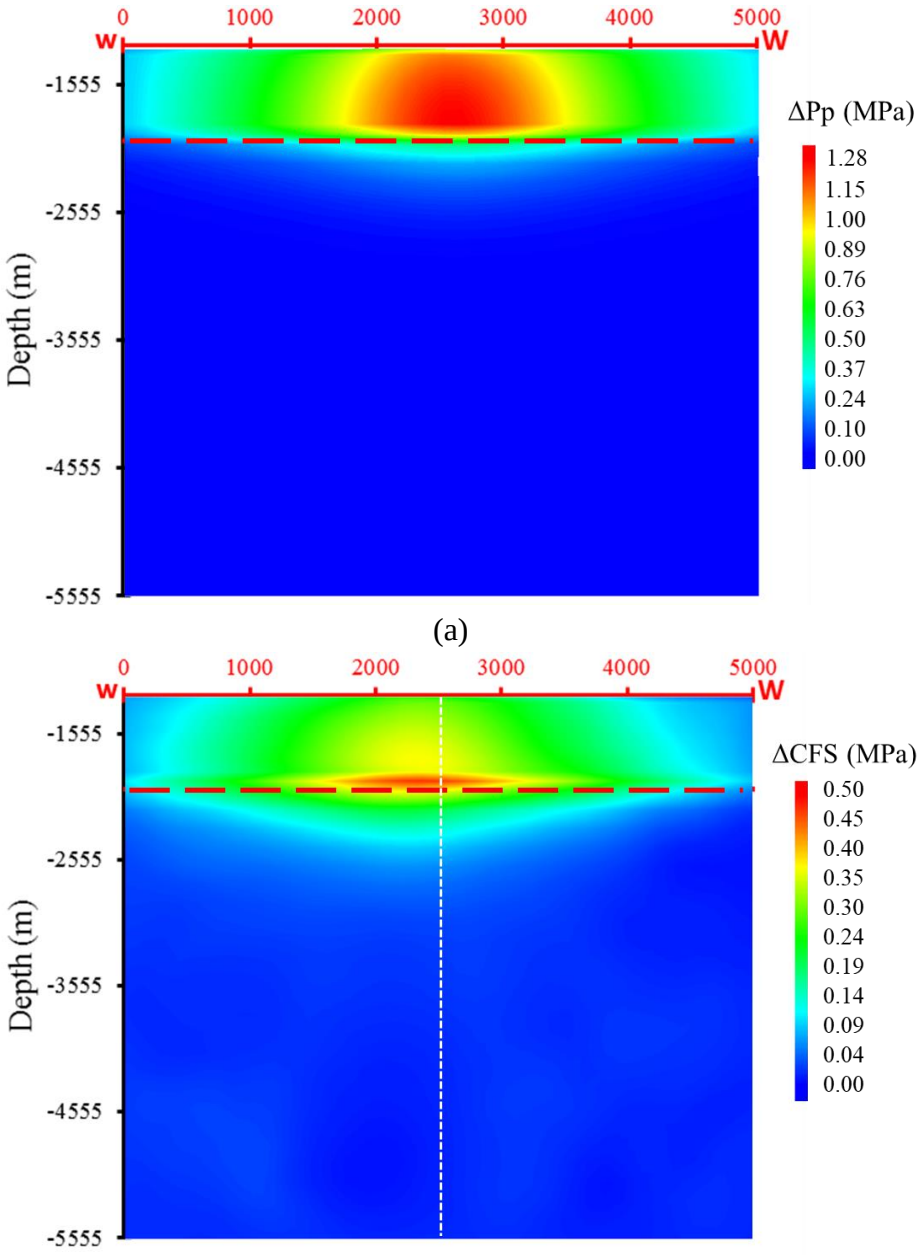


Figure 23: Scenario 3, Case 2 (η_{res} = 0.3): Induced (a) pore pressure ((ΔPp, MPa) and b) CFS (ΔCFS, MPa) on the fault plane after 4 years of injection with a constant rate of 0.03 m^3/s (16300 bbl/day). The red solid and dashed lines show the upper and lower reservoir boundaries, respectively. Impermeable Type I nonconformity contact prevents fluid flow to the basement. CFS increases on the whole fault plane by two mechanisms. At reservoir and shallow basement depths, direct pore pressure (destabilizing) dominates the poroelastic effect which is stabilizing. At greater depths, the reduction in normal stress causes an increase in CFS. The maximum ΔCFS (the tendency for failure) occurs at the basement and the reservoir interface.

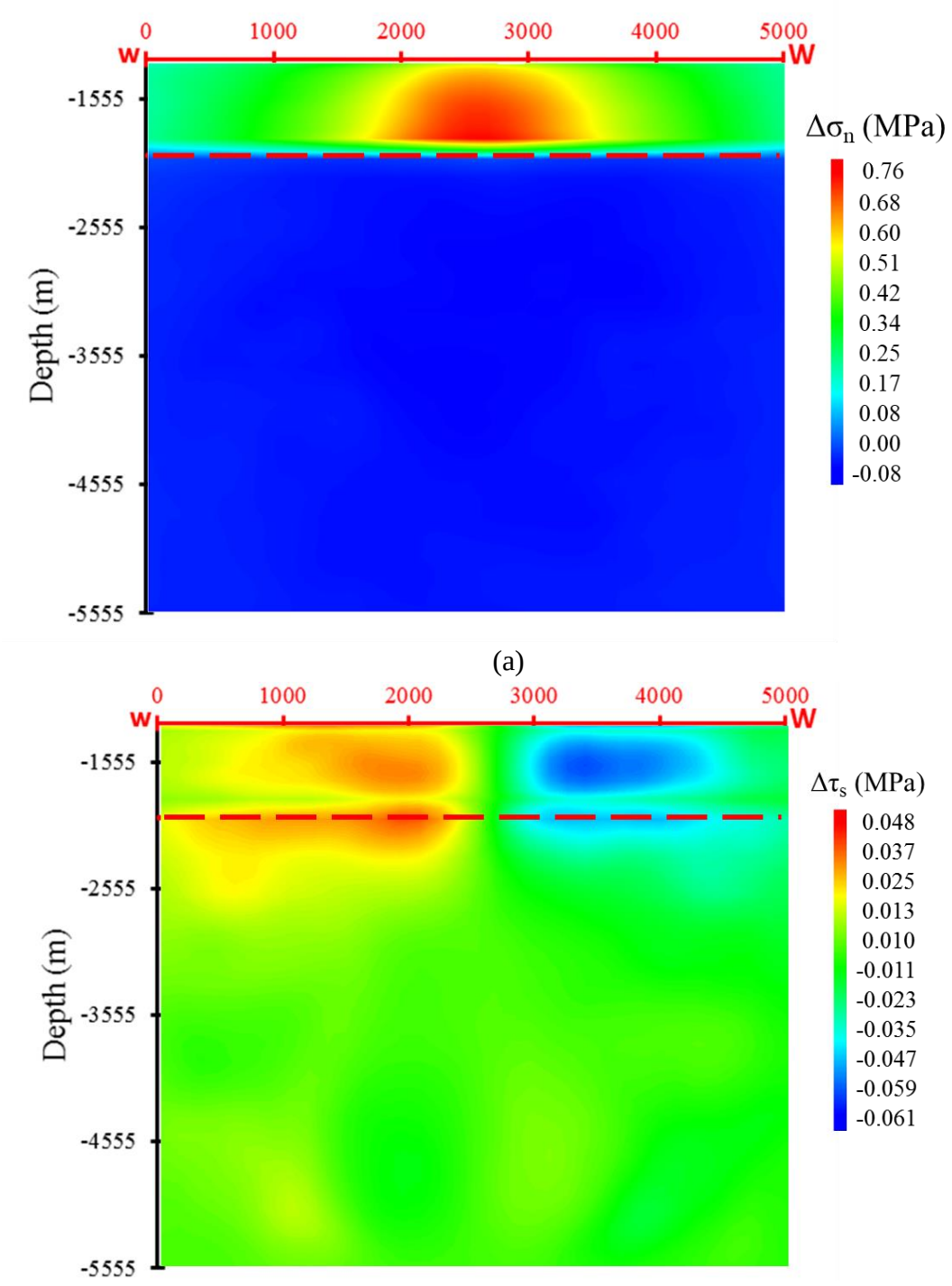


Figure 24: Scenario 3, Case 2 (η_{res} = 0.3): Induced (a) normal stress ($\Delta\sigma_n$, MPa) and (b) shear stress ($\Delta\tau_s$, MPa) on the fault plane after 4 years of injection with a constant rate of 0.03 m^3/s (16300 bbl/day). The red solid and dashed lines show the upper and lower reservoir boundaries, respectively. At greater depths, the pressure front does not propagate, and poroelastic effect is the only process in increasing CFS. Shear stress change values are less than normal stress change by an order of magnitude.

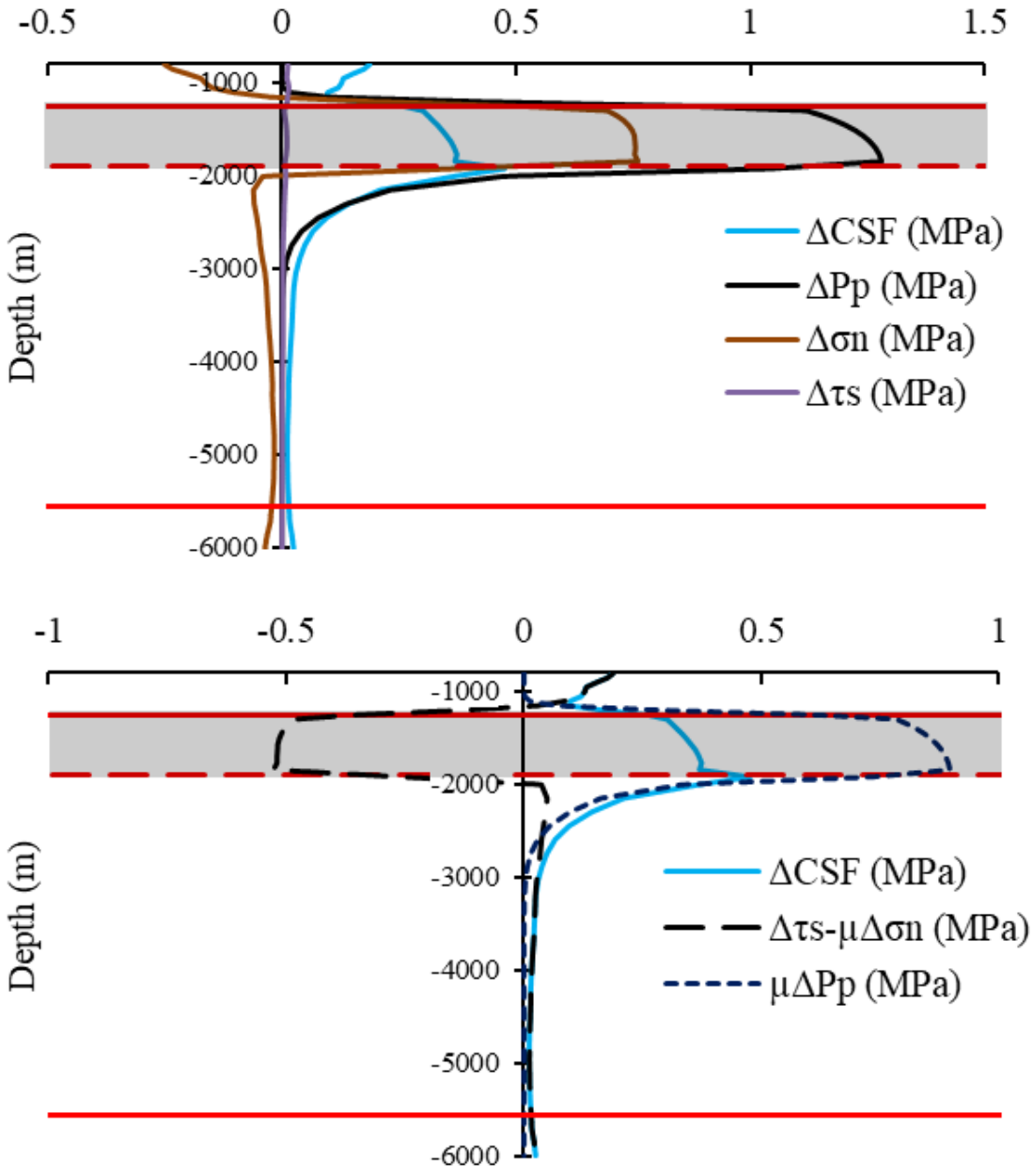


Figure 25: Scenario 3, Case 2 (η_{res} = 0.3): Depth profiles of change of CFS (MPa), pore pressure (MPa), total normal stress (MPa), and shear stress (MPa) (Upper figure), and profiles of change of poroelastic stress (MPa) and pore pressure (MPa) components of ΔCFS (Lower Figure) along the white dashed line on the fault plane along the cross-section W-w (Figure 23b) after 4 years of injection. Solid red lines indicate the fault boundaries and the red dashed line shows the lower boundary of the reservoir. At greater depths, the only process responsible for the ΔCFS increase is poroelastic effect, and direct pore pressure does not have any contribution.

Comparing the values of ΔPp and ΔCFS of case 1 (Figure 20) and case 2 (Figure 23) reveals the following points: (1) compliant reservoir (case 2, $\eta_{res} = 0.3$) has lower ΔPp and ΔCFS (2) CFS has the maximum raise in the reservoir and basement interface in case 2 while in case 1 it is located at the reservoir middle depth. To a better comparison of responses of a compliant and a stiff reservoir to injection, Figure 26 shows the change of pore pressure, normal stress, and shears stress (ΔPp, $\Delta\sigma_n$, and $\Delta\tau_s$) at depth of 1600 km (middle depth of the reservoir). Due to poromechanical properties, less pore pressure and more normal stress are generated in case 2 ($\eta_{res} = 0.3$). The patterns of induced shear stress are different, but the values are almost similar. Figure 27 and Figure 28 compare the depth profiles of ΔPp, $\Delta\sigma_n$, $\Delta\tau_s$, ΔCFS (and its components: $\Delta\tau_s$ -$\mu\Delta\sigma_n$ and $\mu\Delta$Pp) along the white dashed line (Figure 20b and Figure 23b) on the fault plane for cases 1 and 2. It is obvious ΔCFS is greater in case 1 than in case 2 on the whole fault plane. This is due to different mechanisms at different depths. At depths of the reservoir and shallow basement (where there is an excess pore pressure), more pore pressure buildup and less induced normal stress in case 1 ($\eta_{res} = 0.25$) cause ΔCFS is higher than case 2 ($\eta_{res} = 0.3$). At greater depths in the basement, the more induced normal stress and no excess fluid pore pressure are the reasons for higher ΔCFS in case 1 than in case 2. The results reveal that if there is no communication between the reservoir and the basement (e.g. presence of a continuous nonconformity), injection into the compliant reservoir is less harmful than a stiffer reservoir.

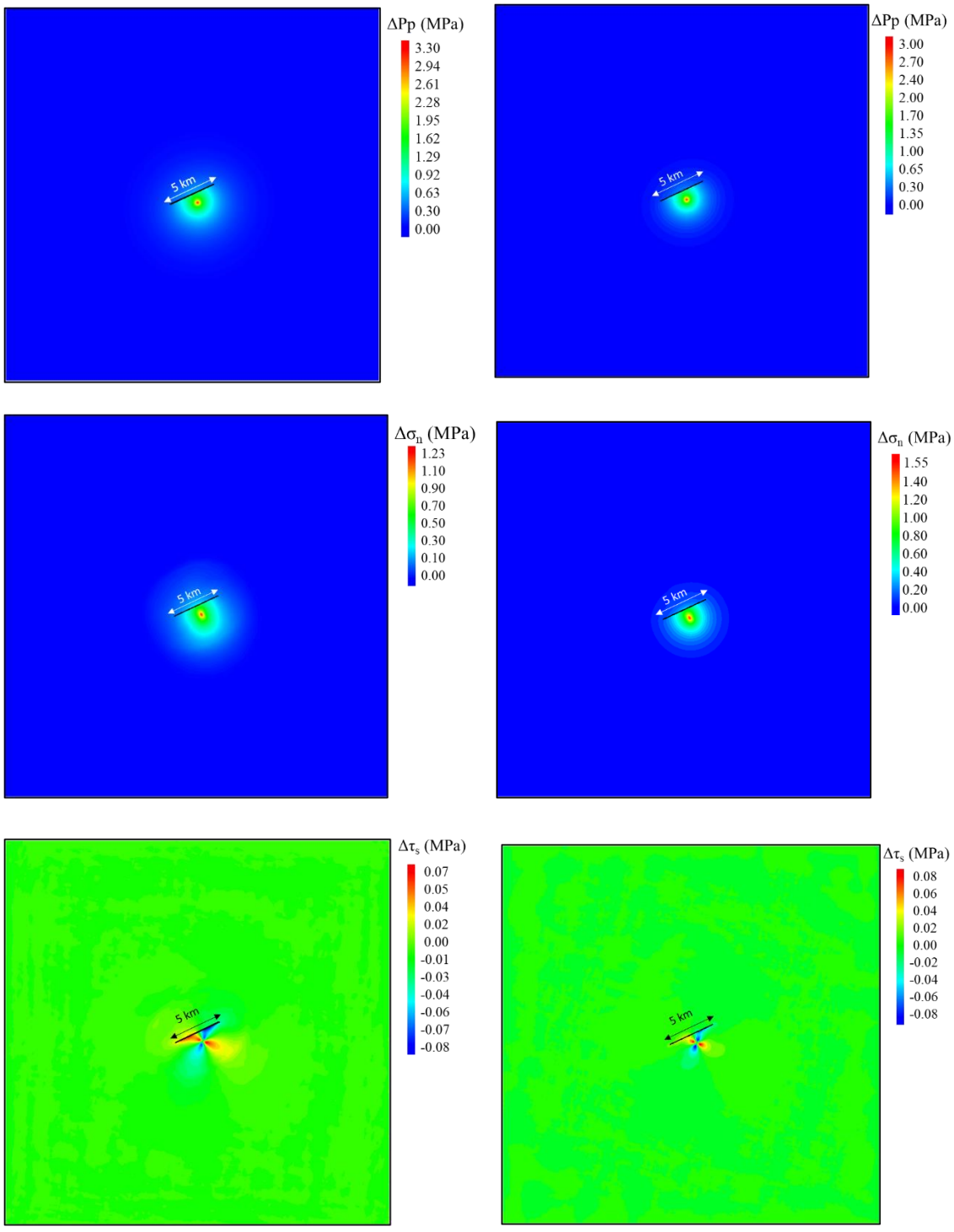
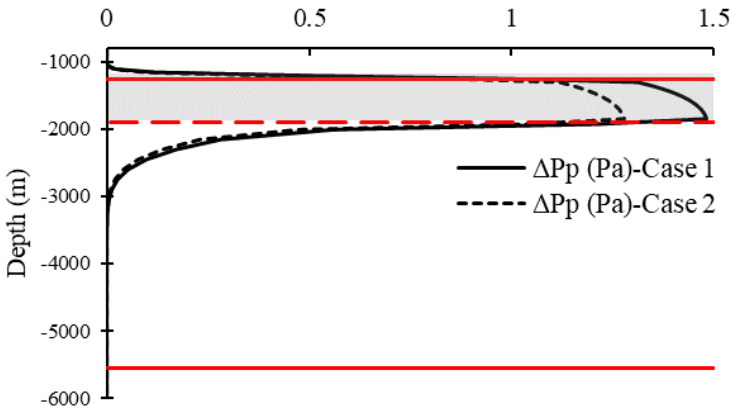
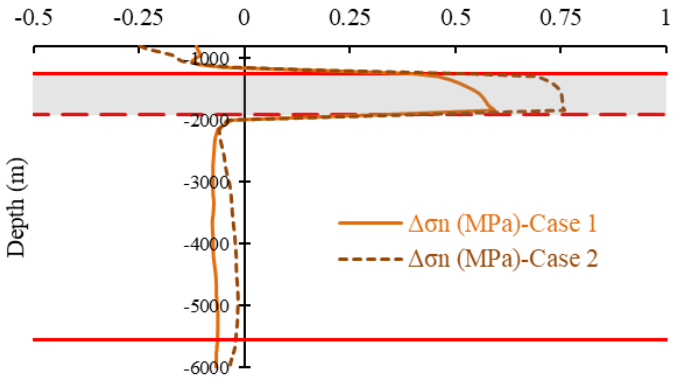


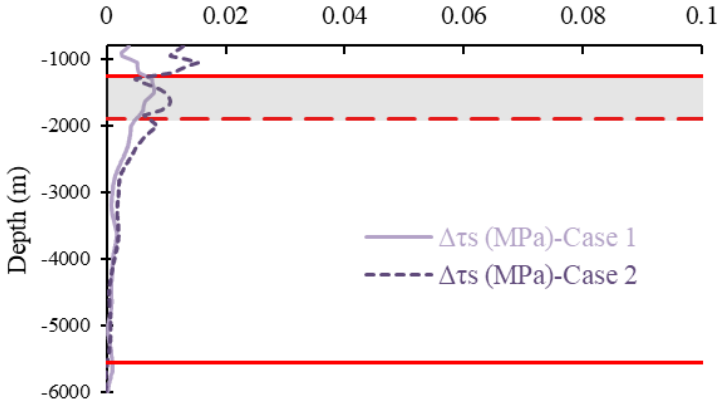
Figure 26: The pore pressure change (ΔPp, MPa) (upper figures), normal stress change ($\Delta\sigma_n$, MPa) (middle figures), and shear stress change ($\Delta\tau_s$, lower figures) in sandstone group at depth of 1600 m after 4 years of injection for (a) case 1 (left column) and (b) case 2 (right column). In case 2 (η_{res} = 0.3), the induced pore pressure and normal stress are less and more than in case 1 (η_{res} = 0.25), respectively. The shear stress changes are similar in both cases.



(a)



(b)



(c)

Figure 27: Scenario 3: Comparison of depth profiles of (a) ΔPp, (b) $\Delta\sigma_n$, and (c) $\Delta\tau_s$ of case 1 (η_{res} = 0.25) and case 2 (η_{res} = 0.3) along the white dashed lines (Figure 20b and Figure 23b). It can be seen that less induced ΔPp and $\Delta\sigma_n$ are generated in the reservoir with higher η_{res}. At the greater depths where there is no pore pressure elevation, more reduction in normal stress is induced in case 1. Shear stresses in both cases are almost similar. Solid red lines are the fault boundaries. The red dashed line shows the lower boundary of the reservoir.

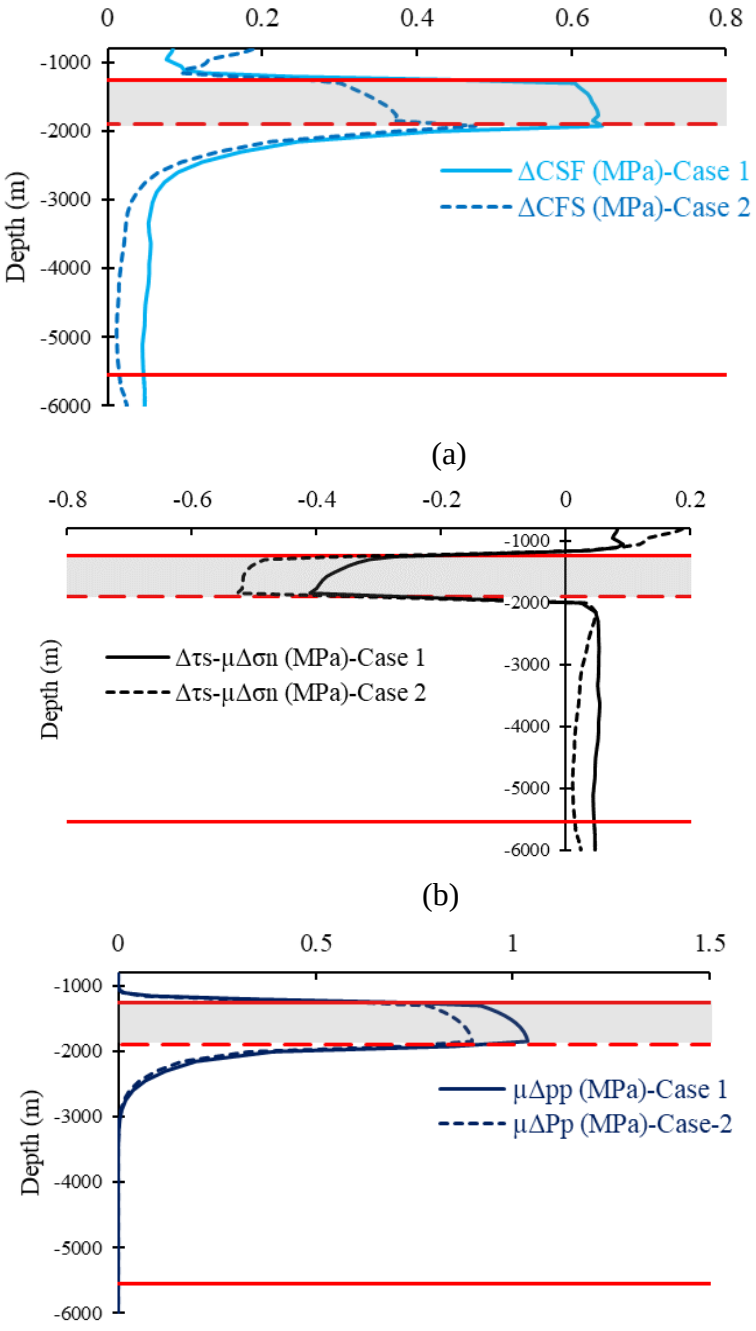


Figure 28: Scenario 3: Comparison of depth profiles (a) ΔCFS (MPa), (b) $\Delta\tau_s$ -$\mu\Delta\sigma_n$ (MPa), and (c) μΔPp (MPa) of case 1 (η_{res} = 0.25) and case 2 (η_{res} = 0.3) along the white dashed line (Figure 20b and Figure 23b). In case 1, ΔCFS is greater than case 2 on the whole fault plane. Solid red lines are the fault boundaries. The red dashed line shows the lower boundary of the reservoir.

Case 3: In this case, it is assumed that the fault does not go through the overlain sedimentary layer. In fact, in this case, it is intended to show how injection into a sealed layer (from top and bottom) affects non-through-going fault (a fault that does not extend up from the basement into the reservoir) stability. The general response of the fault is similar to case 1 except that since there is no fault core in the reservoir, less pore pressure builds up in the reservoir. Figure 29 shows the depth profiles of change of CFS, pore pressure, total normal stress, and shear stress (ΔPp, $\Delta\sigma_n$, and $\Delta\tau_s$, upper figure), and profile of change of poroelastic stress and pore pressure of components of ΔCFS (lower figure) along the line on the fault plane that has the shortest distance from the injection well. At the greater depths in the basement, injected fluid does not penetrate, and normal stress decreases due to the poroelastic effect. Shear stress does not have a significant change on the fault plane and does not contribute to the CFS increase. Then, in the absence of excess pore pressure, the only factor responsible for the increase of CFS is the reduction of normal stress in the basement. This case clarifies how the solely indirect effect of injection (poroelastic effect) causes a fault in the basement to become closer to the failure with no direct pore diffusion.

Case 4: In this case, it is assumed that rock grains are incompressible in all layers ($\alpha = 1$). For a better understanding of the effect of compressibility of the rock grains on the tendency of faults to reactivation by fluid injection, we compare profiles of change of Coulomb failure stress (ΔCFS) and its components (ΔPp, $\Delta\sigma_n$, and $\Delta\tau_s$) along the vertical line on the fault plane that has the shortest distance from the injection well in Figure 30 and Figure 31. It can be seen that ΔCFS is almost similar in cases 1 and 4. At the reservoir depths, both pore pressure elevation and induced increase of normal stress on the faults are higher in case 4 ($\alpha = 1$) than in case 1. These two processes neutralize each other and eventually result in similar

ΔCFS in cases 1 and 4 at reservoir depths. At the shallow basement, the assumption of the incompressible rock grains causes an overestimation of the fault tendency for reactivation (higher ΔCFS). This is due to the less induced normal stress than pore pressure buildup in the shallow basement (Figure 30a and b).

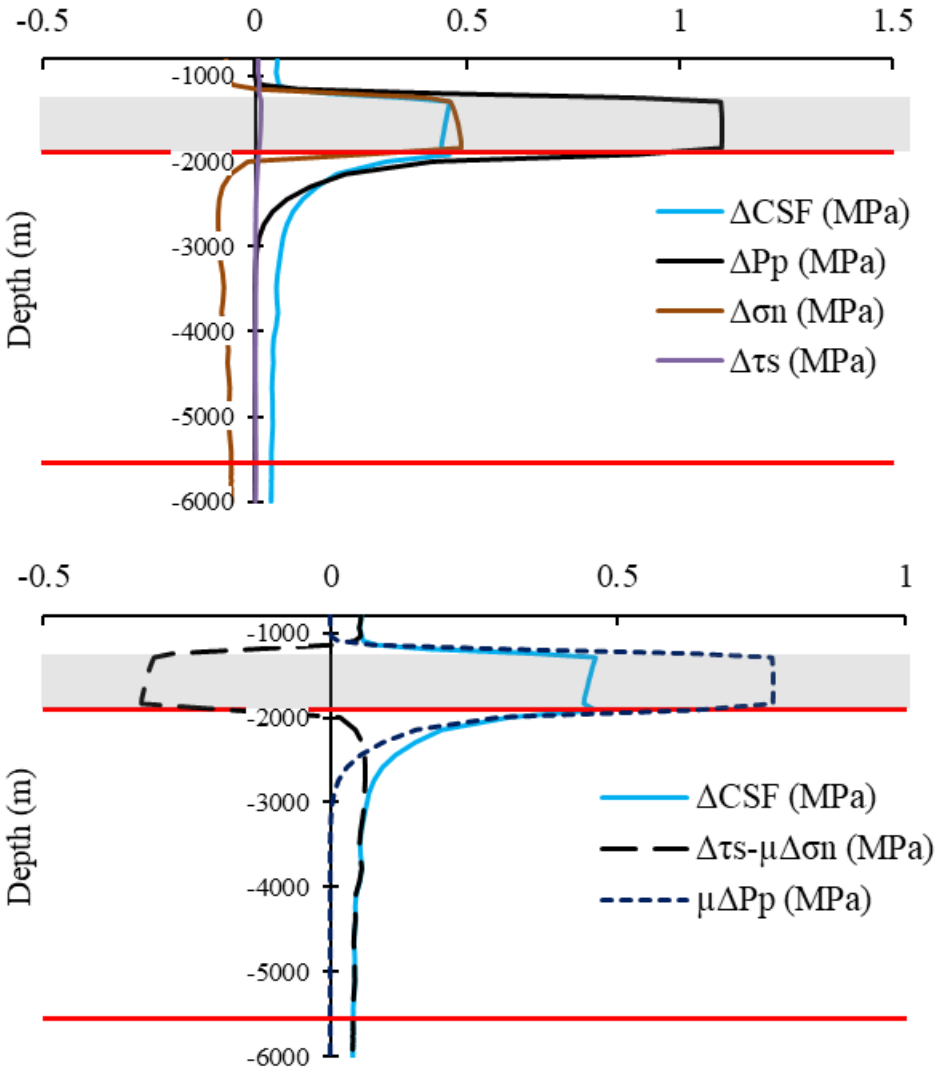


Figure 29: Scenario 3, Case 4: Depth profiles of change of CFS (MPa), pore pressure (MPa), total normal stress (MPa), and shear stress (MPa) (Upper figure), and profiles of change of poroelastic stress (MPa) and pore pressure (MPa) components of ΔCFS (Lower Figure) along the vertical line on the fault plane that has the shortest distance to the injection well. The red lines are the fault boundaries. Solid red lines are the fault boundaries. The red dashed line shows the lower boundary of the reservoir.

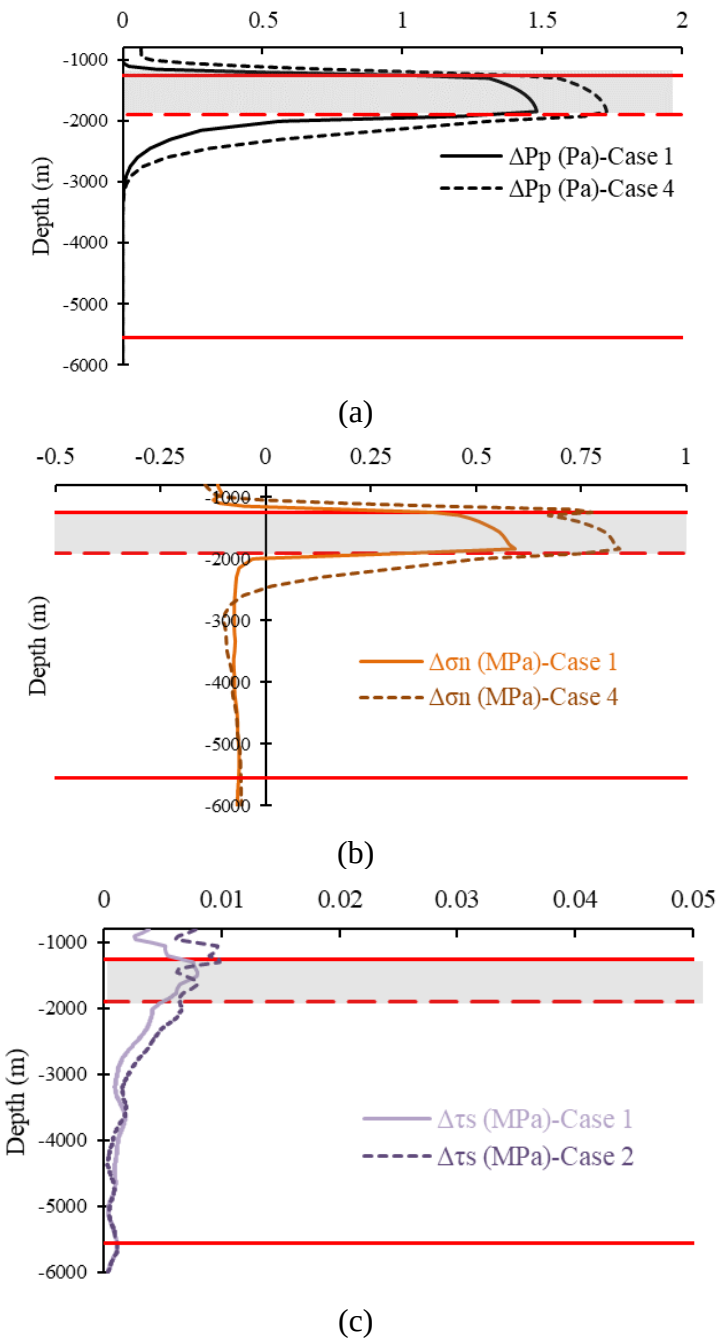


Figure 30: Scenario 3: Comparison of depth profiles of (a) ΔPp, (b) $\Delta\sigma_n$, and (c) $\Delta\tau_s$ of case 1 (α # 1) and case 4 (α = 1 for all layers) along the vertical line on the fault plane that has the shortest distance from the well. At the reservoir and shallow depths, both pore pressure elevation and induced increase of normal stress on the faults are higher in case 4 than in case 1. At greater depths, there is no excess pore pressure and induced normal stresses are similar in cases 1 and 4. Induced shear stresses are similar, and have insignificant values. Solid red lines are the fault boundaries. The red dashed line shows the lower boundary of the reservoir.

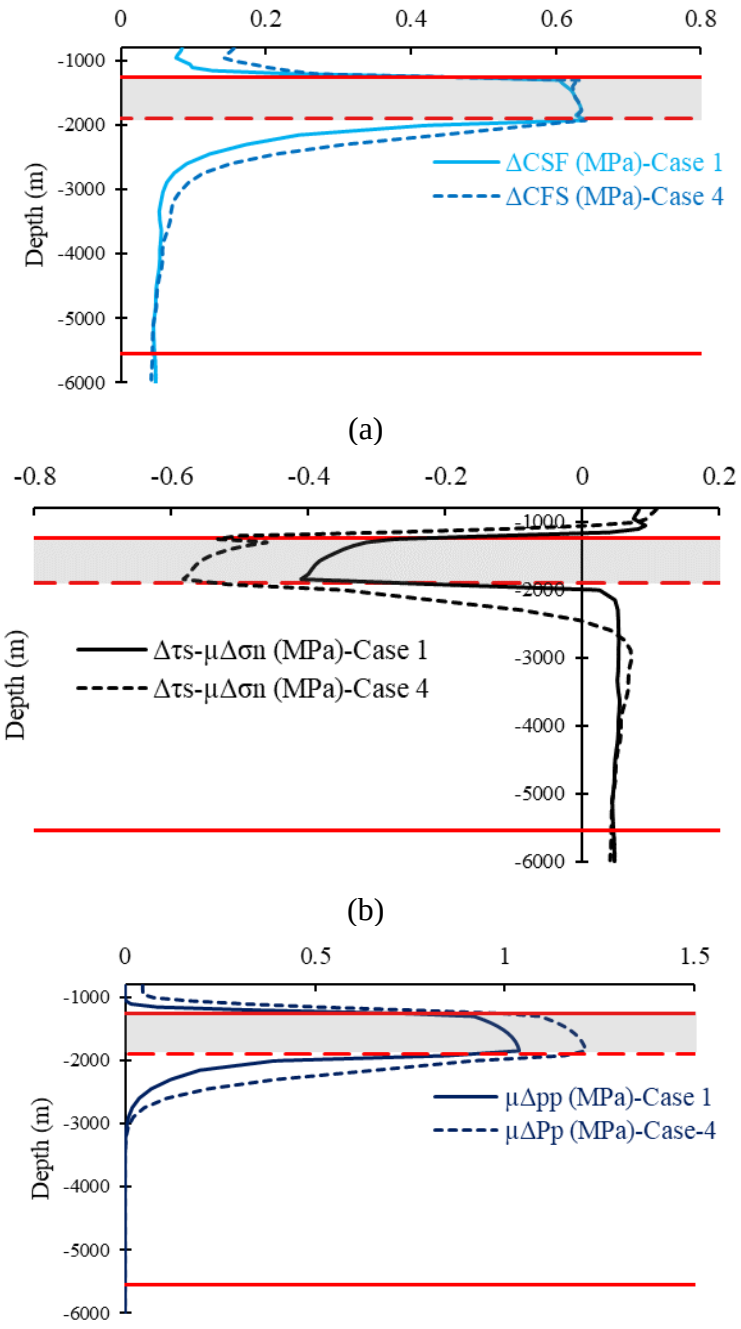


Figure 31: Scenario 3: Comparison of depth profiles of (a) ΔCFS, (b) $\Delta\tau_s - \mu\Delta\sigma_n$, and (c) μΔPp of case 1 (α # 1) and case 4 (α = 1 for all layers) along the vertical line on the fault plane that has the shortest distance from the well. ΔCFS is almost similar in cases 1 and 4. At the shallow basement, the assumption of the incompressible rock grains causes an overestimation of the fault tendency for reactivation (higher ΔCFS). Solid red lines are the fault boundaries. The red dashed line shows the lower boundary of the reservoir.

3.4.4 Scenario 4

Cases 1 and 2: Case 1 of this scenario is identical to case 3 of scenario 2 (Table 2). In case 2, to study the impact of a reservoir with a higher poroelastic coefficient in presence of a fault damage zone, the hydromechanical properties identical to Table 4 are defined for the reservoir. The general trends of cases 1 and 2 are similar and the following main points can be drawn: (1) in contrast to scenario 3, the fault damage zone acts as a fluid conduit through which fluid penetrates the deeper levels (2) CFS is positive on the fault plane meaning that whole fault become closer to the failure (3) direct pore pressure elevation (stabilizing) and indirect poroelastic effect (stabilizing in this scenario) compete to change CFS. The effect of pore pressure is the dominant process and has more contribution than the poroelastic effect. Shear stress change, similar to previous scenarios, does not have any significant effect. (4) The maximum ΔCFS occurred at the shallow basement. For a better understanding of the effect of injection into reservoirs with higher and lower poroelastic stress coefficients, Figure 32 compares ΔPp, ΔCFS, $\Delta\sigma_n$, and $\Delta\tau_s$ in cases 1 and 2 of scenario 4. It can be seen that in case 2 less pore pressure elevation is generated on the fault plane (up to 0.1 MPa). Values of ΔCFS are similar in both cases, but the patterns of the ΔCFS are different. In both cases, the maximum of ΔCFS occurs in the shallow basement. The normal stress change on the fault plane is slightly larger than in case 1. The pattern and value of induced shear stress are similar in both cases. Figure 33 shows the depths profile of ΔCFS and its components along the white dashed line on the fault plane (Figure 32). Figure 34 and Figure 35 compare ΔCFS and its components between case 1 (η_{res} = 0.25) and case 2 (η_{res} = 0.3) of scenario 4 along the white dashed line (Figure 32). It can be seen that, by a very slight difference (order of 10^{-2} MPa), injection into the stiffer reservoir causes more CFS increase.

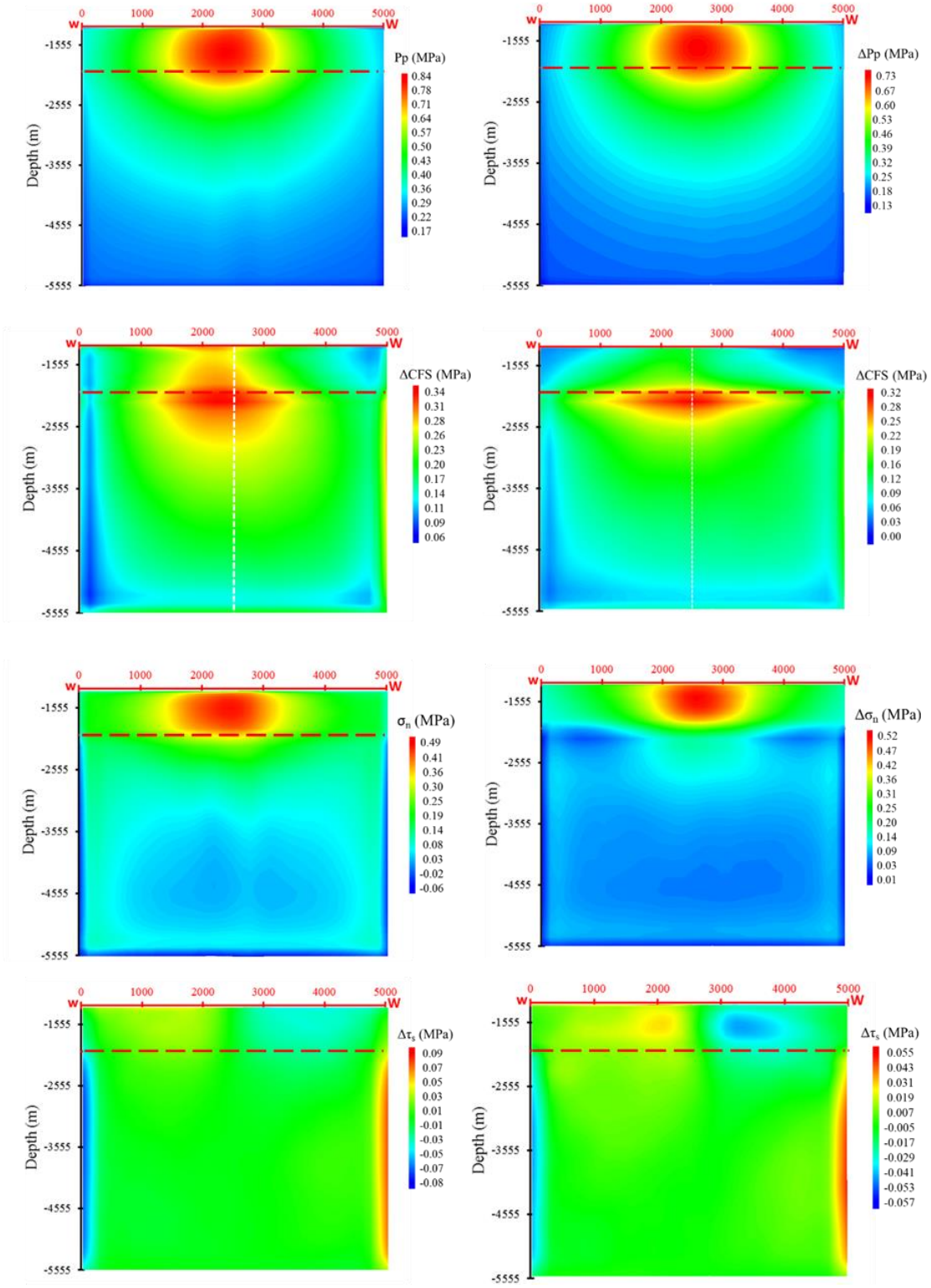


Figure 32: Comparison of ΔPp, ΔCFS, $\Delta\sigma_n$, and $\Delta\tau_s$ on the fault plane in response to injection between case 1 (right column) and case 2 (left column) of scenario 4. Solid red lines are the fault boundaries. The red solid and dashed lines show the upper and lower boundaries of the reservoir.

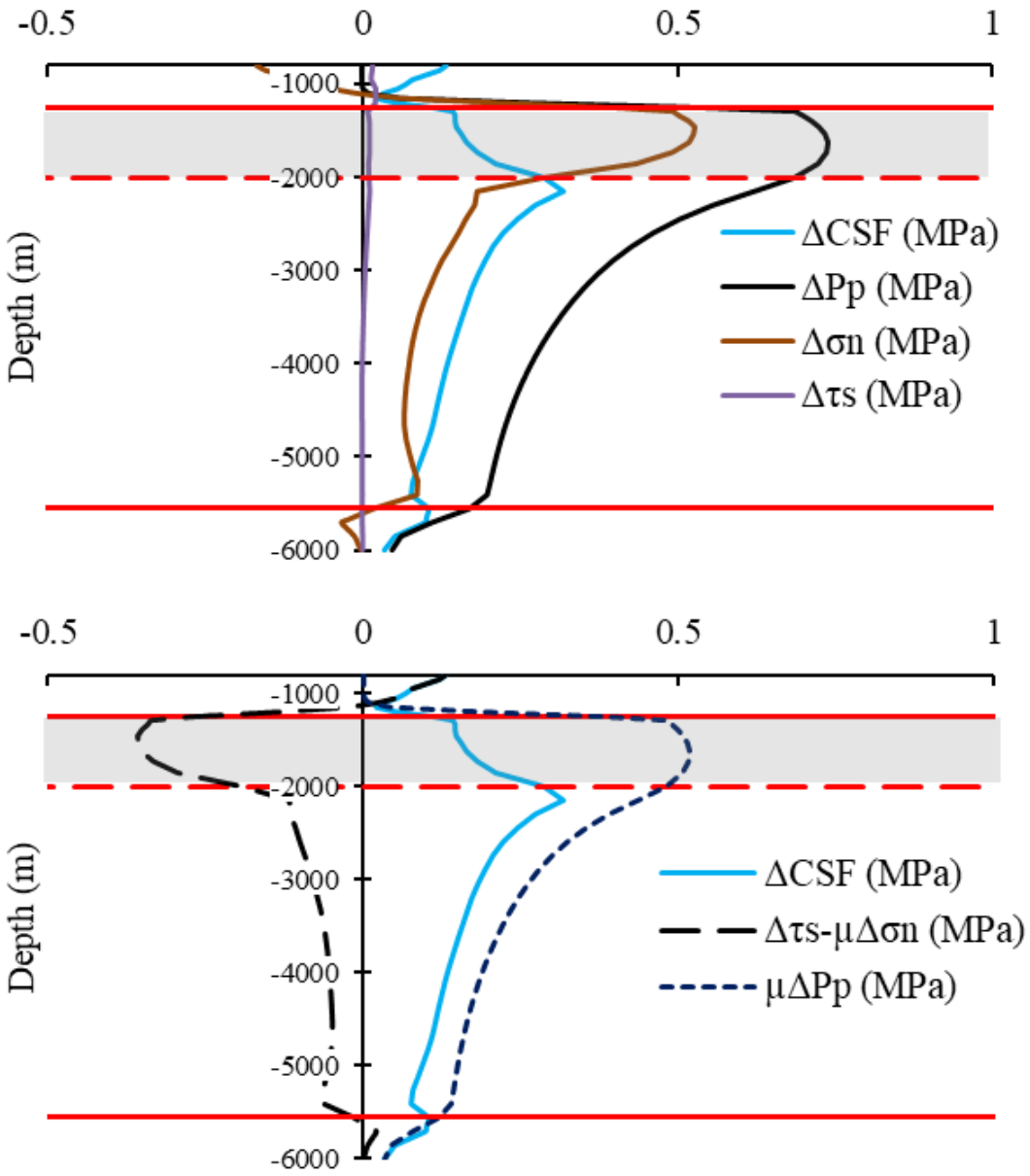
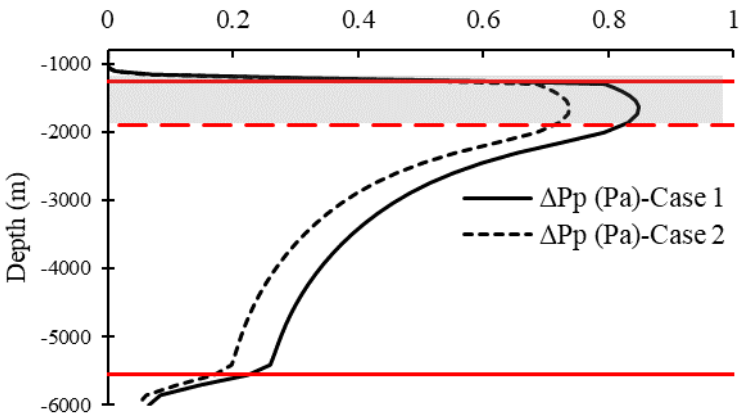
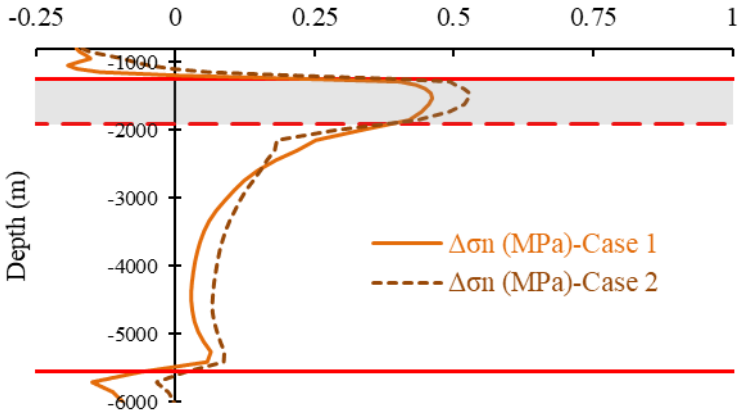


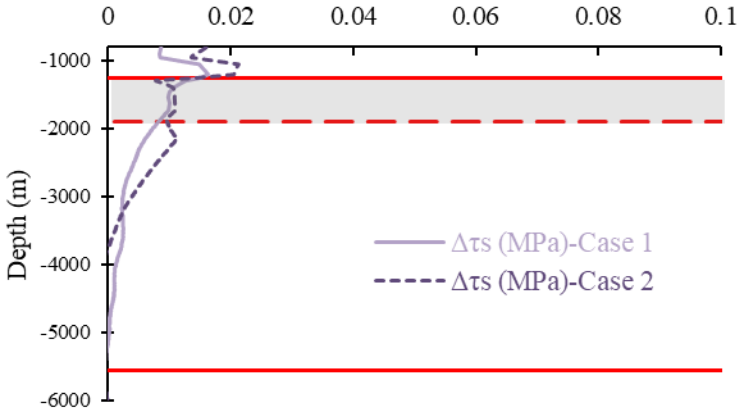
Figure 33: Scenario 4, case 2: Depth profiles of change of CFS (MPa), pore pressure (MPa), total normal stress (MPa), and shear stress (MPa) (upper figure), and profile of change of poroelastic stress (MPa) and pore pressure (MPa) of components of CFS (lower figure) along the dashed line on the fault plane (Figure 32) after 4 years of injection. Solid red lines are the fault boundaries. The red dashed line shows the lower boundary of the reservoir. The maximum ΔCFS occurs in the shallow basement.



(a)

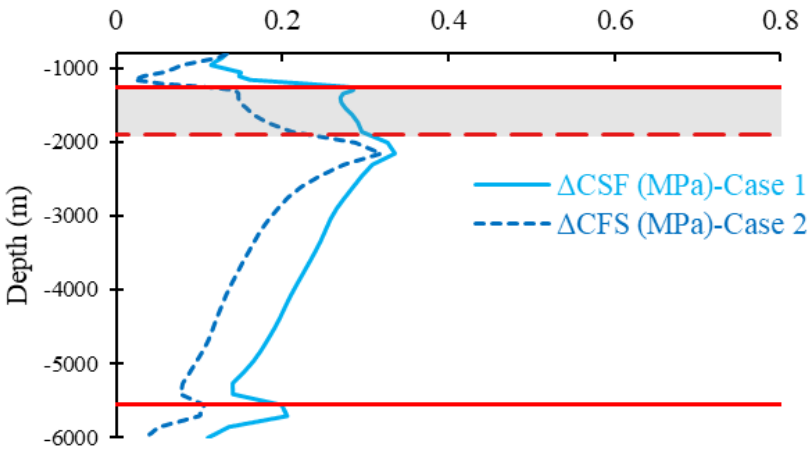


(b)

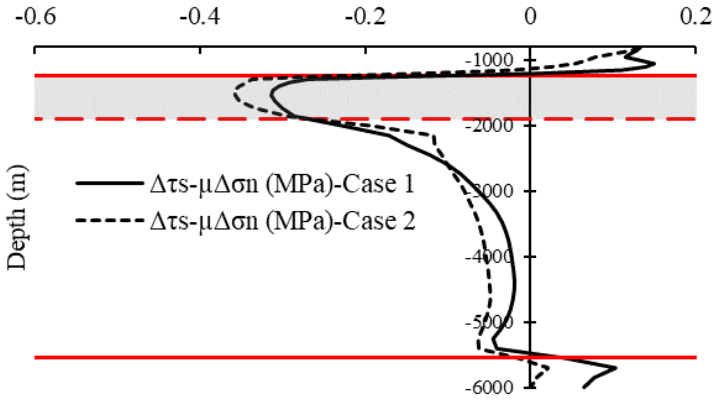


(c)

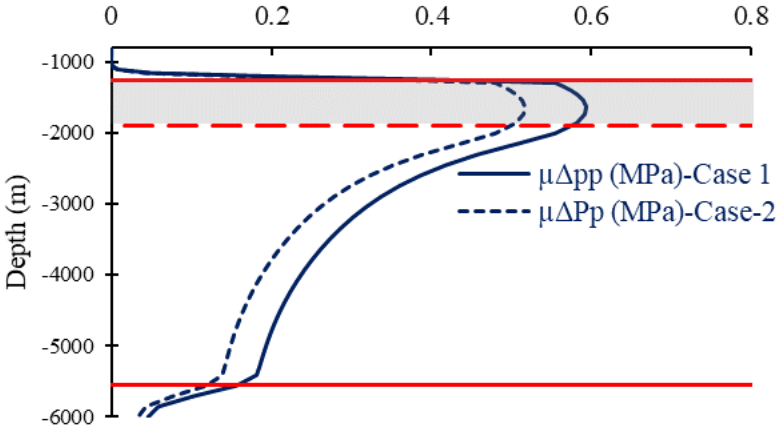
Figure 34: Comparison of a) ΔPp, b) $\Delta\sigma_n$, and c) $\Delta\tau_s$ of case 1 (η_{res} = 0.25) and case 2 (η_{res} = 0.3) of scenario 3 along the white dashed line (the closest point on the fault to the well, Figure 32). Less ΔPp is generated in case 2 with higher η_{res}. Induced shear stresses are almost similar in both cases. Solid red lines are the fault boundaries. The red dashed line shows the lower boundary of the reservoir.



(a)



(b)



(c)

Figure 35: Comparison of a) ΔCFS, b) $\Delta\tau_s$ -$\mu\Delta\sigma_n$, and c) μΔPp of case 1 (η_{res} = 0.25) and case 2 (η_{res} = 0.3) of scenario 3 along the white dashed line (Figure 32). In both cases, the fault has the maximum ΔCFS in the shallow basement. Solid red lines are the fault boundaries. The red dashed line shows the lower boundary of the reservoir.

Case 3: In this case, it is assumed all rock grains are incompressible in all layers and fault damage zone. Figure 36 shows the depths profile of ΔCFS and its components along the vertical line on the fault plane that has the shortest distance from the injection well. For a better understanding of the assumption of incompressible rock grains, we compare this case with case 1 in Figure 37 and Figure 38. Both ΔPp and $\Delta\sigma_n$ in case 3 are more than in case 1. The assumption of incompressible rock grains overestimates ΔCFS on the whole fault plane.

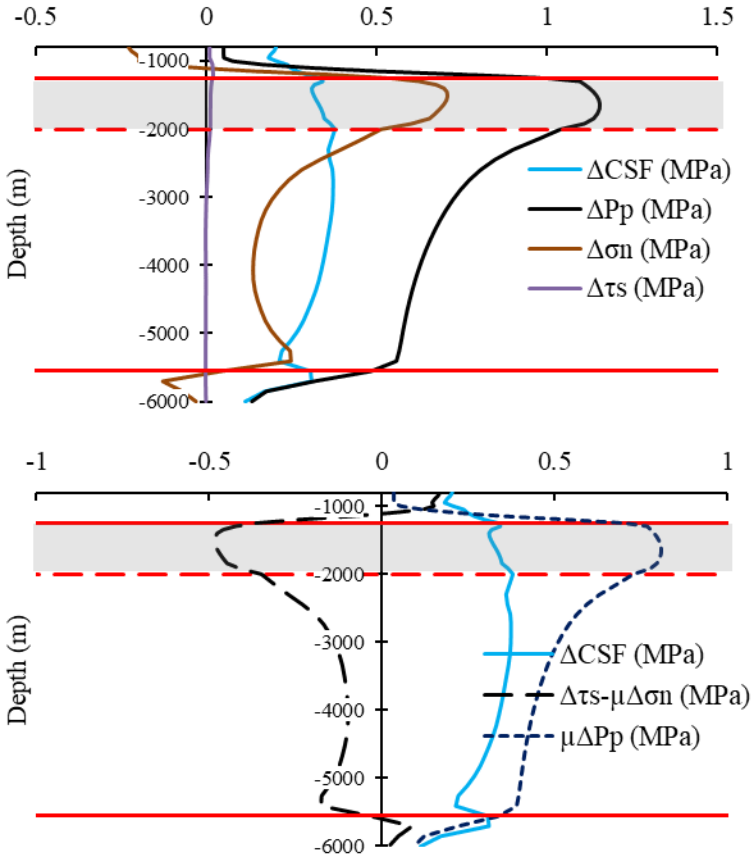


Figure 36: Scenario 4, Case 3: Depth profiles of change of CFS (MPa), pore pressure (MPa), total normal stress (MPa), and shear stress (MPa) (Upper figure), and profiles of change of poroelastic stress (MPa) and pore pressure (MPa) components of ΔCFS (Lower Figure) along the vertical line on the fault plane that has the shortest distance to the injection well. The red lines are the fault boundaries. Solid red lines are the fault boundaries. The red dashed line shows the lower boundary of the reservoir.

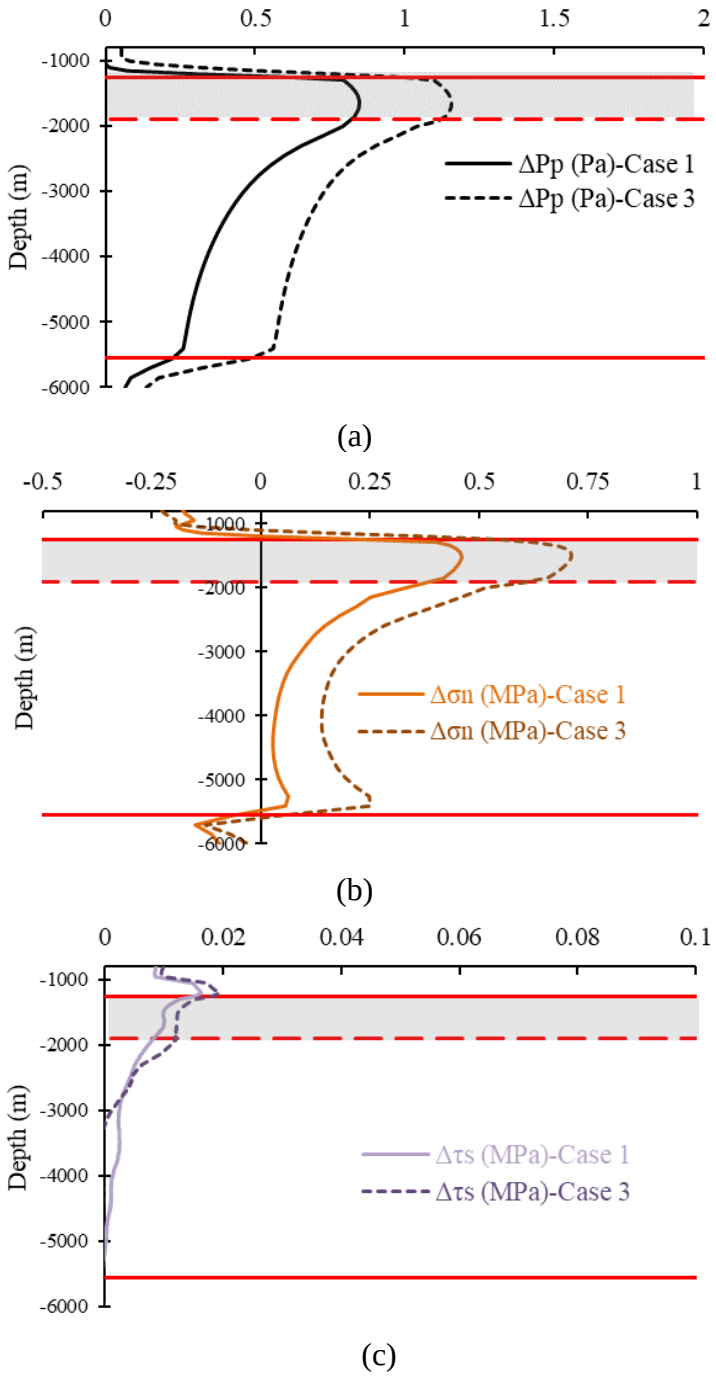


Figure 37: Scenario 4: Comparison of depth profiles of (a) ΔPp, (b) $\Delta\sigma_n$, and (c) $\Delta\tau_s$ of case 1 (α # 1) and case 4 (α = 1 for all layers) along the vertical line on the fault plane that has the shortest distance from the well. At the reservoir and shallow depths, both pore pressure elevation and induced increase of normal stress on the faults are higher in case 4 than in case 1. At greater depths, there is no excess pore pressure and induced normal stresses are similar in cases 1 and 4. Induced shear stresses are similar, and have insignificant values. Solid red lines are the fault boundaries. The red dashed line shows the lower boundary of the reservoir.

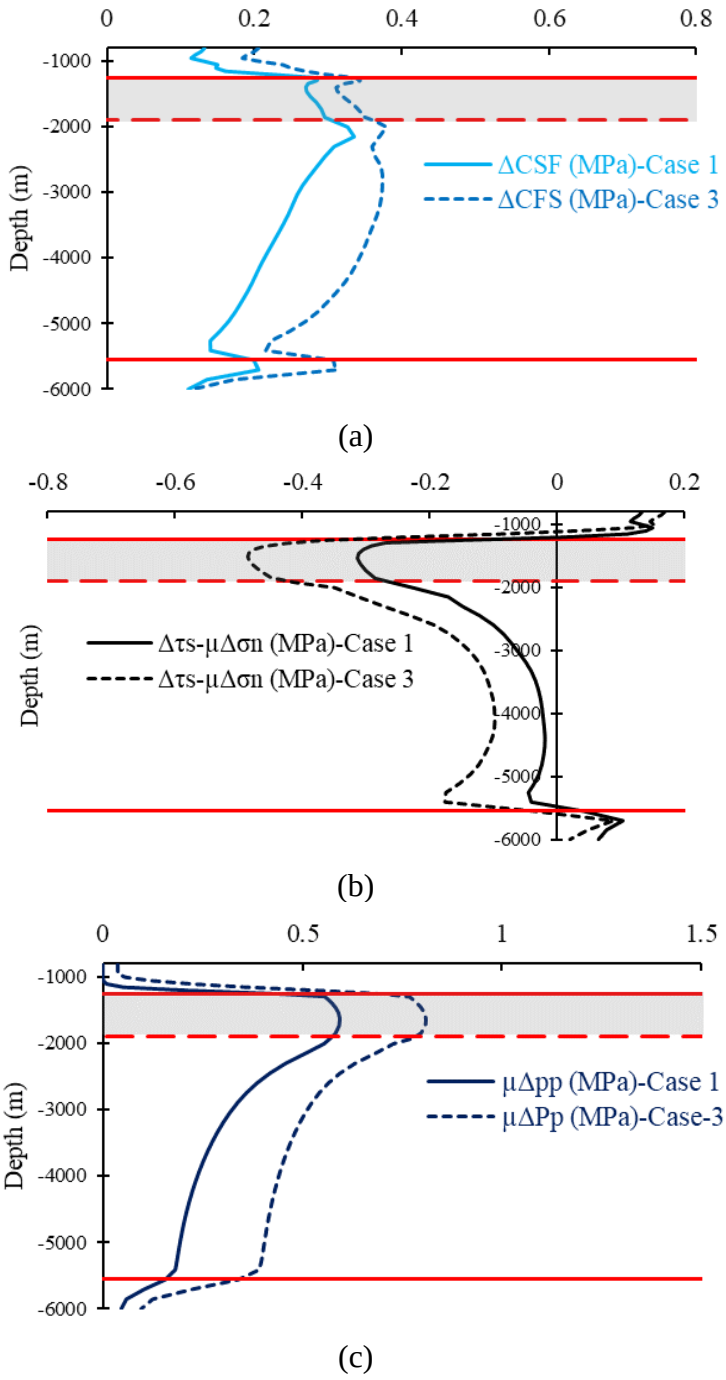


Figure 38: Scenario 3: Comparison of depth profiles of (a) ΔCFS, (b) $\Delta\tau_s$ -$\mu\Delta\sigma_n$, and (c) μΔPp of case 1 (α # 1) and case 4 (α = 1 for all layers) along the vertical line on the fault plane that has the shortest distance from the well. ΔCFS is almost similar in cases 1 and 4. At the shallow basement, the assumption of the incompressible rock grains causes an overestimation of the fault tendency for reactivation (higher ΔCFS). Solid red lines are the fault boundaries. The red dashed line shows the lower boundary of the reservoir.

3D Geomechanical Modeling of the Response of the Wilzetta Fault to Saltwater Disposal

4.1 Introduction

As mentioned in the previous chapters, subsurface injection changes both the pore pressure and the total stresses. The elevated pore pressure due to the fluid diffusion causes reduction and increase in effective and total stresses, respectively. Then, the effect of injection on the fault stability would seem obvious: excess pore pressure causes decrease of the normal effective stress on the fault plane, and facilities fault reactivation. However, the site-specific aspects of the phenomenon are complex. For example, it is challenging to determine the flow path of the injected fluid volume, the specific fault segments that slip, and the injection rates and volumes which may not lead to the occurrence of large events in a given setting. These questions can be addressed by 3D geomechanical modeling that captures the salient aspects of the geological conditions and geomechanics effects.

Small- to moderate-sized earthquakes in the central and eastern United States were historically rare until 2009. Among all states, Oklahoma has experienced the most increase in the number of earthquakes. The rate of $M_w > 4$ earthquakes has increased from one per decade before 2009 to 24 in 2014 (Holland et al. 2014, Petersen et al. 2017). At the same time, the volume of injection has been increased significantly. For instance, the monthly injection volume in the state increased from 80 to 160 million barrels/month which is mostly performed through saltwater disposal wells (SWD) (Walsh and Zoback 2015). The Nov 6, 2011 event in Oklahoma has an M_w 5.7 and occurred in Prague, central Oklahoma. It happened after many foreshocks and was followed by a sequence of aftershocks (including a foreshock and an aftershock, both $M_w = 4.8$, on 5 and 7 Nov 2011, respectively, Oklahoma Geological

Survey (OGS)). These earthquakes were felt in at least 17 states (over 100 widely scattered ZIP codes at distances greater than 1000 km) and caused the increase of concerns about ongoing unconventional oil and gas activities (Keranen et al. 2013, Hough 2014). Since these events occurred in the vicinity of active injection wells, it has been proposed by some authors that these events were induced by injection of oil and gas co-produced wastewater (Keranen et al. 2013, 2014, Sumy et al. 2014, Sun and Hartzell 2014). Some authors have attributed the events to intra-plate tectonics (e.g., Holland and Keller 2013). Analysis of such an important and complicated problem requires using realistic models of pore pressure/stress alteration and fault systems interaction. In the previous studies on seismicity in Oklahoma, the main focus has been on the pore pressure effect without addressing the rock mass deformation. Moreover, some previous work has been limited to 2D modeling (Deng et al. 2020). In this work, we study the effect of wastewater injection on the pore pressure and total in-situ stress changes within the Wilzetta fault zone near Prague, Oklahoma, United States. Rock mechanical and hydraulic properties of different layers and the fault system are used to construct the coupled fluid-mechanical model for the investigation of multi-year injection scenarios.

4.2 The Wilzetta Fault Zone

Figure 39 shows the area of interest in the Oklahoma faults map (Oklahoma Geological Survey (OGS), http://www.ou.edu/ogs/data/fault, the blue box), location of the injection wells (Oklahoma Corporation Commission (OCC), http://www.occeweb.com/og/ogdatafiles2.htm), and seismic events between 2009 and 2011 in the area of interest (OGS, http://www.ou.edu/ogs/research/earthquakes/catalogs). The area of interest is approximately

~1200 square kilometers (approximately ~34 × 36 km) and is located in the northern Pottawatomie and Seminole counties, northwestern Hughes county, southwestern Lincoln county, western Okfuskee county (Figure 39a).

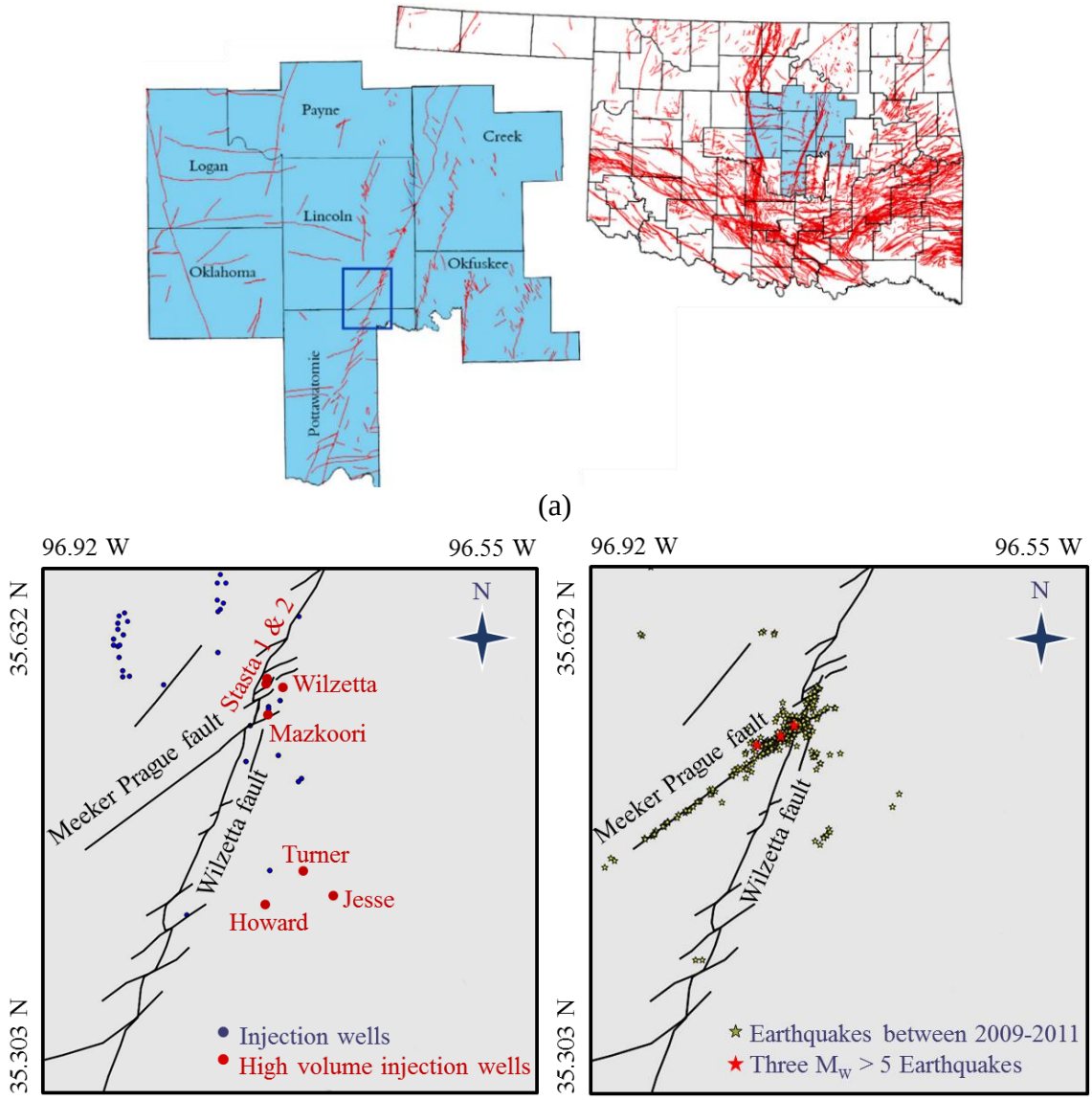


Figure 39: (a) Oklahoma fault map (Oklahoma Geological Survey (OGS), http://www.ou.edu/ogs/data/fault). The fault traces and the area of interest are shown by red lines and the blue box, respectively. (b) Location of injection wells in the area of interest (Oklahoma Corporation Commission (OCC), http://www.occeweb.com/og/ogdatafiles2.htm) (c) Earthquakes between 2009 and 2011 in the area of interest (OGS, http://www.ou.edu/ogs/research/earthquakes/catalogs).

System	Series	Group	Formation	Subsurface Name
Pennsylvanian	Virgillian	Wabanusee	Vanoss	Emporia
			Ada	Pawhuska
		Shawnee		Hoover
			Vamoosa	Oread
		Douglas		Endicott
			Tallant	Tonkawa
	Missourian	Ochelata	Barnsdall	Okesa
			Wann	Perry Gas
			Iola	Avant
			Chanute	Osage Layton
				Cottage Grove
		Skiatook	Dewey	Dewey
			Nellie Bly	
			Hogshooter	Hogshooter
				Layton
			Coffeyville	
			Checkerboard	Checkerboard
				Cleveland
			Seminole	
	Des Moi-nesian	Marmaton	Holdenville-Nowata	
			Oolagah	Big Lime
			Labette	
			Fort Scott	Oswego
				Little Osage
				Excello
		Cabaniss		Prue
			Senora	Verdigris
				Skinner
		Krebs		
			Boggy	Pink
				Redfork
				Inola
				Bartlesville
			Savanna	Brown
			Mc Alester	Booch
`Mississippian	Chesterian		Chester	Caney
	Maramecian		Moorfield	Mayes
	Osagean		Osage	Osage
Devonian	Chattanoogian		Chattanooga	Woodford
Silurian	Hunton		Hunton	Hunton
Ordovician	Cincinnatian	Richmond	Sylvan	Sylvan
	Champlainian	Mohawkian	Viola	Vioal
		Simpson	Bromide	Wilcox
			Tulip Creek	Tulip Creek
			McLish	
			Oil Creek	
	Canadian	Arbuckle	Arbuckle	Arbuckle
Cambrian	Croixan			

Figure 40: Stratigraphic section of the study area above the Precambrian basement (Dycus, 2013)

Selection of this area was based on the location of five high-volume injection wells and two Stasta I and II wells (shown in red Figure 39b), and three ~M_w5 events occurred in 2011. There are more than twenty injection wells in our study area (Figure 39) that inject wastewater into the different subsurface targets such as the Woodford formation, Wilcox formation (Simpson group), Arbuckle group, etc. The total volume injected down the wells in the area of interest up to the end of Nov 2011 is more than 1.2×10^7 m^3 (OCC) among which five wells account for 93% of this injected volume (Table 5). Wilzetta well which is located northeast of the three major events (Figure 39) supplies 32% of the total volume. Mazkoori has the minimum distance to the events, and accounts for 8% of the total volume. The other three high-volume wells (Turner, Jesse, Howard) that account for much of the rest of the total volume (Table 5) have distances of 12 to 15 km southeast of the major events (Figure 39). It should be noted that in this study, it is assumed that the reported data by OGS and OCC including the faults geometry and wells location and injection volume is representative of the in-situ conditions. Wells data (OCC, http://www.occeweb.com/og/ogdatafiles2.htm) including years of operation (until 2011), the volume of the injected fluid, and the target of injection for the five high-volume injections and two Stasta wells are shown in Table 5.

Table 5: Years of operation (until Nov 2011), the total injected volume of fluid ($\times10^6$ m^3), and subsurface target formation for high-volume injection wells and Stasta 1 and 2 wells (OCC, http://www.occeweb.com/og/ogdatafiles2.htm).

Well	Years of Operation	Fluid Volume ($\times 10^6$ m^3)	Subsurface Formation
Wilzetta	1999-2011	3.89	Wilcox-Arbuckle
Mazkoori	2000-2004	1	Arbuckle
Turner	2004-2011	2.57	Wilcox-Arbuckle
Jesse	2003-2011	2.31	Arbuckle
Howard	2008-2011	1.44	Arbuckle
Stasta-1	1993-2011	0.05	Hunton
Stasta-2	2006-2011	0.05	Wilcox-Arbuckle

Table 6: Rock mechanical and hydraulic properties used in the simulations. ((1) Yu 2017; (2) Carell 2014; (3) Cappa 2009; (4) Chester 1993); (5) Kolawole et al. 2019)

	Lower Simpson	Simpson	Arbuckle Group	Basement	Fault Damage zone
Vertical Permeability (mD)	6.7×10^{-4} (2)	6.7×10^{-4} (2)	5-25 (1,2)	6.7×10^{-4} (1,2)	10-50 (3)
Horizontal permeability (mD)	6.7×10^{-4} (2)	6.7×10^{-4} (2)	10-50 (1,2)	6.7×10^{-4} (1,2)	10-50 (3)
Porosity, ϕ	0.13 (2)	0.13 (2)	0.1 (1,2)	0.01 (2)	0.1 (3)
Young's modulus E(GPa)	45 (4)	45 (4)	76 (1)	80 (1)	25 (3)
Poisson ratio, ν	0.14 (4)	0.14 (4)	0.27 (1)	0.3 (1)	0.25 (3)
Friction angle, φ (°)	31 (4)	31 (4)	30 (1)	35.5 (1,5)	25 (3)
Thickness (m)	160	200	750	4000	

The stratigraphic section of the study area is shown in Figure 40 (Dycus 2013). In the model, in addition to the Precambrian basement where the majority of seismic events occurred (more than 3 km below the surface, Keranen et al. 2013), we include those formations which experienced the most volume of injection. They include Arbuckle group and Simpson group. The mechanical parameters for different formations in the model are listed in Table 6. It should be noted that the mentioned thickness of the layers in Table 6 represents the average values of the layers (OGS, personal correspondence).

The Precambrian basement is overlain by Arbuckle group and Simpson group, consecutively. Arbuckle group, which predominantly consists of limestone and dolomite, is a basal sedimentary strata, and has been the main target for the majority of Class II UIC SWD volumes in Oklahoma (Murray and Holland 2014). The geomechanical properties of Arbuckle group rocks can be found in Yu and Ghassemi (2017), Yu (2017), and Kolawole et al. (2019). An extensive joint system that was formed by the basement tectonics (Walters 1958, Carell et al 2014) makes Arbuckle porous and permeable enough to easily accept the injection of wastewater (under the hydrostatic head). However, the injected water does not appear to

remain within Arbuckle and finds its way into basement rocks via natural fractures. The pressurization and stress redistribution within the basement can lead to fault reactivation and increased seismicity. Simpson Group is made up of sands, carbonates, and shales, and has been a great producer of oil and gas in Oklahoma (Statler 1965). The lower section of Simpson group overlies Arbuckle group and is characterized by a thick shaley zone. This shaley layer seals Arbuckle group from the top. In this study, we refer to this zone as the lower Simpson.

It is reported that Arbuckle group is underpressured, and has a hydrostatic pressure of ~9 MPa/km (Carell 2014, Nelson 2015). In this study, we assume the orientation of the maximum principal stress as N83°E (Alt and Zoback 2014) which is in the range of more recent data (Alt and Zoback 2017) and previous studies (Dart 1990) described in chapter 3. The gradients of the maximum and minimum horizontal stresses, and overburden gradients are are $\frac{\partial S_{H,max}}{\partial z} = 30\ \frac{MPa}{km}$, $\frac{\partial S_{h,min}}{\partial z} = 15\ \frac{MPa}{km}$ $\frac{\partial S_{vertical}}{\partial z} = 25\ \frac{MPa}{km}$, respectively (Hair 2012). We consider only the five high-volume wells (Table 5) in our model. All of these wells are located on the eastern side of the Wilzetta fault zone (Figure 39). Wilzetta, Mazkoori, and Stasta wells are within a distance of less than 500 m to the Wilzetta fault while Turner, Jesse, and Howard wells are farther (more than 5 km). Therefore, the former wells potentially have more effect on the Wilzetta fault. In the OCC database, some reported monthly wellhead pressures do not have a consistent trend. At times the wellhead pressure is reported as zero, and then increases again. It is not clear if this has a physical reason (for example propagation of a fracture from the well) or just a missing data point. In these situations, we assume the pressure to be equal to the reading of the closest previous months.

The subsurface permeability distribution is an important aspect of the problem, particularly in the fault zones. In the absence of hydromechanical properties of the Wilzetta fault zone and different subsurface formations, we consider different possible fault architectures. In many geological settings, fault zones are described as meters-to-kilometers thick zones which have a complex architecture, and consist of (1) one or numerous core zones where most displacements take place, and (2) a fractured damage zone with a width of less than 1 m to several hundred meters (Chester 1993, Caine 1996).

The fault core may include different structures such as slip surfaces, gouge, breccias, cataclastic, clay smears, and geochemically altered rock bodies (Chester and Logan 1986, Antonellini and Aydin 1994). The damage zone which is surrounded by the host rock is formed by the growth of the fault zone and it may consist of subsidiary faults, veins, joints, stylolites, cleavage, and folds (Caine 1996). Typically, these fault components and the host rock show obvious differences in hydromechanical properties. Fault zone architecture and the dimension of its components are highly dependent on the type and initial condition of the rocks. For example, the low and high-porosity layers show two types of deformation which result in different variations of the porosity toward the fault core. In high-porosity layers, grains can move and slide more freely leading to the accommodation of the deformation at the grain scale. This causes a decrease in porosity toward the fault core. In contrast, in less porous layers, well-cemented grains, and the rocks are more brittle, so the deformation includes the increase of fracture porosity (Rinaldi 2014). In this study, both possible fault zone architectures are considered; (1) a fault zone (having a core zone and a fractured damage zone), and (2) a simple plane wherein displacements occurred (without any hydromechanical properties difference between the fault zones and host rock).

4.3 Numerical Model

The modeling work in this study was conducted with the FLAC3D software (Itasca, 2018). In the simulations, both fluid flow and coupled stress calculations are considered. The poro-mechanical equations are as follows (for an isothermal process) (Itasca 2016, Cheng 2016).

Fluid Transport (Darcy Law)

$$\boldsymbol{q}^F = -k\boldsymbol{\nabla}\left(P_p - \ \rho_f \ \boldsymbol{g}.\boldsymbol{x}\right) \tag{4.1}$$

where k is the fluid mobility coefficient ($k = \kappa/\mu_f$, where κ is the intrinsic permeability, and μ_f is the fluid dynamic viscosity, and ρ_f is fluid density).

Fluid Mass Balance

$$\frac{\partial P_p}{\partial t} = -M\left[\boldsymbol{\nabla}.\boldsymbol{q}^F + \alpha\frac{\partial(\varepsilon_v)}{\partial t}\right] \tag{4.2}$$

where P_p is fluid pressure, M is the Biot's modulus, ε_v is the volumetric strain.

The mechanical constitutive relations for elastic material are:

$$\frac{\partial\sigma_{ij}}{\partial t} + \alpha\frac{\partial P_f}{\partial t}\delta_{ij} = 2G\left(\frac{\partial\varepsilon_{ij}}{\partial t}\right) \ + (K - \frac{2G}{3})\left(\frac{\partial\varepsilon_{kk}}{\partial t}\right)\delta_{ij} \tag{4.3}$$

Chapter 2 Where σ_{ij} and ε_{ij} are total stresses and strains, α is Biot's effective stress coefficient, K and G are bulk and shear modulus, and δ_{ij} is Kronecker delta.

4.4 Simulation Setup

In building the simulations, we consider the real topography and the spatial geometry of the faults, and incorporate them in the determination of the initial state. The rock layers are assigned the Mohr-Coulomb plasticity constitutive model. There are generally three approaches to simulate fault hydromechanical behavior. These approaches are (1) zero-thickness mechanical interfaces, (2) an equivalent continuum representation using solid elements, (3) a combination of solid elements, and ubiquitous-joints oriented as weak planes (Rutqvist et al. 2002, Cappa 2010, Gan and Elsworth 2014, Gao and Ghassemi 2020). In this study, the zero-thickness mechanical interface is used to model the fault behavior. Interface elements are attached to an element surface. At each time step, the absolute normal penetration

and the relative shear velocity are calculated for each interface node and its contacting target face. Then, by applying the interface constitutive model (Coulomb shear-strength criterion), these values are used to calculate normal and shear-force vectors. We assume the fault core as a plane across which fluid may flow in the normal direction (1D flow).

We construct a simulation domain that is large enough to encompass all the injection wells in our study area. To prevent any boundary effect, we calculate the diffusivity and accordingly set the dimensions of the domain. Using the injection time (t_{inj} = 12 years and 9 months) and other parameters from Table 6, the minimum distance from each well to the domain boundary can be calculated. For example, it is calculated in cases 1 and 2 of scenarios 1 to 3 as:

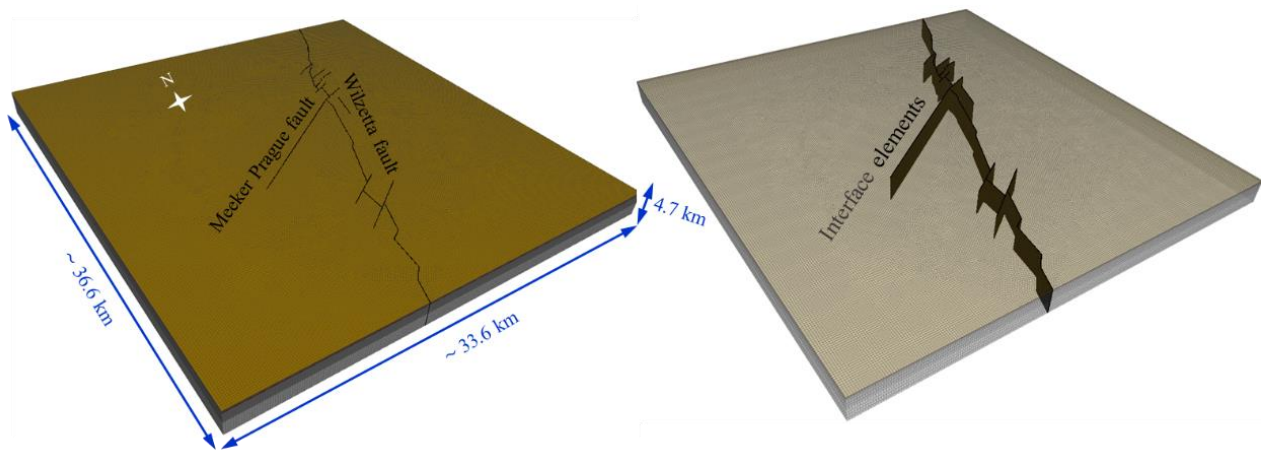
$$\mathrm{L} = \sqrt{\mathrm{ct_{inj}}} = \sqrt{0.27 \times 4.1 \times 10^8} = 10457 \text{ m} \approx 10.5 \text{ km}$$

Where c is the "diffusivity" (Cheng 2016), $\mathrm{c} = \frac{\mathrm{k}}{\mathrm{S}}$ with

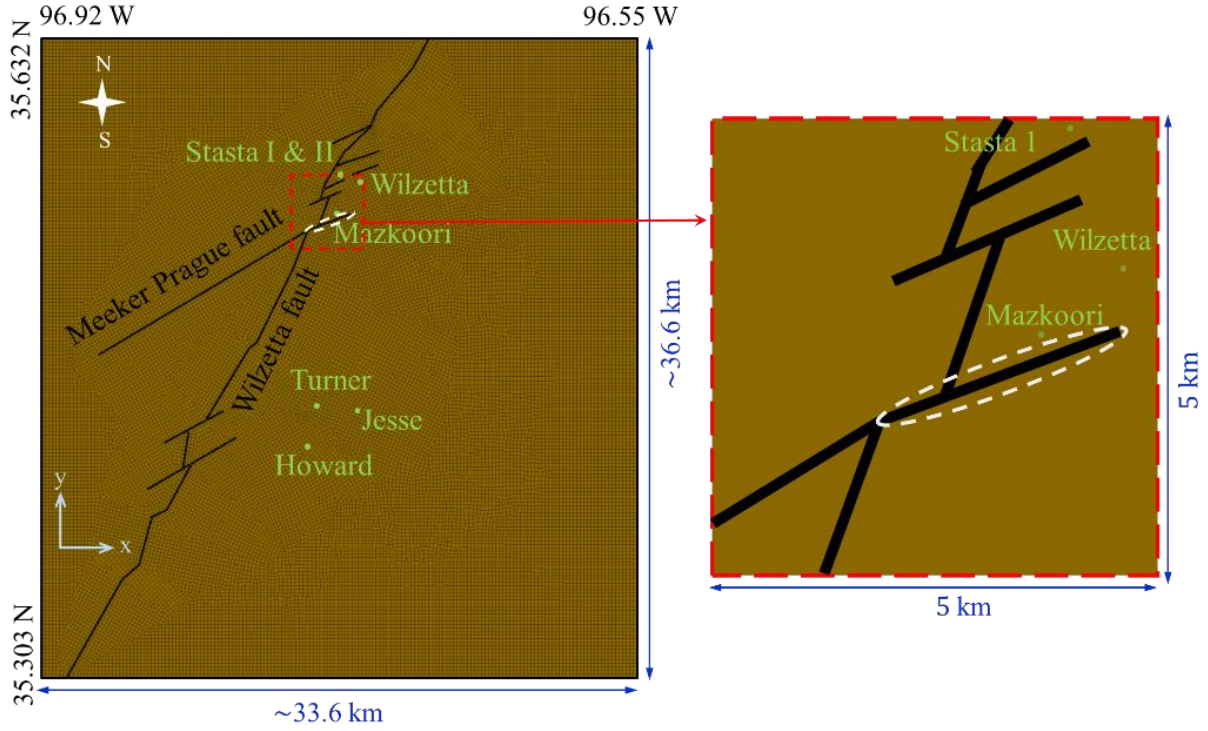
$$S = \frac{1}{M} + \frac{\alpha^2}{K + \frac{4G}{3}} \approx \frac{\phi}{K_f} + \frac{1}{K + \frac{4G}{3}} \tag{4.4}$$

Where M, K_f , ϕ, S are Biot's modulus, fluid bulk modulus, porosity, elastic storage, respectively. In equation 4.4, it is assumed that the grain compressibility is negligible (α =1).

The domain is more than 33.6 km in the east-west, and 36.6 km in the north-south directions, and includes Simpson group, Arbuckle group, and the Precambrian basement. The thickness of our model is 4.7 km, and the top and the bottom of the model are located at depths of 0.8 km and 5.5 km. We defined faults extending up from the basement at depth of ~5 km into Arbuckle group (OGS, Keranen 2013, Kolawole et al. 2019, 2020). Figure 41 shows the dimension of the domain, the geometry of the faults, and the location of seven injection wells inserted into the model.



(a) **(b)**



(c)

Figure 41: (a) The 3D view of the model and the location of the faults b) the sketch of interface elements representative of faults c) the plan of the domain and location of the faults and injection wells. Since most events (especially ~M_w = 5 events, Figure 39) were located on the splay branch of the Wilzetta fault (shown by the dashed white line) and the Meeker Prague fault, we pay special attention to this splay of Wilzetta fault in this study.

The change of pore pressure and the induced stresses are calculated in our model. Wilzetta, Turner, and Stasta-2 wells inject wastewater into both Wilcox and Arbuckle groups, while the other wells inject only into Arbuckle group (Table 5). The only well that injects directly into Hunton layer is Stasta-1 well. Hunton group contains oil in compartments near the Stasta wells (Way 1983) suggesting entrapment of hydrocarbons (so preventing fluid migration to other layers). Although these reservoir compartments in Hunton group suggest no hydraulic communication between the isolated compartments and the surrounding rocks (both within Hunton group and adjacent layers), some authors have proposed there is hydraulic communication between Arbuckle group and the Precambrian basement (Keranen et al. 2013). In the absence of concrete data, we assume that Hunton layer is isolated, and does not have any hydraulic communication with other layers. It should be noted that the Oklahoma Corporation Commission (OCC, http://www.occeweb.com/og/ogdatafiles2.htm) reports the monthly injection volume and the wellhead pressure of all wells. The values of wellhead pressure are reported constant during the month and reflect values of pressure only during pumping. Reservoir pressure near the wellbore is set equal to this value during the pumping and dissipates after injection stops. Over many cycles, the pressure near the wellbore spikes and drops, and after a while, the wellhead pressure would normally increase unless the fluid readily finds open/low-pressure zones. Due to lack of data, we apply a continuous injection in our simulations, and therefore we do not capture the detailed potential pore pressure fluctuating near the wellbore. Instead, we observe a constant increase of pore pressure which is dependent on the injection rate and transmissivity of the target layer. Another point is that there are no observation points to measure the pore pressure changes in the area of interest. Instead, we use the available wellhead pressure (plus the hydrostatic column) to estimate the target layer

pressure. This pressure is not always representative of the reservoir pressure. However, as mentioned before, at the time of injection operation, it is reasonable to consider near-well-bore pressure to be equal to the wellhead pressure plus the hydrostatic column in the well. Therefore, in this article, the pressure buildup calculated by the numerical model may not reflect what exactly happened during the injection operation in reality.

Using wells data (the total injection volume, perforation depths, and injection target layers) and transmissivity of each layer, the volume of injection into each layer can be specified. The transmissivity (T) for horizontal flow in a layer with a saturated thickness h, and horizontal hydraulic conductivity K_h is (Bear 2013)

$$T = K_h h \tag{4.5}$$

Therefore, if a total rate of q_t (the total volume divided by injection time) is injected into n different layers, the rate into the i-th layer is obtained by (continuity):

$$q_i = \frac{K_i h_i}{\sum_{i=1}^{n} K_i h_i} q_t \tag{4.6}$$

Knowing the monthly total injection volume, and using perforation intervals for each well (OCC), and also assuming that the injection operation was performed continuously, we obtain the monthly volume of injection for each group. For example, the injection volume rate of each group by Wilzetta well which injects into Arbuckle and Simpson groups can be calculated by the following equation

$$q_{Arbuckle} = \frac{K_{Arbuckle} h_{Arbuckle}}{K_{Wilcox} h_{Wilcox} + K_{Arbuckle} h_{Arbuckle}} q_t \tag{4.7}$$

Where q_t is the total injection rate.

Due to the limited information on the geomechanical and hydraulic properties of the area, several assumptions were made and different hydraulic relationships between the geological

layers and fault zone are considered. We defined three major scenarios (Table 7) that are subdivided into cases. In each case, we made some assumptions and study the effect of injection on Wilzetta and Meeker Prague faults. For each scenario, we defined different cases where we assigned different properties such as hydraulic properties of fault zones, etc.

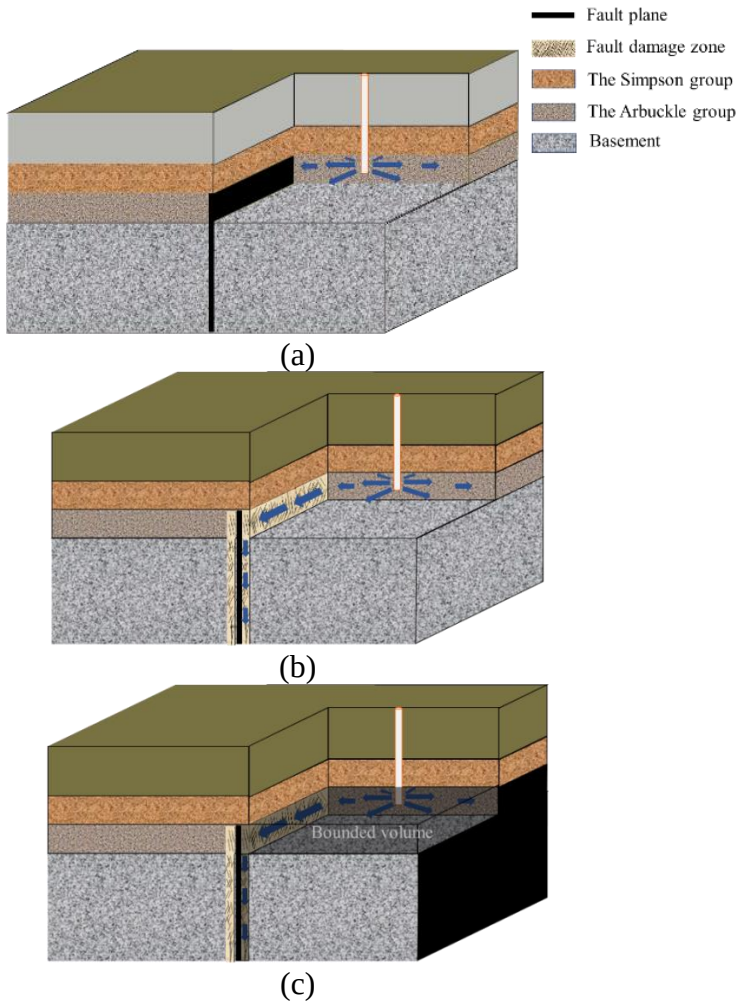


Figure 42: Schematic for (a) scenario 1: there is no communication between Arbuckle group and the basement, and fluid diffuses into Arbuckle in semi-restricted and infinitely open volume in cases with impermeable and permeable, respectively; (b) scenario 2: fluid penetrates the deeper depths through the damage zone; (c) scenario 3: there is only a damage zone around a part of the Wilzetta fault, and there is a bounded volume in Arbuckle group in which wastewater accumulated resulting in pore pressure elevation.

Table 7: Different scenarios and cases in the model

Scenario 1: *No hydraulic communication between geological layers.*
Case 1: Faults are impermeable, $k_{Simpson}$ = 1 mD, $k_{Arbuckle}$ = 10 mD **Case 2:** Faults are permeable, $k_{Simpson}$ = 1 mD, $k_{Arbuckle}$ = 10 mD **Case 3:** Faults are impermeable, $k_{Simpson}$ = 1 mD, $k_{Arbuckle}$ = 100 mD **Case 4:** Faults are permeable, $k_{Simpson}$ = 1 mD, $k_{Arbuckle}$ = 100 mD
Scenario 2: *Hydraulic communication between geological layers by the fault damage zone.*
Case 1: Faults are impermeable, $k_{Simpson}$ = 1 mD, k_{fault} = 10 mD, $k_{Arbuckle}$ = 10 mD **Case 2:** Faults are permeable, $k_{Simpson}$ = 1 mD, k_{fault} = 10 mD, $k_{Arbuckle}$ = 10 mD **Case 3:** Faults are impermeable, $k_{Simpson}$ = 1 mD, k_{fault} = 100 mD, $k_{Arbuckle}$ = 10 mD **Case 4:** Faults are permeable, $k_{Simpson}$ = 1 mD, k_{fault} = 100 mD, $k_{Arbuckle}$ = 10 mD **Case 5:** Faults are impermeable, hydraulic communication between geological layers by the fault damage zone, and there is a permeability anisotropy (vertical to horizontal direction ratio of 0.5). $k_{h\ Simpson}$ = 1 mD, k_{fault} = 10 mD, $k_{h\ Arbuckle}$ = 10 mD **Case 6:** Faults are impermeable, hydraulic communication between geological layers by the fault damage zone exists only on a portion and some splay branches of the Wilzetta fault (constrained by the white dashed line in Figure 53), $k_{Simpson}$ = 1 mD, k_{fault} = 10 mD, $k_{Arbuckle}$ = 10 mD **Case 7:** Faults are impermeable, hydraulic communication between geological layers by the fault damage zone exists only on a splay branch of the Wilzetta fault (constrained by the white dashed line in Figure 53), $k_{Simpson}$ = 1 mD, k_{fault} = 10 mD, $k_{Arbuckle}$ = 10 mD
Scenario 3: *There is only a damage zone around a part of the Wilzetta fault, and there is a bounded volume in Arbuckle group into which Wilzetta and Mazkoori wells inject*
Faults are impermeable, $k_{Simpson}$ = 1 mD, k_{fault} = 10 mD, $k_{Arbuckle}$ = 10 mD

In the first scenario, we assume that there is no hydraulic communication between different geological units and groups (Figure 42a). For example, we assume that Arbuckle group is sealed, and there is no hydraulic connection with Simpson group and the basement from the top and the bottom, respectively. Both Simpson group (the lower section which directly overlies Arbuckle group consists of shale) and the basement have very low matrix permeability. In this scenario, the possibility of fluid flow through fractures in the basement is neglected. Therefore, the entire injected water diffuses into the target layer, and does not escape to the upper and lower adjacent layers. In the second scenario (Figure 42b), we consider the possibility of hydraulic communication between different geological layers. To be more specific, this communication is through the fractures around the fault plane (i.e., the damage zone) through which fluid penetrates the deep crystalline basement. Since most events (especially the M5 foreshock, Figure 39) were located on part of Wilzetta fault which is shown by the white dashed line in Figure 41, we pay special attention to this part of Wilzetta fault. In scenario 3, it is assumed that the damage zone is located only around the part of Wilzetta fault (shown by the white dashed line in Figure 41c), and there is a bounded volume in Arbuckle group into which Wilzetta and Mazkoori wells inject. It should be mentioned that we make this assumption based on the fact that there used to be an oil field in the area (Keranen et al. 2013; OCC; http://www.ogs.ou.edu/fossilfuels/MAPS/GM-36.pdf).

4.5 Simulation Results

4.5.1 Scenario 1- Cases 1 and 2: Impermeable and Permeable Faults with Low Arbuckle Permeability

Using equation 4.7, it can be shown that in cases 1 and 2 of this scenario more than 99 % of the total injection volume goes into Arbuckle group. Figure 43 shows the change in pore pressure of Arbuckle group (at a depth of 1600 m, i.e., almost the middle depth of Arbuckle

group) in Nov 2011 (after 12 years and 10 months of injection and at the time of main fore-shocks) after injection of 11.2 million m^3 of wastewater in six wells for cases 1 and 2, respectively. In both cases 1 and 2, the injection induces the maximum pressure change of ~0.8-0.9 MPa near the Howard well. In case 1, there is a maximum pore pressure increase of 0.9 MPa around the Wilzetta well, and an increase of 0.3-0.6 MPa increase over a relatively large area (7 km×17 km) between the northern and southern wells in Arbuckle group at depth of 1600 m. Due to the cross-fault flow in case 2, the pore pressure is affected over a larger area, and the overall values of the excess pore pressure (the average of 0.2-0.3 MPa) are less than those of case 1. The change of pore pressure on the splay branch of the Wilzetta fault plane (W-w) in Nov 2011 (after 12 years of injection) for cases 1 and 2 of scenario 1 are shown in Figure 43a and b, respectively. The maximum values of the pressure elevation on the fault plane are 0.63 and 0.33 MPa in cases 1 and 2, respectively. This is because in case 1, it is assumed that faults are impermeable preventing fluid flow into the target layers, and consequently a higher pore pressure buildup. In this scenario, since there is no fluid path (e.g., fault damage zone) between the target layers and the basement, the fluid only penetrates the basement to a depth of 3.4 km, and therefore without changing the pore pressure in the location of the main events. Figure 44 compares the injection-induced pore pressures at the end of 2001, 2005, and 2010 at depth of 1600 m for cases 1 and 2 of scenario 1, respectively. It can be seen that the pattern and the values of the pressure elevation are not constant during the years of injection due to the variation of wells operational times and different injection volumes. For example, the Mazkoori well started injection in 2000 and ended in 2004. Since the Mazkoori has the shortest distance from the Wilzzeta fault, it is

expected that it has the most effect on the pore pressure of the Wilzetta fault plane along the section W-w.

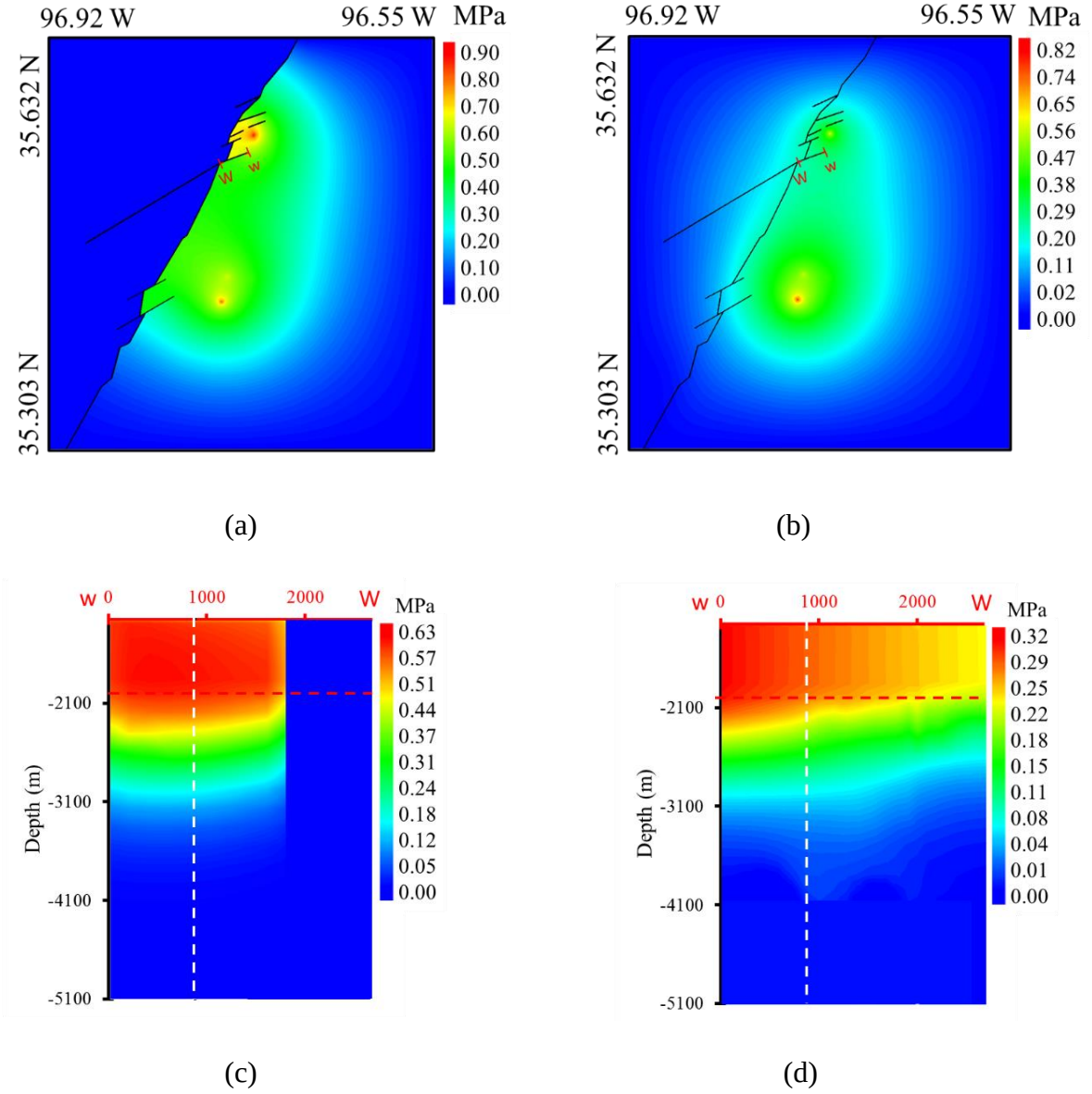
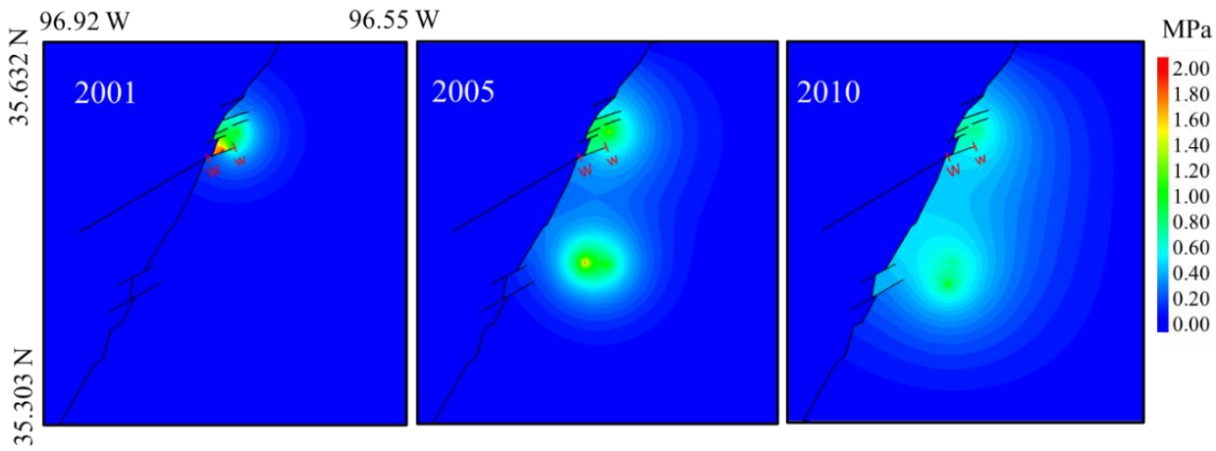
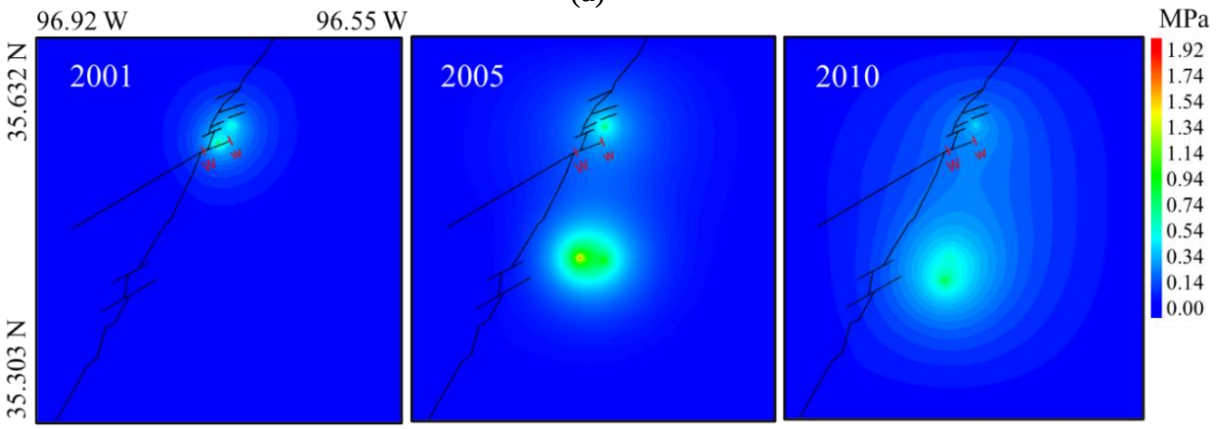


Figure 43: Scenario 1: The change of pore pressure (MPa) in Arbuckle group at a depth of 1.6 km in Nov 2011 (after 12 years and 10 months of injection) for (a) case 1, and (b) case 2. The change of pore pressure on the splay branch of Wilzetta fault plane along the W-w for (c) case 1 and (d) case 2. The top and the lower boundaries of Arbuckle group are shown by the red solid and dashed lines, respectively. The white dashed line is the vertical line on the fault plane that has the shortest distance to the Mazkoori well.



(a)



(b)

Figure 44: Scenario 1: The pore pressure change (MPa) in Arbuckle group at depth of 1.6 km at the end of 2001 (left), 2005 (middle), and 2010 (right) for (a) case 1 and (b) case 2.

Figure 45 c and d show the change of pore pressure on the splay branch of the Wilzetta fault plane along the section W-w in 2001, 2005, and 2010 for cases 1 and 2, respectively. As expected, in case 1, the operation of Mazkoori well and the impermeable nature of the faults can cause the maximum pressure buildup of 2 MPa along the W-w fault plane while in case 2, permeable faults result in lower pressure of 1 MPa. After 2005, when injection into the Mazkoori well ended, the induced pore pressure on the section W-w (Figure 45) is reduced, and after a couple of months remains at an almost constant value of 0.3 MPa until the end of the simulation (Nov 2011). As mentioned before, injection causes change of total stresses.

For example, Figure 46 shows the change of the total horizontal stress components σ_{xx} and σ_{yy} corresponding to east-west and north-south directions caused by injection in scenario 1 after 12 months and 10 months of injection (in Nov 2011), respectively. It can be seen that based on the pore pressure and poroelastic properties, the induced total $\Delta\sigma_{xx}$ and $\Delta\sigma_{yy}$ are 0.45 MPa and 0.38 MPa in cases 1 and 2, respectively. To study the stability of faults, different values of coefficient of friction in the range proposed by Byerlee (1978, under high normal stress the range is 0.6 to 1 corresponding to a friction angle of 31° to 45°) are assigned for the faults in the model to study if the induced changes in pore pressure and total stresses are enough to cause slip on faults.

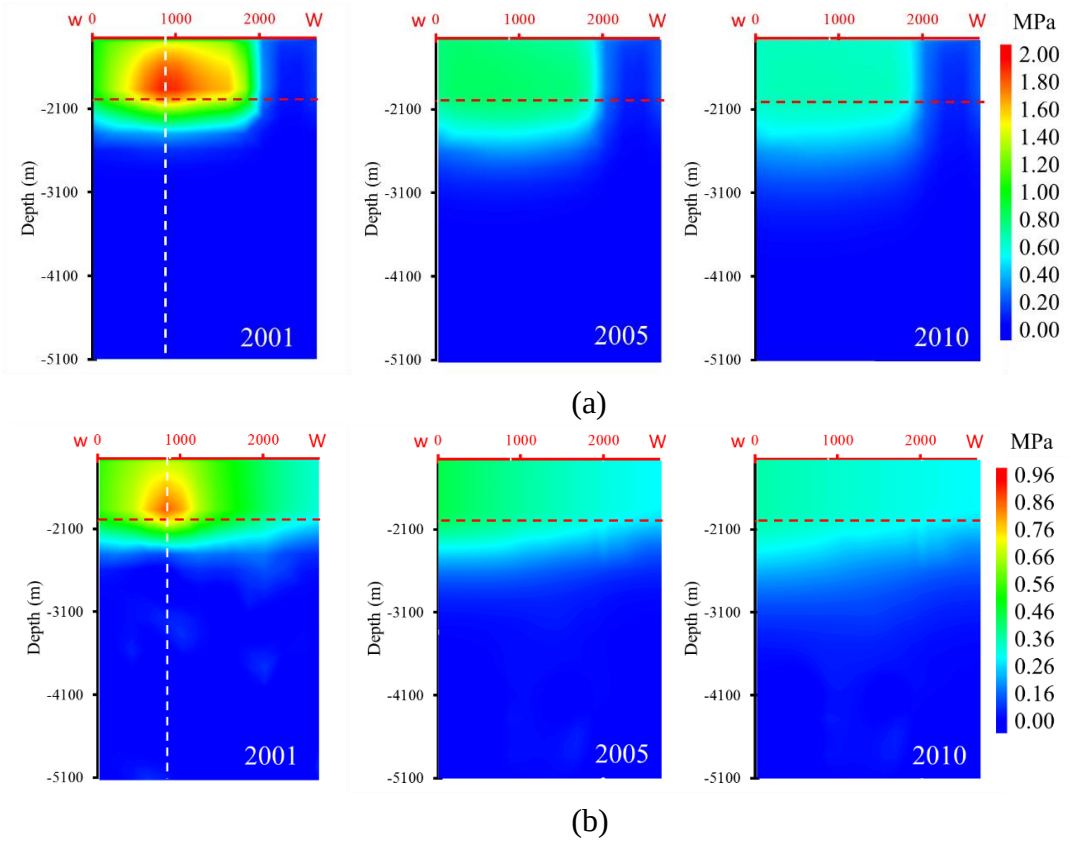


Figure 45: Scenario 1: The pore pressure change (MPa) on the splay branch of Wilzetta fault plane along the cross-section W-w at the end of 2001 (left), 2005 (middle), and 2010 (right) for (a) case 1 and (b) case 2. The top and the lower boundaries of Arbuckle group are shown by the red solid and dashed lines, respectively. The white dashed line is the vertical line on the fault plane that has the shortest distance to the Mazkoori well.

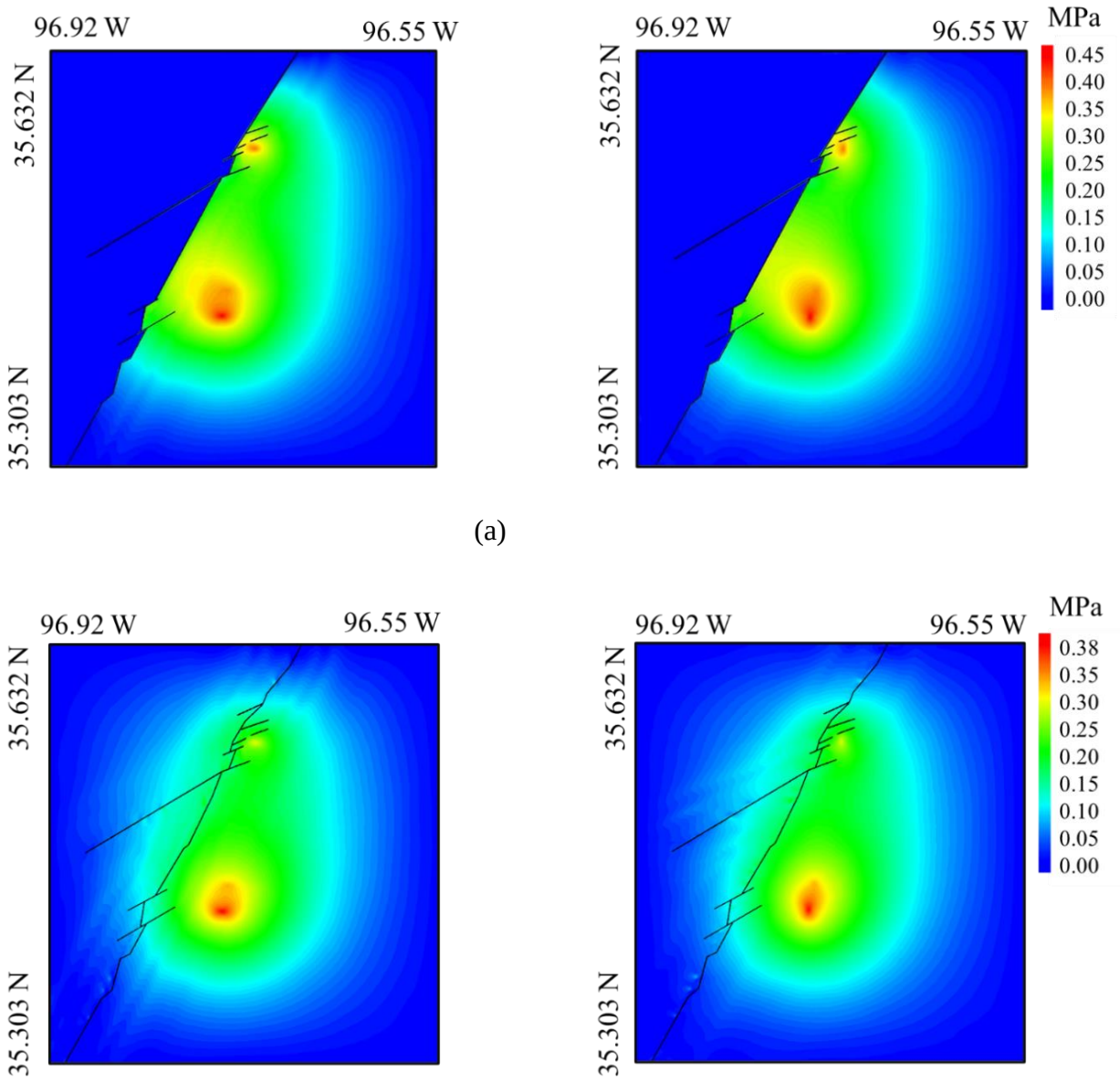
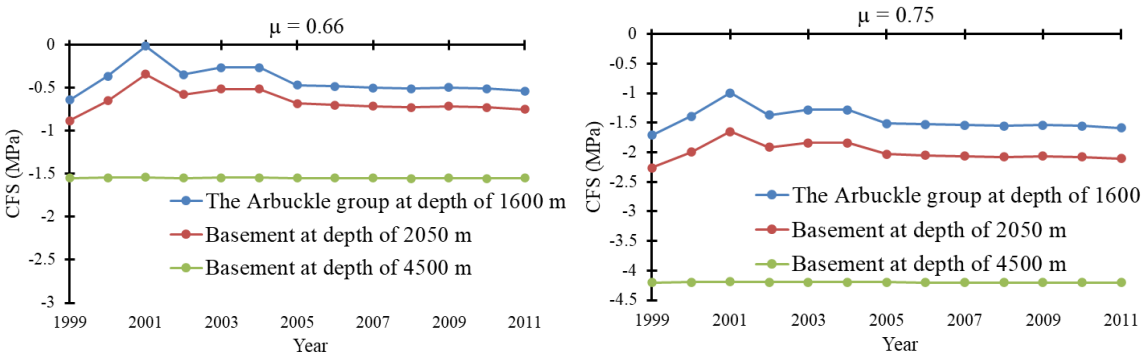


Figure 46: Scenario 1: Change in the horizontal total stresses ($\Delta\sigma_{xx}$ and $\Delta\sigma_{yy}$) (MPa) of Arbuckle group at depth of 1600 m in Nov 2011 (after 12 months and 10 months of injection) for (a) case 1 and (b) case 2 induced by injection. $\Delta\sigma_{xx}$ (east-west) and $\Delta\sigma_{yy}$ (north-south) are shown in the left and right figures, respectively.

Figure 47 shows the values of the difference between the shear stress and the shear strength (CFS) of the three points at depths of 1600 m, 2050 m, and 4500 m corresponding to the middle of Arbuckle group, the shallow basement, and the deep basement along the vertical

dotted white line (Figure 45, the closest point to the Mazkoori well) on the splay branch of the Wilzetta fault plane along the cross-section W-w (Figure 44) during the history of injection (for case 1 of scenario 1).



(a) (b)

Figure 47: Scenario 1, case 1: Variation of CFS (MPa) at three points located on the fault plane along the dashed line on the splay branch of Wilzetta fault plane along the cross-section W-w (Figure 45) during simulation for (a) μ = 0.63 and (b) μ = 0.75. For the value of μ = 0.63, CFS becomes positive (fault failure) at depth of 1600m. The fault remains stable during injection for μ = 0.75. Due to permeable faults, there is less pressure buildup in this case than in case 1, and therefore the fault fails at the lower coefficient of friction of 0.63.

It can be seen that the variation trend of CFS is similar for all three points at different depths. For a friction coefficient of 0.75, the CFS remains negative during the simulation. It increases from the start of the injection operation during the history of injection, and reaches to its maximum in 2001, and decreases till 2005 after which remains constant. This trend of CFS is mostly affected by the operation of the Mazkoori well which has the maximum volume of injection in 2001 and stopped operation at the end of 2004. Since there is no fluid penetration into the deeper depths, CFS remains almost constant at the depth of 4500 m (Figure 47) indicating that no fault reactivation is expected in the deeper depth in this case.

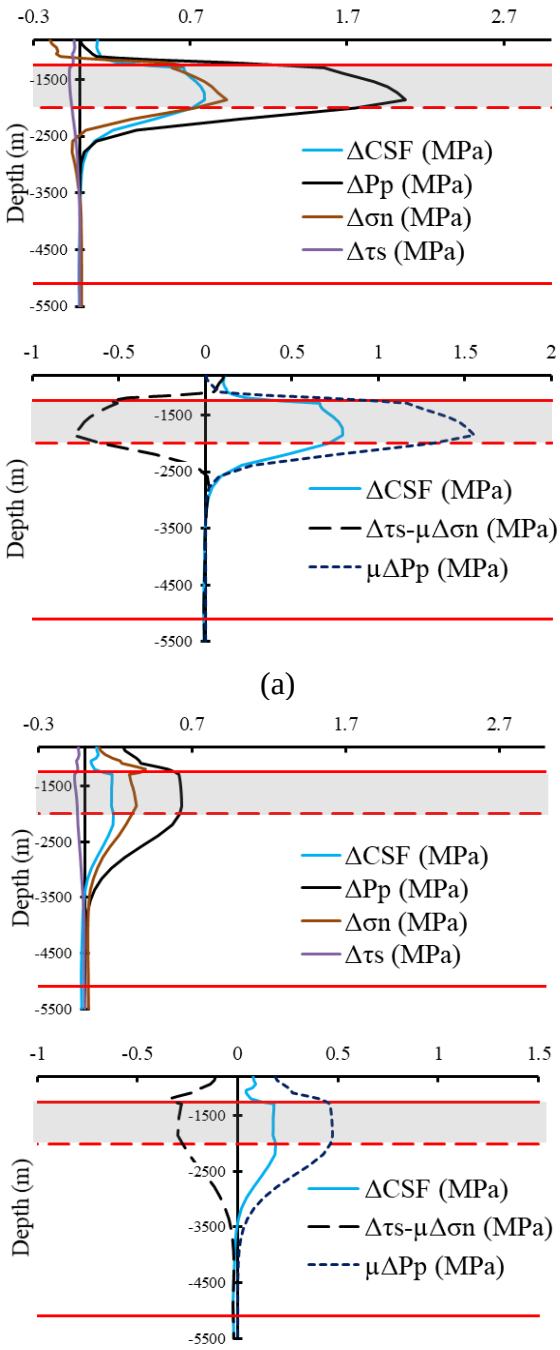
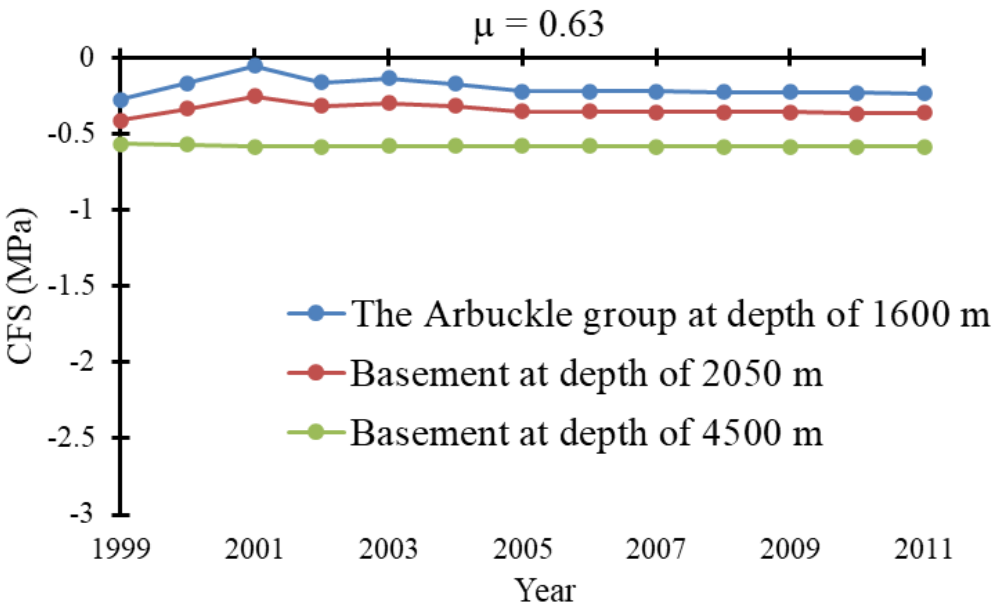
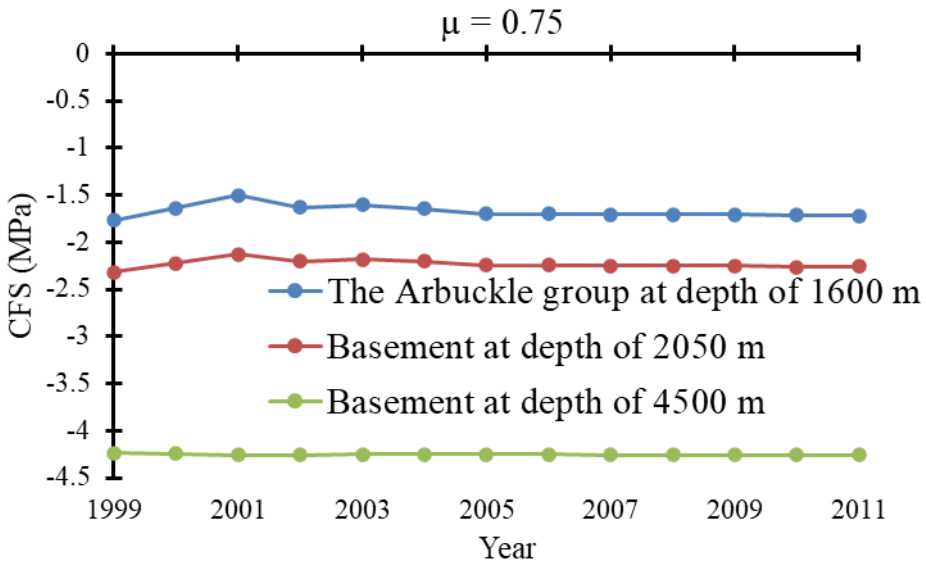


Figure 48: Scenario 1, case 1: Depth profiles of change of CFS (MPa), pore pressure (MPa), total normal stress (MPa), and shear stress (MPa) (Upper figure), and profile of change of poroelastic stress (MPa) and pore pressure (MPa) components of CFS (Lower Figure) along the dashed line on the splay branch of Wilzetta fault plane along the cross-section W-w (Figure 43) in a) Dec 2001 and b) Nov 2011. Solid red lines are the fault boundaries. The red dashed line shows the lower boundary of the reservoir. (μ = 0.75)

Figure 48 depicts the change of components of CFS for both 2001 and 2011($\mu = 0.7$). The total normal stress increases in the reservoir and the part of the basement where fluid diffuses. At the deeper depth in the basement with no fluid diffusion, a reduction in the total normal stress can be observed. The shear stress does not change considerably on the fault plane and remains almost constant. It is obvious that the poroelastic stress contribution to the CFS is not enough to cause instability on the fault in the deeper locations, and the change in pore pressure (ΔPp) is dominant at shallower depths. For a value of friction coefficient of $\mu = 0.66$, CFS becomes positive in 2001 at the depth of 1600 (Figure 47) indicating that fault at the shallower depths becomes active before deeper depths. It also shows that due to Mazkoori well operation and its volume of injection, the most critical year is 2001. Figure 47 and Figure 48 present the CFS and ΔCFS components for case 2 of scenario 1, respectively ($\mu = 0.7$). As mentioned before, the excess pore pressure is less than in case 1 because the cross-fault flow is allowed in case 2. The general trends of the pore pressure, normal stress and shear stress variations are similar to case 1, but with less tendency for fault reactivation. For example, Figure 49 shows that the fault becomes unstable for a coefficient of friction of 0.63 in 2001 at a depth of 1600 m while this value is 0.66 for case 1 (Figure 49). Since no events happened in 2001 in reality, it can be concluded the assigned properties of the fault and layers need to be modified. Another possible condition is that the mechanical and failure properties of rocks change during the injection operation which is not captured in the numerical simulations. It should be noted that the coefficient of friction is assumed uniform along the fault.



(a)



(b)

Figure 49: Scenario 1, case 2: Variation of CFS (MPa) at three points located on the fault plane along the dashed line on the splay branch of Wilzetta fault plane along the cross-section W-w (Figure 45) during simulation for (a) μ = 0.66 and (b) μ = 0.75. For the value of μ = 0.66, CFS becomes positive (fault failure) at depth of 1600m. The fault remains stable during injection for μ = 0.75.

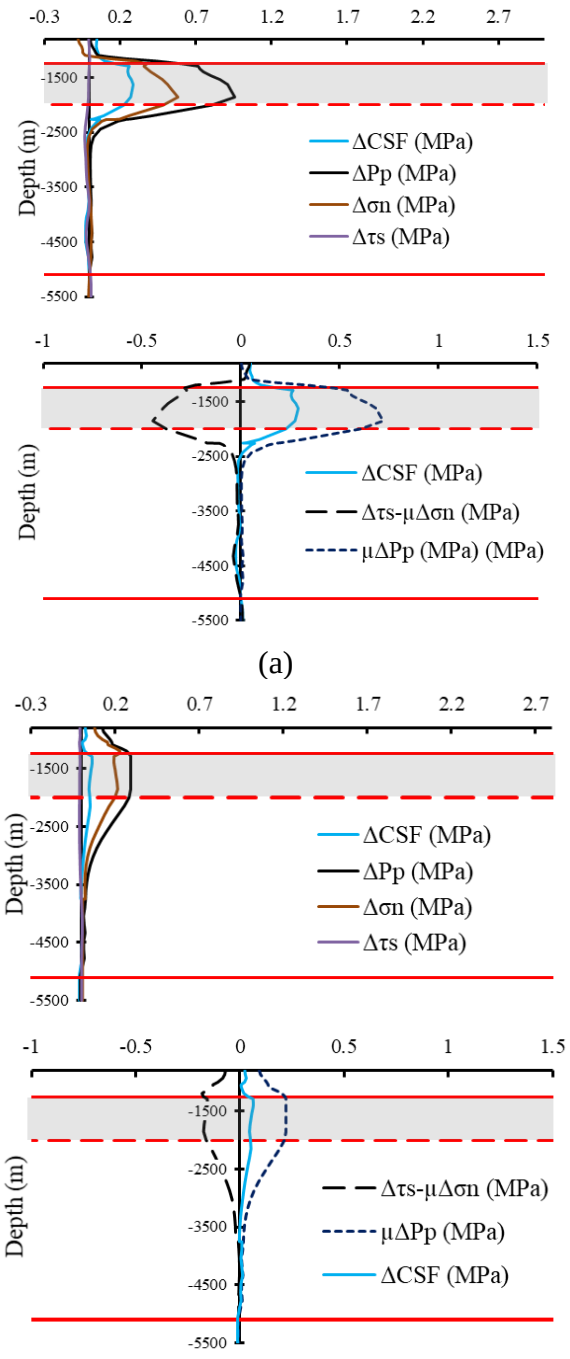
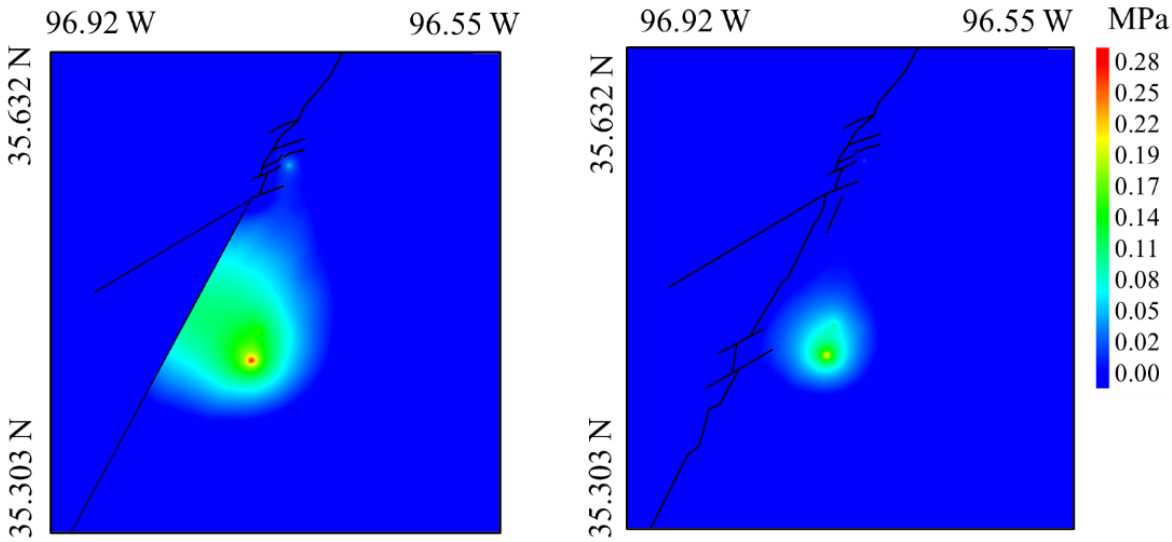


Figure 50: Scenario 1, case 2: Depth profiles of change of CFS (MPa), pore pressure (MPa), total normal stress (MPa), and shear stress (MPa) (Upper figure), and profile of change of poroelastic stress (MPa) and pore pressure (MPa) components of ΔCFS (Lower Figure) along the dashed line on the splay branch of Wilzetta fault plane along the cross-section W-w (Figure 45) in (a) Dec 2001 and (b) Nov 2011. Solid red lines are the fault boundaries. The red dashed line shows the lower boundary of the reservoir. (μ = 0.75)

4.5.2 Scenario 1- Cases 3 and 4: Impermeable and Permeable Faults with High Arbuckle Permeability

According to Equation 4.7 and considering permeability of Arbuckle group as 100 mD, more than 99.9% of saltwater enters into Arbuckle group. Our results show that in both cases 3 and 4 the pressure buildup is not high enough to induce instability on the Wilzetta fault. Figure 51 shows the pressure elevation at the end of 2011 at the depth of 1600 m in Arbuckle group for cases 3 and 4. In both cases, the injected water diffuses into Arbuckle group easily, and therefore the pressure buildup needed to reactivate the faults is not reached. These cases suggest there is an upper bound for the permeability of Arbuckle group above which the injected volume (reported by OCC) flows easily in the layer without significant excess pressure build-up, and accordingly without inducing seismicity.



(a) (b)

Figure 51: Scenario 1: The change of pore pressure (MPa) in Arbuckle group at depth of 1600 m in Nov 2011(after 12 years and 10 months of injection) for (a) case 3, and (b) case 4.

4.5.3 Scenario 2: Hydraulic Communication Between Geological Layers via Fault Damage Zones, Low and High Arbuckle Permeability

In this scenario, it is assumed that there is a damage zone adjacent to the faults through which the injected fluid penetrates the deeper depths (more than 4 km) where most seismic events were located. In the absence of mechanical and hydrological data for the area, we define different cases (Table 3). In cases 1 through 4, both permeable and impermeable faults with different Arbuckle group permeabilities of 10 mD and 100 mD were studied. In case 5, we include the permeability anisotropy of the geological layers and the fault zone. We assumed that there is an anisotropy with the ratio of vertical to horizontal permeability of 0.5, and study the effect of anisotropy on pore pressure distribution. In cases 6 and 7, we evaluate the possibility of the presence of the damage zone in only a portion and some splay branches of the Wilzetta zone (not the whole fault zone in cases 1 to 4).

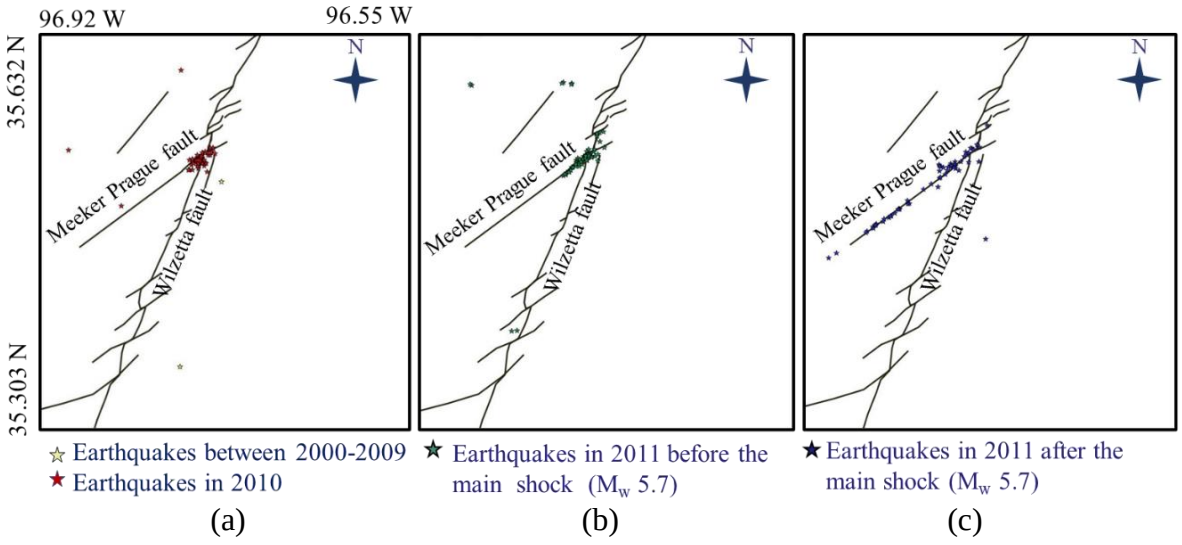


Figure 52: Earthquakes (a) between 2000 and 2010, (b) in 2011before the main shock (M_w 5.7), and (c) in 2011 after the main shock (M_w 5.7) (OGS, http://www.ou.edu/ogs/research/earthquakes/catalogs).

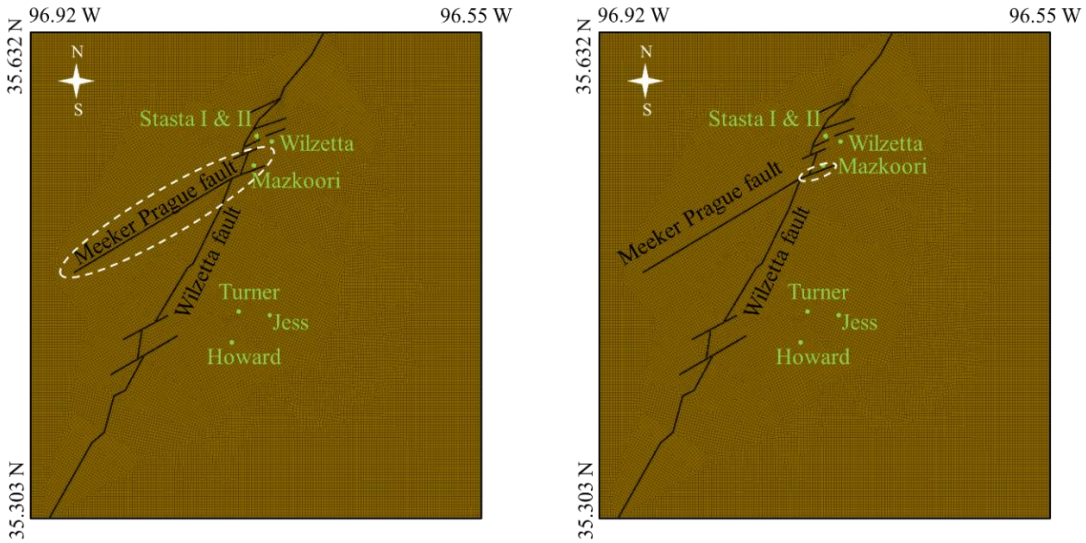


Figure 53: The damage zone exists only in a portion and some splay branches of the Wilzetta Fault in (a) case 6 and (b) case 7 of scenario 2. The white dashed line shows the portion and splay branches of the Wilzetta faults for which the damage zone is defined in the model. The locations of high-volume injection wells are shown by green dots.

Figure 52 shows the seismic events from 2000 to 2011. It can be seen that between 2000 and 2009, there is no event in the area of interest. In 2010 and 2011, there are many events near the Wilzetta and the Meeker Prague faults intersection. After the main event (M_w 5.7 on Nov 6, 2011), the events transferred to the southwest direction and occurred mostly on the Meeker Prague fault. This observation suggests a plausible scenario in which the damage zone exists only in a portion of the Wilzetta zone and some splay branches. During the years of injection, the induced pore pressure eventually triggers seismic events in both Arbuckle and the basement. Based on this scenario, we define cases 6 and 7 as shown in Figure 53. In case 6, it is assumed the damage zone exists only on the portion and some splay branches of Wilzetta fault as shown by the white dashed line in Figure 53a. In case 7, the damage zone is defined only on the splay branch of the Wilzetta fault zone that hosted the foreshocks (Figure 53b). In cases 6 and 7, the effect of the existence of the damage zone only around a portion of

Wilzetta fault on the pore pressure elevation and subsequent stress disturbance is studied. Our results indicate that the general responses are similar in different cases of scenario 2 although there are quantitative differences. Therefore, here we only present the results of case 7 in which the highest excess pore pressure is observed.

Figure 54 and Figure 55 show the pore pressure change at the end of 2001, 2005, 2010, and Nov 2011 in Arbuckle group at depth of 1600 m and on the splay branch of Wilzetta fault plane along the cross-section W-w for case 7 in scenario 2, respectively. It can be seen that injection induces a pore pressure up to 0.9 MPa in the area between northern and southern wells in both cases in Nov 2011 (Figure 54d). The maximum pore pressure increase of the splay branch of the Wilzetta fault plane along the cross-section W-w is 0.63 MPa after 12 years and 10 months of injection (Figure 55d). In this scenario, in contrast to scenario 1, the injected fluid diffuses into the deeper depths through the fault damage zone, and causes more pressure buildup in the fault zone around the basement, and less pressure elevation in Arbuckle group (Figure 55). The general pattern of change of pore pressure of Arbuckle group is the same as scenario 1, but with lower values, because the fluid may flow through the fault damage zone. In 2001, the pore pressure of the Wilzetta fault plane along the cross-section W-w has the highest elevation of 1.7 MPa at depth of 1150 m-1600 m. Similar to scenario 1, the operation of the Mazkoori well during 2000 and 2004 leads to the formation of a high-pressure zone on the splay branch of the Wilzetta fault plane along the cross-section W-w (Figure 55). This zone of high pressure vanishes gradually after Mazkoori well stops operation in 2004, and fluid diffuses into the whole fault damage zone. Eventually, the operation of the other injection wells keeps the pore pressure increase of the Wilzetta fault plane along the cross-section W-w to almost a constant value of 0.6 MPa. It should be noted that in

contrast to Scenario 1, due to the damage zone, the injected fluid penetrates deeper where the hypocenters of the main and most foreshock events are located.

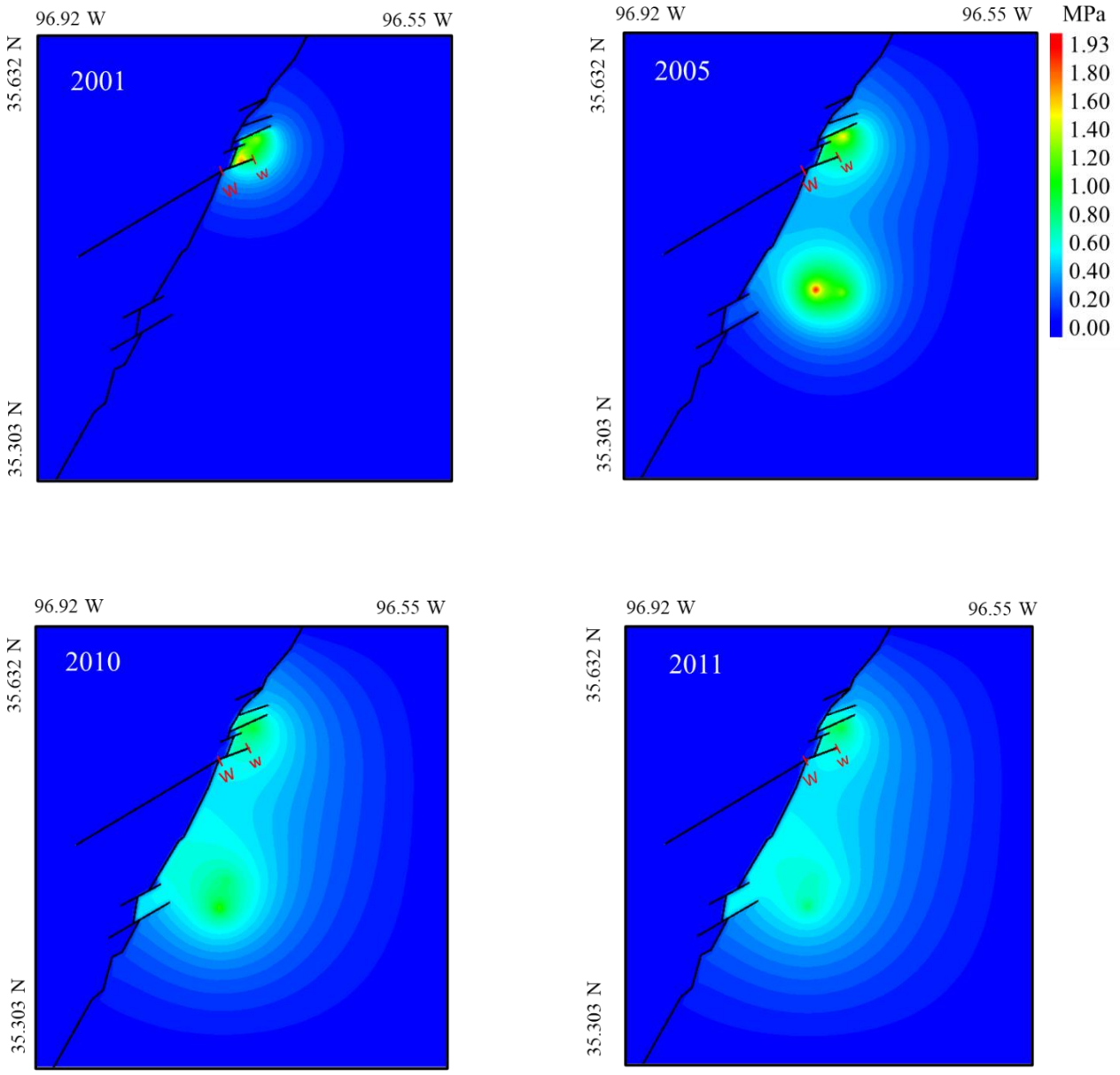


Figure 54: Scenario 2, Case 7: The pore pressure change (MPa) in Arbuckle group at depth of 1600 m at the end of 2001, 2005, 2010, and Nov 2011.

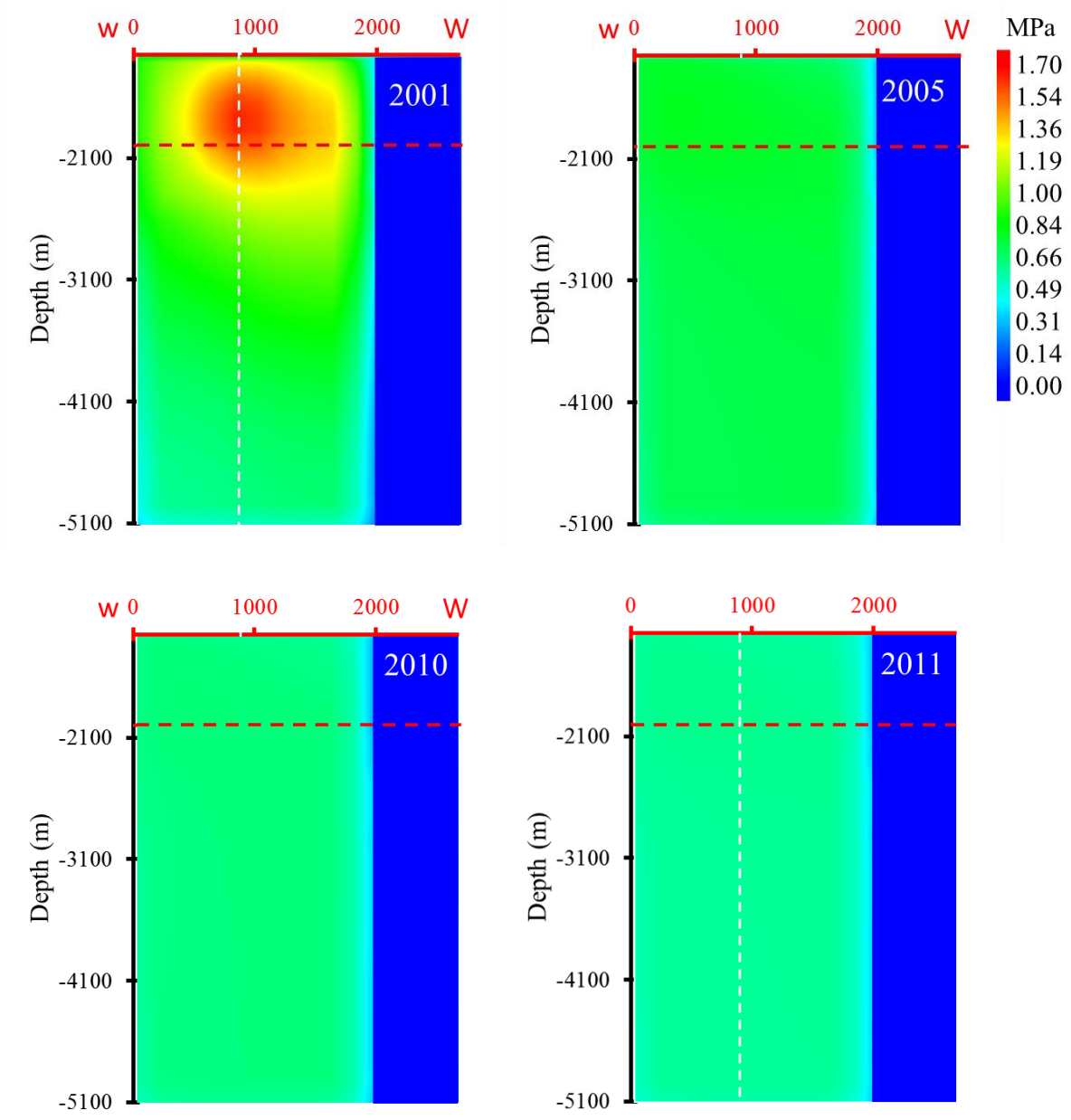
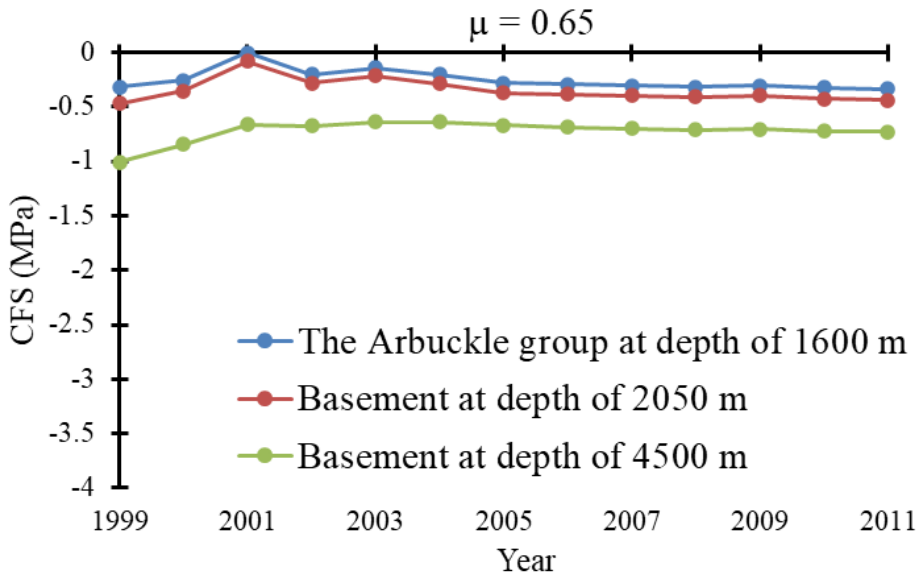
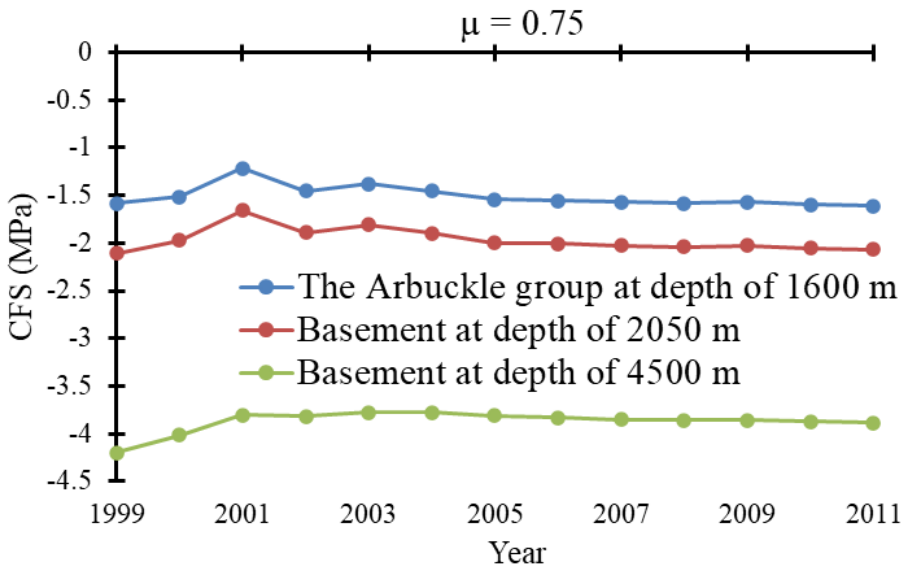


Figure 55: Scenario 2, case 7: The pore pressure change (MPa) on the splay branch of Wilzetta fault plane along the cross-section W-w in Dec 2001, 2005, 2010, and Nov 2011. The top and the lower boundaries of Arbuckle group are shown by the red solid and dashed lines, respectively. The white dashed line is the vertical line on the fault plane that has the shortest distance to the Mazkoori well.

Figure 56 shows the variation of CFS for three points located on the Wilzetta fault located on the white dashed line (Figure 55) at depths of the middle of Arbuckle, shallow basement, and deep basement. Our results show that the fault reactivation occurred in 2001 for a friction coefficient of 0.65, and it remains stable for the value of 0.75. It can be seen that similar to scenario 1, the CFS has the maximum value in 2001 due to the Mazkoori well operation. Also, the model shows an earthquake would first happen in Arbuckle group and shallow basement. In contrast to scenario 1, in the deeper depths and due to the fluid diffusion, CFS increases but still is not high enough compared to the shallower depths. It should be noted that these results are obtained assuming a uniform frictional property for the fault. Figure 57 shows the depth profile of variation of ΔCFS and its components along the white dashed line (Figure 55). It can be seen that in 2011 when the pore pressure is almost uniform on the fault plane, CFS increase is more in the deeper zones. This is because of the lower poroelastic process at depth.

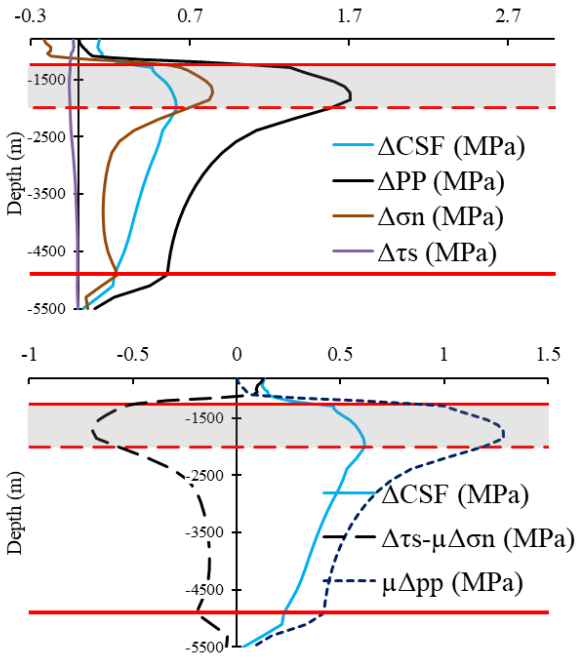


(a)

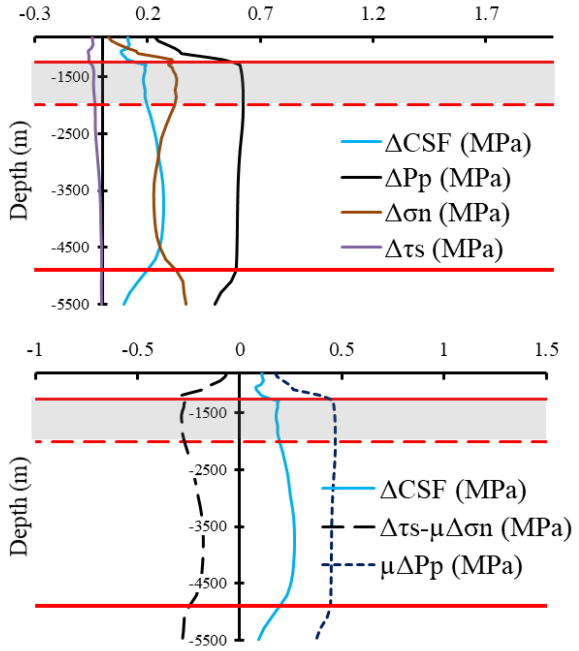


(b)

Figure 56: Scenario 2, case 7: Variation of CFS (MPa) at three points located on the fault plane along the dashed line on the splay branch of Wilzetta fault plane along the cross-section W-w (Figure 55) during simulation for (a) μ = 0.65 and (b) μ = 0.75. For the value of μ = 0.65, CFS becomes positive (fault failure) at depth of 1600m. The fault remains stable during injection for μ = 0.75. At all depths, the CFS has the maximum value due to Mazkoori well operation, and after 2005 remains almost constant.



(a)



(b)

Figure 57: Scenario 2, case 7: Depth profiles of change of CFS (MPa), pore pressure (MPa), total normal stress (MPa), and shear stress (MPa) (Upper figure), and profile of change of poroelastic stress (MPa) and pore pressure (MPa) components of ΔCFS (Lower Figure) along the dashed line on the splay branch of Wilzetta fault plane along the cross-section W-w (Figure 55) in (a) Dec 2001 and (b) Nov 2011. Solid red lines are the fault boundaries. The red dashed line shows the lower boundary of the reservoir. (μ = 0.75)

4.5.4 Scenario 3: Injection from Mazkoori and Wilzetta flows into an isolated compartment

It has been shown that in some cases in scenarios 1 and 2, injection causes elevation of the pore pressure in the reservoir which remains for many years (even though the eastern side is infinitely open) as observed in the previous studies (Hsieh and Bredehoeft, 1981, Keranen et al., 2013). Both scenarios 1 and 2 show that the injected volume can cause instability on the Wilzetta fault in 2001, i.e., almost 10 years before the 2011 sequence. Therefore, it can be concluded that neither scenarios 1 and 2 can explain the 2011 seismic events.

This strengthens the possibility that in this problem there is an isolated volume where the injected fluid increases the pore pressure which eventually results in reactivation of the fault. In this scenario, we assume that there is another boundary on the eastern side of the Mazkoori and Wilzetta wells (marked by the white dashed line in Figure 58). We also assume that there is a damage zone as that of case 7 in scenario 2. Therefore, in contrast to the previous scenarios, the total volume of injected fluid by Mazkoori and Wilzetta wells diffuses into a bounded volume and causes a continuous increase of the pore pressure. The increase of pore pressure at a depth of 1600 m in Arbuckle group and on the fault plane along the cross-section W-w are shown in Figure 58 and Figure 59. The pore pressure increases continuously till it reaches its maximum of 4.25 MPa in 2011. The pore pressure increases continuously till it reaches its maximum of 4.25 MPa in 2011. On the fault plane along the cross-section W-w, this value is 4 MPa, and has a pattern different from the previous scenarios. It is obvious that even though the Mazkoori well operation finished at the end of 2004, the pore pressure of the fault continues to increase due to the operation of the Wilzetta well.

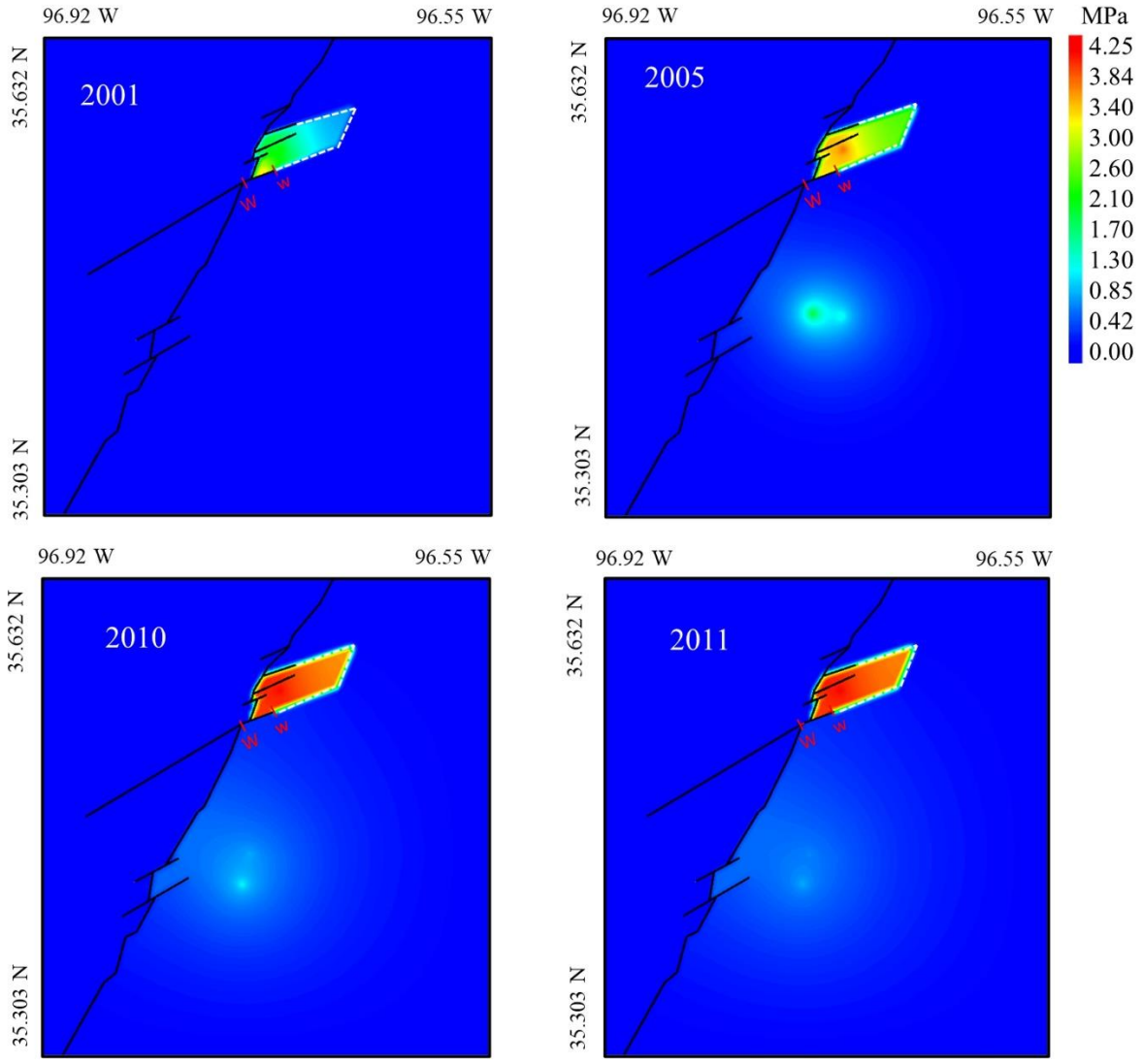


Figure 58: Scenario 3: The pore pressure change (MPa) in Arbuckle group at depth of 1600 m in Dec 2001, 2005, 2010, and Nov 2011. Since injection is performed in a bounded area, in contrast to previous scenarios, the pore pressure increases continuously.

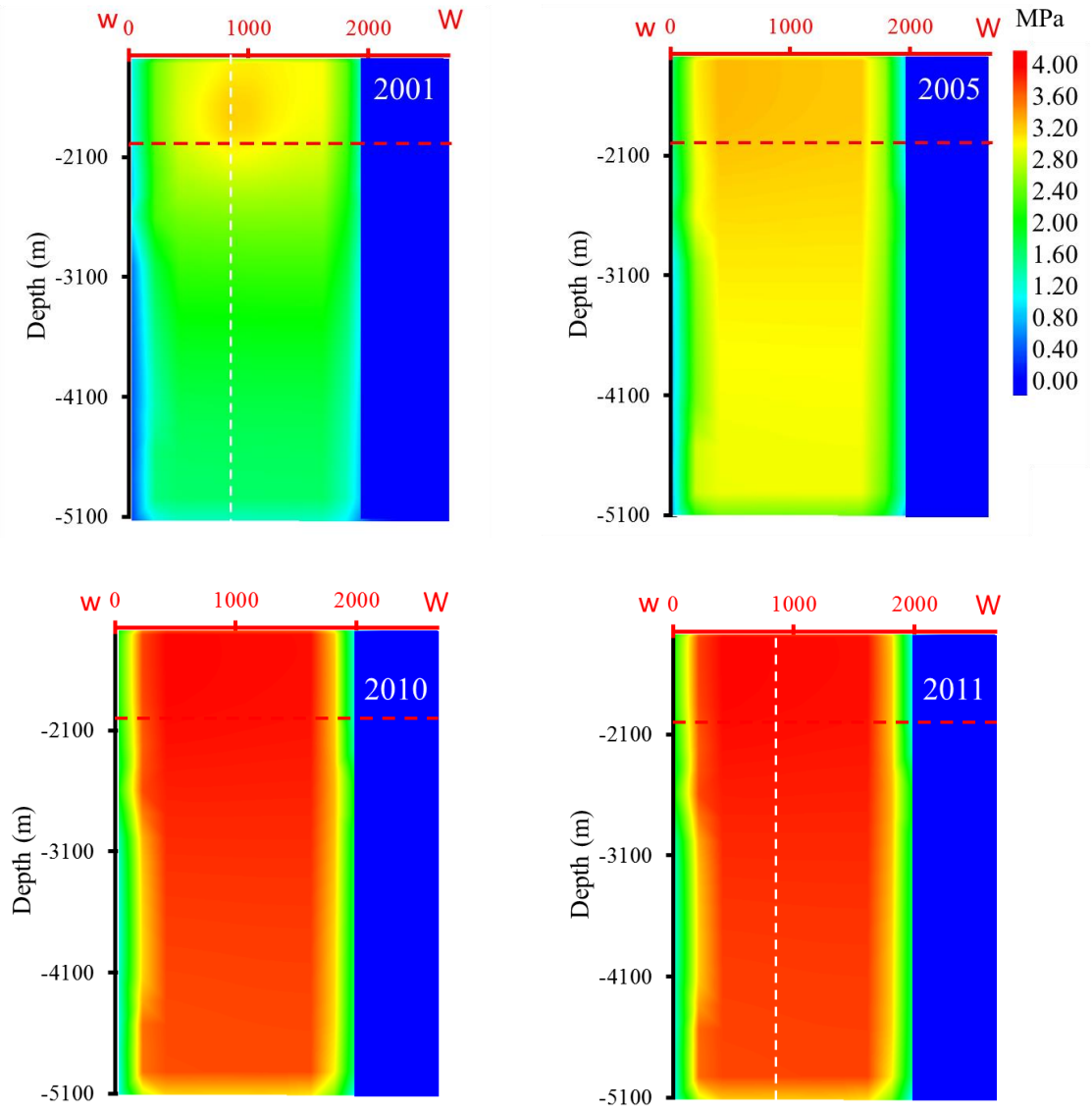


Figure 59: Scenario 3: The pore pressure change (MPa) on the splay branch of Wilzetta fault plane along the cross-section W-w in Dec 2001, 2005, 2010, and Nov 2011. The top and the lower boundaries of Arbuckle group are shown by the red solid and dashed lines, respectively. The white dashed line is a vertical line on the fault plane that has the shortest distance to the Mazkoori well.

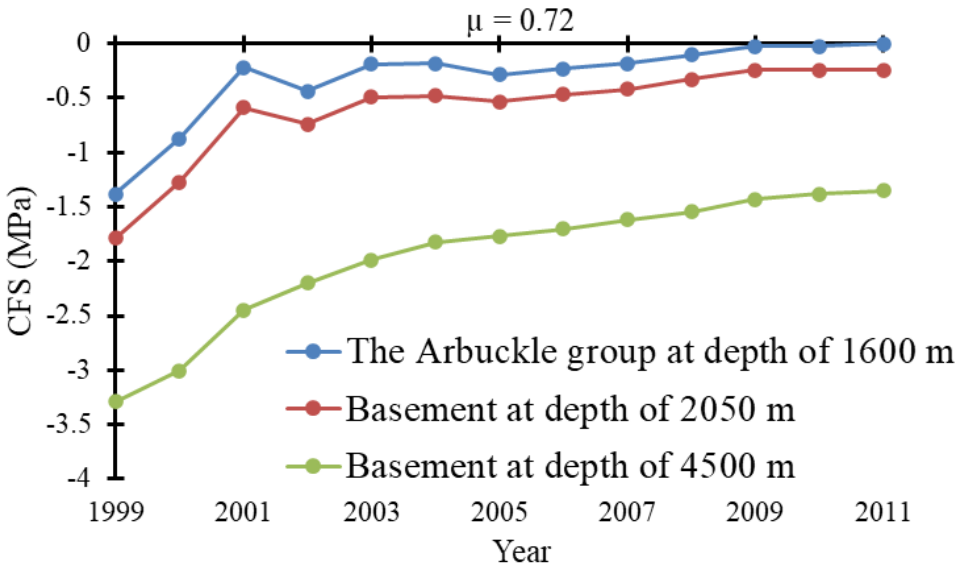
The pore pressure increases continuously until it reaches its maximum of 4.25 MPa in 2011.

On the fault plane along the cross-section W-w, this value is 4 MPa, and has a pattern dif-

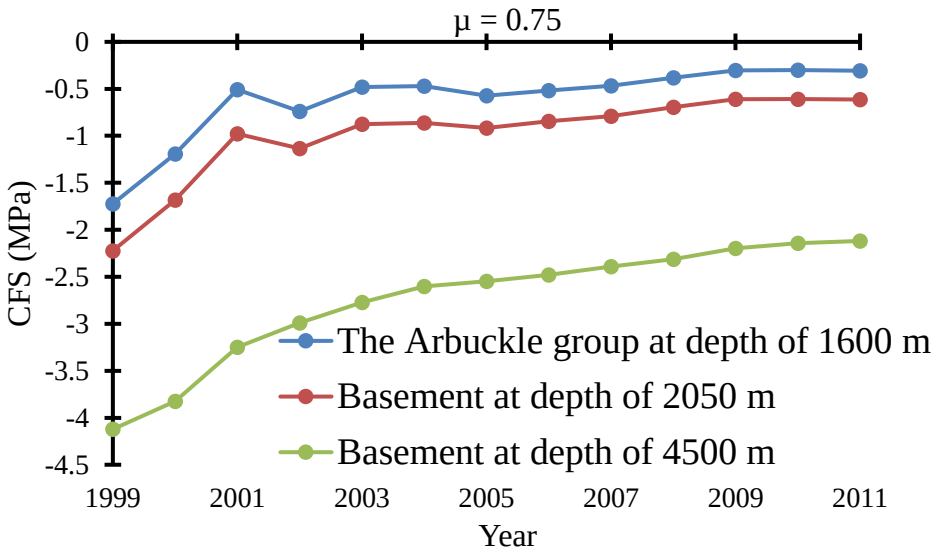
ferent from the previous scenarios. It is obvious that even though the Mazkoori well operation finished at the end of 2004, the pore pressure of the fault continues to increase due to the operation of the Wilzetta well.

Figure 60 shows the variation CFS during the years of simulation at depths of 1600m, 2050 m, and 4500 m located the white dashed line on the fault (Figure 59). It can be seen that CFS at depths of 1600 m and 2050 m has some fluctuation due to the activity of Mazkoori well, and after 2005 increases continuously. In contrast, CFS increases continuously with a greater slope at a depth of 4500 m. Figure 61 shows the profile of the changes of pore pressure and normal stress and shear stress on the fault plane along the cross-section W-w (shown by the white dashed line in Figure 59).

It can be seen that the normal stress increases due to the poroelastic effect when the pore pressure is increased. This increase is more pronounced in Arbuckle layer, and less in the deeper depths. Shear stress has less change compared to normal stress. In the late years of the history of injection, the pore pressure increase is more uniform on the fault plane than in previous years, but in contrast, the changes of normal and shear stresses are not uniform. This results in more increase of the CFS at a deeper depth than Arbuckle group and shallower depths at the basement. Figure 60 reveals that although CFS increases at a higher rate in the deeper depths than shallower ones, still values of CFS in the shallower depths are greater than those in the deeper depths. Therefore, fault reactivation happens at the shallower depths. It should be noted that this conclusion is due to the assumption of a uniform coefficient of friction. Therefore, for example, a greater coefficient of friction for sallower depths, and a lower one at the deeper depths can explain the 2011 sequence spatiotemporally.



(a)



(b)

Figure 60: Scenario 3: Variation of CFS (MPa) during simulation for (a) μ = 0.72 and (b) μ = 0.75. The CFS becomes zero in 2011 at depth of 1600 m for μ = 0.72. In contrast to scenarios 1 and 2, CFS continues to increase at all depths. Due to the poroelastic effect at greater depths, the rate of CFS increase is higher than shallower depths.

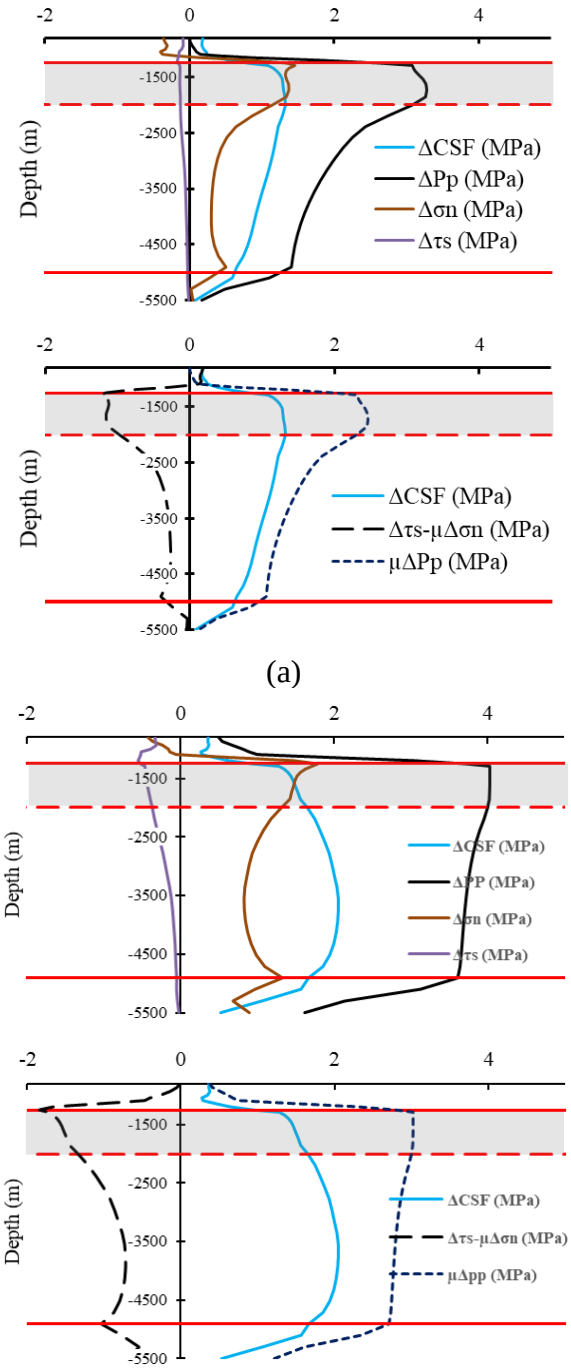


Figure 61: Scenario 3: Depth profiles of change of CFS (MPa), pore pressure (MPa), total normal stress (MPa), and shear stress (MPa) (Upper figure), and profile of change of poroelastic stress (MPa) and pore pressure (MPa) components of ΔCFS (Lower Figure) along the dashed line on the splay branch of Wilzetta fault plane along the cross-section W-w (Figure 59) in (a) Dec 2001 and (b) Nov 2011. Solid red lines are the fault boundaries. The red dashed line shows the lower boundary of the reservoir. (μ = 0.75)

4.6 Discussion

There are five high-volume wells (Stasta wells are not high-volume wells compared to the other wells, Table 5) in our model among which the Mazkoori and Wilzetta wells have the smallest distance to the Wilzetta fault. The Mazkoori well is located within less than 200 m of the portion of Wilzetta fault on which the 2011 sequence was located, and therefore has the greatest effect. Wilzetta well has a less but still notable effect on the fault, and Hess, Turner, and Howard wells have insignificant effects on the fault plane pore pressure. It should be noted that the Mazkoori well (the closest well to the fault) operation started in 2000 and ended in 2005 (six years before the 2011 earthquakes). Therefore, there should be a process to explain almost a decade of delay between the start of injection and the 2011 events.

Our model results show that the injected fluid must penetrate the basement via a damage zone to cause fault reactivation at larger depths. In the absence of such a path, although the poroelastic stress change tends to favor fault reactivation in the deep basement, its magnitude is small so that a very near critical fault state would be needed to induce seismicity. In scenario 1 in which there is no such a path, we evaluated this condition. In this scenario, fluid does not penetrate the deep basement and diffuses only into the target layer. In cases with permeable faults, fluid flows in all directions while in cases with impermeable faults, it flows only in the eastern direction. In the deep basement, where there is no fluid diffusion, the normal stress is reduced by the poroelastic effect and tends to reduce the stabilizing normal stress on the fault. This reduction in normal stress (poroelastic effect) is small to cause the reactivation of basement fault that already are not in a near-critical condition. Still, the injected fluid by high-volume wells, and especially to a greater extent by the Mazkoori well,

causes fault reactivation in 2001 which does not agree spatiotemporally with observation (2011 earthquakes).

There is a damage zone in scenario 2 around the fault through which fluid penetrates into the deeper levels. To include different plausible situations, we investigated many cases in which there is a damage zone around the fault. In the most critical case (case 7), the pore pressure diffuses to the deep basement and is accompanied by an increase of normal stress (poroelastic effect) which tends to stabilize the fault, but still, stability is affected mostly by the direct pore pressure diffusion process and is high enough to induce fault reactivation. The general trend of failure potential variation is, however, similar to scenario 1 and fault reactivation happens 10 years before the 2011 sequence in 2001 (due to operation of Mazkoori well) in the Arbuckle group and shallow basement.

In the third scenario, in contrast to other scenarios, we assume that there is an effectively sealed compartment into which Wilzetta and Mazkoori were injected. We assume the isolated compartment is bounded by the Wilzetta fault (all directions but the eastern side), and define a boundary for the eastern side. Therefore, the reservoir-bounding faults consist of the Wilzetta faults and a fictitious boundary on the eastern side. Our simulations suggest that injection-induced fault instability is plausible in 2011 at shallow basement and Arbuckle group. So, in this scenario, in contrast to others, the simulation results have a good agreement with observations in terms of the time of induced events. Our simulations suggest that the maximum fault tendency for failure occurs at depths of 3.6 to 3.8 km. Comparing these values with the depth of the main foreshock from OGS (3.4 km) suggests that the model is in general agreement with field data. The difference of 0.2 to 0.4 km between the real event

locations and our model is not highly significant in view of all of the uncertainties in parameters, and the simplifying assumptions used. For example, assuming a uniform frictional property for the fault can contribute to the discrepancy between the model results and field observations (assuming they are 100% accurate). The results show that failure and seismicity potential increase with a higher rate in the deeper basement (compared with Arbuckle group and shallow basement) due to a relatively lower increase of the normal stress (poroelastic effect). This scenario reveals that it is unlikely that injection was performed in an infinitely open or semi-restricted reservoir (Wilzetta fault) even with a damage zone, and there must be a fault-bounded compartment to create geomechanical conditions conducive to an earthquake in 2011.

4.7 Conclusion

Three earthquakes with M_w of 4.8, 5.7, and 4.8 occurred in November 2011 within the North American midcontinent near Prague, Oklahoma, the United States at the depth of ~3.5 km to 5km. We have carried out a study to simulate the potential contribution of disposal wells to pore pressure and stress perturbations in the fault zone under different permeability structures. In particular, we have constructed a coupled fluid-mechanical geomechanical model to study the effect of saltwater injection on the fault reactivation and earthquake sequence in November 2011 based on end-member values for permeability and fault structure. We constructed three main scenarios. In Scenario 1, we assumed that there is no hydraulic communication between formation layers that are subjected to injection. In contrast, a damage zone that acts as a path for fluid to penetrate the deeper depth is considered in Scenarios 2 and 3. We especially pay attention to the part of the Wilzetta fault where 2011 foreshocks started, and address the question if the pore pressure elevation is capable to cause instability on the

fault plane. The following conclusions can be drawn from our simulation: (1) When there is no communication of wastewater between Arbuckle group and the crystalline basement (e.g., through a damage zone around faults) and the Wilzetta fault is the only barrier to fluid flow (semi-restricted reservoir), the fluid penetrates only to a shallower depth (3.5 km after 11 years of injection). This causes a small destabilizing poroelastic stress in the deeper basement, but this is not sufficient to reactivate the fault. The shear stress change is insignificant compared to normal stress change. The model suggests a fault reactivation in 2001 at shallow basement and the reservoir which is not agreeable with reality (2) When there is a damage zone through which the fluid penetrates the basement and for either a semi-restricted zone or an infinitely open one, the fluid penetrates deeper basement zones causing a normal stress increase on the fault plane. Yet, the simulation shows the pore pressure increase to be enough to reactivate the fault in 2001 at shallow basement and in Arbuckle group. Again, this does not agree with what happened in the 2011 sequence. (3) In scenario 3, in contrast to other scenarios, it is assumed that the injection zone is not semi-restricted and the fluid is pumped into a fully bounded volume. The simulation for this scenario shows a continuous increase of pore pressure which eventually leads to fault reactivation in 2011 which is in good agreement with reality. The poroelastic stress increases the tendency of fault reactivation at a relatively deeper zone of 3.6 to 3.8 km whereas, the actual main foreshock occurred at a depth of 3.4 km. This suggests that our model reflects the general response of the Wilzetta fault zone to the injection well, and some idealization and assumptions cause this difference.

Overall, the numerical results show that the volume of injection is sufficient to lead the fault reactivation based on the reported in-situ stress magnitudes, and fault (Wizletta and

Meeker-Prague faults) geometry and hydromechanical properties of different layers. However, modeling idealization of the subsurface conditions causes a discrepancy between the time of occurrence of instability and potential seismicity in numerical simulations. Oklahoma basement rocks can become seismically unstable under in-situ depth conditions of temperature, pressure, and water saturation of 3–6 km at depth, and tend to slip unstably rather than creep (Kolawole et al. 2019). More data regarding the fault systems and the geological units and their hydrological properties are needed to enable a more accurate analysis to help improved and management of the injection operations to minimize risks.

Application of Coupled Discrete Element Model

5.1 Numerical Analysis of Shear Stimulation and Permeability Enhancement in Granite

5.1.1 Introduction

Permeability of tight hydrocarbon reservoirs and Enhanced Geothermal Systems (EGS) sites are enhanced via injection by different processes: (1) formation and opening of new fractures (hydraulic fracturing) and (2) shear slippage of natural fractures. Typically, in EGS, the main mechanism of stimulation is assumed to be induced dilatant slip on preexisting fractures while in oil and gas reservoirs, the mechanism of stimulation is opening and propagation of new fractures. Although many studies have been conducted on the shear stimulation process, there are still many ambiguities in the mechanism and controlling factors of the shear stimulation process.

Injection in the rock mass elevates pressure in rock pores and fractures, and induces shear slippage by reducing the effective stress. This slippage, most of the time, is accompanied by a phenomenon called self-propping which causes the enhancement of the ability of slipped fractures to transfer fluid flow. Understanding the permeability evolution via shear stimulation requires a deep knowledge of the physical process behind such a phenomenon. Experiments and numerical models are useful means to shed light on such a complicated process. Most experimental tests which addressed the dilatant shear slip have been performed by inducing slippage mechanically, and not by injection. Yu and Ghassemi (2018) developed and performed a novel test in which shear slip is induced by injection directly, and followed by stress relaxation. This test was the first experimental test that is able to model the whole shear stimulation process under reservoir conditions that are likely faced in EGS projects including the permeability enhancement before and after a shear slip, stress relaxation, effect

of fracture surface damage, etc. Numerical modeling of the experiment can be useful to understand better the mechanism and physical process during the.

This study provides the results of a numerical hydro-mechanical coupled model of the shear stimulation test based on the experimental results from Reservoir Geomechanics and Seismicity Research Lab (RGSRG Lab) at the University of Oklahoma (Yu & Ghassemi, 2017, 2019). The numerical model is carried out using 3DEC, a discrete element software (3DEC, Itasca, 2016), for Sierra White granite test to study the response and mechanism of the rock. First, by assigning an effective aperture to the fracture, we studied the mechanism of the permeability evolution and the extent of the retained enhanced permeability. Second, using the real topography of the fracture surface (imported to the model from laser results) and calculating the aperture on the fracture, we performed the same numerical model to study the effect of fracture roughness on the mechanics of the shear stimulation process.

5.1.2 Motivation and Objectives

To reproduce shear stimulation process which results in improvement of fluid flow in tight reservoirs and EGS sites a series of novel experiments were performed on granite and shale samples at RGSRG Lab at the University of Oklahoma. The results shed light on the shear processing for both before and after shear slip, and are useful to understand the relationship between different factors such as shear and normal effective stresses on the fracture, shear and normal displacements, dilation, and self-propping phenomenon. In an effort to better understand the mechanism of the test, a numerical model is carried out using the concepts of mechanics of the fracture and rock, and fluid flow inside the fractures. Here are some of the main objectives of this work:

• To learn the mechanism of the permeability enhancement during the injection of fluid into fractures and the impact of shear dilation on the permeability enchantment

• To study the retained enhanced permeability of a sheared fracture

• To evaluate the role of the fracture surface topography on the fluid flow and mechanism of the shear stimulation

5.1.3 Literature Review

Tight oil/gas shale reservoirs and Enhanced Geothermal System (EGS) sites generally are characterized by very low permeability formations. A common practice to improve the capability of the formation to transfer fluid is shear stimulation or hydroshearing. In contrast to the hydraulic fracturing (fracking) operation, in hydroshearing operation, the injected fluid pressure is kept below the minimum principal stress magnitude and close to the pressure required to induce dilated frictional shear slip. This dilated shear slip causes a mismatch of asperities and creates additional void space between the fracture walls resulting in enhancement of transmissivity of the fracture, a mechanism called "self-propping' (Barton, 1985; Esaki et al. 1999). The enhancement of permeability of natural fractures is permanent (during the production time scale) even after pressure decline. Fractures in brittle rocks are more proper for self-propping (Lutz et al. 2010). After a slip, the creep of asperities can cause the time-dependent loss of enhanced permeability of natural fractures. This can likely occur in clay-rich rocks.

For the first time, in early 1980, hydroshearing was confirmed and developed by Pine and Batchelor (1984). They reported that the major process after injection of a massive volume of fluid is not formation and opening of new fractures (hydraulic fractures) but is a shearing slip of well-oriented natural fractures. They described that the formation of downward

microseismic events caused by injection is due to shearing mechanism which in turn is caused by the local ratio of maximum to minimum principal effective stresses. Hydroshearing occurs when the fluid reduces the effective normal stress on the fracture planes, and causes the frictional slippage before fracture propagation. The observed microseismic events during injection into subsurface at the Cornwall hot dry project in Carnmenellis granite illustrated strike-slip shear slips which are in agreement with the orientation of the natural joints and in situ stress state. An early investigation n on the change of the fracture conductivity caused by fracture normal and shear displacement was performed by Makurat et al. (1990) at the Norwegian Geotechnical Institute. They used a biaxial cell for coupled shear-flow-temperature testing on a rough natural joint. Under controlled normal stress conditions, the joints were closed, sheared, and dilated, and water with different temperatures was flushed through the joint. They reported that a high joint compressive strength to normal stress ratio (JCS/σn) and a distinct joint roughness morphology can cause small shear displacements which are enough to induce dilation in joints and improve the fluid conductivity by two to three orders of magnitudes. They also reported that although compliant rocks show dilation during shearing, the main controlling factor is joint roughness coefficient (JRC) values. They noticed that with ongoing shearing, the conductivity improvement decreases as gouge formation. This gouge material distorts the parallel plate analogy by blocking the fluid flow paths.

Shear stimulation has been applied in many EGS projects (e.g. Hijoiro and Ogachi, Japan, Soultz-sous-Forêts, and Cooper Basin in Australia, etc (Tester 2006, Ziagos et al. 2013)) and hydrocarbon production projects (e.g. Rutledge, Phillips et al. 2004, Maxwell et al. 2002, etc). During the last 30 years, the experience has been gained from the shear stimulation

process in different projects reveals the need for further analysis of this phenomenon to understand the mechanism and controlling variants of hydroshearing process. At the beginning of the EGS experience, the flow from the wellbore was localized and the microseismic events did not align on a planar feature perpendicular to the minimum principal stress (Pine and Batchelor 1984). Many authors proposed other models to justify the observation (Mur-phy and Fehler, 1986), but the shear stimulation concept (Pine and Batchelor 1984, Tester 2006, Ito Hayeshi 2003) was recognized.

Many experiments (Ye and Ghassemi 2018, 2019, Bauer et al. 2016, Hu and Ghassemi, 2019, etc) and numerical studies (Kohl and Hopkrik 1995, Bruel 1995, Jing et al 2000, Rahman et al. 2002, Kohl and Megel 2007, Rachez and Gentier 2010, Zhou and Zhou Ghassemi 2011, Riahi and Damjanac 2013, Bauer et al, 2016, Ye et al. 2018, etc, Cheng et al 2019, Verde and Ghassemi 2015) have been performed to improve our knowledge of EGS stimulation processes. The most used method to simulate this process is construction of a model in which a fracture network is generated stochastically, and accordingly, the hydroshearing is simulated.

Kelkar et al. (2012) utilized software code FEHM (Finite Element Heat and Mass transfer) which was originally developed to simulate fluid flow in the Hot Dry Rocks geothermal reservoirs. FEHM is a continuum code, and is based on the control volume finite element approach, capable of handling non-isothermal, multiphase, multi-component fluid flow, heat transfer, and chemical transport in dual-porosity, dual permeability media on unstructured grids. The reported three stages of stimulation progression during hydroshear stimulations involve relatively cool water by comparison of the numerical results and data from the Desert Peak EGS stimulation. In Stage I, the system responds as the permeability and fluid

properties are fixed. In Stage II, the injection rate raises at constant pressure in response to the stress dependence of permeability. Both Mohr-Coulomb failure and injection-induced cooling of the formation are responsible for this stage. In stage III, fluid continues to increase at a lower rate. Dempsey et al. (2013) used the same simulator to model the shear simulation of the Desert Peak EGS, and could capture the timing and magnitude of infectivity increases. Koyoma et al (2006) investigated fluid flow anisotropy in a single rock fracture during a shear process is using FEM modeling, considering evolutions of aperture and transmissivity with shear displacement history. They utilized the digitalized surfaces of a rock fracture replica to produce distributions of fracture aperture during shearing. They performed it by numerically manipulating relative translational movements between two surfaces of the fractures. They also used the fractal approach to investigate the scale dependence of fluid behavior. The author showed that the fracture aperture increase during shearing is an anisotropic change, and is more noticeable in the direction perpendicular to the shear displacement leading to considerable fluid flow channeling effect researchers.

Weng et al. (2015) investigated induced shear stimulation cussed by fracturing fluid lead off to natural fractures. The authors evaluate analytically the shear-slip condition and its propagation along a natural fracture under remote normal and shear stresses when it is exposed to the fluid pressure in a hydraulic fracture. They used a 2D coupled displacement discontinuity numerical model and illustrated rock stress anisotropy, initial natural fracture conductivity, and fluid properties on the evolution of the fluid and slip fronts along the natural fracture and the associated permeability enhancement.

Cheng et al. (2018) used PFC2D, a discrete element code, to simulate the shear behavior of rock joints with variable roughness and sand infilling thickness. Rock joint roughness is

evaluated by the joint roughness coefficient (JRC), and sand infilling thickness is evaluated by a thickness ratio (i.e., a ratio of infill thickness to rock height) ranging from 0.02 to 0.20. The authors showed that peak shear strength decreases with the thickness ratio with a hyperbolic relation, and also measure the permeability evolution during shearing and find that the permeability of infilled rock joints increases with both the thickness ratio and JRC.

5.1.4 Problem Setup

The numerical simulation aims to study the physical process and mechanism during which a fracture undergoes dilatant shear slip leading to the fracture permeability enhancement. The numerical model setup and dimension are shown in Figure 62 and Table 8, respectively. We constructed a three-dimensional coupled discrete element model to simulate the experiment that addressed hydroshearing phenomenon in Sierra White granite (Ye et al. 2017, Ye & Ghassemi 2018). Mechanical properties of the samples are shown in Table 9 (obtained from the experiment in the RGSRG Lab). Hydromechanical properties of the fracture that determine the fracture coupled fluid-mechanical response to fluid injection are shown in Table 8. The test setup is composed of a rock sample and two platens. The sample has a fracture and two wells: injection and production wells. Since the interaction between testing machine and the rock sample is not considered in this study, it is assumed that the platens rigid and there is no friction between the sample and the platens. During the test, the injection pressure is kept bellow the confining pressure (the minimum principal stress).The test procedure includes stepwise increase of the injection pressure from 5 MPa to the pressure required to induce slip on the fracture. At each target injection pressure (step), the simulation

is continued till the steady state flow regime condition is reached. Both injection and production volume rates have similar values after the model reaches the steady state flow regime, and this volume rate is reported as the flow rate at each injection pressure.

To reach the initial and boundary conditions of the experiment, the following steps should be performed. First, a confining pressure of 30 MPa is applied on the external surface of the sample by fixed traction normal to grids on the sample external surface. The pore pres-sure for both injection and production is set to 5MPa, and we let the system reaches equilibrium. After reaching equilibrium, the sample is loaded by moving the lower platen upward while fixing the upper platter. After the axial stress reaches the desired value, the lower platen is fixed too. This experimental setup had the advantage of capturing stress re-laxation after slippage on the fracture.

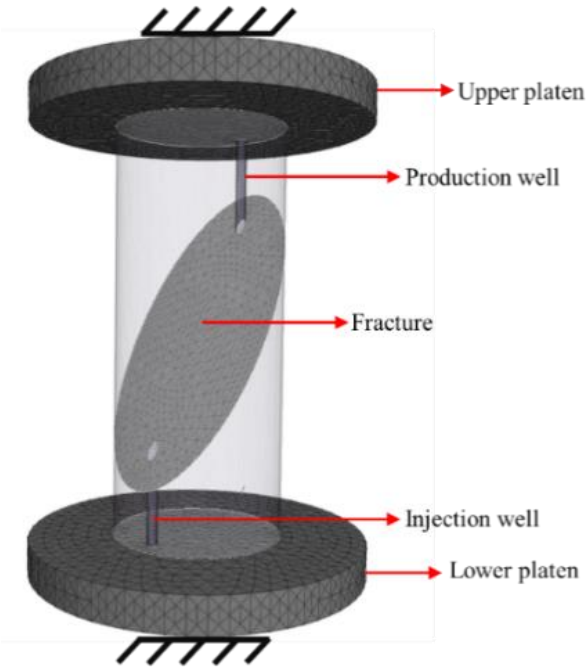


Figure 62: The setup of numerical simulation. The BC is applied in three stages. First, a constant confining pressure is applied on the external surface of the sample by normal traction on each gridpoint. Second, by applying initial pressure on both wells, the fracture pressure is uniform and constant. Then, by fixing the upper platen and moving the lower platen, the desired axial stress is generated in the sample. Finally, in the last stage, the upper platen is fixed.

In 3DEC, the fluid flow timestep is calculated by the size of the blocks (and their finite difference elements) and the permeability of the fracture and rock matrix. The model has elements in the order of 10^{-4}-10^{-3} m resulting in a very small timestep (order of 10^{-7}). With this value of timestep, it is very time-consuming to conduct the simulation in real-time similar to the experiment. Since in this study, we are interested in the steady-state condition (and not transient), it is possible to conduct modeling with this small time step and capture the response of the system without the need to conduct the numerical model in the experiment time scale. The method by which Ye and Ghassemi (2019) estimated the normal and shear displacements on the fracture is different from the method we use in this study. Here, we calculate these values by taking an average of the shear and normal displacements among all gridpoints.

Table 8: Fracture mechanical and hydraulic properties (after calibration) of Sierra White granite.
***Angle is measured from the long axis of the sample**
****The values shear and normal stiffness are not constant and are stress-dependent.**

	Sierra White granite
Length (mm)	120
Diameter (mm)	50
Fracture angle (°)*	50
w_{zero} (μm)	67
w_{max} ((μm)	5
w_{res} (μm)	0.01
JRC	150
Normal stiffness, k_n (Pa/m)**	3×10^{13}
Shear stiffness, k_s (Pa/m)**	2×10^{13}

Table 9: Mechanical and hydraulic properties of Sierra White granite (all values were measured at The Halliburton Rock Mechanics Laboratory at The University of Oklahoma)

	Sierra White granite
Young's modulus, E (GPa)	67
Poisson's ratio, ν	0.32
Tensile strength (MPa)	11
Uniaxial compressive strength (MPa)	150
Permeability (m^2)	5×10^{-19} - 10^{-18}
Joint frictional angle, φ (°)	41-51

5.1.5 Calculation of Hydraulic Aperture from the 3-D Scanning Contours of the Two Surfaces of Fractures

Ye and Ghassemi (2018 a, b) measured the topography of the fracture surfaces of the Sierra White granite samples using a 3-D laser scanning system (model #CMDM88), with a 2-μm resolution laser beam. The output of the scanning system includes more than 40000 sets of xyz where x, y, and z are the long axis (length), the short axis (width), and the fracture asperity, respectively. The color scale in the contour indicates the distance between the point and the lowest point of the fracture surface. The real scanning area of the fracture surfaces is not perfectly elliptical and is a little larger than the contours. So, they cropped the elliptical contours to avoid any boundary effect. Since the measurements of each fracture surface were carried out separately, it is not possible to match the corresponding points on two fracture surfaces precisely. Another factor that makes it impossible to precisely match two fracture surfaces is that the surfaces were cropped, so the origin of the axis is not precise. Each fracture surface has an xyz data file contains more than 40000 data, and needs to be organized to match with the other surface. In this study, both fracture surfaces are divided into small areas (the finer area results in better estimation of asperities), and the average value of asperities within each area is calculated. These average values represent the asperity of each

area by which the hydraulic aperture can be calculated. In the following, the process of the hydraulic aperture calculation is explained in detail.

Assuming that a matched xyz data set for both fracture surfaces (top and bottom) is available. For each point (x,y), there are two values of z (each belongs to the top and the bottom surfaces) indicating the distance of the point from the lowest point of the fracture (Figure 63). Using xyz data, the aperture can be evaluated as :

$$w(x,y,z) = d - z_1(x,y) - z_2(x,y) \quad (5.1)$$

Where d is the maximum value of z_1+z_2 among all points (i.e. all the x and y) on the fracture surface.

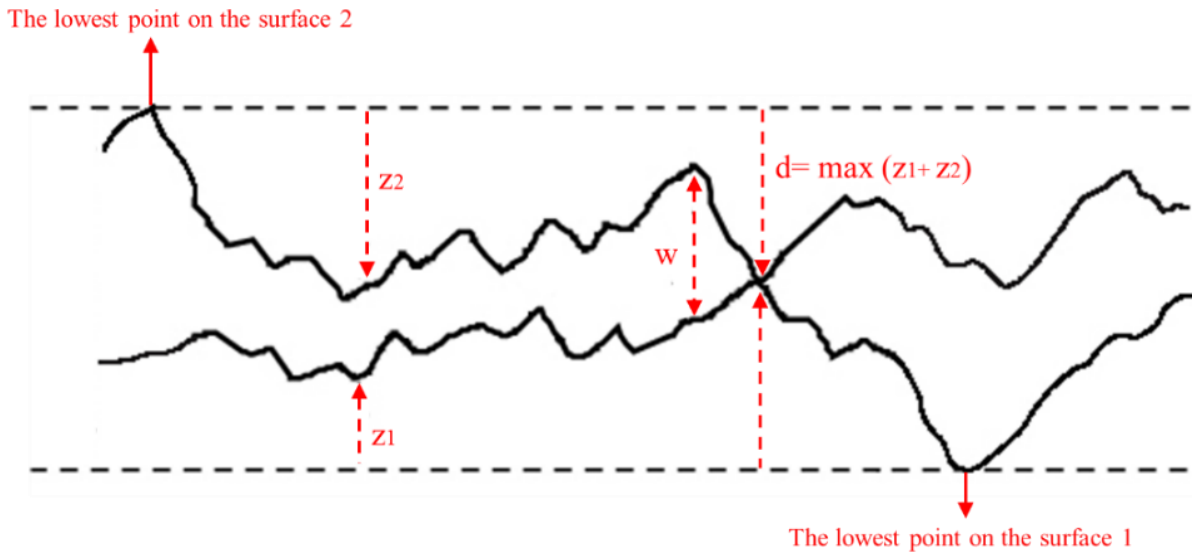


Figure 63: Determination of the aperture from the real fracture surface.

Using reported data, a rectangle with dimensions equal to the axes of the ellipse is defined, and discretized with rectangular mesh (Figure 64). For better estimation of the hydraulic aperture, the area of each section ($\sim 1 \times 1$ mm) on the discretized fracture is chosen close to the area of the fracture elements in the model as much as possible. For each zone of the rectangle, an average of z is assigned by calculating the average of z components of points located in the zone. The same process is carried out for the other fracture surface, and then

using equation 6 the hydraulic aperture is calculated and assigned for each section of the rectangle. The calculated values of the aperture are exported to 3DEC, and assigned as the hydraulic aperture of each element at zero normal stress (w_{zero}). It should be noted that it is necessary to transform all xyz points to a unique coordinate system to be able to aperture calculation. Figure 65 and Figure 66 show the topography of the fracture surfaces for both the scanner machine output (top) and 3DEC model (bottom) for Sierra White granite (SW-T1 & SW-S3 samples). As mentioned, a portion of the surface is cropped to avoid any boundary effect, and therefore data on asperities of this portion is not available (or reliable). In the numerical model, for this portion of the fracture, a very low value (10^{-8} m) is assigned for the hydraulic aperture of the fracture.

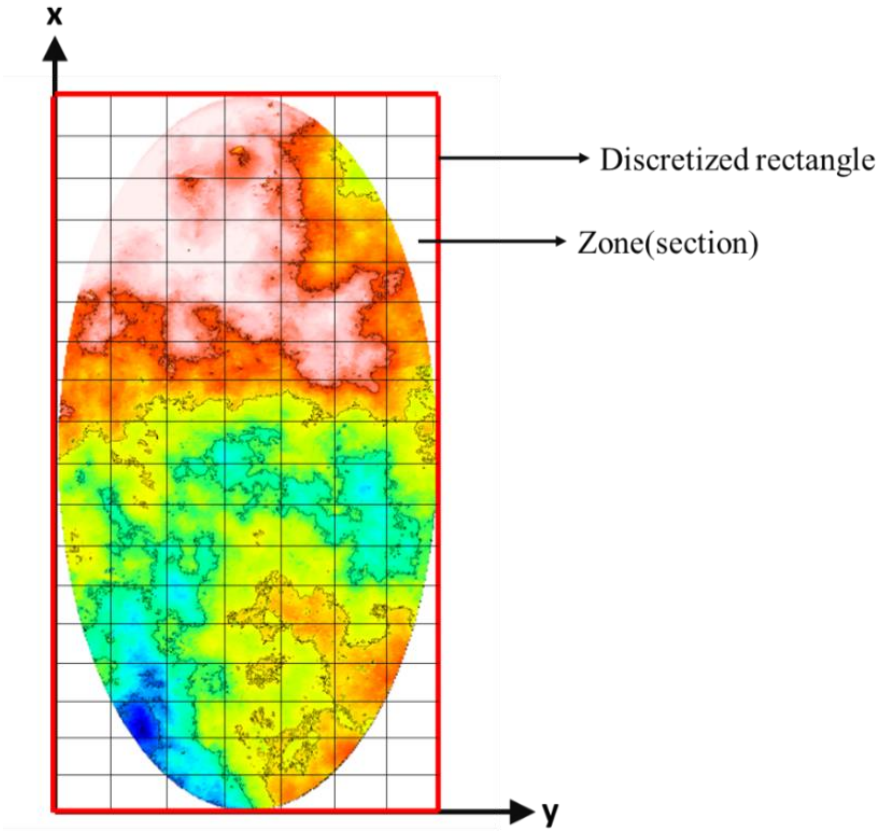


Figure 64: The discretized rectangle on the fracture. An increasing number of discretization (finer mesh) leads to a more precise estimation of the hydraulic aperture calculation.

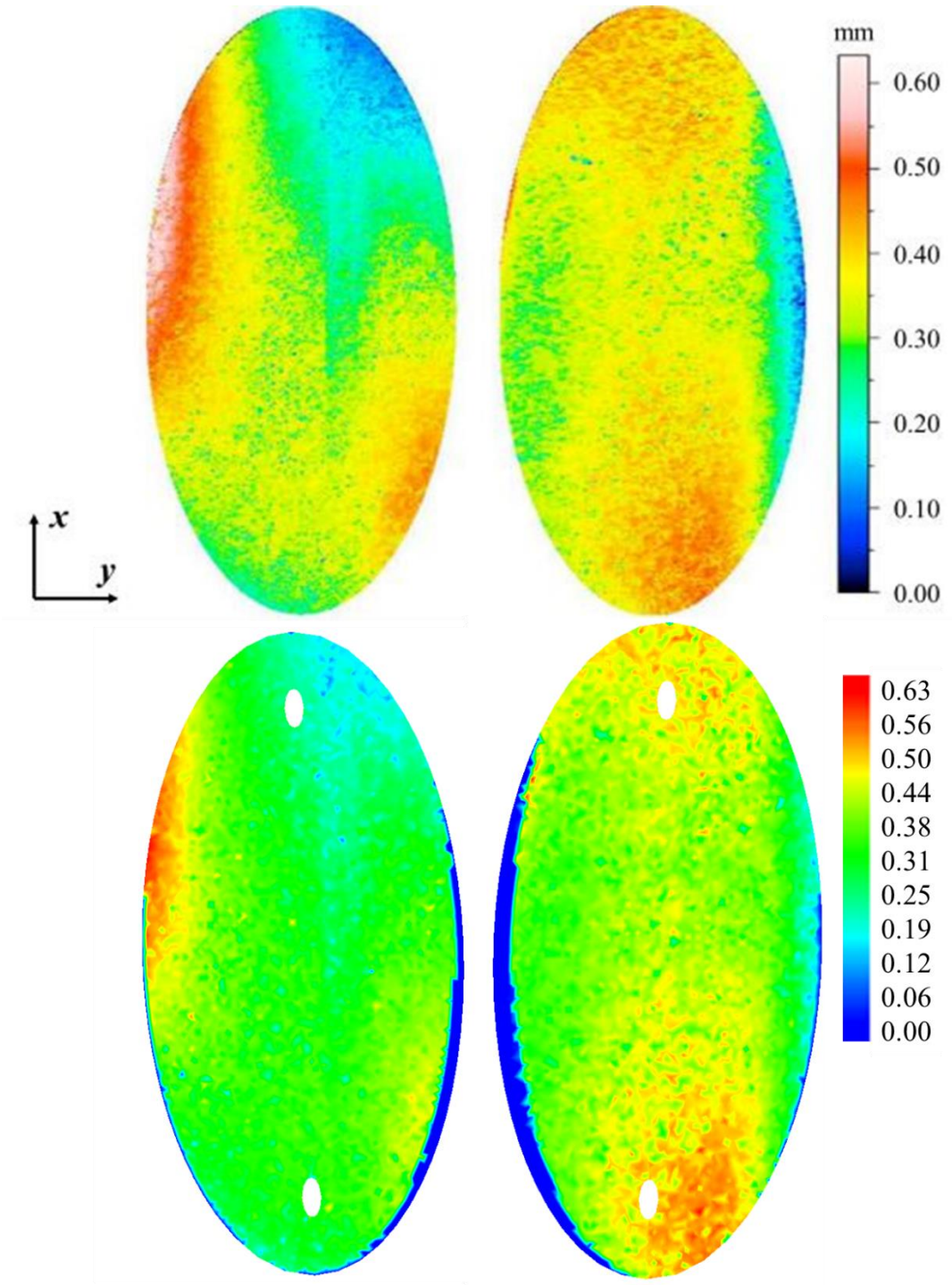


Figure 65: Sierra White granite, SW-S3 sample (Yu and Ghassemi 2018): Top: the topography of the fracture surfaces (the output of the scanning machine). Bottom: Exported data into 3DEC and regeneration of the topography fracture surfaces. The dark blue in the 3DEC surfaces indicates the cropped area. The color indicates the distance (mm) between the high point and the lowest point.

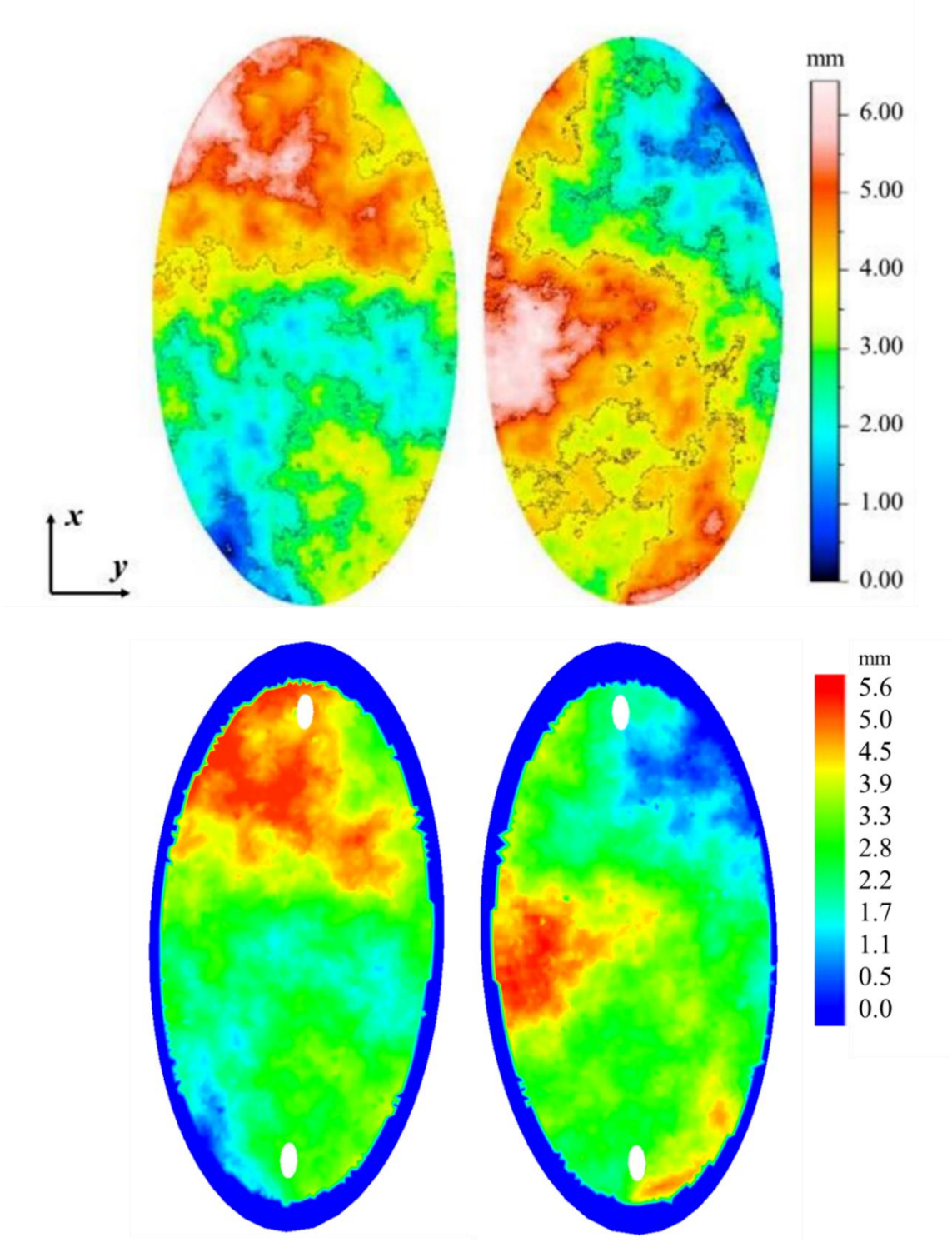
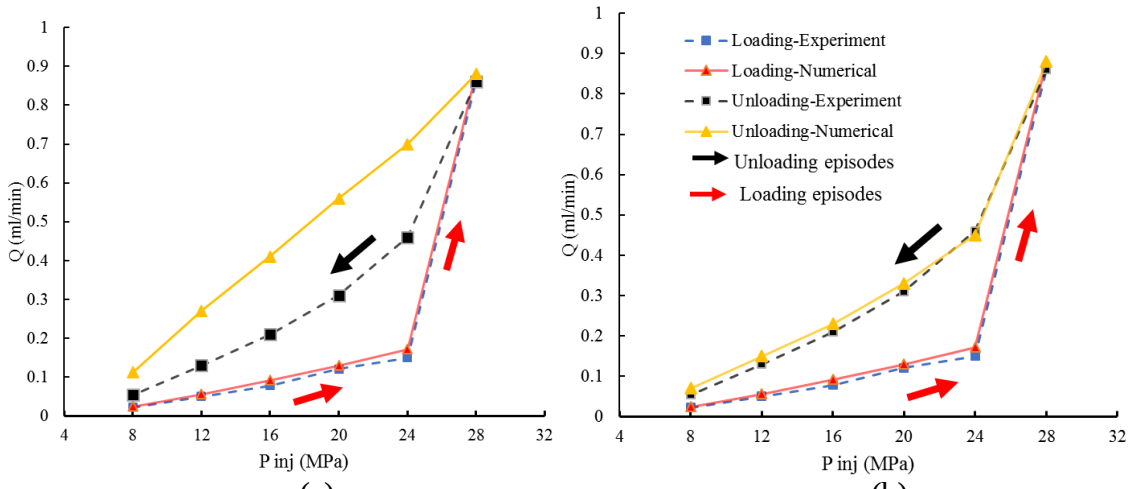


Figure 66: Sierra White granite SW-T1 (Yu and Ghassemi, 2018): Top: the topography of the fracture surfaces (the output of the scanning machine). Bottom: Exported data into 3DEC and regeneration of the topography fracture surfaces. The dark blue in the 3DEC surfaces indicates the cropped area. The color indicates the distance (mm) between the high point and the lowest point.

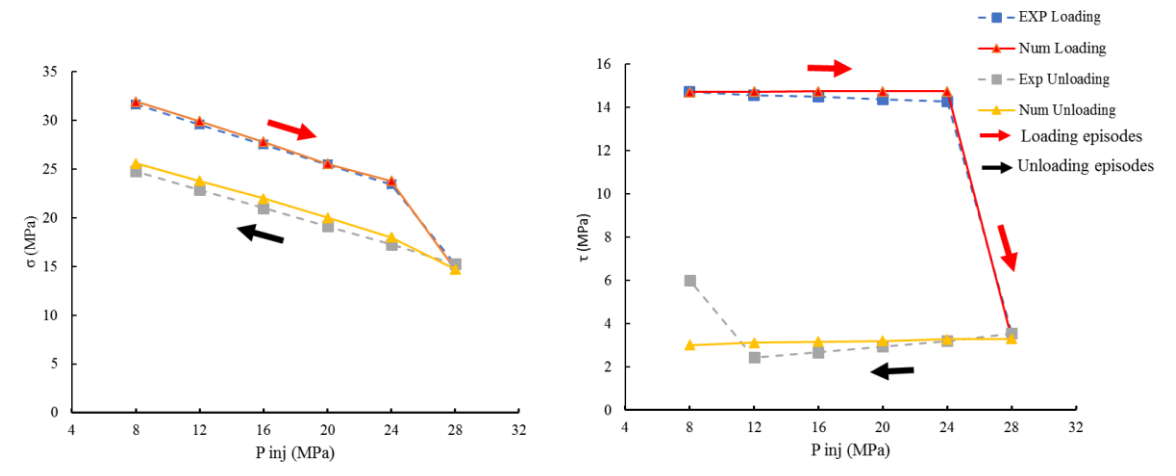
Figure 67 compares the volume rates of the numerical model and experimental test of the SW-S3 sample of Sierra White granite (Wu and Ghassemi 2018). In the following figures, the simulation and experimental results, are shown by dashed and solid lines, respectively. Also, the loading stages are blue and red, and the unloading ones are gray and yellow for experimental test and numerical results, respectively. Figure 67a shows a good agreement (less than 5% difference) between experimental and numerical results during the loading stage, but there is no good match (with more than 20% difference) during the unloading stage. In fact, it shows that with a constant value of the normal stiffness, the volume rate is overestimated by the numerical model. Yu and Ghassemi (2018) stated that during the unloading due to degradation and gauge production, the elevated permeability decreases to some extent but is still greater than the initial one. By decreasing the normal stiffness to 5×10^{12} Pa/m, a good agreement can be achieved during the unloading stage (Figure 67b). In the first section (injection pressure of 8 MPa to 24 MPa) which is corresponded to the elastic deformation, the small opening of the fracture, and slight elastic shear displacement (order of 10^{-7}) have a slight contribution (in comparison to the increase of the injection pressure) on the flow rate enhancement. In contrast, the main sudden increase in the flow rate occurs in the second section (starts from pressure injection of 28 MPa) corresponding to plastic deformation (slippage of the fracture). In our model, by assigning the angle of dilation of 5° we could capture a sudden increase of aperture after slippage which is the main reason for the sudden volume rate increase. Figure 68 shows the average shear and normal stresses on the fracture. As expected, in the loading stage, there is no significant change in the value of the shear stress till it drops suddenly at the failure point. In our model, this behavior is captured by assigning a slip-weakening model for the fracture. By assigning the residual friction

angle of 15°, the shear stress drop of ~9 MPa which is close to what was observed in the experiment is obtained. After the MC criteria is satisfied on part of the fracture with higher pore pressure around the injection well, the whole fracture slips suddenly, and the shear stress drops according to the dynamic friction of coefficient (μ_d). The normal stress also drops by a significant value of~8 MPa after slippage. This stress relaxation is captured by a fixed (no displacement) boundary condition for both platens. Figure 68 shows the fracture steady-state pore pressure at different values of injection pressure during the loading episode. It can be seen that, even at high injection pressure, the pressure of a relatively large area of the fracture surface does not reach the critical value to induce slippage. In fact, for fracture slippage, there is no need for pore pressure of all elements on the fracture to reach the critical pressure, and the small area on the fracture (close to the injection well with higher pressure) causes slippage on the whole fracture.



(a) (b)

Figure 67: SW-S3 sample of Sierra White granite: Flow rate (ml/min) (a) with similar normal stiffness value during loading stage and (b) with a decreased value of normal stiffness to 5×10^{12} Pa/m. This decrease enables the numerical model to simulate the reduction in permeability due to degradation and gauge production during the un-loading stage.



(a) (b)

Figure 68: SW-S3 sample of Sierra White granite: (a) normal stress and (b) shear stress of the fracture during the test. The boundary condition (no displacement for rigid platens) causes the stress relaxation after slippage at which the normal stress decreases by ~8 MPa.

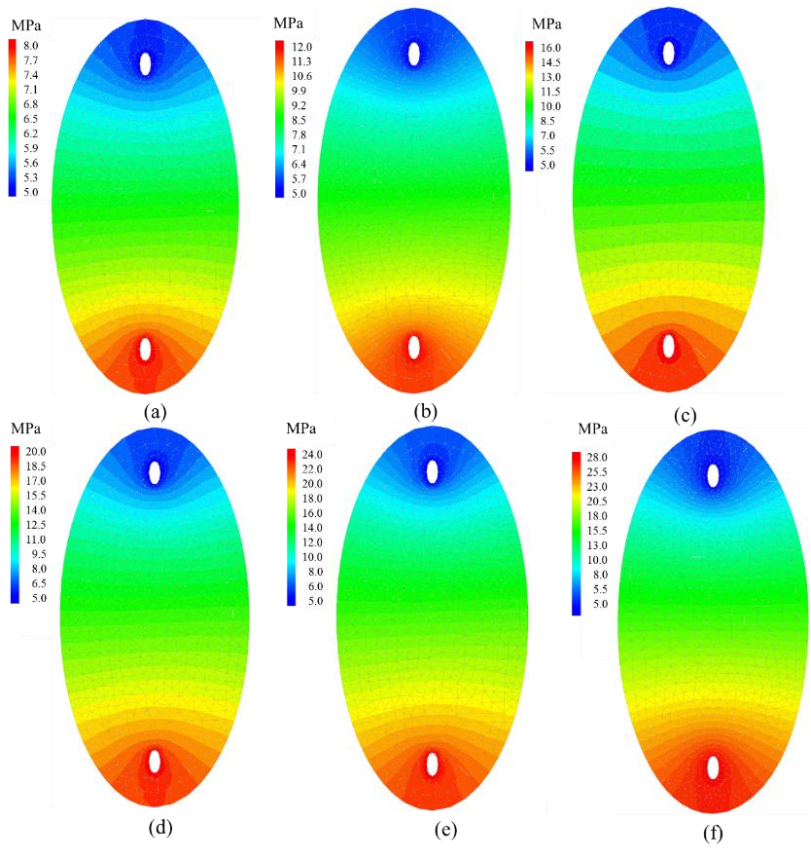


Figure 69: : SW-S3 sample of Sierra White granite: Pore pressure (MPa) of the fracture during loading episode for injection pressure (P_{inj}) (a) 8MPa, (b) 12 MPa, (c) 16 MPa, (d) 20 MPa, (e) 24 MPa, and (f) 28 MPa .

Figure 70 shows the normal stress (compression is positive) of the fracture during the loading stages. As expected, the effective normal stress of the fracture generally decreases during the test as injection pressure increases. It should be noted that even at higher injection pressure the effective normal stress around the production well does not change too much (relative to the area around the injection well), and remain almost constant. But, after initiation of the slip on a relatively small area of the fracture around the injection well (injection pressure of 24 MPa), the slippage propagates on the whole fracture surface, and leads to slippage of all elements of the fracture.

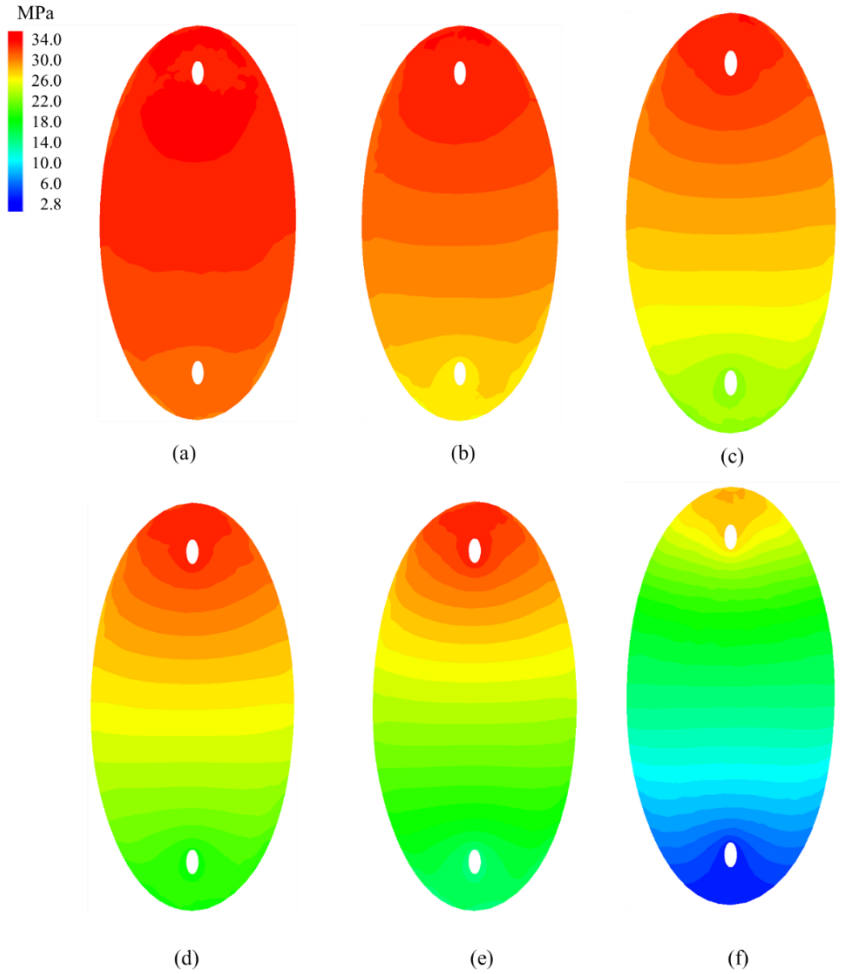


Figure 70: SW-S3 sample of Sierra White granite: Normal stress (MPa) of the fracture during loading episode for injection pressure (P_{inj}) (a) 8MPa, (b) 12 MPa, (c) 16 MPa, (d)20 MPa, (e)24 MPa, and (f) 28 MPa

Figure 71 shows the normal displacement (closure is negative) of the fracture during the loading stages. As expected, the value of normal displacement decreases from the injection well toward the production well as the pore pressure decreases. It can be seen that the normal displacement increases (fractures opening) with decreasing effective normal stress. This increase of opening and injection pressure is the reason for the fluid rate before the fracture slippage.

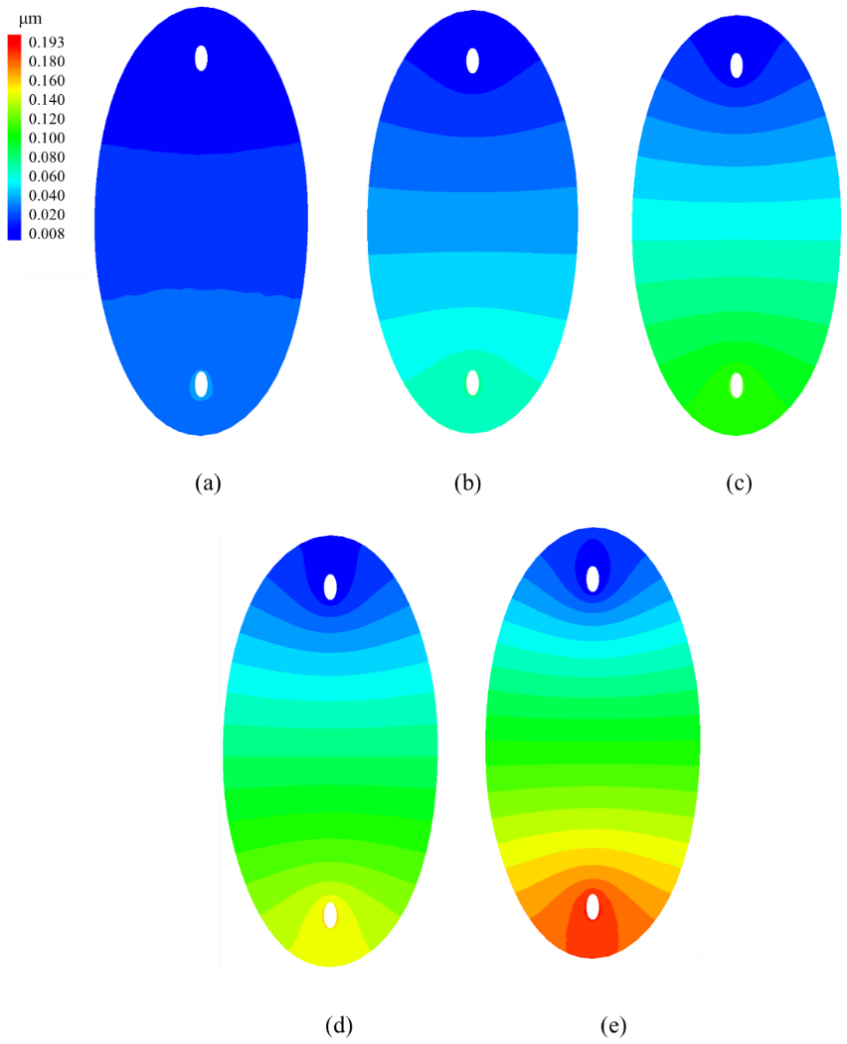


Figure 71: SW-S3 sample of Sierra White granite: Normal displacement (µm) of the fracture during loading stages for injection pressure (P_{inj}) (a) 8MPa, (b) 12 MPa, (c) 16 MPa, (d) 20 MPa, and (e) 24 MPa. Closure is negative.

Figure 72 shows the failed element on the fracture and corresponding shear displacement on the fracture at injection pressure of 20, 24, 28 MPa. As mentioned, at lower injection pressure, no element fails while at higher injection pressure elements around the injection well, where higher pressure builds up, fail and at injection pressure of 28 MPa the whole fracture fails abruptly. It can be seen that even failure in a small part of the fracture induces noticeable

displacement on the fracture. After slippage, the displacement increased by a couple of orders of magnitudes which leads to a sudden rise in the fluid volume rate (due to dilation). Figure 73 shows the displacement vector at injection pressure of 28 MPa after slippage. As expected, all shear vectors are parallel to the dip of the fracture and have a major contribution to the top surface displacement.

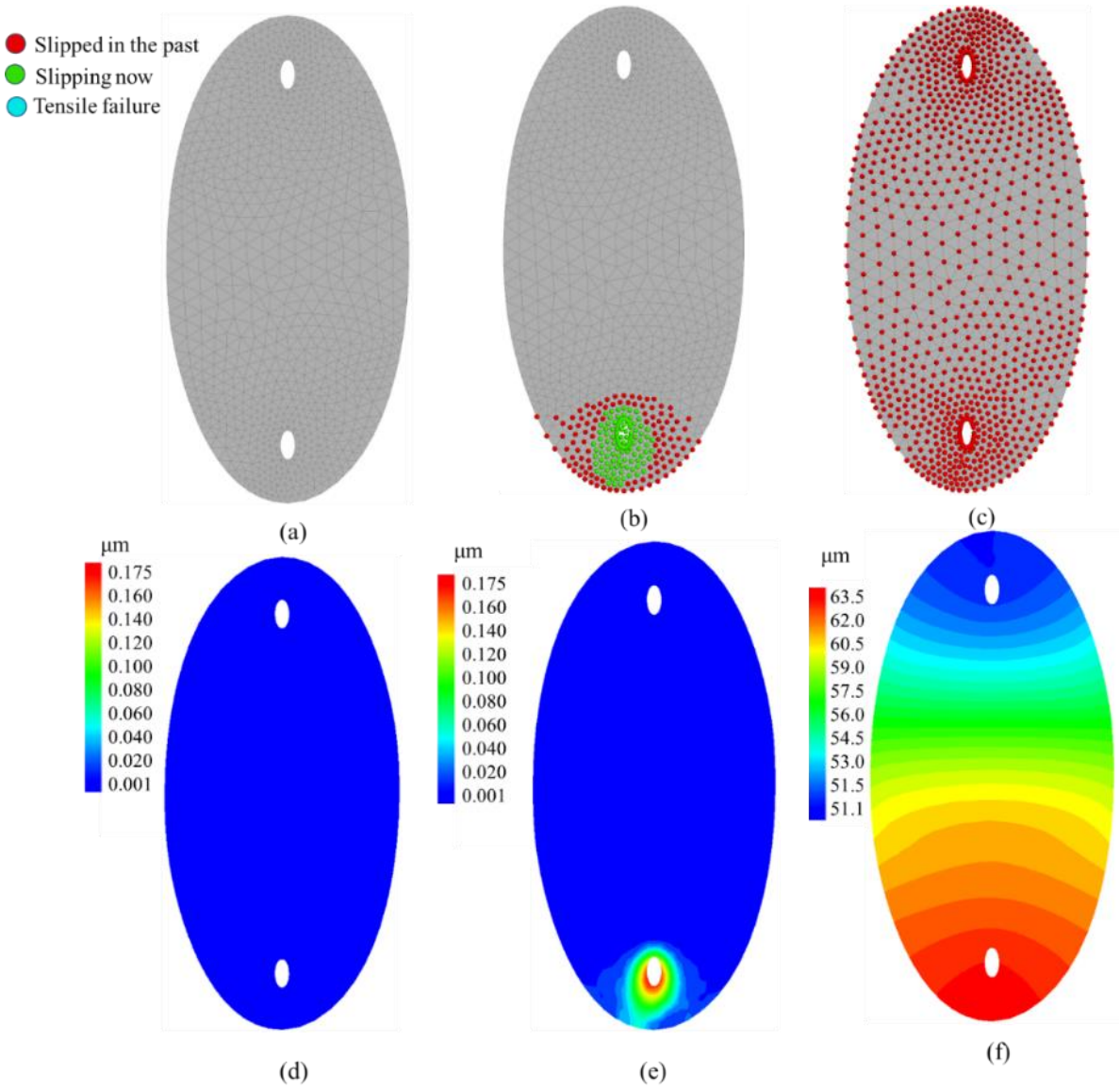


Figure 72: SW-S3 sample of Sierra White granite: failure on the fracture surface at the injection pressure of (a) 20 MPa, (b) 24 MPa, and (c) 28 MPa. Shear displacement (µm) of the fracture during loading stages for injection pressure (P_{inj}) (a) 20 MPa, (b) 24 MPa, and (c) 28 MPa.

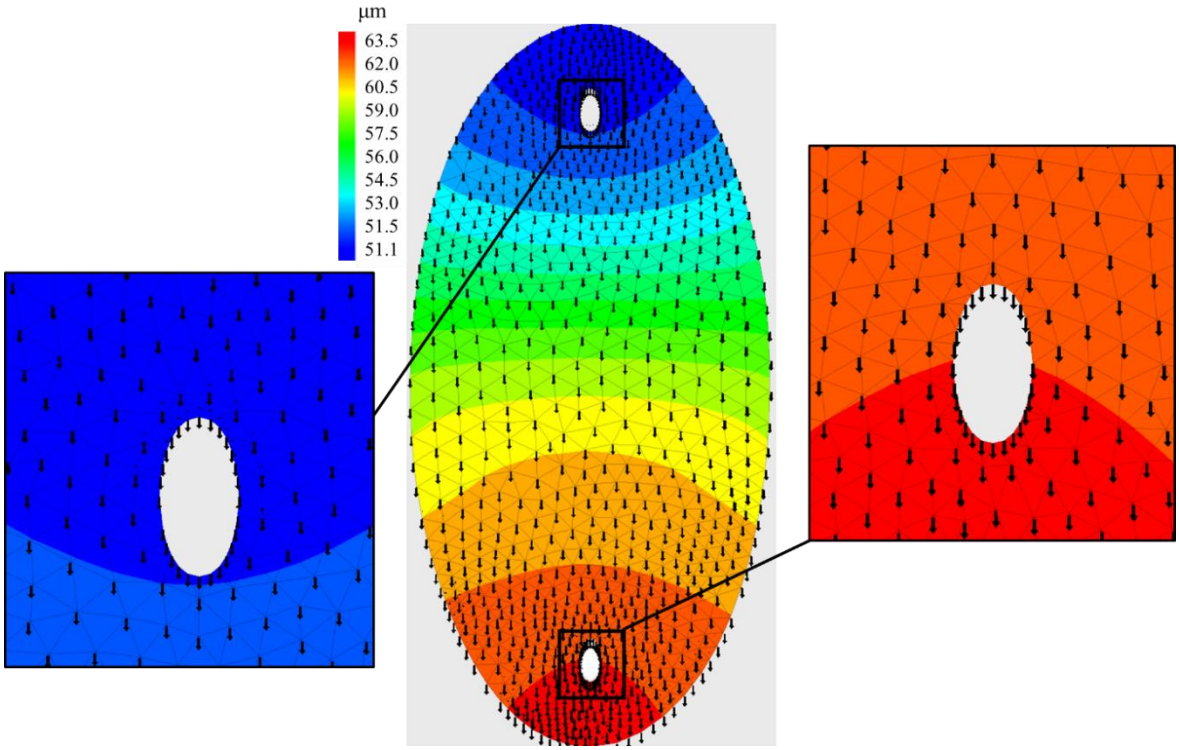


Figure 73: Shear displacement contour (µm) and vectors of the fracture after slippage at the injection pressure of 28 MPa. For a better view, the vectors around the injection and production wells are shown separately.

5.1.6 Sierra White Granite Using the Surface Topography

In this section, the numerical results of the test in which the hydraulic aperture of the fracture is calculated from the real topography are explained. Figure 74 shows the fracture topography in the model which is calculated from the real topography of the fracture surfaces (output of 3-D laser scanner) at zero stress and after applying the initial boundary condition. The average of hydraulic aperture at zero stress is 0.16 mm. The fluid volume rates of both experimental data and the numerical model are shown in Figure 75. Similar to the previous case (the model with uniform aperture), there is a good match between experimental and numerical results during the loading stage, and a mismatch during the unloading stage. Here

again, by decreasing the stiffness of the fracture (to 5×10^{-12} Pa/m) to reproduce the degradation and gauge production (shear-induced asperity degradation) a good match can be obtained.

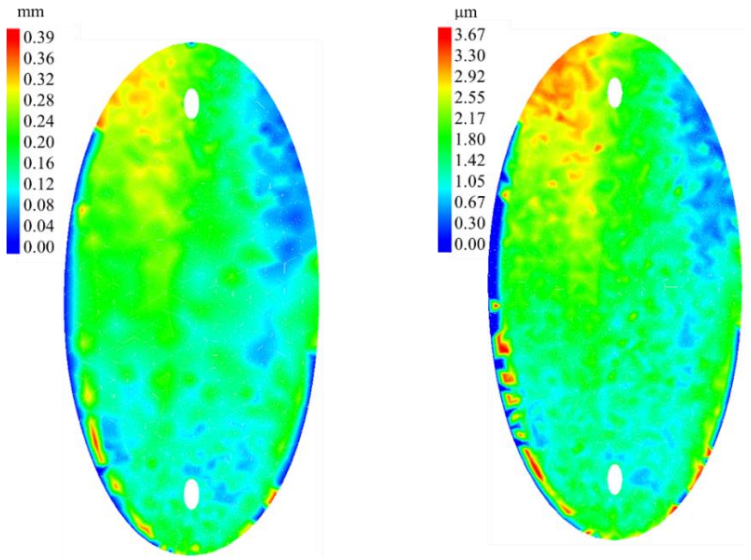
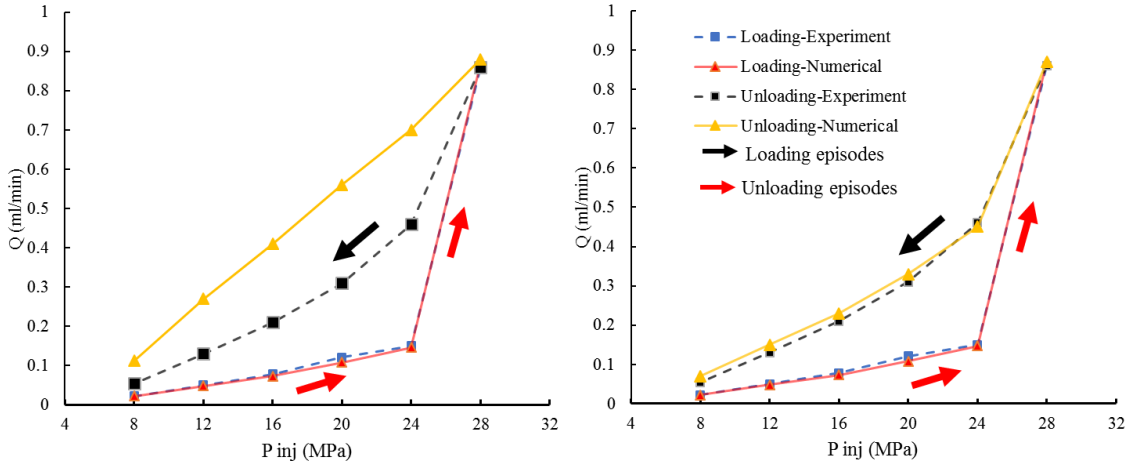


Figure 74: The aperture of the fracture surface in the simulation (calculated from the real topography reported by Ye and Ghassemi (2019)) at zero stress (left) and after applying boundary conditions (right).



(a) **(b)**

Figure 75: SW-S3 sample of Sierra White granite: Flow rate (ml/min) a) with constant normal stiffness value during loading stage and b) with the decreased value of normal stiffness to 5×10^{12} Pa/m. This decrease enables the numerical model to simulate the reduction in permeability due to degradation and gauge production during the unloading stage.

Pore pressure values of the fracture for different values of injection pressure during the loading stages are shown in Figure 76. Due to the non-uniform aperture values on the fracture surface, the pore pressure does not have a symmetric gradient (as Figure 69). Although the pressure contour is asymmetric, the general trend of pore pressure distribution is similar to the previous case. Figure 77 compares the pore pressure distribution and discharge vector on the fracture surface when the fracture has a uniform and nonuniform aperture. It is obvious that the real topography of the fracture surface has a significant effect on the fluid flow path. Area with a higher aperture has a larger discharge value. It should be mentioned that the figures do not have the same scale for discharge vector, and the figures are describing the processes qualitatively. Fluid in this area determines the total fluid discharge, and other areas with lower aperture do not affect significantly the value of total fluid discharge.

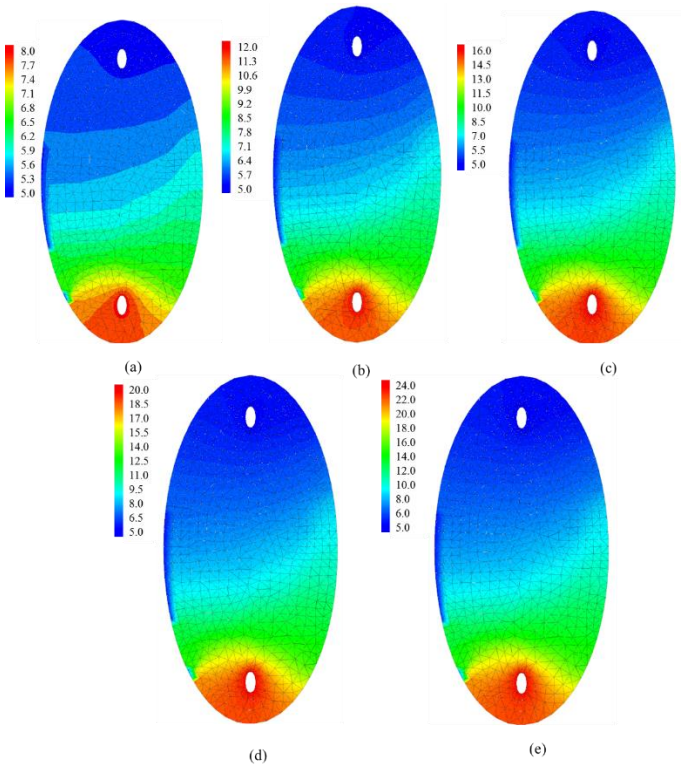


Figure 76: Pore pressure (MPa) of the fracture that has real topography during loading stages when injection pressure is (a) 8 MPa, (b) 12 MPa, (c)16 MPa, (d)20 MPa, and (d)24 MPa.

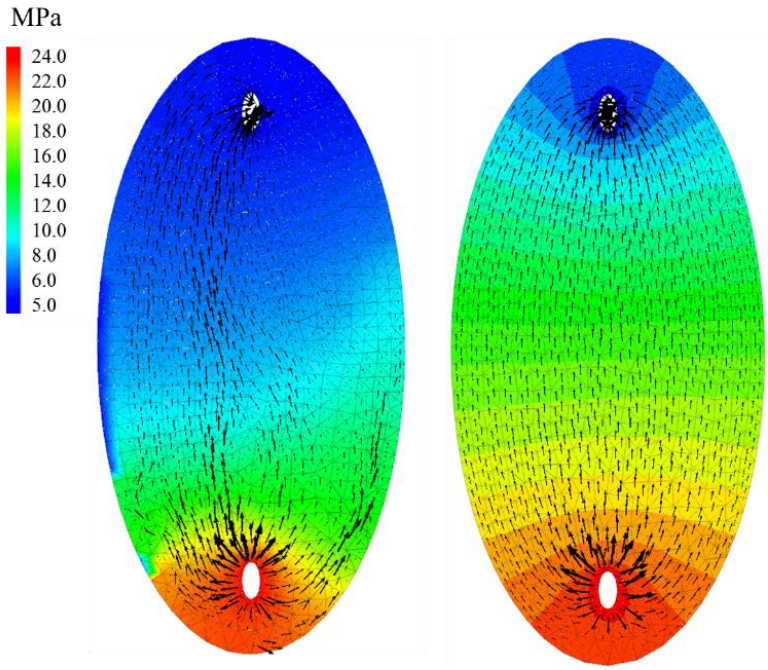


Figure 77: Comparison of the pore pressure (MPa) distribution and discharge vector on the fracture surface for SW-S3 sample for Sierra White granite when aperture is uniform (right) and nonuniform (calculated by the real topography of the fracture surfaces) at an injection pressure of 24 MPa.

Figure 78 shows the effective normal stress of the fracture during the loading stage. The general trend of the normal stresses is similar to the case with a uniform aperture. Similar to the pore pressure distribution, the effective normal stress does not symmetric shape. It can be seen that normal stress drop (stress relaxation) after slippage at an injection pressure of 28 MPa. After slippage, in some areas, the fracture surfaces are not in contact (zero normal stress) which is due to numerical instability after slippage. Normal displacements of the fracture during the loading stages are shown in Figure 79. The maximum normal displacement belongs to the failed points, and the other points on the fracture have the opening value proportional to the induced pore pressure. Figure 81 shows the shear displacement and vectors on the fracture. Similar to the case with uniform aperture, the shear displacement vectors are parallel to the fracture dip.

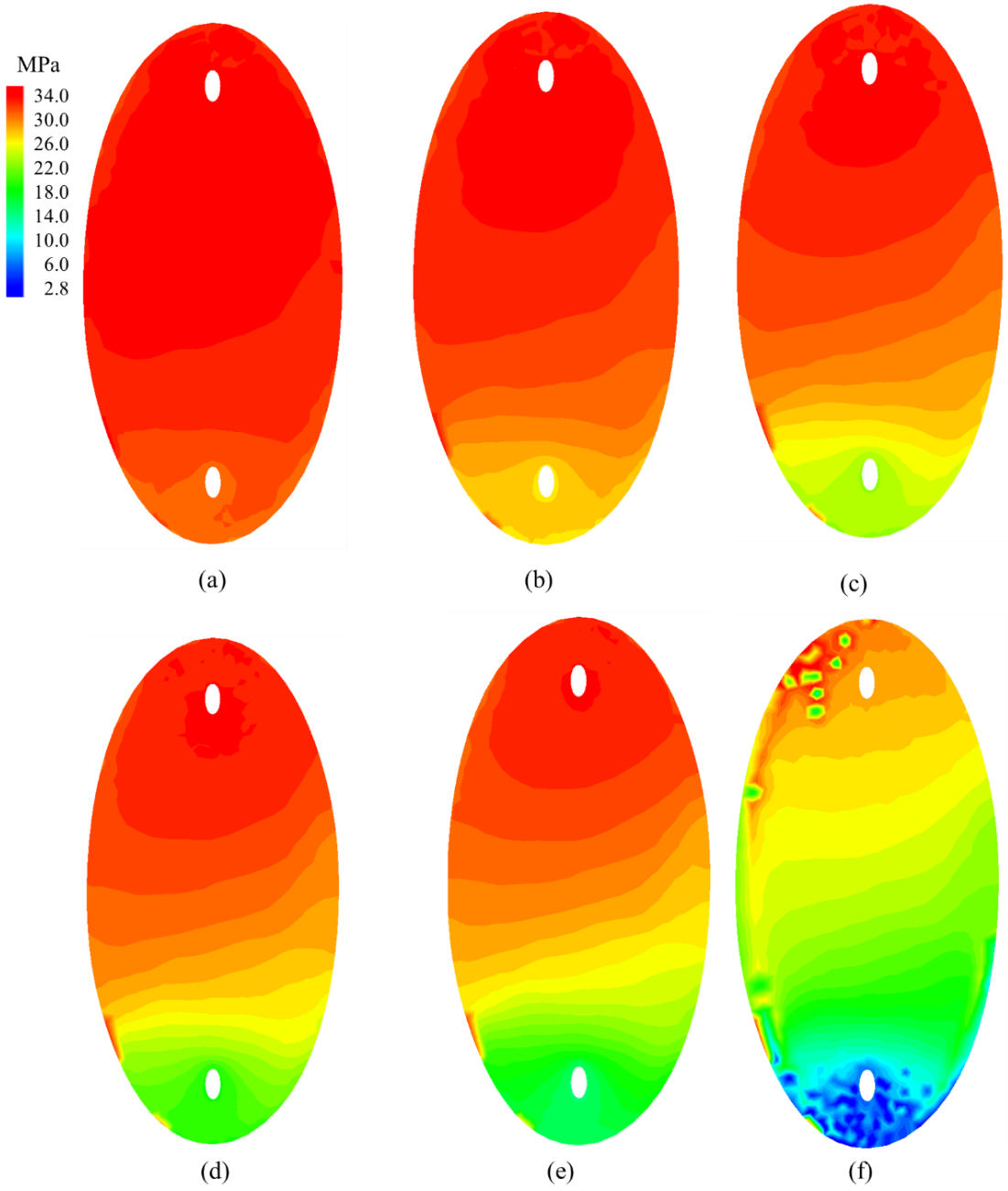


Figure 78: SW-S3 sample of Sierra White granite: Normal stress (MPa) of the fracture during loading episode for injection pressure (P_{inj}) (a) 8MPa, (b) 12 MPa, (c) 16 MPa, (d)20 MPa, and (e) 24 MPa when the fracture does not have a uniform aperture.

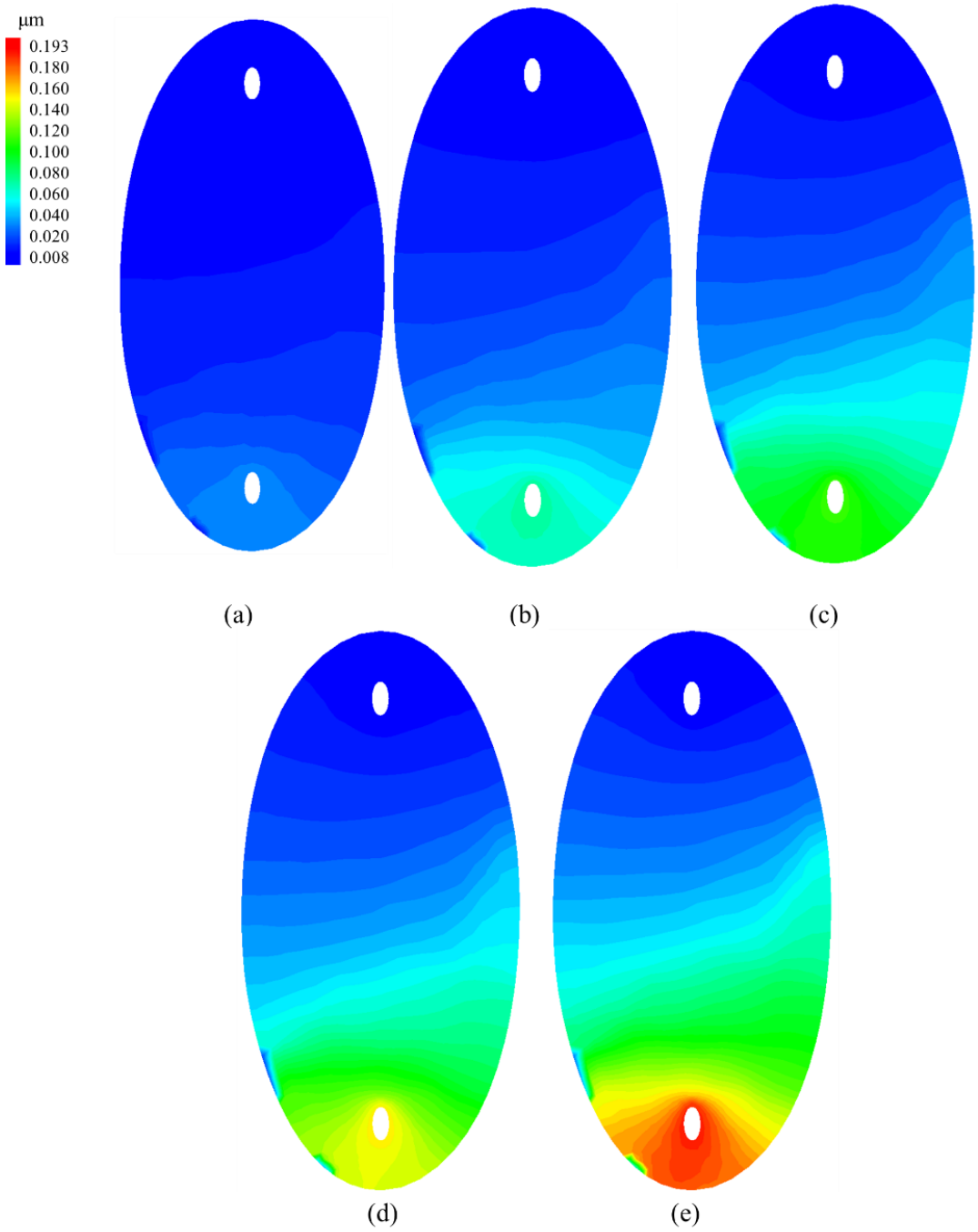


Figure 79: SW-S3 sample of Sierra White granite: Normal displacement (µm) of the fracture during loading episode for injection pressure (P_{inj}) (a) 8MPa, (b) 12 MPa, (c) 16 MPa, (d) 20 MPa, and (e) 24 MPa when the fracture does not have a uniform aperture.

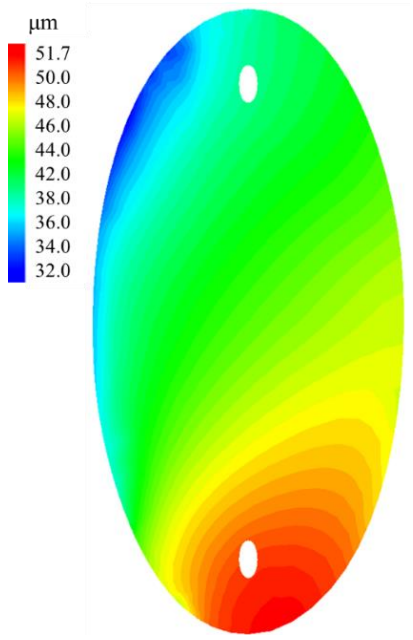


Figure 80: Shear displacement (µm) after slippage at the injection pressure of 28 MPa.

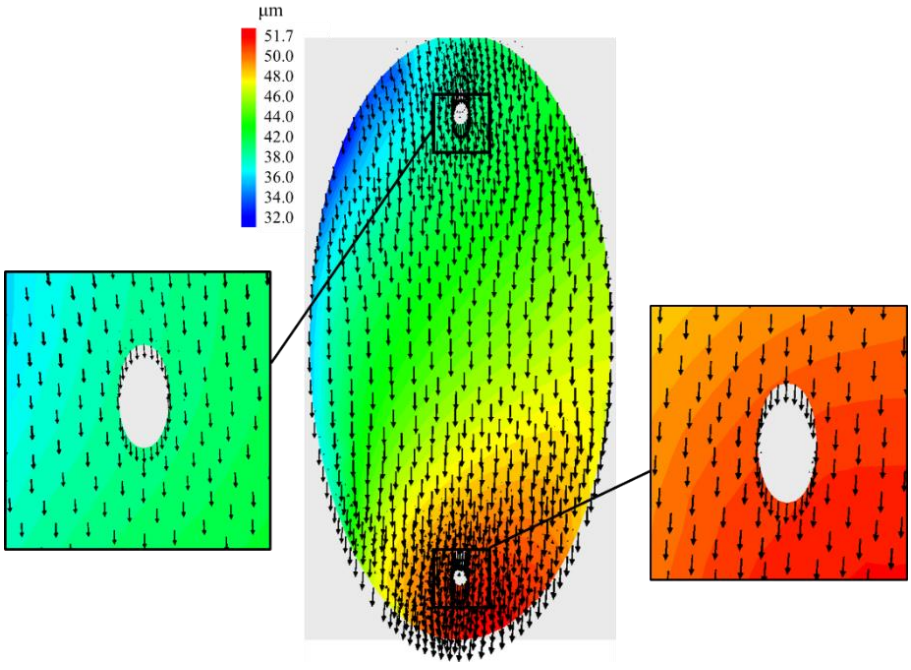


Figure 81: Shear displacement contour (µm) and vectors of the fracture after slippage at the injection pressure of 28 MPa. Enlarged views of displacement vectors around the injection and production wells are shown in the boxes.

5.2 Numerical Investigation of the Slippage of a Natural Fracture Resulting from an Approaching Hydraulic Fracture

5.2.1 Introduction

This section provides the numerical analysis of an experiment that addressed slippage of a natural fracture resulting from an approaching hydraulic fracture. The experiment was performed at the Reservoir Geomechanics and Seismicity Research lab (RGSRG Lab) at the University of Oklahoma (Hu et al. 2019, Hu and Ghassemi, 2021). Using 3DEC, a fully coupled hydro-mechanical discrete element model is used to simulate the experiment. In our simulation, the rock matrix and both the natural and hydraulic fracture are represented by deformable blocks and discontinuities, respectively. To understand the physical process, we define two cases based on what we observed in the lab and study the effect of the pressurization and propagation of a hydraulic fracture on a nearby natural fracture. We assume that the hydraulic fracture propagates and hits the natural fracture in Case I, but not in Case 2 as observed in the experiments. A cohesive zone approach is used to simulate hydraulic fracture propagation. We considered a pre-defined fracture path with non-zero tensile strength and cohesion. A 0.25 cm notch is also modeled, and the fluid is injected into it. As the fluid injection continues, the pressure increases in the wellbore and the notch, and eventually leads to fracture propagation.

Figure 82 shows the numerical setup and the boundary condition for both cases. The simulation domain consists of the rock sample and two rigid platens. The platens have 20 cm diameter and 2.5 cm height, respectively, and are smooth and rigid to eliminate the effect of the testing machine- sample interaction. The samples in Case I and II have a natural fracture with 45° and 32° dip, respectively, and a pre-defined hydraulic fracture with dimensions shown in Figure 82c. Before injection, a confining pressure of 3.5 MPa for Case I and 10

MPa for Case II is applied to the sample, and the sample is allowed to reach equilibrium. Then the axial stress is increased to ~5.5 MPa and 30 MPa in Case I and II, respectively. The stress is applied by moving the upper platen at a constant rate while fixing the lower platen. After the axial stress reaches the desired level we fix the upper platen as well. After reaching equilibrium, the fracturing fluid (density of 0.873 g/cm^3 and viscosity of 43 mPa.s at a temperature of 20° C) is injected at a constant rate of 1.5 cm^3/min, and 0.2 cm^3/min for Case I and II, respectively. Before the propagation of the pre-defined fracture, the fluid is compressed as the pressure of the opening and notch increases. The pressurization of the notch and its deformation induce displacement on the natural fracture. The relative displacement is calculated from the strain gangue output by multiplying the strain to the initial distance between two endpoints. By calculating similar values for the same points in our model, we are able to compare the experimental and the numerical results.

5.2.2 Simulation Results

The injection causes the pressure in the notch to increase and eventually to propagation of a fracture from the notch. This is simulated by opening the predefined hydraulic fracture plane. Figure 83 shows the aperture of the propagating hydraulic fracture after 0.3, 2, 4 ms of propagation. The hydraulic fracture propagates rapidly and reaches the sample sides and the natural fracture in a very short time (less than 1 second) as observed in the experiments. In our model, both the initial aperture (aperture when the normal stress is zero) and residual aperture (the aperture below which increasing the normal stress does not reduce the aperture) are defined as 0.1 mm. Therefore, the aperture remains at 0.1 mm before any opening of the hydraulic fracture. Figure 83 shows the aperture of the propagating hydraulic fracture after 0.3, 2, and 4 ms of propagation.

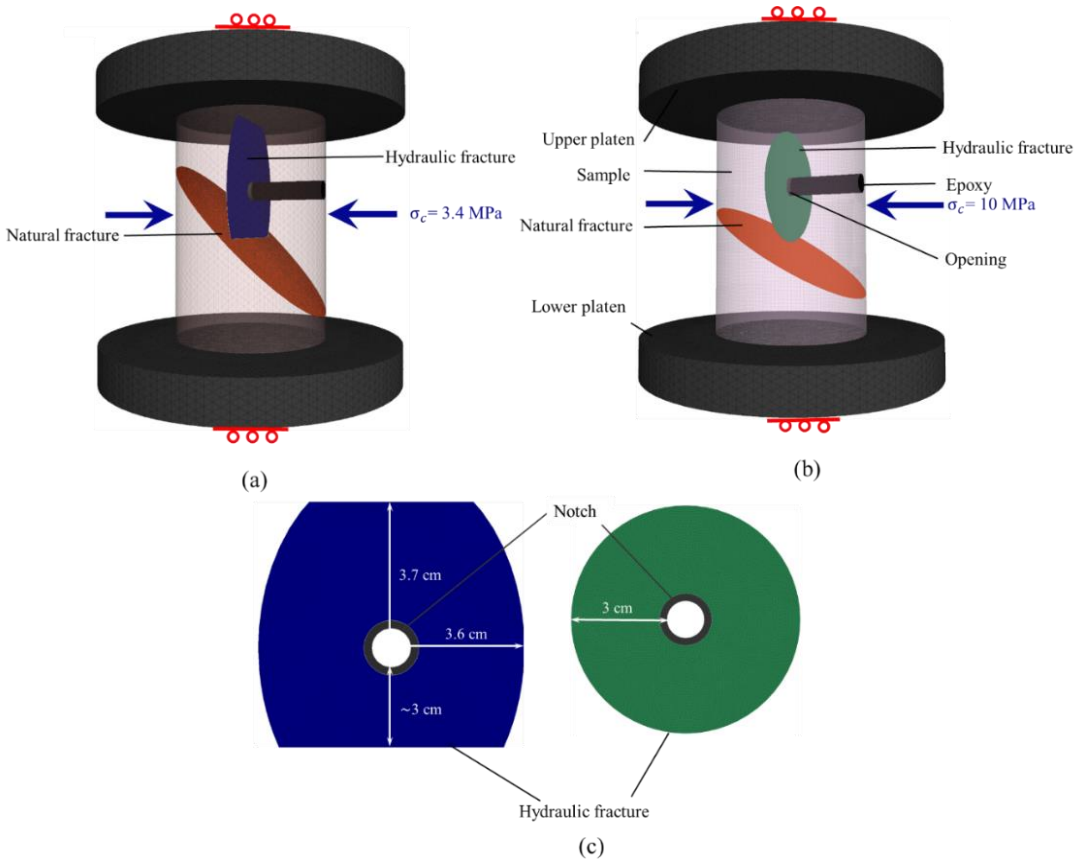


Figure 82: Test setup for (a) Case I and (b) Case II. The pre-defined hydraulic fracture does not touch the natural fracture in Case II, and reaches the natural fracture in Case I. The boundary and loading condition includes applying the confining pressure, and moving down the upper platen while the lower one is fixed. After the axial stress reaches the desired value (~5.5 MPa and 30 MPa in Case I and II, respectively) the upper platen is fixed. (c) Dimension and geometry of the pre-defined hydraulic fracture in Case I (left) and Case II (right).

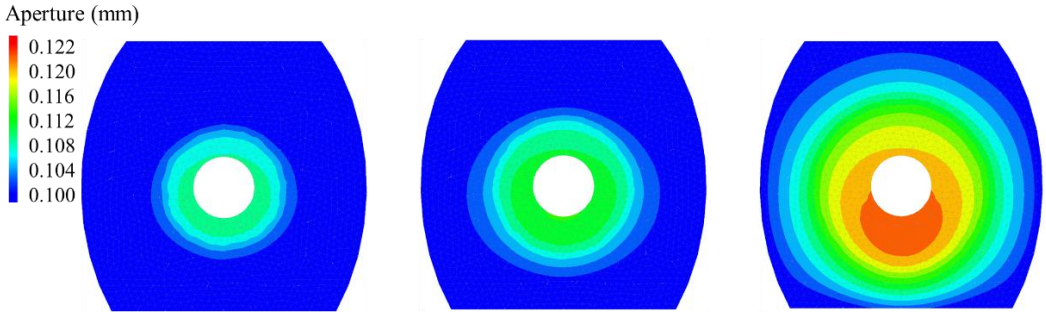


Figure 83: Aperture of the propagating hydraulic fracture after 0.3, 2, and 4 ms of propagation (left, middle, and right respectively. Both the aperture at zero normal stress and residual aperture (minimum hydraulic aperture) are 0.1 mm.

The pressurization of the notch and the opening of the hydraulic fracture induce shear displacement on the natural fracture. Figure 84 shows the displacements of the natural fracture caused by the notch pressurization in Case I. Two zones of normal displacement can be observed; the natural fracture tends to open in the zone with positive displacement values (closure is negative) which are located along the hydraulic fracture plane (tensile stress zones). Both the zone extent and the displacement magnitude increase as the wellbore and the notch pressure rise. The zone with negative normal displacement is where the natural fracture tends to close. It can be seen that the closure values are larger than opening and cover a larger area of the natural fracture. The induced shear displacement has its maximum value at the upper end of the natural fracture. It should be noted that patterns of induced shear and normal stress are very sensitive to many factors such as natural fracture stiffness and relative angle of hydraulic and natural fracture, confining pressure and deviatoric stress, size, and geometry of the notch, etc. The displacements shown in Figure 84 are based on the properties and boundary conditions we applied in the experiment.

Figure 85 shows the induced normal and shear displacement on the natural fracture after hydraulic fracture propagation. It is clear that the approaching hydraulic fractures caused the natural fracture to slip. The pattern of both induced normal and shear displacements is similar to when the notch is pressurized (Figure 84), with zones of the maximum and minimum displacements. It should be noted that the predefined hydraulic fracture has a slight effect on the displacements of the natural fracture (Figure 85).

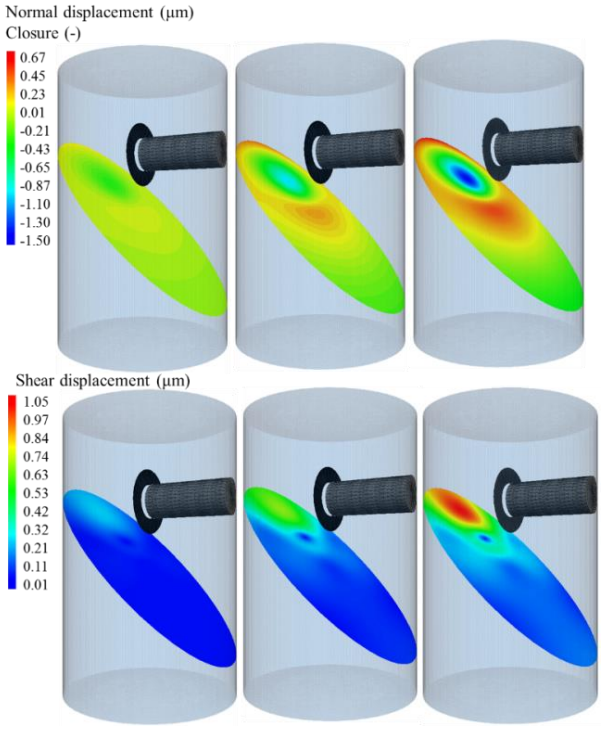


Figure 84: Case I: Induced normal (up) and shear (down) displacements (µm) of natural fracture when pressure of the notch is 5, 15, 22 MPa (left, middle, and right respectively). (Closure is negative)

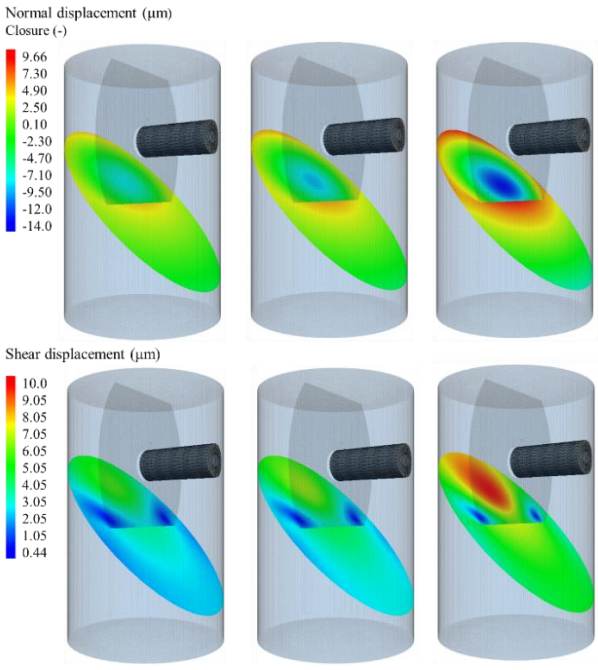


Figure 85: Case I: Induced normal (up) and shear (down) displacements (µm) of natural fracture after 0.3, 2, and 4 ms of propagation (left, middle, and right respectively). (Closure is negative)

Figure 86 shows the comparison of the numerical and experimental results of Case I. It can be seen that there is a reasonable agreement between the numerical and experimental results. Sections I and II (Figure 86) represent the pressurization of the notch and the hydraulic fracture propagation, respectively. The displacement in Section II is greater than Section I by an order of magnitude. Both experimental data and the numerical simulation show a gradual increase of the induced displacement as injection continues before any fracture propagation. The departure of the numerical results from the experimental data is due to main factors such as the idealization of the fracture propagation in the model and not considering the inhomogeneity of the rock, and some of the geometric details of the fracture, notch, etc.

Section III includes displacement induced by slippage of the natural fracture after the hydraulic fracture hits the natural fracture, and fluid flows into the natural fracture. The fluid pressurizes the natural fracture and eventually causes it to further slip. The slip magnitude of Section III is greater than that of Section II by an order of magnitude. As mentioned, the propagation of hydraulic fracture and slippage of the natural fracture happens in less than 1 s. It is noteworthy that in the experiments, the hydraulic fracture not only hits the natural fracture but also reaches the side of the sample. As a result, some of the fluid escapes from the side of the sample, and the rest flows through the natural fracture. As mentioned before, the geometry of the hydraulic fracture is pre-defined in our model, so it is not possible to replicate every detail of the test.

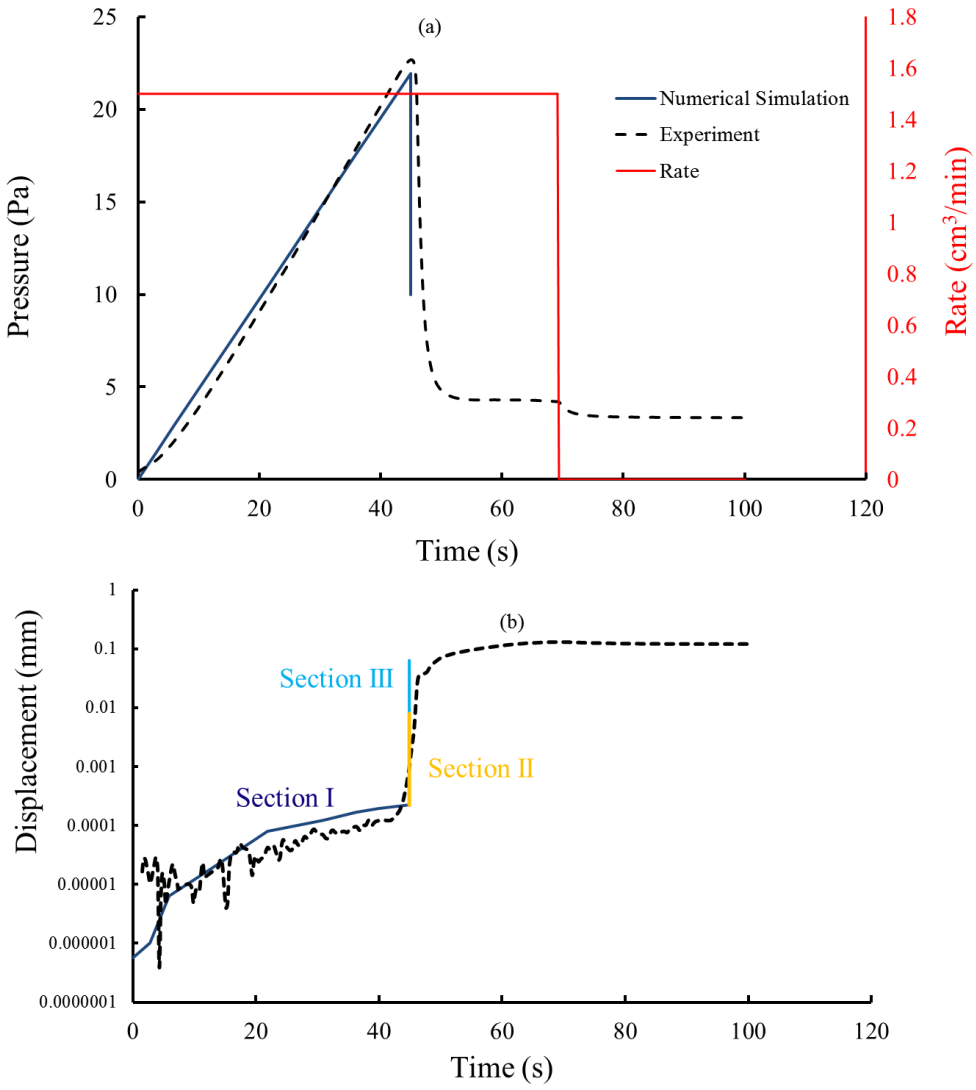


Figure 86: The comparison of the experimental (dashed line) and the numerical simulation (solid line) results of Case I. Sections I and II corresponds to the notch pressurization and hydraulic fracture propagation, while section III is due to slippage of the natural fracture after fluid flows into the natural fracture and pressurizes it.

Figure 87 shows the normal stress and shear stresses on the natural fracture in Case I corresponding to a notch pressure of 0 (equilibrium condition), 5, 15, and 22.0 MPa (the maximum notch pressure observed in the lab experiments is 22.7 MPa). Although no significant difference is observed in the stresses of natural fracture, the pattern of stress is noteworthy. Along the pressurized notch, there is a zone where normal and shear stresses are minimum

and maximum, respectively. Continued pressurization of the notch leads to the expansion of the joint deformation zone with the maximum and minimum stresses. The difference between the maximum and minimum stress values on the natural fracture increases with the notch pressurization. For example, before injection (equilibrium condition), the difference of the minimum and the maximum values of the normal stress on the natural fracture is 0.1 MPa, while when the pressure of the notch is 22 MPa this value rises to 0.2 MPa.

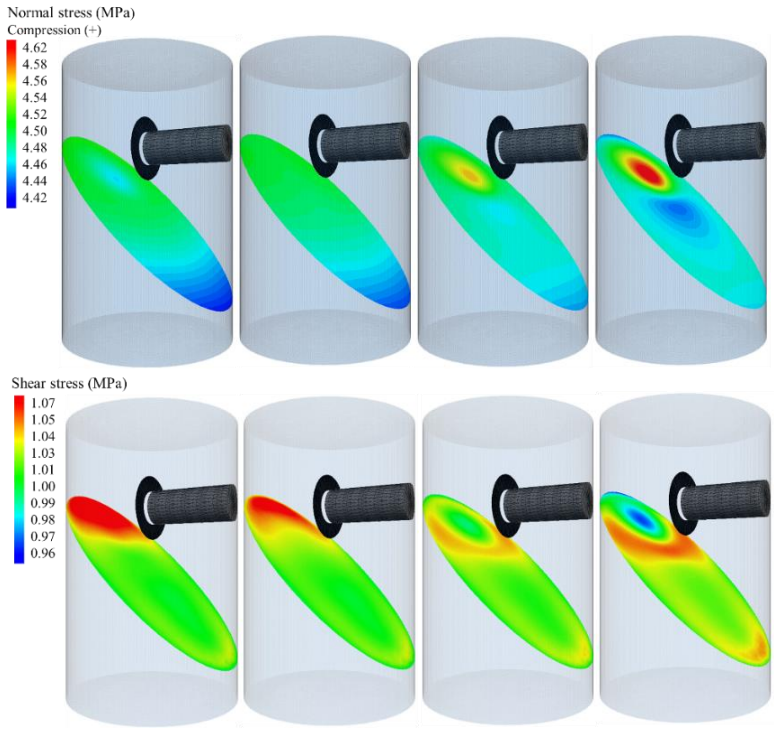


Figure 87: Case I: Normal (up) and shear (down) stress (MPa) of natural fracture when the pressure of the notch is 0 (equilibrium condition), 5, 15, 22 MPa (from left to right respectively). (Compression is positive)

In Case II, the hydraulic fracture does not reach the natural fracture. Our numerical results show that even though the hydraulic and natural fractures do not intersect, the hydraulic fracture is able to induce a considerable displacement and stress perturbation on the natural fracture as it propagates. Similar to Case 1, both normal and shear-induced displacements

increased by an order of magnitude after the hydraulic fracturing starts. Figure 88 shows the induced displacements for the notch pressurization of 5, 15, 23 MPa (the maximum notch pressure observed in the lab is 23.5 MPa). Figure 89 shows the induced displacements by hydraulic fracturing after 0.13, 1.8, 3 ms of propagation. It should be noticed that the pattern of induced displacement is different from that of Case I. This is because of the difference in the geometry of the problem (e.g. natural fracture dip angle, the distance of hydraulic and natural fractures, etc.), the boundary condition, and mechanical properties of the rock. The value of the maximum relative displacement on the natural fracture after hydraulic fracture propagation obtained from the numerical model and experimental work is in good agreement (0.0053 mm for numerical model vs 0.0085 mm for experimental result).

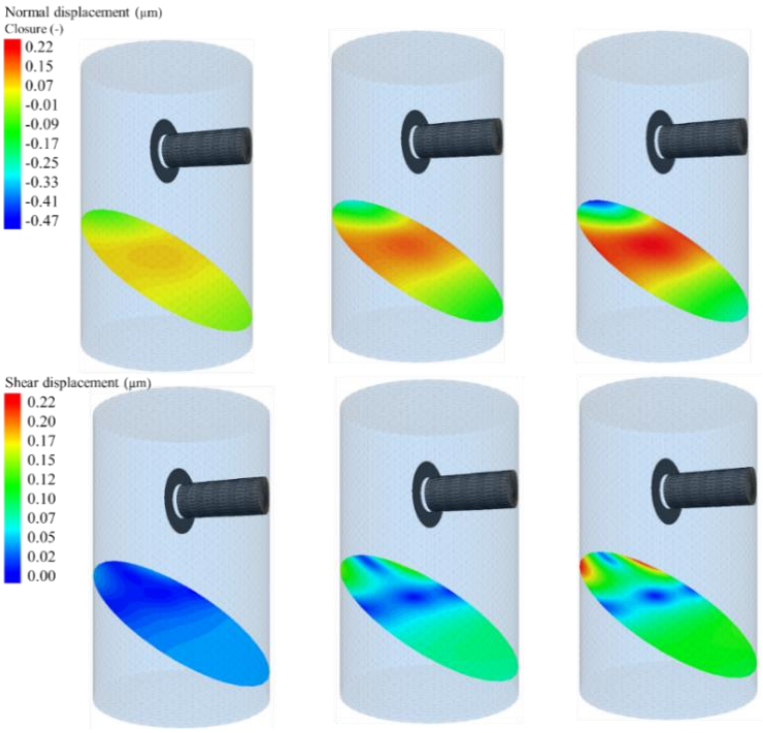


Figure 88: Case II: Induced normal (up) and shear (down) displacements (μm) of natural fracture when the pressure of the notch is 5, 15, 23 MPa (left, middle, and right, respectively). (Closure is negative).

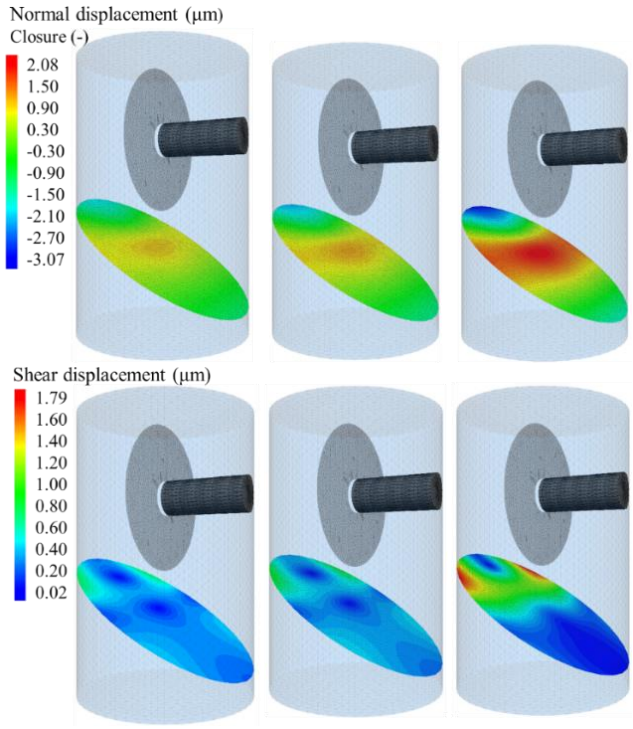


Figure 89: Case II: Induced normal (up) and shear (down) displacements (μm) of natural fracture by propagating hydraulic fracture after 0.13, 1.8, 3 ms of propagation. (left, middle, and right respectively). (Closure is negative).

5.2.3 Summary and Conclusions

A coupled numerical model is constructed to study experiments conducted to investigate the interaction between a natural fracture and a hydraulic fracture with a focus on slippage on a natural fracture or a bedding plane discontinuity due to an approaching hydraulic fracture. The tests were conducted on a 101.6 mm diameter cylinder sample with a horizontal wellbore. Injection pressure, deviator stress, acoustic emission, and sample deformation are monitored during the test. The numerical simulations of the experiments capture the overall experimental observations. Shear stress on the joint is induced by an approaching hydraulic fracture causing it to slip. The maximum value of induced shear displacement on the natural fracture increases by an order of magnitude as the hydraulic fracture propagates. The experimental and numerical analysis help better explain the field observations during hydraulic fracturing operations and contribute to better design practices.

Conclusions and Future Work

In this work, a 3D fluid-mechanical coupled numerical model is used to study the induced seismicity caused by wastewater injection in more detail than previous studies. Since Oklahoma has experienced the most increase in the number of induced earthquakes in the last decade, the initial conditions of our model are set to those believed to occur in Central Oklahoma. A coupled geomechanical model is utilized to investigate the effect of different factors on fault reactivation in Oklahoma. First, assuming that injection is performed in a homogeneous isotropic rock, the angle between the maximum horizontal stress azimuth and fault strike is 27° to 28° in the most critical faults. Numerical results reveal that although the dominant process in fault reactivation is direct pore pressure, the poroelastic effect can play an important role in fault reactivation. It is shown that in injection into sealed reservoirs that do not have hydraulic communication with the basement, poroelastic effect is the only driving mechanism that increases the tendency of fault in the basement. In contrast, in injection into reservoirs that are hydraulically connected to the basement (e.g. via fault damage zone), poroelastic acts as stabilizing factor by increasing normal stress on the faults. There is a competition between the direct effect of pore pressure (the dominant effect) and the indirect effect of poroelastic effect. Although the effects of poroelastic stresses are smaller, their value determines which part of the fault has the more tendency for reactivation. Results show that injection into a more compliant reservoir can reduce the tendency of faults for reactivation. This is the case in both sealed reservoirs and reservoirs including hydraulic connection with the basement. Also, the assumption of incompressible grains for rocks overestimates the induced pore pressure and normal stress reduction. In some cases, this causes overestimation of faults tendency for failure.

As a practical application for the model, the 2011 Prague, Oklahoma sequence is analyzed. Using the available data on the in-situ stress and pore pressure gradient, also Wilzetta fault geometry, it is found that reported injection volume is enough for induced fault reactivation. For injection into an open or semi-restricted reservoir (Arbuckle group), the induced earthquake happens on the same part

of the Wilzetta fault but in 2001, almost 10 years before the main sequence. While injection into a bounded reservoir leads to an event in 2011 that is in agreement with observations.

In the numerical modeling, some assumptions were made that can be modified in future work. First, we considered a constant property for the fault which is not always the case. It has been shown that rocks show different responses at various depths due to confining a temperature (e.g. Kolawole et al. 2019). So, considering these variations can modify the accuracy of the model output. Second, the analysis is quasi-static, while seismicity is a dynamic phenomenon. Conducting dynamic analysis results in more realistic results.

In addition, a 3D distinct element model was used in this work to analyze the shear stimulation process during a novel test developed and performed at the Reservoir Geomechanics and Seismicity Research lab (RGSRG Lab) at the University of Oklahoma (YU and Ghassemi 2018). The numerical tests were performed for Sierra White Granite. The numerical results reproduced the general trend of the test very well, and the values of different variables such as normal and shear stress, fluid rate, normal and shear displacements were within an acceptable range. The numerical results indicate that instability on a relatively small area of the fracture can induce a slippage on the fracture which causes permanent permeability enhancement. The models can be improved by calibrating the values of the normal and shear stiffness for a better match. In the granite sample, the slippage was sudden results in an increase in fluid rate. During unloading, the enhanced permeability is retained. In the numerical model, decreasing normal stiffness enabled capturing the effects of degradation and gauge production very well. Again, conducting dynamic simulation can improve the result.

In the last section, a 3D coupled discrete element model was used to simulate an experiment (developed and performed at RGSRG Lab) that addressed the interaction of natural and approaching hydraulic fracture. The model and the lab results were in good agreement. Three distinct sections on the induced shear displacement on the natural fracture were observed. The first and second sections include before natural and hydraulic fractures hit. The third section occurs after hydraulic and natural

fractures hit, and fluid flows in the natural fracture. This fluid flow can slippage on the natural fracture which is more pronounced than previous shear displacements.

References

Ake, J., Mahrer, K., O'Connell, D., & Block, L. (2005). Deep-injection and closely monitored induced seismicity at Paradox Valley, Colorado. Bulletin of the Seismological Society of America, 95(2), 664-683.

Alt, R. C., & Zoback, M. D. (2017). In situ stress and active faulting in Oklahoma. Bulletin of the Seismological Society of America, 107(1), 216-228.

Atkinson, G. M., Eaton, D. W., Ghofrani, H., Walker, D., Cheadle, B., Schultz, R., ... & Kao, H. (2016). Hydraulic fracturing and seismicity in the Western Canada Sedimentary Basin. Seismological research letters, 87(3), 631-647.

Batchelor, G. K. (1967). 1967, An Introduction to Fluid Dynamics. Cambridge: Cambridge University Press.

Bachu, S. (2008). CO2 storage in geological media: Role, means, status and barriers to deployment. Progress in energy and combustion science, 34(2), 254-273.

Barton, N., Bandis, S., & Bakhtar, K. (1985, June). Strength, deformation and conductivity coupling of rock joints. In International journal of rock mechanics and mining sciences & geomechanics abstracts (Vol. 22, No. 3, pp. 121-140). Pergamon.

Bauer, S. J., Huang, K., Chen, Q., Ghassemi, A., & Barrow, P. (2016, June). Experimental and Numerical Investigation of Hydro-Thermally Induced Shear Stimulation. In 50th US Rock Mechanics/Geomechanics Symposium. American Rock Mechanics Association.

Bickle, M. J. (2009). Geological carbon storage. Nature Geoscience, 2(12), 815-818.

Biot, M. A. (1941). General theory of three‐dimensional consolidation. Journal of applied physics, 12(2), 155-164.

Bear, J. (2013). Dynamics of fluids in porous media. Courier Corporation.

Benson, S. M., & Cole, D. R. (2008). CO2 sequestration in deep sedimentary formations. Elements, 4(5), 325-331.

Brown, D. W., Duchane, D. V., Heiken, G., & Hriscu, V. T. (2012). Mining the earth's heat: hot dry rock geothermal energy. Springer Science & Business Media.

Bruel, D. (1995). Heat extraction modelling from forced fluid flow through stimulated fractured rock masses: application to the Rosemanowes hot dry rock reservoir. Geothermics, 24(3), 361-374.

Cappa, F. (2009). Modelling fluid transfer and slip in a fault zone when integrating heterogeneous hydromechanical characteristics in its internal structure. Geophysical Journal International, 178(3), 1357-1362.

Carder, D. S. (1945). Seismic investigations in the Boulder Dam area, 1940-1944, and the influence of reservoir loading on local earthquake activity. Bulletin of the Seismological Society of America, 35(4), 175-192.

Carr, J. E., McGovern, H. E., Gogel, T., & Doveton, J. H. (1986). Geohydrology of and potential for fluid disposal in the Arbuckle aquifer in Kansas (No. 86-491). US Geological Survey,.

Carrell, J. R. 2014. Field-scale hydrogeologic modeling of water injection into the Arbuckle zone of the midcontinent (Doctoral dissertation, University of Oklahoma).

Chang, K.W. and P. Segall. 2016. Seismicity on basement faults induced by simultaneous fluid injection–extraction. Pure and Applied Geophysics, 173(8): 2,621-2,636

Chang, K.W. and P. Segall. 2016. Injection ‐ induced seismicity on basement faults including poroelastic stressing. Journal of Geophysical Research: Solid Earth, 121(4): 2,708-2,726.

Cheng, A. H. D. (2016). Poroelasticity (Vol. 27). Switzerland: Springer International Publishing.

Cheng, Q., Wang, X., & Ghassemi, A. (2019). Numerical simulation of reservoir stimulation with reference to the Newberry EGS. Geothermics, 77, 327-343.

Chester, F. M., & Logan, J. M. (1986). Implications for mechanical properties of brittle faults from observations of the Punchbowl fault zone, California. Pure and applied geophysics, 124(1), 79-106.

Cox, R. T. (1991). Possbile Triggering of Earthquakes by Underground Waste Disposal in the El Dorado, Arkansas Area. Seismological Research Letters, 62(2), 113-122.

Cundall, P. A. (1971). A computer model for simulating progressive, large-scale movement in blocky rock system. In Proceedings of the International Symposium on Rock Mechanics, 1971.

Cundall, P. A., & Strack, O. D. (1979). A discrete numerical model for granular assemblies. geotechnique, 29(1), 47-65.

Cheng, J., Zhang, H., & Wan, Z. (2018). Numerical Simulation of Shear Behavior and Permeability Evolution of Rock Joints with Variable Roughness and Infilling Thickness. Geofluids, 2018.

Dart, R. L., 1990. In Situ Stress Analysis of Wellbore Breakouts from Oklahoma and the Texas Panhandle – USGS Bulletin 1866-F, 36 p.

Dempsey, D., et al. "Modeling shear stimulation of the desert peak EGS well 27-15 using a coupled thermal-hydrological-mechanical simulator." 47th US Rock Mechanics/Geomechanics Symposium. American Rock Mechanics Association, 2013.

Deng, K., Liu, Y., Chen, X. 2020. Correlation Between Poroelastic Stress Perturbation and Multidisposal Wells Induced Earthquake Sequence in Cushing, Oklahoma. JGR.

Detournay, E. (1980, January). Hydraulic Conductivity of Closed Rock Fracture: an Experimental and Analytical Study. In Can Rock Mech Symp Proc 13th, Underground Rock Eng, The HR Rice Mem Symp.

Dycus M, B Tapp. (2013), Structural Characterization of the Wilzetta Fault Zone; Lincoln, Pottawatomie, and Creek Counties, Oklahoma. Master thesis. The University of Tulsa.

Ellsworth, W. L. (2013). Injection-induced earthquakes. Science, 341(6142).

Elsworth, D., Spiers, C. J., & Niemeijer, A. R. (2016). Understanding induced seismicity. Science, 354(6318), 1380-1381.

Esaki, T., Du, S., Mitani, Y., Ikusada, K., & Jing, L. (1999). Development of a shear-flow test apparatus and determination of coupled properties for a single rock joint. International Journal of Rock Mechanics and Mining Sciences, 36(5), 641-650.

Fan, Z., P. Eichhubl and P. Newell. 2019. Basement fault reactivation by fluid injection into sedimentary reservoirs: Poroelastic effects. Journal of Geophysical Research: Solid Earth, 124(7), pp.7354-7369.

FJÆR, E., Holt, R. M., Raaen, A. M., & Horsrud, P. (2008). Petroleum related rock mechanics. Elsevier.

Feizi Masouleh, S., D. Kumar and A. Ghassemi. 2020. Three-Dimensional Geomechanical Modeling and Analysis of Refracturing and “Frac-Hits” in Unconventional Reservoirs. Energies, 13(20), p.5352.

Frohlich, C., & Brunt, M. (2013). Two-year survey of earthquakes and injection/production wells in the Eagle Ford Shale, Texas, prior to the Mw4. 8 20 October 2011 earthquake. Earth and Planetary Science Letters, 379, 56-63.

Franseen, E. K., Byrnes, A. P., Cansler, J. R., Steinhauff, D. M., & Carr, T. R. (2004). The geology of Kansas—Arbuckle Group. Midcontinent Geoscience, 1-43.

Faulkner, D. R., Jackson, C. A. L., Lunn, R. J., Schlische, R. W., Shipton, Z. K., Wibberley, C. A. J., & Withjack, M. O. (2010). A review of recent developments concerning the structure, mechanics and fluid flow properties of fault zones. Journal of Structural Geology, 32(11), 1557-1575.

Ge, S., Liu, M., Lu, N., Godt, J. W., & Luo, G. (2009). Did the Zipingpu reservoir trigger the 2008 Wenchuan earthquake?. Geophysical research letters, 36(20).

Häring, M. O., Schanz, U., Ladner, F., & Dyer, B. C. (2008). Characterisation of the Basel 1 enhanced geothermal system. Geothermics, 37(5), 469-495.

Haddad, M. and P. Eichhubl. 2020. Poroelastic models for fault reactivation in response to concurrent injection and production in stacked reservoirs. Geomechanics for Energy and the Environment,24:100181.

Hair, T. J. 2012. Constructing a geomechanical model of the Woodford Shale, Cherokee Platform, Oklahoma, USA effects of confining stress and rock strength on fluid flow (Doctoral dissertation, Texas Christian University).

Hamilton, D. H., & Meehan, R. L. (1971). Ground rupture in the Baldwin Hills. Science, 172(3981), 333-344.

Healy, J. H., Rubey, W. W., Griggs, D. T., & Raleigh, C. B. (1968). The denver earthquakes. Science, 161(3848), 1301-1310.

Hemami, B., Feizi Masouleh, Sh., Ghassemi, A. (2021). Basement Fault Reactivation in Response to Injection into Overlying Layers. In 55th US Rock Mechanics/Geomechanics Symposium.

Hemami, B., Feizi Masouleh, Sh., Ghassemi, A. (2021). 3D Geomechanical Modeling of the Response of the Wilzetta Fault to Saltwater Disposal. Earth and Planetary Physics

Hu, L., & Ghassemi, A. (2021). Laboratory-Scale Investigation of the Slippage of a Natural Fracture Resulting from an Approaching Hydraulic Fracture. Rock Mechanics and Rock Engineering, 54(5), 2547-2558.

Hu, L., Hemami, B., Ghassemi, A., Riley, S., Kahn, D., & Langton, D. (2019, July). Experimental and Numerical Investigation of the Slippage of a Natural Fracture Resulting from an Approaching Hydraulic Fracture. In SPE/AAPG/SEG Unconventional Resources Technology Conference. OnePetro.

Häring, M. O., Schanz, U., Ladner, F., & Dyer, B. C. (2008). Characterisation of the Basel 1 enhanced geothermal system. Geothermics, 37(5), 469-495.

Hasegawa, H. S., Wetmiller, R. J., & Gendzwill, D. J. (1989). Induced seismicity in mines in Canada—an overview. pure and applied geophysics, 129(3), 423-453.

Holland, A.A., 2013. Optimal fault orientations within Oklahoma. Seismological Research Letters, 84(5), pp.876-890.

Holland, A. A., Keller Jr, G. R., Darold, A. P., Murray, K. E., & Holloway, S. D. (2014, December). Multidisciplinary approach to identify and mitigate the hazard from induced seismicity in Oklahoma. In AGU Fall Meeting Abstracts (Vol. 2014, pp. U34A-04).

Hornbach, M. J., H. R. DeShon, W.L. Ellsworth, B.W. Stump, C. Hayward, C. Frohlich, ... & J. H. Luetgert .2015. Causal factors for seismicity near Azle, Texas. Nature communications, 6(1), 1-11.

Horton, S. (2012). Disposal of hydrofracking waste fluid by injection into subsurface aquifers triggers earthquake swarm in central Arkansas with potential for damaging earthquake. Seismological Research Letters, 83(2), 250-260.

Hooker, V. E., & Johnson, C. F. (1969). Near-surface horizontal stresses including the effects of rock anisotropy (Vol. 7224). US Department of the Interior, Bureau of Mines.
Itasca PFC (Particle Flow Code in 2 and 3 Dimensions), Version 5.0, Minneapolis, Itasca Consulting Group, Inc., Minneapolis, 2014.

Hough, S. E. (2014). Shaking from injection‐induced earthquakes in the central and eastern United States. Bulletin of the Seismological Society of America, 104(5), 2619-2626.

Hornbach, K.M., H.M. Savage, G.A. Abers, and E.S. Cochran. 2013. Potentially induced earthquakes in Oklahoma, USA: Links between wastewater injection and the 2011 Mw 5.7 earthquake sequence. Geology. 41(6): 699-702.

Hsieh, P. A., Tracy, J. V., Neuzil, C. E., Bredehoeft, J. D., & Silliman, S. E. (1981, June). A transient laboratory method for determining the hydraulic properties of 'tight' rocks—I. Theory. In International Journal of Rock Mechanics and Mining Sciences & Geomechanics Abstracts (Vol. 18, No. 3, pp. 245-252). Pergamon.

Hsieh, P. A., & Bredehoeft, J. D. (1981). A reservoir analysis of the Denver earthquakes: A case of induced seismicity. Journal of Geophysical Research: Solid Earth, 86(B2), 903-920.
Itasca 3DEC (3 Dimensional Distinct Element Code), Version 5.2, Itasca Consulting Group, Inc., Minneapolis, 2016.

Itasca FLAC3D (Fast Lagrangian Analysis of Continua), Version 7.0, Itasca Consulting Group, Inc., Minneapolis, 2018.

Itasca PFC (Particle Flow Code in 2 and 3 Dimensions), Version 5.0, Minneapolis, Itasca Consulting Group, Inc., Minneapolis, 2014.

Itasca 3DEC (3 Dimensional Distinct Element Code), Version 5.2, Itasca Consulting Group, Inc., Minneapolis, 2016.

Ito, H. (2003). Inferred role of natural fractures, veins, and breccias in development of the artificial geothermal reservoir at the Ogachi Hot Dry Rock site, Japan. Journal of Geophysical Research: Solid Earth, 108(B9).

Jaeger, J. C., Cook, N. G., & Zimmerman, R. (2009). Fundamentals of rock mechanics. John Wiley & Sons.

Jing, Z., Willis‐Richards, J., Watanabe, K., & Hashida, T. (2000). A three‐dimensional stochastic rock mechanics model of engineered geothermal systems in fractured crystalline rock. Journal of Geophysical Research: Solid Earth, 105(B10), 23663-23679.

Kovach, R. L. (1974). Source mechanisms for Wilmington oil field, California, subsidence earthquakes. Bulletin of the Seismological Society of America, 64(3-1), 699-711.

Kaven, J. O., Hickman, S. H., McGarr, A. F., & Ellsworth, W. L. (2015). Surface monitoring of microseismicity at the Decatur, Illinois, CO2 sequestration demonstration site. Seismological Research Letters, 86(4), 1096-1101.

Keranen, K. M., Weingarten, M., Abers, G. A., Bekins, B. A., & Ge, S. (2014). Sharp increase in central Oklahoma seismicity since 2008 induced by massive wastewater injection. Science, 345(6195), 448-451.

Keranen, K. M., & Weingarten, M. (2018). Induced seismicity. Annual Review of Earth and Planetary Sciences, 46, 149-174.

Kerner, K., Mozley, P., Evans, J., & Person, M. (2015). Geologic Controls on Injection Related Reactivation of Basement Faults. In AAPG Annual Convention and Exhibition.

Kelkar, S., Lewis, K., Hickman, S., Davatzes, N. C., Moos, D., & Zyvoloski, G. (2012, January). Modeling coupled thermal-hydrological-mechanical processes during shear stimulation of an EGS well. In Thirty-Seventh Workshop on Geothermal Reservoir Engineering, Stanford University, Stanford.

Kim, W. Y. (2013). Induced seismicity associated with fluid injection into a deep well in Youngstown, Ohio. Journal of Geophysical Research: Solid Earth, 118(7), 3506-3518.

Kohl, T., & Hopkirk, R. J. (1995). "FRACure"—A simulation code for forced fluid flow and transport in fractured, porous rock. Geothermics, 24(3), 333-343.

Kohl, T., & Mégel, T. (2007). Predictive modeling of reservoir response to hydraulic stimulations at the European EGS site Soultz-sous-Forêts. International Journal of Rock Mechanics and Mining Sciences, 44(8), 1118-1131.

Kolawole, F., Johnston, C.S., Morgan, C.B., Chang, J.C., Marfurt, K.J., Lockner, D.A., Reches, Z. and Carpenter, B.M., 2019. The susceptibility of Oklahoma's basement to seismic reactivation. Nature Geoscience, 12(10), pp.839-844.

Koyama, T., Fardin, N., Jing, L., & Stephansson, O. (2006). Numerical simulation of shear-induced flow anisotropy and scale-dependent aperture and transmissivity evolution of rock fracture replicas. International Journal of Rock Mechanics and Mining Sciences, 43(1), 89-106.

Kumar, D., S. Feizi Masouleh, A. Ghassemi, S. Riley and B. Elliott. 2018. A 3D Geomechanical Analysis of Horizontal Well Refracturing and "Frac- Hits". In Proceedings of the 52nd U.S. Rock Mechanics /Geomechanics Symposium, Seattle, 17-20 June

Lee, S.H., A. Ghassemi. 2011. Three-dimensional thermo-poro-mechanical modeling of reservoir stimulation and induced micro-seismicity in geothermal reservoir. 36th Stanford Geothermal Workshop, Stanford, CA.

Li, T., Cai, M. F., & Cai, M. (2007). A review of mining-induced seismicity in China. International Journal of Rock Mechanics and Mining Sciences, 44(8), 1149-1171.

Liu, H. H., Rutqvist, J., Zhou, Q., & Bodvarsson, G. S. (2004). Upscaling of normal stress-permeability relationships for fracture networks obeying fractional Levy motion. In Elsevier Geo-Engineering Book Series (Vol. 2, pp. 263-268). Elsevier.

Lorenz, J. C., Teufel, L. W., & Warpinski, N. R. (1991). Regional fractures I: A mechanism for the formation of regional fractures at depth in flat-lying reservoirs. AAPG bulletin, 75(11), 1714-1737.

Loucks, R. G. (2008). Review of the lower Ordovician Ellenburger group of the Permian basin, West Texas. 2014-10-25] http://www. beg. utexas. edu/resprog/permianbasin/PBGSP_members/writ_synth/Ellenburger Draft_022206. pdf.

Lu, J., & Ghassemi, A. (2019). Coupled Thermo-Hydro-Mechanical-Seismic Modeling of Fractured Reservoir Stimulation with Application to EGS Collab. In Proceedings, 44th Workshop on Geothermal Reservoir Engineering, Stanford University, SGP-TR-214.

Lutz, S. J., Hickman, S., Davatzes, N., Zemach, E., Drakos, P., & Robertson-Tait, A. (2010, February). Rock mechanical testing and petrologic analysis in support of well stimulation activities at the Desert Peak Geothermal Field, Nevada. In Proceedings 35th workshop on geothermal reservoir engineering.

Makurat, A. (1990). Joint conductivity variation due to normal and shear deformation. In Proc. Int. Symp. Rock Joints, 1990 (pp. 535-540). Balkema.

Majer, E. L., & Peterson, J. E. (2007). The impact of injection on seismicity at The Geysers, California Geothermal Field. International Journal of Rock Mechanics and Mining Sciences, 44(8), 1079-1090.
Mandl, G., Jong, L. N. J., & Maltha, A. (1977). Shear zones in granular material. Rock Mechanics. Volume, 9, 95-144.

Maxwell, S. C., Urbancic, T. I., Steinsberger, N., & Zinno, R. (2002, January). Microseismic imaging of hydraulic fracture complexity in the Barnett shale. In SPE annual technical conference and exhibition. Society of Petroleum Engineers.

Mitchell, T. M., & Faulkner, D. R. (2009). The nature and origin of off-fault damage surrounding strike-slip fault zones with a wide range of displacements: A field study from the Atacama fault system, northern Chile. Journal of Structural Geology, 31(8), 802-816.

Murray, K. E. (2014). Class II underground injection control well data for 2010–2013 by geologic zones of completion, Oklahoma. Oklahoma Geological Survey Open File Report OF1, 32.

Murray, K. E., & Holland, A. A. (2014). Inventory of class II underground injection control volumes in the midcontinent.

National Research Council. (2013). Induced seismicity potential in energy technologies. National Academies Press.

Nelson, P. H., Gianoutsos, N. J., & Drake, R. M. (2015). Underpressure in Mesozoic and Paleozoic rock units in the Midcontinent of the United States. AAPG Bulletin, 99(10), 1861-1892.

Norbeck, J. H. (2016). Hydromechanical and frictional faulting behavior of fluid-injection-induced earthquakes (Doctoral dissertation, Stanford University).

Ohtake, M. (1974). Seismic activity induced by water injection at Matsushiro, Japan. Journal of Physics of the Earth, 22(1), 163-176

Oklahoma Corporation Commission, OCC: https://oklahoma.gov/occ/divisions/oil-gas/oil-gas-data.html

Ortiz, J. P., Person, M. A., Mozley, P. S., Evans, J. P., & Bilek, S. L. (2019). The role of fault‐zone architectural elements on pore pressure propagation and induced seismicity. Groundwater, 57(3), 465-478.

Perrin, C., Manighetti, I., & Gaudemer, Y. (2016). Off-fault tip splay networks: A genetic and generic property of faults indicative of their long-term propagation. Comptes Rendus Geoscience, 348(1), 52-60.

Petersen, M. D., Mueller, C. S., Moschetti, M. P., Hoover, S. M., Shumway, A. M., McNamara, D. E., ... & Rukstales, K. S. (2017). 2017 one‐year seismic‐hazard forecast for the central and eastern United States from induced and natural earthquakes. Seismological Research Letters, 88(3), 772-783.

Petrie, E. S., Bradbury, K. K., Cuccio, L., Smith, K., Evans, J. P., Ortiz, J. P., ... & Mozley, P. (2020). Geologic characterization of nonconformities using outcrop and core analogs: hydrologic implications for injection-induced seismicity. Solid Earth, 11(5), 1803-1821.

Pine, R. J., & Batchelor, A. S. (1984, October). Downward migration of shearing in jointed rock during hydraulic injections. In International Journal of Rock Mechanics and Mining Sciences & Geomechanics Abstracts (Vol. 21, No. 5, pp. 249-263). Pergamon.

Pratt, W. E., & Johnson, D. W. (1926). Local subsidence of the Goose Creek oil field. The Journal of Geology, 34(7, Part 1), 577-590.

Rachez, X., & Gentier, S. (2010, April). 3D-hydromechanical behavior of a stimulated fractured rock mass.

Raleigh, C. B., Healy, J. H., & Bredehoeft, J. D. (1976). An experiment in earthquake control at Rangely, Colorado. Science, 191(4233), 1230-1237.

Riahi, A., & Damjanac, B. (2013, May). Numerical study of interaction between hydraulic fracture and discrete fracture network. In ISRM International Conference for Effective and Sustainable Hydraulic Fracturing. OnePetro.

Rice, J. R., & Cleary, M. P. (1976). Some basic stress diffusion solutions for fluid‐saturated elastic porous media with compressible constituents. Reviews of Geophysics, 14(2), 227-241.

Rinaldi, A. P., Jeanne, P., Rutqvist, J., Cappa, F., & Guglielmi, Y. (2014). Effects of fault‐zone architecture on earthquake magnitude and gas leakage related to CO2 injection in a multi‐layered sedimentary system. Greenhouse Gases: Science and Technology, 4(1), 99-120.

Rubinstein, J. L., & Mahani, A. B. (2015). Myths and facts on wastewater injection, hydraulic fracturing, enhanced oil recovery, and induced seismicity. Seismological Research Letters, 86(4), 1060-1067.

Rutledge, J. T., Phillips, W. S., & Mayerhofer, M. J. (2004). Faulting induced by forced fluid injection and fluid flow forced by faulting: An interpretation of hydraulic-fracture microseismicity, Carthage Cotton Valley gas field, Texas. Bulletin of the Seismological Society of America, 94(5), 1817-1830.

Rutqvist, J., Wu, Y. S., Tsang, C. F., & Bodvarsson, G. (2002). A modeling approach for analysis of coupled multiphase fluid flow, heat transfer, and deformation in fractured porous rock. International Journal of Rock Mechanics and Mining Sciences, 39(4), 429-442.

Safari, R., A. Ghassemi. 2016. Three-Dimensional poroelastic modeling of injection induced permeability enhancement and micro-seismicity. Int. J. Rock Mechanics. 84, 47–58.

Savage, H. M., & Brodsky, E. E. (2011). Collateral damage: Evolution with displacement of fracture distribution and secondary fault strands in fault damage zones. Journal of Geophysical Research: Solid Earth, 116(B3).

Seeber, L., Armbruster, J. G., & Kim, W. Y. (2004). A fluid-injection-triggered earthquake sequence in Ashtabula, Ohio: Implications for seismogenesis in stable continental regions. Bulletin of the Seismological Society of America, 94(1), 76-87.

Segall, P. (1989). Earthquakes triggered by fluid extraction. Geology, 17(10), 942-946.

Simpson, D. W. (1986). Triggered earthquakes. Annual Review of Earth and Planetary Sciences, 14(1), 21-42.

Simpson, D. W., Leith, W. S., & Scholz, C. H. (1988). Two types of reservoir-induced seismicity. Bulletin of the Seismological Society of America, 78(6), 2025-2040.

Sumy, D. F., Cochran, E. S., Keranen, K. M., Wei, M., & Abers, G. A. (2014). Observations of static Coulomb stress triggering of the November 2011 M5. 7 Oklahoma earthquake sequence. Journal of Geophysical Research: Solid Earth, 119(3), 1904-1923.

Sun, X., & Hartzell, S. (2014). Finite‐fault slip model of the 2011 Mw 5.6 Prague, Oklahoma earthquake from regional waveforms. Geophysical Research Letters, 41(12), 4207-4213.

Tester, J. W. (2006). The Future of Geothermal Energy, Part 1, Summary and Part 2, Full Report. Cambridge, MA: Massachusetts Institute of Technology.

Tester, J. W., Murphy, H. D., Grigsby, C. O., Potter, R. M., & Robinson, B. A. (1989). Fractured geothermal reservoir growth induced by heat extraction. SPE reservoir engineering, 4(01), 97-104.

Toomey, A., Fowler, S., Gestel, J. P. V., Kristiansen, T. G., Brew, G., Horiuchi, M., & Levine, R. (2017). Stress arching and its impact on 4D seismic amplitudes and traveltimes. The Leading Edge, 36(11), 895-901.

Van Poollen, H. K., & Hoover, D. B. (1970). Waste disposal and earthquakes at the rocky mountain arsenal, Derby, Colorado. Journal of Petroleum Technology, 22(08), 983-993.

van Thienen-Visser, K., & Breunese, J. N. (2015). Induced seismicity of the Groningen gas field: History and recent developments. The Leading Edge, 34(6), 664-671.

Verde, A., & Ghassemi, A. (2015). Modeling injection/extraction in a fracture network with mechanically interacting fractures using an efficient displacement discontinuity method. International Journal of Rock Mechanics and Mining Sciences, 77, 278-286.

Von Schönfeldt, H., Kehle, R. O., & Gray, K. E. (1971). Mapping of Stress Field in the Upper Earth Crust of the US. Center for Earth Sciences and Engineering, University of Texas.

Warpinski, N. (2009). Microseismic monitoring: Inside and out. Journal of Petroleum Technology, 61(11), 80-85.

Warpinski, N. R., Du, J., & Zimmer, U. (2012). Measurements of hydraulic-fracture-induced seismicity in gas shales. SPE Production & Operations, 27(03), 240-252.

Weng, X., Sesetty, V., & Kresse, O. (2015, November). Investigation of shear-induced permeability in unconventional reservoirs. In 49th US Rock Mechanics/Geomechanics Symposium. American Rock Mechanics Association.

Witherspoon, P. A., Wang, J. S., Iwai, K., & Gale, J. E. (1980). Validity of cubic law for fluid flow in a deformable rock fracture. Water resources research, 16(6), 1016-1024.

Ye, Z., Janis, M., Ghassemi, A., & Riley, S. (2017, September). Laboratory investigation of fluid flow and permeability evolution through shale fractures. In Unconventional Resources Technology Conference, Austin, Texas, 24-26 July 2017 (pp. 2038-2052). Society of Exploration Geophysicists, American Association of Petroleum Geologists, Society of Petroleum Engineers.

Ye, Z., & Ghassemi, A. (2018). Experimental study on injection-induced fracture propagation and coalescence for EGS stimulation. In Proceeding: 43rd Workshop on Geothermal Reservoir Engineering, Stanford, California, USA.

Ye, Z., & Ghassemi, A. (2019, October). Investigation of Micro-Seismicity and Permeability Evolution in Shale Fractures During Stimulation. In Unconventional Resources Technology Conference, Denver, Colorado, 22-24 July 2019 (pp. 32-42). Unconventional Resources Technology Conference (URTeC); Society of Exploration Geophysicists.

Ye, Z., Sesetty, V., & Ghassemi, A. (2018, January). Experimental and numerical investigation of shear stimulation and permeability evolution in shales. In SPE Hydraulic Fracturing Technology Conference and Exhibition. Society of Petroleum Engineers.

Yehya, A., Yang, Z., & Rice, J. R. (2018). Effect of fault architecture and permeability evolution on response to fluid injection. Journal of Geophysical Research: Solid Earth, 123(11), 9982-9997.

Ziagos, J., Phillips, B. R., Boyd, L., Jelacic, A., Stillman, G., & Hass, E. (2013, February). A technology roadmap for strategic development of enhanced geothermal systems. In Proceedings of the 38th Workshop on Geothermal Reservoir Engineering, Stanford, CA (pp. 11-13).